

Functional MRI : Methods and Applications



Stuart Clare

**Submitted to the University of Nottingham
for the degree of Doctor of Philosophy**

October 1997

Table of Contents

Abstract.....	1
Acknowledgements.....	2
Chapter 1.....	3
Introduction.....	3
1.1 Probing the Secrets of the Brain.....	3
1.2 Pictures of the Mind.....	3
1.3 The Scope of this Thesis.....	4
1.4 References.....	5
Chapter 2.....	6
Principles of Magnetic Resonance Imaging.....	6
2.1 Introduction.....	6
2.2 Nuclear Magnetic Resonance.....	6
2.3 Magnetic Resonance Imaging.....	17
2.4 Image Contrast in Biological Imaging.....	31
2.5 Image Artefacts.....	36
2.6 Imaging Hardware.....	39
2.7 Safety Considerations in MRI.....	43
2.8 References.....	45
Chapter 3.....	48
Magnetic Resonance Imaging of Brain Function.....	48
3.1 Introduction to Neuroimaging.....	48
3.2 The Structure of the Brain.....	53
3.3 Functional Magnetic Resonance Imaging.....	63
3.4 References.....	69
Chapter 4.....	73
Optimisation of MRI for Functional Imaging.....	73
4.1 Introduction.....	73
4.2 The Effect of Echo Time on fMRI Signal.....	73
4.3 Artefact Reduction in fMRI Data.....	80
4.4 Fast IR Sequence for Anatomical Reference Scans.....	91
4.5 Standard fMRI Protocol.....	92
4.6 References.....	93
Chapter 5.....	95
Functional MRI using Interleaved EPI.....	95
5.1 Introduction.....	95
5.2 The Theory of Interleaved EPI.....	95
5.3 The Benefits and Problems of Using Interleaved EPI.....	100
5.4 Implementation at 3.0 Tesla.....	107
5.5 Summary.....	109
5.6 References.....	109

Table of Contents

Chapter 6.....	111
The Analysis of fMRI Data.....	111
6.1 Introduction.....	111
6.2 Preparing MR Images for Statistical Analysis.....	112
6.3 Statistical Analysis of the Data.....	117
6.4 Statistical Inference.....	130
6.5 Summary.....	138
6.6 References.....	139
Chapter 7.....	142
Functional MRI of Motor Function.....	142
7.1 Introduction.....	142
7.2 Methods.....	143
7.3 Results.....	148
7.4 Discussion.....	149
7.5 References.....	150
Chapter 8.....	151
Discussion.....	151

Abstract

The technique of functional magnetic resonance imaging is rapidly moving from one of technical interest to wide clinical application. However, there are a number of questions regarding the method that need resolution. Some of these are investigated in this thesis.

High resolution fMRI is demonstrated at 3.0 T, using an interleaved echo planar imaging technique to keep image distortion low. The optimum echo time to use in fMRI experiments is investigated using a multiple gradient echo sequence to obtain six images, each with a different echo time, from a single free induction decay. The same data are used to construct T_2^* maps during functional stimulation. Various techniques for correcting the N/2 ghost are tested for use in fMRI experiments, and a method for removing the image artefact caused by external r.f. interference in a non-linearly sampled matrix is presented.

The steps in the analysis of fMRI data are detailed, and two new non-directed analysis techniques, particularly for data from single events, as opposed to epoch based paradigms, are proposed. The theory behind software that has been written for fMRI data analysis is also given.

Finally, some of the results from an fMRI study into the initiation of movement are presented, illustrating the power of single event experiments in the separation of cognitive processes.

Acknowledgements

I would like to thank my supervisors, Prof. Peter Morris and Dr. Richard Bowtell, for the support and advice they have provided throughout the duration of my Ph.D. I am also indebted to Dr. Jon Hykin for teaching me the art of functional MRI and to Dr. Miles Humberstone for providing the impetus for much of my work. I would also like to thank all the people with whom I have worked over the past three years without whom none of this work could have been done, and particularly those who have patiently laid in the scanner for my experiments. Finally I would like to thank the University of Nottingham for their funding.

I would also like to thank Peter Hobden (FMRIB, University of Oxford) for generating new graphics for some of the figures in this thesis, particularly in Chapter 3.

Chapter 1

Introduction

1.1 Probing the Secrets of the Brain

The brain is the most fascinating, and least understood, organ in the human body. For centuries, scientists and philosophers have pondered the relationship between behaviour, emotion, memory, thought, consciousness, and the physical body. In the Middle Ages there was much controversy as to whether the soul was located in the brain or in the heart. As ideas developed however, it was suggested that mental processes were located in the ventricles of the brain. According to this theory 'common sense' was located in the lateral ventricles, along with imagination accommodated in the posterior part. The third ventricle was the seat of reasoning, judgement and thought, whilst memory was contained in the fourth ventricle.

It was in the 17th century that Thomas Willis proposed that various areas of the cortex of the brain had specific functions, in particular the circle of vessels at the base of the brain which now bear his name. In the 19th century, Gall put forward his 'science' of phrenology, where the presence or absence of bumps on the skull revealed the strength or weakness of various mental and moral faculties. Despite the dubious method he used, Gall put forward two very important concepts: that the brain was the seat of all intellectual and moral faculties; and that particular activities could be localised to some specific region of the cerebral cortex.

The study of brain function progressed in the late 19th century through work involving the stimulation of the cortex of animal brains using electrical currents. This led to the mapping of motor function in animals and, later, in humans. These results however contained many inconsistencies. More reliable work was carried out in the mid 20th century by Penfield, who managed to map the motor and somatosensory cortex using cortical stimulation of patients undergoing neurosurgery. In the latter half of this century, most progress in the study of brain function has come from patients with neurological disorders or from electrode measurements on animals. It has only been in the last decade or so that brain imaging techniques have allowed the study of healthy human subjects.

1.2 Pictures of the Mind

The impact of medical imaging on the field of neuroscience has been considerable. The advent of x-ray computed tomography (CT) in the 1970's allowed clinicians to see features inside the heads of patients without the need for surgery. By making the small step of placing the source of radiation within the patient, x-ray CT became autoradiography, so that now not only structure but also blood flow and metabolism could be followed in a relatively non-invasive way. A big step forward was made by choosing to use a positron emitter as the radioisotope. Since a positron almost immediately annihilates with an electron, emitting two photons at 180 degrees to each other, much better localisation of the radioisotope within the scanner is obtained. Using labelled water, positron emission tomography (PET) became the first useful technique which allowed researchers to produce maps of the mind, by measuring blood flow during execution of simple cognitive tasks. Since local blood flow is intimately related to cortical activity, regions of high regional blood flow indicate the area in the cortex responsible for the task being performed.

At around the same time, another technique which promised even better anatomical pictures of the brain was being developed. Magnetic resonance imaging (MRI), based on the phenomenon of nuclear magnetic resonance, produces images of the human body with excellent soft tissue

contrast, allowing neurologists to distinguish between grey and white matter, and brain defects such as tumours. Since MRI involves no ionising radiation, the risks to the subject are minimised. The development of contrast agents suitable for dynamic MRI studies, and improvements in the speed of imaging, opened up the possibility of using the technique for functional brain studies. In 1991 the first experiment using MRI to study brain function was performed, imaging the visual cortex whilst the subject was presented with a visual stimulus. A contrast agent was used in this first study, but it was not much later when the first experiment was carried out using the blood as an endogenous contrast agent. The haemoglobin in the blood has different magnetic properties depending on whether it is oxygenated or not; these differences affect the signal recorded in the MR image. By imaging a subject at rest and whilst carrying out a specific task, it became possible to image brain function in a completely non-invasive way.

The 'pictures of the mind' that have been produced over the past few years have started to make a big impact on the way neuroscience is approached. There are, however, still areas of the technique of functional MRI that require refinement. The fast imaging method of echo planar imaging, which is essential for fast dynamic studies, can suffer from poor image quality. In addition some areas of the brain are not visible on its scans. The mechanisms behind the observed activation response are not well understood, and there are issues involved in the way that the data from such experiments are analysed. However, the potential of fMRI, alongside that of PET, means that the study of the human brain has entered a new era, offering new insights into neurology, psychiatry, psychology and perhaps even contributing to the philosophical debate about the relationship between mind and brain.

1.3 The Scope of this Thesis

The material presented in this thesis covers a number of the aspects concerning the technique and application of functional MRI.

The second chapter covers the theory of magnetic resonance imaging, including the classical and quantum mechanical descriptions of nuclear magnetic resonance, and the variety of techniques that can be used to image biological samples. The origin of contrast in MRI is then described and the sources of image artefacts discussed. The chapter ends with two sections on practical imaging, one on the hardware that is required for MRI and another on the safety aspects of putting human volunteers inside MR scanners.

Chapter Three is concerned primarily with brain function. An outline of the main techniques used for functional neuroimaging, including positron emission tomography, magnetoencephalography and magnetic resonance spectroscopy, is given. Some basic aspects of neuroscience are then covered, and the main structures in the brain, its biochemistry and functional organisation are described. The technique of fMRI is covered in detail, describing how brain activity affects the contrast in the MR image, how experiments are performed and how the data are analysed.

The three chapters that follow cover improvements in the technique of fMRI. Chapter Four deals with the optimisation of MRI for functional brain imaging. Experiments that determine the optimum image echo time (TE) to use in an fMRI study are described. These use a technique that acquires six images, each with a different echo time, in a single shot. The reduction of image artefact is the subject of the next section. A number of post-processing techniques that reduce the Nyquist or N/2 ghost are compared for effectiveness on fMRI data sets and a method for removing the bands on images that result from external r.f. interference is demonstrated. Finally in this chapter, a technique for the fast acquisition of inversion recovery anatomical reference scans is described.

The implementation of the technique of interleaved echo planar imaging is the subject of the fifth chapter. The reasons for using the technique are explained, and the problems that have arisen in its use for high resolution, low distortion fMRI are discussed. Chapter Six covers aspects relating to the analysis of fMRI data to produce statistically robust results. The theory and implementation of a number of image pre-processing techniques is described and the statistical techniques that can be used to detect regions of activation are outlined. Two new statistical analysis methods are described, both of which make no assumptions as to the shape of the activation response that is expected. The theory behind software that is used to draw inference from the resulting statistics is explained and ways of presenting the final data are described.

Chapter Seven presents the results from an fMRI study of motor function in normal volunteers and patients with Parkinson's disease. Aspects of the stimulus paradigm design and implementation are covered, as is the optimisation of the imaging and experimental protocol.

1.4 References

The material on the history of the study of brain function comes from:

- Clarke, E. and Dewhurst, K. (1972) 'An Illustrated History of Brain Function', Sandford Publications, Oxford.

Detailed references on the history of PET and fMRI are given in Chapter 3, however basic introductions to these topics are given in:

- Ter-Pogossian, M. M., Raichle, M. E. and Sobel, B. E. Positron Emission Tomography. *Scientific American* October 1980.
- Pykett, I. L. NMR Imaging in Medicine. *Scientific American* May 1982.
- Raichle, M. E. Visualizing the Mind. *Scientific American* April 1994.

Chapter 2

Principles of Magnetic Resonance Imaging

2.1 Introduction

The property of Nuclear Magnetic Resonance (NMR) was first described by Purcell [1] and Bloch [2] in 1946, work for which they received the Nobel prize in 1952. Since then NMR has become a powerful tool in the analysis of chemical composition and structure. In 1973 Lauterbur [3] and Mansfield [4] used the principles of NMR to describe a technique for determining physical structure. Since then Magnetic Resonance Imaging (MRI) has been used in many biomedical, chemical and engineering applications.

In this chapter the theoretical foundations, first of nuclear magnetic resonance and then magnetic resonance imaging are explained. Then the practical implementation of MRI is outlined, and an explanation of the artefacts that affect MR images given. The chapter ends with a discussion of the safety of MRI as a medical imaging modality. This chapter serves only as an outline of the basic principles of nuclear magnetic resonance spectroscopy and imaging. More detail is found in the standard texts on the subject, such as those by Abragam [5], and Callaghan [6].

2.2 Nuclear Magnetic Resonance

2.2.1 The Quantum Mechanical Description of NMR

The quantum mechanical description of atomic nuclei, as described by Dirac in 1930, predicted the property of spin angular momentum. In fact the property of electron spin was observed six years earlier by Stern and Gerlach [7], who passed a beam of neutral atoms through a non-uniform magnetic field, and observed the effect of half-integral angular momentum, that could not be explained by the previously accepted Bohr model.

This spin angular momentum is characterised by the spin quantum number I , such that the total spin angular momentum is Ih . The value of I is an intrinsic property of the nucleus, examples of which are given in Table 2.1.

Nucleus	Spin Quantum Number I
^1H	$1/2$
^2H	1
^{12}C	0
^{13}C	$1/2$
^{19}F	$1/2$
^{31}P	$1/2$

Table 2.1 Spin quantum numbers for some atomic nuclei

To exhibit the property of magnetic resonance the nucleus must have a non-zero value of I . As far as medical applications are concerned, the proton (^1H) is the nucleus of most interest, because of its high natural abundance. However, other nuclei have been studied, most noticeably ^{13}C whose low natural abundance relative to ^{12}C makes it suitable for tracer studies.

The magnitude of the spin angular momentum is given by

$$|\mathbf{P}| = \hbar \sqrt{I(I+1)} \quad (2.1)$$

but since \mathbf{P} is a vector, its orientation must be taken into account. In a magnetic field, applied along the z axis, the possible values of the z-components of the angular momentum are given by

$$P_z = \hbar m_I$$

where

$$m_I = I, (I-1), (I-2), \dots, -I. \quad (2.2)$$

So for the proton, with spin 1/2, there are two possible values for P_z , that is $\pm \frac{1}{2}\hbar$. The eigenfunction describing the spin state of the proton nucleus can be written as $|+\frac{1}{2}\rangle$ or $|-\frac{1}{2}\rangle$, and since in quantum mechanics every physical observable has an associated operator, we can write an eigenvalue equation to describe the observation of the spin state as

$$I_z |m_I\rangle = m_I |m_I\rangle \quad (2.3)$$

where I_z is the operator describing measurement of the angular momentum along the z axis. There are similar operators for measuring the angular momentum along the x and y axes, so we have a range of eigenvalue equations for a spin 1/2 system as follows:

$$\begin{aligned} I_x |+\frac{1}{2}\rangle &= +\frac{1}{2} |+\frac{1}{2}\rangle & I_x |-\frac{1}{2}\rangle &= -\frac{1}{2} |-\frac{1}{2}\rangle \\ I_x |+\frac{1}{2}\rangle &= +\frac{1}{2} |-\frac{1}{2}\rangle & I_x |-\frac{1}{2}\rangle &= +\frac{1}{2} |+\frac{1}{2}\rangle \\ I_y |+\frac{1}{2}\rangle &= +\frac{1}{2}i |-\frac{1}{2}\rangle & I_y |-\frac{1}{2}\rangle &= -\frac{1}{2}i |+\frac{1}{2}\rangle \\ i &= \sqrt{-1} \end{aligned} \quad (2.4)$$

To measure the energy of the spin system it is necessary to construct a Hamiltonian operator. The form of the Hamiltonian can be derived from classical electromagnetism for the energy of a magnetic moment placed in a magnetic field.

Nuclei have a magnetic moment, μ , which is proportional to the angular momentum,

$$\mu = \gamma \mathbf{P} \quad (2.5)$$

Nuclei with the constant of proportionality, γ , being called the magnetogyric ratio. The magnetogyric ratio is a property of the particular nucleus, and has a value of 2.675×10^8 rad/s/T for protons. When this magnetic moment is placed in a magnetic field, \mathbf{B} , it has energy

$$E = -\boldsymbol{\mu} \cdot \mathbf{B} \quad (2.6)$$

and so by combining equations 2.5 and 2.6 a Hamiltonian can be defined as

$$H = -\hbar \boldsymbol{\beta} \cdot \mathbf{I} \quad (2.7)$$

Since by definition the B field is applied parallel to the z-axis the Hamiltonian becomes

$$H = -\hbar \beta_z I_z \quad (2.8)$$

and is known as the Zeeman Hamiltonian. Now using the Schrödinger equation, the energy of the eigenstate is found.

$$\begin{aligned} H|m_I\rangle &= E|m_I\rangle \\ &= -\hbar \beta_z I_z |m_I\rangle \\ &= -\hbar \beta_z m_I |m_I\rangle \\ \therefore E &= -\hbar \beta_z m_I. \end{aligned} \quad (2.9)$$

So for a proton with $m_I = \pm \frac{1}{2}$, a transition between the two states represents a change in energy

$$\Delta E = \hbar \beta_z \quad (2.10)$$

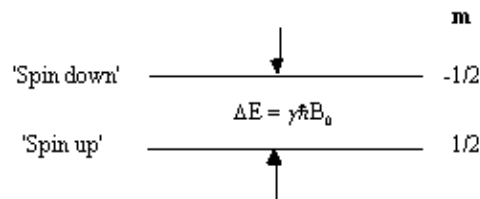


Figure 2.1 Energy level diagram for a proton under the Zeeman interaction.

This is called the Zeeman splitting, and is shown as an energy level diagram in Figure 2.1. These two states are given a variety of labels, but most commonly referred to as 'spin up', and 'spin down', with the spin-down state having a higher energy than the spin-up state. Transitions between the two states can be induced by absorption or emission of a photon of frequency ν_0 , such that

$$\begin{aligned} \Delta E &= \hbar \beta_z = h \nu \\ \therefore \nu &= \frac{\gamma}{2\pi} B_z \end{aligned}$$

(2.11)

Expressing the frequency in angular terms gives the Larmor equation which underpins the whole of NMR

$$\omega = \gamma B_0$$

(2.12)

the characteristic frequency, ω , being the Larmor frequency. The magnetic field, labelled B_0 , is still assumed to be applied along the z axis, and is now subscripted with a '0' to distinguish it from the applied radio frequency field which will be introduced later.

This description of the quantum mechanical behaviour of an atomic nucleus leads to the way NMR is performed. Transitions between the two energy states, spin-up and spin-down, can occur by absorption or emission of electromagnetic radiation of frequency given by the Larmor equation. This frequency depends, for a given species of nuclei, purely on the applied magnetic field. It is the strength of the field experienced by the nucleus that enables structure to be determined in spectroscopy experiments, and position to be found in imaging experiments.

In a real system there is not just one nucleus in isolation, but many nuclei all of which could occupy a particular spin state. This means that the theory must be extended to consider an ensemble of spins.

To do this a single eigenstate Ψ , which is a linear combination of the possible spin states for a single nucleus is defined

$$|\Psi\rangle = \sum_{m_I} a_{m_I} |m_I\rangle$$

(2.13)

When making a measurement on such a system, the expectation value of the operation on this superposition of states is

$$\langle \Psi | I_z | \Psi \rangle = \sum_{m_I} |a_{m_I}|^2 m_I$$

(2.14)

where the value $|a_{m_I}|^2$ represents the probability of finding a single nucleus in the state m_I . So for the case of a proton, with two spin states

$$|\Psi\rangle = a_{+\frac{1}{2}} |+\frac{1}{2}\rangle + a_{-\frac{1}{2}} |-\frac{1}{2}\rangle$$

(2.15)

The ratio of the populations of the two energy states from Boltzman statistics is

$$\begin{aligned} \frac{|a_{-\frac{1}{2}}|^2}{|a_{+\frac{1}{2}}|^2} &= \exp\left(\frac{-\Delta E}{k_B T}\right) \\ &= \exp\left(\frac{-\hbar \gamma B_0}{k_B T}\right) \\ &\approx 1 - \frac{\hbar \gamma B_0}{k_B T} \quad \text{provided } k_B T \gg \hbar \gamma B_0. \end{aligned}$$

(2.16)

so the difference between the number of spins in the spin-up state and the spin-down state is

$$\begin{aligned} |a_{+\frac{1}{2}}|^2 - |a_{-\frac{1}{2}}|^2 &\approx |a_{+\frac{1}{2}}|^2 \cdot \frac{\hbar \gamma B_0}{k_B T} \\ &\approx \frac{\hbar \gamma B_0}{2k_B T}. \end{aligned}$$

(2.17)

If we now assume that all the 'spin up' nuclei have a magnetic moment of $\frac{1}{2}\hbar\gamma$ and the 'spin down' nuclei have a magnetic moment of $-\frac{1}{2}\hbar\gamma$, then we can write the bulk magnetisation of the ensemble as

$$\begin{aligned} \mathbf{M} &= N \left(\frac{\hbar \gamma}{2}\right) \left(\frac{\hbar \gamma B_0}{2k_B T}\right) \\ &\approx N \left(\frac{\hbar \gamma}{2}\right)^2 \frac{B_0}{k_B T} \end{aligned}$$

(2.18)

where N is the number of spins in the ensemble. Being able to treat the behaviour of all the spins in the system in terms of magnetisation allows a transfer from a quantum mechanical to a classical description of NMR. The advantage of the classical description is that it gives a simpler picture of the NMR experiment.

2.2.2 The Classical Description of NMR

If the spin magnetisation vector \mathbf{M} is placed in a magnetic field \mathbf{B} , \mathbf{M} will experience a torque. The equation of motion for \mathbf{M} can be written

$$\frac{d\mathbf{M}}{dt} = \mathbf{M} \times \mathbf{B}$$

(2.19)

If \mathbf{B} is a static (time-independent) field along the z axis such that $\mathbf{B} = B_0 \mathbf{k}$ then equation 2.19 becomes

$$\frac{dM_x}{dt} = \gamma M_y B_0 \quad \frac{dM_y}{dt} = -\gamma M_x B_0 \quad \frac{dM_z}{dt} = 0 \quad (2.20)$$

which has solutions

$$\begin{aligned} M_x(t) &= M_x(0) \cos \omega_0 t + M_y(0) \sin \omega_0 t \\ M_y(t) &= -M_x(0) \sin \omega_0 t + M_y(0) \cos \omega_0 t \\ M_z(t) &= M_z(0) \end{aligned} \quad (2.21)$$

where $\omega_0 = \gamma B_0$. These equations describe the precession of the magnetisation vector about the z axis as shown in Figure 2.2. The angular frequency of the precession is identical to the Larmor frequency derived in the quantum mechanical description above (equation 2.12), showing how the classical and quantum mechanical pictures coincide.

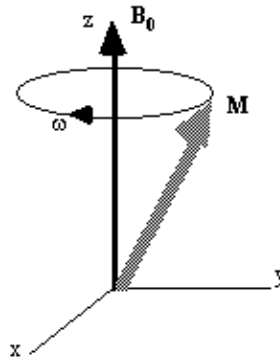


Figure 2.2 Precession of the magnetisation vector in a static magnetic field aligned along the z-axis.

Now, as well as the static B_0 field applied along z, consider a time varying field B_1 , applied perpendicularly to B_0 and oscillating at ω_0 . If only the circularly polarised component of B_1 rotating in the same direction as the precessing magnetisation vector is considered

$$\mathbf{B}_1(t) = B_1 \cos \omega_0 t \mathbf{i} - B_1 \sin \omega_0 t \mathbf{j} \quad (2.22)$$

which when put into equation 2.19 yields

$$\begin{aligned} \frac{dM_x}{dt} &= \gamma [M_y B_0 + M_x B_1 \sin \omega_0 t] \\ \frac{dM_y}{dt} &= \gamma [M_x B_1 \cos \omega_0 t - M_y B_0] \\ \frac{dM_z}{dt} &= \gamma [-M_x B_1 \sin \omega_0 t - M_y B_1 \cos \omega_0 t] \end{aligned} \quad (2.23)$$

If a starting condition $\mathbf{M}(0)=M_0\mathbf{k}$ is defined, then the solutions for \mathbf{M} are

$$\begin{aligned}M_x(t) &= M_0 \sin \omega_1 t \sin \omega_0 t \\M_y(t) &= M_0 \sin \omega_1 t \cos \omega_0 t \\M_z(t) &= M_0 \cos \omega_1 t\end{aligned}$$

(2.24)

where $\omega_1 = \gamma B_1$.

This implies that by applying an oscillating magnetic field of frequency ω_0 , the magnetisation simultaneously precesses about B_0 at ω_0 and B_1 at ω_1 , as shown in Figure 2.3a.

At this point it is appropriate to introduce a new frame of reference for viewing the evolution of the magnetisation vector, the rotating frame, which rotates about the z-axis at frequency ω_0 . If in the rotating frame an axis system (x',y',z) is defined then equation 2.19 can be written

$$\frac{d\mathbf{M}}{dt} = \mathbf{M} \times \mathbf{B}_{\text{eff}}$$

(2.25)

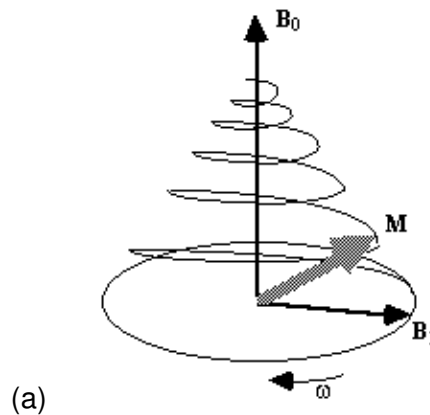
where

$$\mathbf{B}_{\text{eff}} = \left(B_0 - \frac{\omega}{\gamma}\right)\mathbf{k} + B_1\mathbf{i}'$$

(2.26)

and $(\mathbf{i}',\mathbf{j}',\mathbf{k})$ are unit vectors in the (x',y',z) directions. The result of solving these two equations is a magnetisation vector which precesses about \mathbf{B}_{eff} , as shown in Figure 2.3b. If

$B_0 = \omega/\gamma$ then $\mathbf{B}_{\text{eff}} = B_1\mathbf{i}'$ and \mathbf{M} precesses about the x' axis shown in Figure 2.3c. Applying the \mathbf{B}_1 field has the effect of rotating the magnetisation vector about the x' -axis at an angular frequency $\omega_1 = \gamma B_1$.



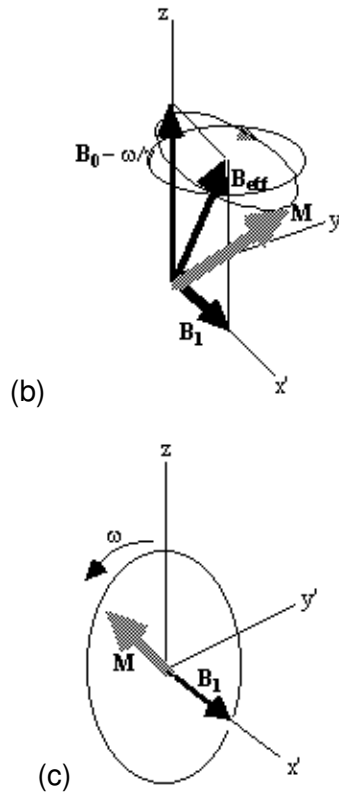


Figure 2.3 Precession of magnetisation (a) in the laboratory frame under the influence of longitudinal field B_0 , and transverse field B_1 , (b) in the rotating frame under the influence of field B_{eff} and (c) in the rotating frame when $B_0 = \omega/\gamma$.

The most common way to carry out an NMR experiment is to apply a short burst of resonant r.f. field. If the duration of this r.f. pulse is t , then the magnetisation will rotate by an angle $\Theta = \gamma B_1 t$. If that angle is 90 degrees then the pulse is referred to as a 90_x pulse, the x subscript showing that the precession is about the x' axis. In a typical NMR experiment a 90_x pulse is applied, which tips the magnetisation vector from the longitudinal plane (parallel to B_0) to the transverse plane (perpendicular to B_0). Once in the transverse plane the magnetisation can be detected as it precesses about the z-axis, and this is what gives rise to the NMR signal, which is discussed in the next section.

2.2.3 Relaxation and Signal Detection

Since the application of a resonant r.f. pulse disturbs the spin system, there must subsequently be a process of coming back to equilibrium. This involves exchange of energy between the spin system and its surroundings. Such a process is called spin-lattice relaxation, and the rate at which equilibrium is restored is characterised by the spin-lattice or longitudinal relaxation time, T_1 , in a new equation of motion for M_z

$$\frac{dM_z}{dt} = \frac{-(M_z - M_0)}{T_1}$$

(2.27)

The spins however do not only exchange energy with the surrounding lattice, but also among themselves. This is generally a faster process than spin-lattice relaxation, and is characterised by the spin-spin relaxation time, T_2 , in the equations describing the evolution of M_x and M_y

$$\frac{dM_x}{dt} = \frac{-M_x}{T_2}, \quad \frac{dM_y}{dt} = \frac{-M_y}{T_2}$$

(2.28)

Equations 2.27 and 2.28, when combined with the earlier equations of motion form what are known as the Bloch equations

$$\begin{aligned} \frac{dM_x}{dt} &= \gamma M_y (B_0 - \alpha I \gamma) - \frac{M_x}{T_2} \\ \frac{dM_y}{dt} &= -\gamma M_x B_1 - \gamma M_x (B_0 - \alpha I \gamma) - \frac{M_y}{T_2} \\ \frac{dM_z}{dt} &= -\gamma M_y B_1 - \frac{(M_z - M_0)}{T_1} \end{aligned}$$

(2.29)

given here for the rotating frame of reference.

Immediately following the application of a Θ_x pulse, the magnetisation vector has components

$$\begin{aligned} M_x(0) &= 0 \\ M_y(0) &= M_0 \sin \Theta \\ M_z(0) &= M_0 \cos \Theta \end{aligned}$$

which when put in the Bloch equations give

$$\begin{aligned} M_x(t) &= M_0 \sin \Theta \sin(\omega_0 t) \exp\left(-\frac{t}{T_2}\right) \\ M_y(t) &= M_0 \sin \Theta \cos(\omega_0 t) \exp\left(-\frac{t}{T_2}\right) \\ M_z(t) &= M_0 \left[1 - (1 - \cos \Theta) \exp\left(-\frac{t}{T_1}\right)\right] \end{aligned}$$

(2.30)

The relaxation times T_1 and T_2 are very important in imaging, as they have the greatest effect in determining contrast.

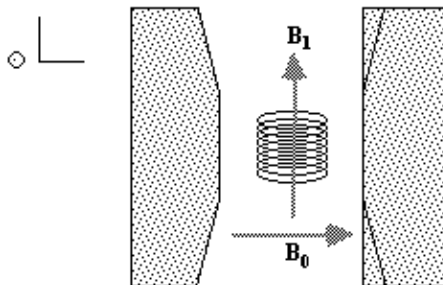


Figure 2.4 Orientation of the r.f. coil within the static field.

To detect the NMR signal it is necessary to have an r.f. coil which is in the transverse plane, that is perpendicular to the \mathbf{B}_0 field (Figure 2.4), in which an e.m.f. is induced which is proportional to M_x . The signal from the coil is first transformed to the rotating frame by phase sensitive detection. Normally this involves separately mixing the e.m.f. with two reference signals, both oscillating at the Larmor frequency, but 90 degrees out of phase with each other. Thus the signal detected in the coil has the form

$$S(t) = S_0 \exp\left(\frac{-t}{T_2}\right) \cos(\omega t) \tag{2.31}$$

which after phase sensitive detection has 'real' and 'imaginary' components

$$S_x(t) = S_0 \exp\left(\frac{-t}{T_2}\right) \cos(\Delta t)$$

$$S_y(t) = S_0 \exp\left(\frac{-t}{T_2}\right) \sin(\Delta t) \tag{2.32}$$

where $\Delta = \omega - \omega_0$. If $\omega = \omega_0$ then the signal is just an exponential decay, however if $\omega \neq \omega_0$ then the signal will oscillate at a frequency Δ . The signal after phase sensitive detection is known as the Free Induction Decay (FID). Fourier transformation of the FID gives the value of Δ as shown in Figure 2.5. The width of the peak is governed by T_2 . This relationship is explored further in Chapter 5.

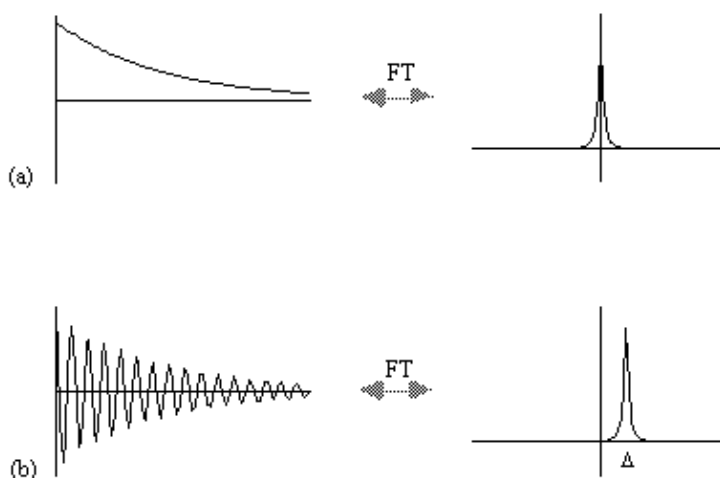


Figure 2.5 The 'real' and imaginary component of the FID and its Fourier transform for (a) resonance signal and (b) off-resonance signal.

A summary of the theory of NMR as presented so far under a classical description is that, a static magnetic field, B_0 , polarises the sample such that it has a bulk magnetisation aligned with the direction of the field. An oscillating magnetic field at the Larmor frequency applied for a short time orthogonally to B_0 will cause the longitudinal magnetisation to be tipped into the transverse plane.

This makes the Larmor precession of the magnetisation under B_0 detectable, and Fourier transformation of the phase sensitively detected signal yields its offset from the expected value.

It is this offset from expected value that is most useful in magnetic resonance, as the B_0 field experienced by the different spins in the system is sensitive to nature of the chemical environment and can be manipulated by the application of external magnetic field gradients. The former is exploited in Magnetic Resonance Spectroscopy (MRS) and the latter in Magnetic Resonance Imaging.

2.2.4 Chemical Shift and Magnetic Resonance Spectroscopy

The electrons that surround each nucleus can act to slightly perturb the magnetic field at the spin site. This causes the Larmor precession frequency to be modified by the chemical environment of the spin. The effect of chemical shift is described by the equation

$$B = (1 - \sigma)B_0 \tag{2.33}$$

where σ is the shielding constant. This modifies the Larmor frequency such that

$$\omega = \gamma(1 - \sigma)B_0 \tag{2.34}$$

and is detected upon Fourier transformation of the FID as a shift in frequency away from that expected if chemical shift played no part. For a sample containing spins with a number of different chemical shifts, the resulting spread of frequencies represents a chemical spectrum. An example of an NMR spectrum is shown in Figure 2.6.

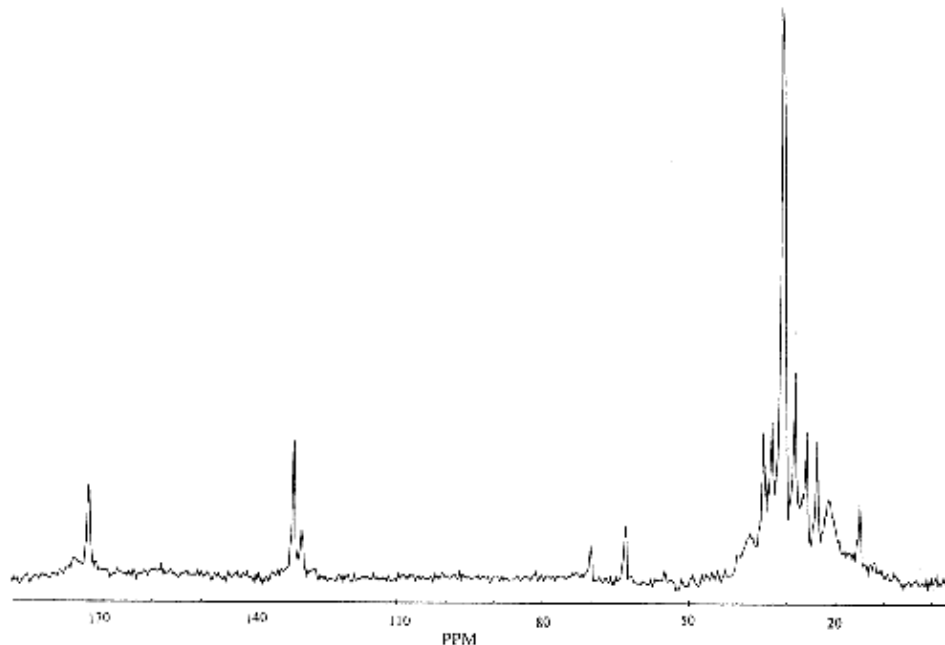


Figure 2.6 A ^{13}C spectrum of human muscle acquired *in vivo* at 3.0 Tesla

It is common to express the chemical shift of a peak in the spectrum in terms of the relative difference in frequency from some reference peak. The chemical shift in parts per million (p.p.m.) is therefore defined as

$$\delta = \frac{\nu - \nu_{\text{ref}}}{\nu_{\text{ref}}} \cdot 10^6 \text{ p.p.m.} \quad (2.35)$$

where ν and ν_{ref} are the resonant frequencies of the spectral peak of interest and the reference component respectively. Chemical shifts in ^1H spectra are of the order of a few p.p.m.

Another spin effect that is useful in MRS is the scalar, or spin-spin coupling. This arises from interactions between the nuclear spins, mediated by the delocalised electrons. However this effect is not very important in imaging, since its magnitude is so small. There are a number of other features of spin behaviour which affect the NMR signal. Some of these will be described, where appropriate, in other chapters.

2.3 Magnetic Resonance Imaging

2.3.1 Magnetic Field Gradients

As has been shown in Section 2.2, the fundamental equation of magnetic resonance is the Larmor equation, $\omega = \gamma B_0$. In an NMR experiment a measurement of the frequency of precession of the magnetisation gives information on the field experienced by that group of spins. By manipulating the spatial variation of the field in a known way, this frequency information now yields spatial information.

Consider a linear field gradient in \mathbf{B} which increases along the x axis, such that

$$\mathbf{B} = (B_0 + Gx)\mathbf{k} \quad (2.36)$$

where G is the gradient strength. This makes the Larmor equation

$$\omega(x) = \gamma(B_0 + Gx) \quad (2.37)$$

or in its more general three dimensional form

$$\omega(\mathbf{r}) = \gamma(B_0 + \mathbf{G} \cdot \mathbf{r}) \quad (2.38)$$

Under a linear field gradient along the x axis, all the spins which lie at a particular value of x will precess at the same frequency. The FID from such a sample will contain components from each of the x values represented by the sample, and the frequency spectrum will therefore represent the

number of spins that lie along that plane

$$\mathcal{A}(\omega) = \mathcal{A}(x) = \int \mathcal{A}(x,y) dy$$

(2.39)

as shown in Figure 2.7c.

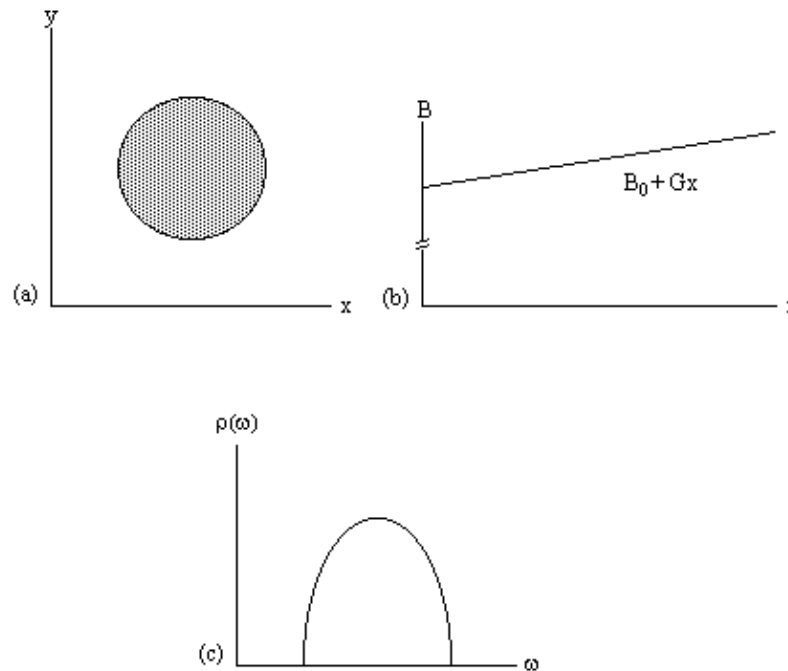


Figure 2.7. (a) A cylindrical object aligned along the z-axis. (b) Linear field gradient applied along the x-axis. (c) Plot of the number of spins at frequency ω

This simple spectrum therefore gives the spatial information about the object being imaged along one dimension. To build up the complete 3D image it is necessary to apply time varying field gradients. A number of methods for doing this are described later in this section, but first the notion of k-space is introduced, which is useful in describing all these techniques.

2.3.2 Reciprocal (k) space

Having denoted the number of spins at a particular location \mathbf{r} , as the spin density, $\rho(\mathbf{r})$, the signal from the sample can be written

$$S(t) = \iiint \mathcal{A}(\mathbf{r}) \exp[i\mathcal{G} \cdot \mathbf{r}t] d\mathbf{r}$$

(2.40)

The reciprocal space vector is defined

$$\mathbf{k} = \mathcal{G}t$$

and the Fourier relationship between signal and spin density becomes obvious

$$S(\mathbf{k}) = \iiint \mathcal{A}(\mathbf{r}) \exp[i\mathbf{k} \cdot \mathbf{r}] d\mathbf{r}$$

$$\mathcal{A}(\mathbf{r}) = \iiint S(\mathbf{k}) \exp[-i\mathbf{k} \cdot \mathbf{r}] d\mathbf{k}$$

(2.41)

Thus \mathbf{k} is the conjugate variable for \mathbf{r} . The resolution of the image depends on the extent of k -space that is sampled, and it is by looking at how different imaging techniques cover k -space that they can usefully be compared [8]. For example in the previous section a gradient along the x -axis was applied to a cylindrical sample. This meant that values in k_x could be sampled, but not in k_y and so the complete 2D structure could not be obtained.

There are imaging techniques which sample all three dimensions of k space, but most techniques reduce the problem to two dimensions by applying slice selection.

2.3.3 Slice Selection

Slice selection is a technique to isolate a single plane in the object being imaged, by only exciting the spins in that plane. To do this an r.f. pulse which only affects a limited part of the NMR spectrum is applied, in the presence of a linear field gradient along the direction along which the slice is to be selected (Figure 2.8). This results in the excitation of only those spins whose Larmor frequency, which is dictated by their position, is the same as the frequency of the applied r.f. pulse.

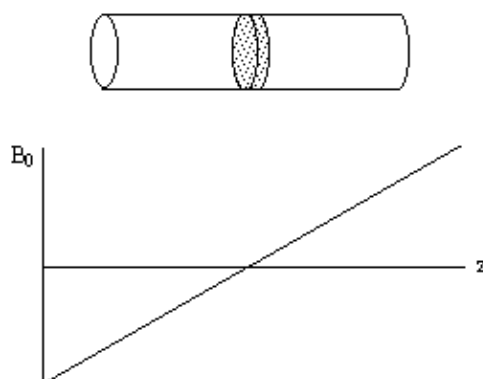


Figure 2.8. A long cylindrical object aligned along the z -axis in a field gradient which increases linearly with increasing z .

Consider an r.f. pulse of duration 2τ which is applied in the presence of a gradient along some axis, say z , such that $2\tau\gamma B_1 = \pi/2$ (a 90 degree pulse). The spins where $B=B_0$ (i.e. $z=0$) will precess into the transverse plane, whilst those where $B \gg B_0$ (i.e. $z \gg 0$) will precess about $B_{\text{eff}} = \Delta\omega/\gamma \mathbf{k} + B_1 \mathbf{i}$, and have little effect on the transverse magnetisation (Figure 2.9).

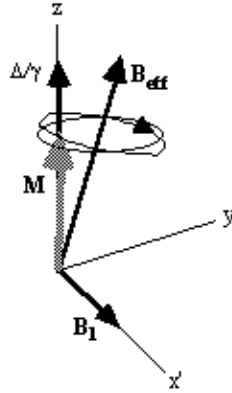


Figure 2.9. Effect of a 90 degree pulse on (a) off-resonant spins and (b) near-resonant spins.

To tailor the shape of slice selected it is necessary to modulate the pulse profile. For small flip angles the relationship between the pulse modulation and slice profile can be derived. To do this consider applying an r.f. pulse lasting from $t=-T$ to $+T$, to a sample in a gradient G_z . The Bloch equations as shown earlier (equation. 2.29) in the rotating frame, neglecting T_1 and T_2 relaxation, become

$$\begin{aligned}\frac{dM_x}{dt} &= \gamma M_y G_z z \\ \frac{dM_y}{dt} &= \gamma (M_z B_1(t) - M_x G_z z) \\ \frac{dM_z}{dt} &= -\gamma M_y B_1(t)\end{aligned}\tag{2.43}$$

Now these are transformed to another frame of reference which rotates at angular frequency $\gamma G_z z$. Each slice will have a different reference frame, depending on the value of z , but considering just one of these gives

$$\begin{aligned}\frac{dM_{x'}}{dt} &= -\gamma M_{z'} B_y = -\gamma M_z B_1(t) \sin[\gamma G_z z(t+T)] \\ \frac{dM_{y'}}{dt} &= \gamma M_z B_x = -\gamma M_z B_1(t) \cos[\gamma G_z z(t+T)] \\ \frac{dM_{z'}}{dt} &= \gamma (M_{x'} B_y - M_{y'} B_x)\end{aligned}\tag{2.44}$$

with the two reference frames coinciding at $t=-T$. If the assumption is made that the flip angles are small then it is possible to say that M_z varies very little, and takes the value M_0 . So equations 2.44 become

$$\begin{aligned}\frac{dM_x'}{dt} &= -\gamma M_0 B_1(t) \sin[\gamma G_z z(t+T)] \\ \frac{dM_y'}{dt} &= \gamma M_0 B_1(t) \cos[\gamma G_z z(t+T)] \\ \frac{dM_z'}{dt} &= 0\end{aligned}$$

(2.45)

If M_x' and M_y' are treated as real and imaginary parts of the complex magnetisation M_+ , the equation of motion becomes

$$\frac{dM_+}{dt} = i \gamma M_0 B_1(t) \exp[i \gamma G_z z(t+T)]$$

(2.46)

By integrating and converting back to the original (rotating) frame of reference, since

$$M_+(T) = M_+'(T) \exp(-i \gamma G_z z 2T)$$

gives

$$M_+ = i \gamma M_0 \exp[-i \gamma G_z z T] \int_{-T}^T B_1(t) \exp[i \gamma G_z z t] dt$$

(2.47)

This is the Fourier transform of the r.f. pulse profile, so a long pulse gives a narrow slice and vice-versa. This equation also shows one other thing about the magnetisation in the slice after the pulse. There is a phase shift through the slice of $\gamma G_z z T$ which will cause problems for imaging later. This can be removed by reversing the gradient G_z for a duration T , which is known as slice refocusing.

To excite a sharp edged slice, the r.f. pulse modulation required is a sinc function. For practical implementation of this kind of pulse it is necessary to limit the length of the pulse, and so usually a five lobe sinc function is used. The above approximation is only correct for small pulse angles. For larger flip angles, it is hard to analytically determine the pulse modulation required for a desired slice profile, and so it is usually necessary to use some form of iterative method to optimise pulses [9]. Using such techniques it is possible to design a range of pulses which are able to select different slice profiles and carry out other spin manipulation techniques such as fat or water suppression. It is also possible to design pulses which do not require refocusing [10]. Usually the limit in such novel designs is their practical implementation, and so the most common three pulse modulations used are a 'hard' pulse, with top-hat modulation, a Gaussian modulation or a 'soft' pulse, with truncated sinc modulation.

If any slice other than the central ($B=B_0$) slice is required, then the frequency of oscillation can be altered and the slice selected will be at the position along the z-axis given by

$$G_z = \frac{\omega}{\gamma} - B_0$$

2.3.4 Early MR Imaging Techniques

The extensively used techniques in MRI are all Fourier based, that is the 'spin-warp' technique and Echo Planar Imaging (EPI) [11]. However the early MR images used point and line methods and these are described here, along with the technique of projection reconstruction.

The f.o.n.a.r. technique (*field focused nuclear magnetic resonance*) was proposed by Damadian, and was used to produce the first whole body image in 1977 [12]. The basis of the technique is to create a shaped B_0 field which has a central homogeneous region, surrounded by a largely inhomogeneous region. The signals from the inhomogeneous regions will have a very short T_2^* and can thus be distinguished from the signal from the homogeneous region. By scanning the homogeneous field region across the whole of the sample an image can be made up. This is a time consuming procedure taking tens of minutes for a single slice. The two advantages of the technique are its conceptual simplicity and the lack of a requirement for the static field to be homogeneous over a large area. Shaped r.f. pulses can also be used to isolate a small region, and such methods form the basis of localised spectroscopy.

As was shown in section 2.3.1, if we have only a one dimensional object then a single linear gradient is sufficient to locate position directly from the FID by Fourier transformation. If then the three dimensional sample can be reduced to a set of one dimensional components then the whole sample can be imaged. This can be done by selective irradiation, or slice selection, in two of the dimensions. First, in the presence of a gradient along the z-axis, a selective pulse is applied which saturates all the spins outside the plane of interest (Figure 2.10a). Then a gradient is applied along the x-axis, and those spins not saturated are tipped into the transverse plane by a selective 90 degree pulse (Figure 2.10b). Immediately after the second r.f pulse the only region with any coherent transverse magnetisation is the line of intersection of the two selected planes. A gradient is now applied along the y-axis, and the evolution of the FID recorded. Fourier transform of the FID gives the proton densities along that line. By repeating the line selection for all the lines in the plane, an image of the whole of the plane can be built up. There are many variations of the line scan technique, some of which utilise 180 degree pulses, but they are inefficient in comparison to the Fourier methods discussed in the next section.

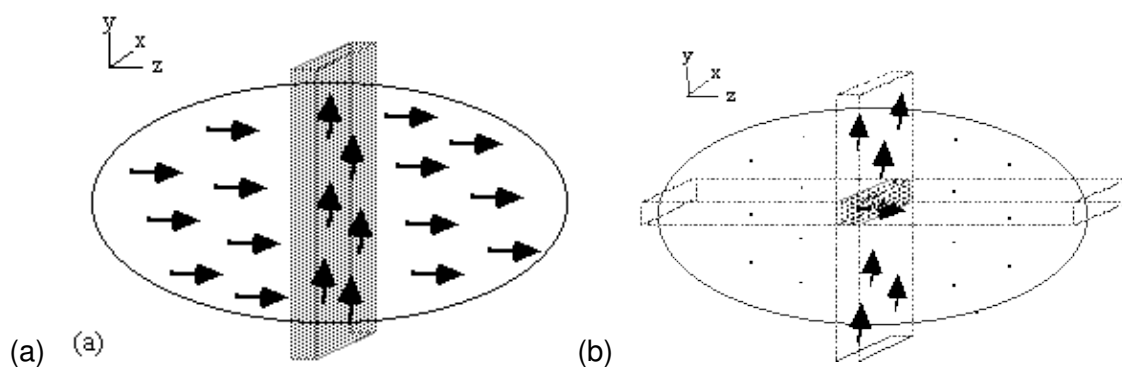


Figure 2.10. Line selection using two rf pulses. (a) In the presence of a gradient along the z-axis, all spins outside the shaded plane are saturated. (b) In the presence of a gradient along the x-axis those spins not saturated in the selected horizontal plane are tipped into the transverse plane and can be observed in the presence of a gradient along the y-axis

One final method of interest is projection reconstruction. This is the method used to build up X-ray CT scans [13], and was the method used to acquire the early MR images. Following slice selection, a gradient is applied along the x-axis and the projections of the spin densities onto that axis

obtained by Fourier transformation of the FID. Then a linear gradient is applied along an axis at some angle to the x-axis, θ . This can be achieved by using a combination of the x and y gradients

$$G_y = G \sin \theta \quad G_x = G \cos \theta$$

(2.49)

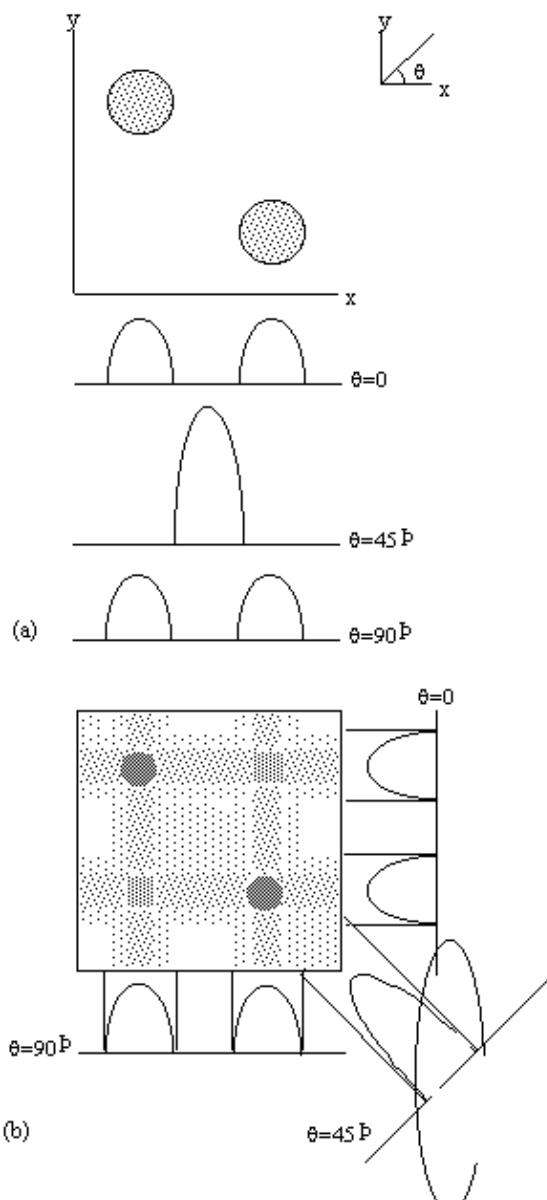


Figure 2.11. The technique of Projection Reconstruction. (a) Two cylindrical objects are placed in the x-y plane and their projection onto three axes, angled at 0, 45 and 90 degrees to the x-axis are recorded, (b) By back projecting the projections, the location of the objects can be ascertained.

Projections are taken as θ is incremented up to 180 degrees (Figure 2.11a). The set of projections can then be put together using back projection. This distributes the measured spin densities evenly along the line normal to the axis it was acquired on. By reconstructing all the angled projections the image appears. There is however a blurred artefact across the whole image, where an attempt was made to assign spin density to areas where there is in fact none, and star artefacts where a finite number of projections have been used to define point structures. This can be corrected using a

technique called filtered back projection, which convolves each of the profiles with a filter

$$\frac{1}{(r - r')^2}$$

(2.50)

This is done in the Fourier domain by dividing the Fourier projections by the modulus of the vector \mathbf{k} as defined in section 2.3.2.

Projection reconstruction has been largely superseded by methods which sample k-space more uniformly.

2.3.5 Fourier and Echo Planar Imaging

Quadrature detection of the FID means that the phase as well as the frequency of the signal can be recorded. This is utilised in the Fourier techniques described in this section.

The 'spin-warp' method (often called 2DFT) as described by Edelstein *et al.* [14] is a development of the earlier technique of Fourier zeugmatography proposed by Kumar, Welti, and Ernst [15]. The Fourier zeugmatography sequence can be split into three distinct sections, namely slice selection, phase encoding, and readout. The pulse sequence diagram for the sequence is shown in Figure 2.12. Such diagrams are commonly used to describe the implementation of a particular MR sequence, and show the waveform of the signal sent to the three orthogonal gradient coils and the r.f. coil.

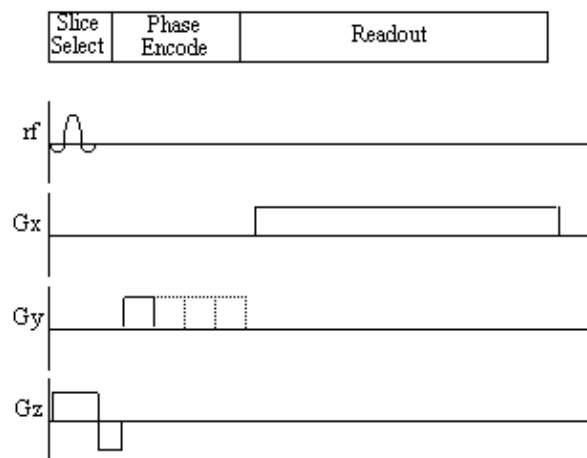


Figure 2.12. Pulse sequence diagram for the Fourier zeugmatography imaging technique.

Having excited only those spins which lie in one plane, a gradient is applied along the y-axis. This will cause the spins to precess at a frequency determined by their y position, and is called phase encoding. Next a gradient is applied along the x-axis and the FID is collected. The frequency components of the FID give information of the x-position and the phase values give information of the y-position.

More specifically, if a gradient of strength G_y is applied for a time t_y during the phase encoding stage, and then a gradient G_x is applied for a duration t_x the signal recorded in the FID is given by

$$S(t_x, t_y) = \iint \mathcal{A}(x, y) \exp \left[i \gamma (G_x x t_x + G_y y t_y) \right] dx dy \quad (2.51)$$

By writing $k_x = \gamma G_x t_x$ and $k_y = \gamma G_y t_y$ equation (2.51) becomes

$$S(k_x, k_y) = \iint \mathcal{A}(x, y) \exp \left[i(k_x x + k_y y) \right] dx dy \quad (2.52)$$

so the single step is equivalent to sampling one line in the k_x direction of k-space. To cover the whole of k-space it is necessary to repeat the sequence with slightly longer periods of phase encoding each time (Figure 2.13).

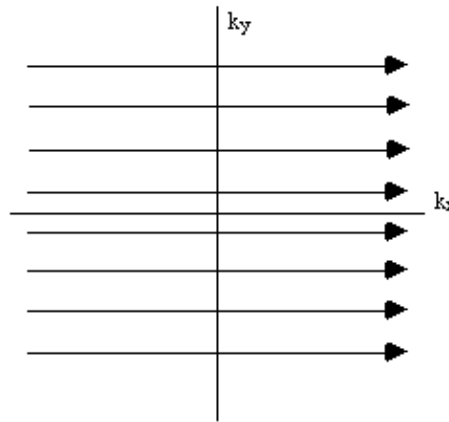


Figure 2.13. K-space sampling with Fourier zeugmatography

Having acquired data for all values of k_x and k_y , a 2D Fourier transform recovers the spin density function

$$\mathcal{A}(x, y) = \iint S(k_x, k_y) \exp \left[-i(k_x x + k_y y) \right] dx dy \quad (2.53)$$

Figure 2.14 illustrates how the magnetisation evolves under these two gradients.

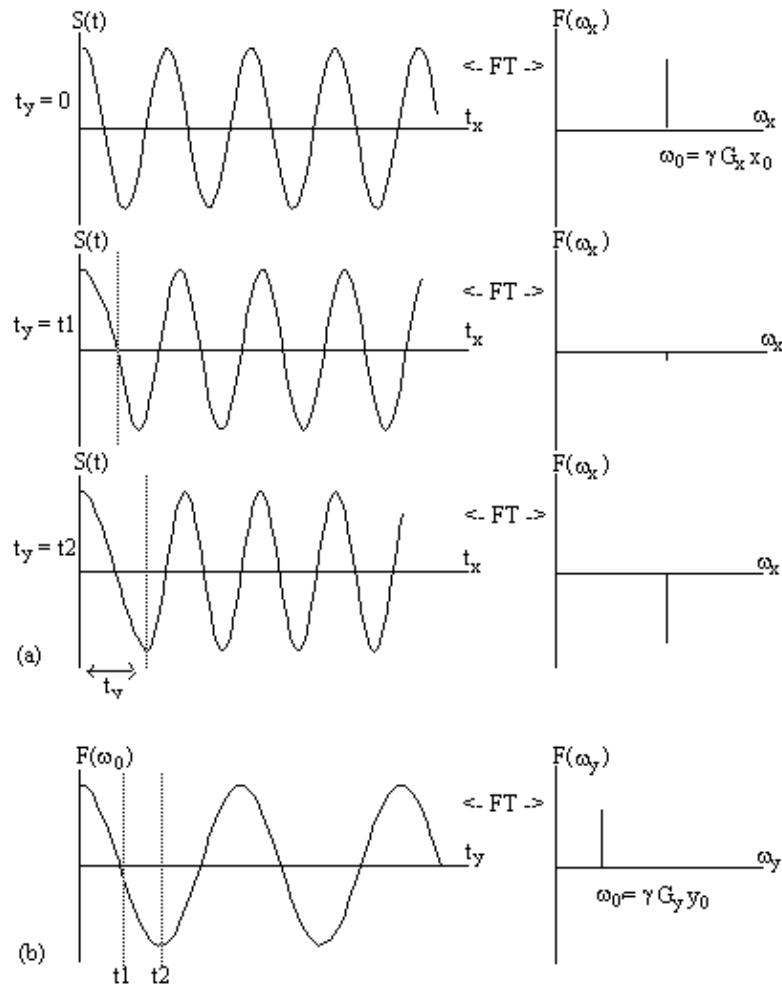


Figure 2.14. Two dimensional Fourier image reconstruction following Fourier zeugmatography. (a) A single magnetisation vector at position (x_0, y_0) , is allowed to evolve under a gradient along the y axis for a time t_y , before being observed under an x gradient. The real components of the Fourier transform of the FID's are shown, giving the x position. (b) Having acquired FID's for all values of t_y , a Fourier transform along the second dimension gives the y position.

One drawback of this technique is that the time between exciting the spins, and recording the FID varies throughout the experiment. This means that the different lines in the k_y direction will have different weighting from T_2^* magnetisation decay. This is overcome in spin-warp imaging by keeping the length of the y gradient constant for each acquisition, and varying k_y by changing the gradient strength. The pulse diagram for this technique is shown in Figure 2.15.

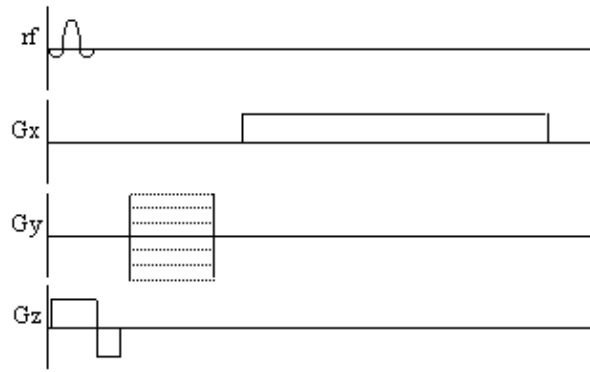


Figure 2.15. Pulse sequence diagram for the spin-warp technique. Phase encoding is performed by varying the magnitude of the y gradient.

It is desirable to have as much signal as possible for each FID, and a necessity that the amount of transverse magnetisation available immediately after the r.f. pulse is the same for each line. This can be a problem since the recovery of longitudinal magnetisation is dependent on spin-lattice relaxation, and T_1 values in biomedical imaging are of the order of seconds. Keeping the time between adjacent spin excitations, often known as TR, the same throughout the image acquisition will keep the transverse magnetisation the same for each FID, provided the first few samples are discarded to allow the system to come to a steady state. Leaving the magnetisation to recover fully, however, would be very costly in time, so it is usually necessary to have a TR which is less than T_1 . To maximise the signal received for small TR values it is possible to use a smaller flip angle than 90 degrees. The transverse magnetisation that is available after such a pulse is less than it would be after a 90 degree pulse, but there is more longitudinal magnetisation available prior to the pulse. To optimise the flip angle θ , for a particular TR, we first assume that the steady state has been reached, that is that

$$M_z(0) = M_z(T_R) = M' \tag{2.54}$$

Now the magnetisation is flipped by a θ degree pulse, and the z-magnetisation becomes

$$M_z(0') = M' \cos \theta \tag{2.55}$$

The recovery of the magnetisation is governed by the equation

$$\frac{dM_z}{dt} = - \frac{(M_0 - M_z)}{T_1} \tag{2.56}$$

which can be integrated to find M' ,

$$M' = M_0 \frac{1 - \exp(-T_R/T_1)}{1 - \cos \theta \exp(-T_R/T_1)} \quad (2.57)$$

The transverse magnetisation following the pulse, which we want to maximise, is given by

$$M_y = M' \sin \theta = M_0 \frac{1 - \exp(-T_R/T_1)}{1 - \cos \theta \exp(-T_R/T_1)} \sin \theta \quad (2.58)$$

which has its maximum value when

$$\cos \theta = \exp(-T_R/T_1) \quad (2.59)$$

The angle this occurs at is known as the Ernst angle [16]. The amount of signal available is very dependent on the repetition time TR. For example, if a sample has a T_1 of 1s, then at a TR of 4s $M'=0.98M_0$, however as TR is reduced to 500ms, $M'=0.62M_0$.

If a 3D volume is to be imaged then it is possible to acquire extra slices with no time penalty. This is because it is possible to excite a separate slice, and acquire one line of k-space, whilst waiting for the longitudinal magnetisation of the previous slice to recover. This technique is called multi-slicing.

The common implementation of the spin-warp technique, FLASH (Fast Low-Angle SHot imaging) [17], uses very small flip angles (~5 degrees) to run at with a fast repetition rate, acquiring an entire image in the order of seconds.

In Echo Planar Imaging [18, 19] (EPI) the whole of k-space is acquired from one FID. This is possible because, having acquired one set of frequency information, the sign of the readout gradients can be reversed and the spins will precess in the opposite direction in the rotating frame (Figure 2.16) and subsequently rephase causing a regrowth of the NMR signal. This is called a gradient echo. By switching the readout gradient rapidly, the whole of k-space can be sampled before spin-spin (T_2) relaxation attenuates the transverse magnetisation. Phase encoding is again used in order to sample k_y .

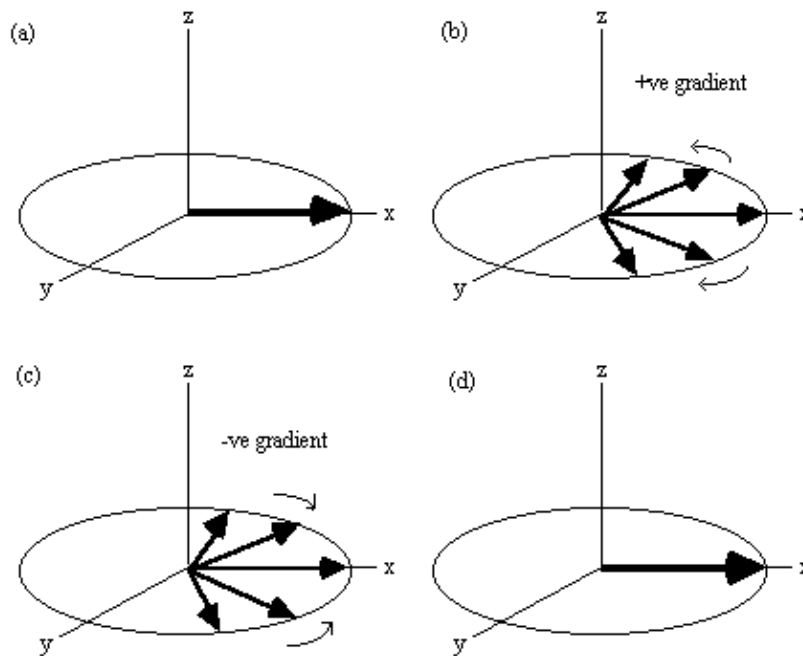


Figure 2.16. Evolution of the magnetisation vector in the rotating frame, under a gradient echo (assuming no T_2 relaxation). (a) Immediately after a 90 degree pulse all the spins are in phase. (b) A gradient will increase the precession frequency of some spins and reduce that of others. (c) Reversal of the gradient at time T causes the spins to refocus, (d) coming back to their initial state at time $2T$.

The pulse sequence diagrams and k-space trajectories for EPI are shown in Figure 2.17.

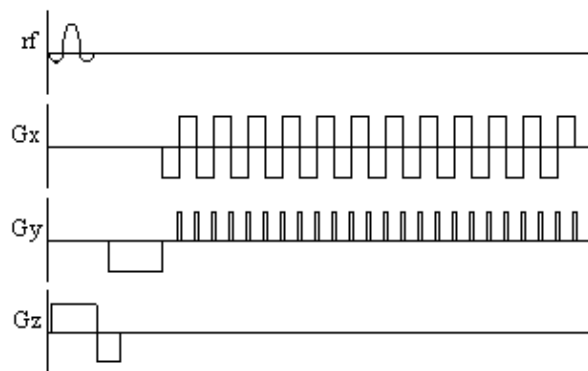


Figure 2.17. (a) Pulse sequence diagram and (b) k-space sampling pattern for echo planar imaging

The three gradients in EPI are usually labelled the slice select (z), blipped (y) and switched (x), because of their respective waveforms. Echo planar imaging is a technically demanding form of MRI, usually requiring specialised hardware, however it has the advantage of being a very rapid imaging technique, capable of capturing moving organs like the heart, and dynamically imaging brain activation. This is only a brief introduction to EPI, since its strengths and limitations are discussed in more detail in the following chapters.

2.3.6 Other Imaging Sequences

There are numerous variations on the basic MRI sequences described above. Several of them, notably interleaved EPI, are explained in other chapters. Other important sequences are outlined here.

It was shown in the previous section how phase encoding enabled the information on the second dimension to be added to the one dimensional line profile. It is possible to extrapolate this procedure to the third dimension by introducing phase encoding along the z axis. Thus the 2D-FT technique is extended to a 3D-FT technique [20]. All such volumar imaging sequences first involve the selection of a thick slice, or slab. Then phase encoding is applied in the z-direction and the y-direction, followed by a readout gradient in the x-direction, during which the FID is sampled. The assembled FID's are then subject to a three dimensional Fourier transform yielding the volume image. Phase encoding can also be used in EPI instead of multi-slicing. The slice select gradient and r.f. pulse being replaced by a slab selective pulse and a phase encoding gradient along the z-axis.

Going even further, it is possible to acquire all the data to reconstruct a 3D volume from one FID, in the technique called Echo Volumar Imaging (EVI) [21]. This uses another blipped gradient in the z direction, as shown in Figure 2.18. The limitation in EVI is the need to switch the gradients fast enough to acquire all the data, before T_2^* destroys the signal.

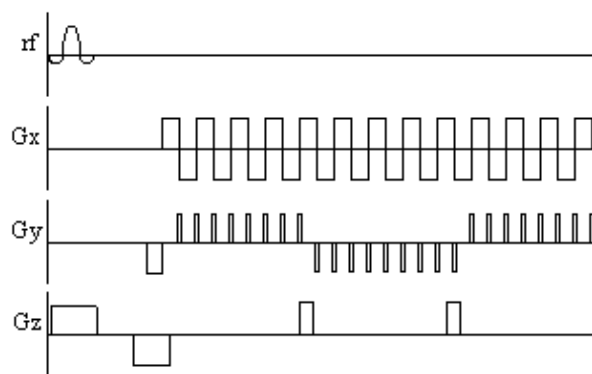


Figure 2.18. Pulse sequence diagram for Echo Volumar Imaging

Often the main limitation in implementing fast imaging sequences such as EPI is switching the gradients at the fast rates required. A sequence which is similar to EPI, but slightly easier to implement is spiral imaging. This covers k-space in a spiral from the centre outwards, which requires sinusoidal gradients in x and y, increasing in amplitude with time. Such gradient waveforms are easier to produce than the gradients required for EPI. Spiral imaging also has the advantage of sampling the centre of k-space first, and so the low spatial frequencies, that affect the image the most are sampled first, when the signal has not been eroded by T_2^* . The pulse sequence diagram and coverage of k-space for spiral imaging are shown in Figure 2.19.

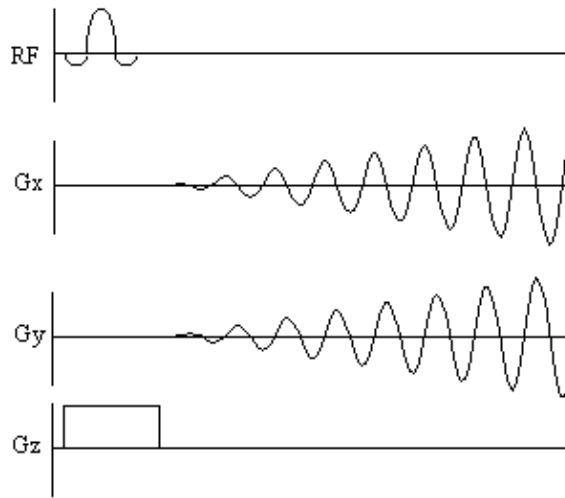


Figure 2.19 Pulse sequence diagram and k-space sampling diagram for spiral imaging

In general imaging, the chemical shifts of the protons are ignored, and usually seen only as an artefact. However it is possible to image the chemical shifts, which gives not only spatial information but also spectral information. The technique, called Chemical Shift Imaging (CSI) [22], treats the chemical shift as an extra imaging gradient in the fourth dimension. By introducing a variable delay between the excitation pulse and imaging gradients, the chemical shift 'gradient' will phase encode in this direction. Fourier transformation in this case gives the conventional NMR spectrum.

Finally, it is possible to image nuclei other than the proton. Sodium, phosphorus and carbon-13 have all been used to form biomedical images. In the case of ^{13}C , its low natural abundance makes it useful for tracer studies.

2.4 Image Contrast in Biological Imaging

Unlike many other medical imaging modalities, the contrast in an MR image is strongly dependent upon the way the image is acquired. By adding r.f. or gradient pulses, and by careful choice of timings, it is possible to highlight different components in the object being imaged. In the sequence descriptions that follow it is assumed that the imaging method used is EPI, however identical or similar methods can be used with the other MR imaging techniques outlined above.

The basis of contrast is the spin density throughout the object. If there are no spins present in a region it is not possible to get an NMR signal at all. Proton spin densities depend on water content, typical values of which are given in Table 2.2 for various human tissues [23]. The low proton spin density of bone makes MRI a less suitable choice for skeletal imaging than X-ray shadowgraphs or X-ray CT. Since there is such a small difference in proton spin density between most other tissues in the body, other suitable contrast mechanisms must be employed. These are generally based on the variation in the values of T_1 and T_2 for different tissues.

Tissue	% Water Content
Grey Matter	70.6
White Matter	84.3
Heart	80.0
Blood	93.0
Bone	12.2

Table 2.2 Water content of various human tissues

When describing the effect of the two relaxation times on image contrast, it is important to distinguish between relaxation time maps, and relaxation time weighted images. In the former the pixel intensities in the image have a direct correspondence to the value of the relaxation time, whilst in the latter the image is a proton density image which has been weighted by the action of the relaxation.

2.4.1 T₁ Contrast

The spin-lattice relaxation time T₁, is a measure of the time for the longitudinal magnetisation to recover. A proton density image can be weighted by applying an r.f. pulse which saturates the longitudinal magnetisation prior to imaging. Spins that have recovered quickly will have greater available z-magnetisation prior to imaging than those which recover slowly. This effect is apparent if the same slice, or set of slices, are imaged rapidly, because the excitation pulse of the previously imaged slice affects the magnetisation available for the current slice. More commonly however, if T₁ maps, or T₁ weighted images are required then the imaging module is preceded by a 180 degree pulse (Figure 2.20). The 180 degree pulse will invert the longitudinal magnetisation, whilst not producing any transverse magnetisation. The recovery of the longitudinal magnetisation is governed by the Bloch equation for M_z, which has the solution

$$M_z = M_0 [1 - 2 \exp(-t/T_1)] \tag{2.60}$$

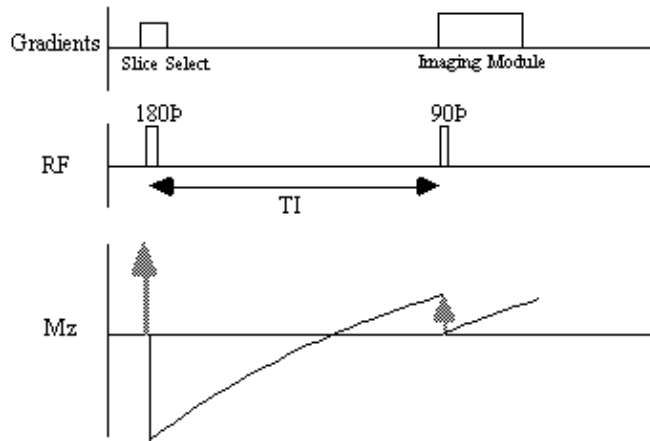


Figure 2.20. Inversion recovery sequence for obtaining a T₁ weighted image

The magnetisation is allowed to recover for a time TI, after which it is imaged using a 90 degree pulse, and usual imaging gradients. The amount of signal available will depend on the rate of recovery of M_z. If, as in Figure 2.21, the sample has spins with several different relaxation times, it is possible to choose TI such that the signal from spins with one recovery curve is nulled completely, whilst giving a good contrast between spins with other recovery curves. Figure 2.22 shows some examples of T₁ weighted images. In order to calculate the values of T₁, to create a T₁ map, it is necessary to obtain a number of points along the magnetisation recovery curve, and then fit the points to the equation 2.60. The most straightforward way to do this is to repeat the inversion recovery sequence for a number of values of TI, but there are techniques which acquire all the data in a single recovery curve [24, 25].

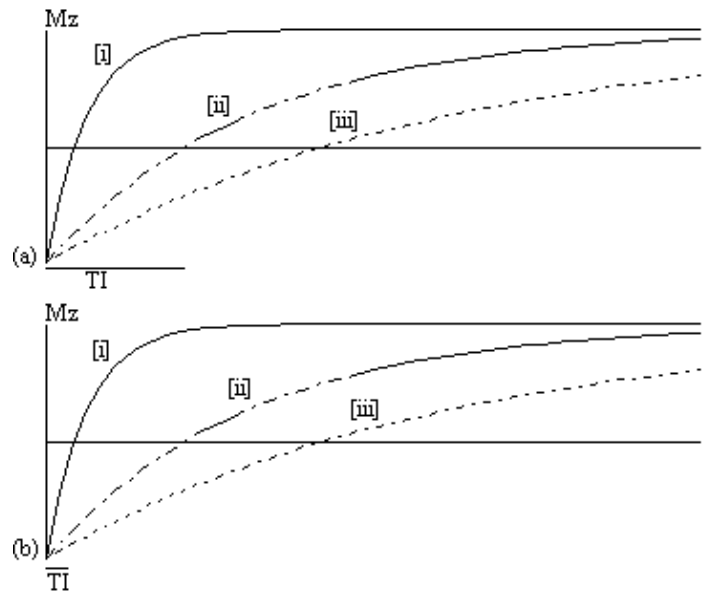


Figure 2.21. Curves showing the recovery of longitudinal magnetisation following an inversion pulse for spins with different values of T_1 . The image is acquired after two different inversion times (TI). (a) Image will have no signal from areas with recovery curve [ii], and good contrast between areas with recovery curves [i] and [iii]. (b) Image will have no signal from areas with the recovery curve [i], and poor contrast between areas with recovery curves [ii] and [iii].

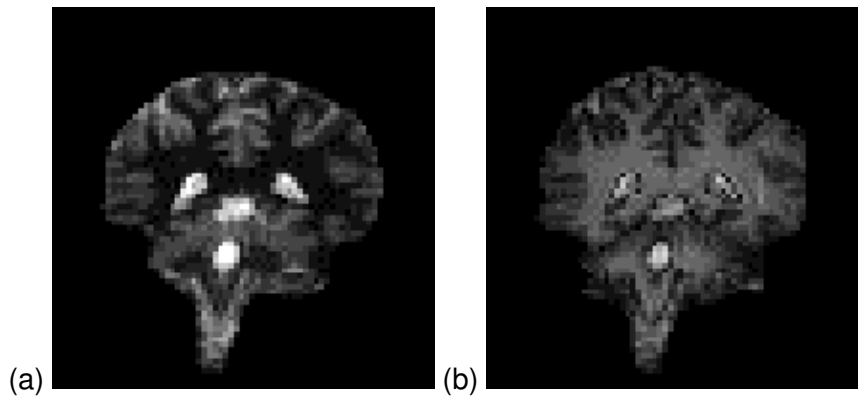


Figure 2.22. Examples of T_1 weighted images of the brain at 3.0 T. (a) White matter nulled image, with an inversion time TI = 400 ms. (b) Grey matter nulled image, with an inversion time TI = 1200 ms.

2.4.2 T_2^* Contrast

The problem with measuring T_2 with a sequence which relies on a gradient echo (as EPI does) is that there is a confounding effect which erodes the transverse magnetisation in the same way that spin-spin relaxation does, which is that of field inhomogeneities. If the spins in a single voxel do not experience exactly the same field, then the coherence of their magnetisation will be reduced, an effect which increases with time. The combined effect of spin-spin relaxation and an inhomogeneous field on transverse magnetisation is characterised by another time constant T_2^* , and the decay of the signal is governed by the equation

$$S = S_0 \exp\left(-t/T_2^*\right)$$

(2.61)

In fact T_2^* weighted images are desirable for functional MRI applications, as is explained in the next chapter. To change the T_2^* weighting of an image, it is only necessary to change the time between the excitation pulse and the imaging gradients. The longer the delay, the greater the T_2^* weighting, as shown in Figure 2.23. Examples of T_2^* weighted images are shown in Figure 2.24. T_2^* maps can be obtained by taking several images with different delays, and fitting to equation 2.61. A technique for obtaining T_2^* maps from a single FID is explained in Chapter 4.

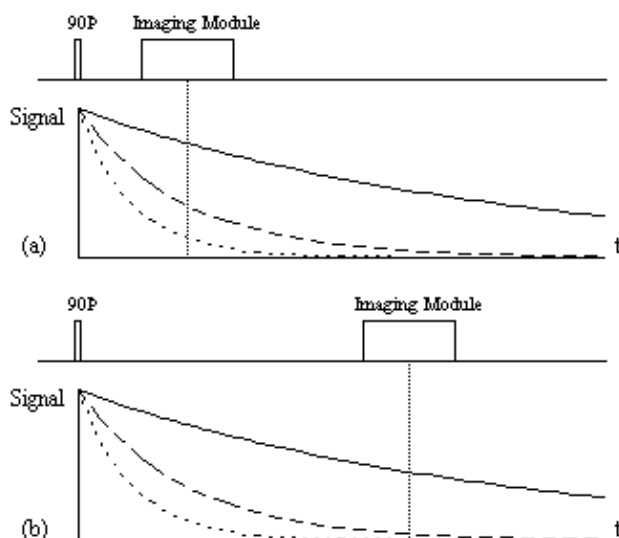


Figure 2.23 T_2^* weighted imaging. (a) A short delay between the r.f. excitation pulse imaging module, gives signal from spins with all three decay curves, (b) a long delay however means that signal is only available from spins with a long T_2^* .

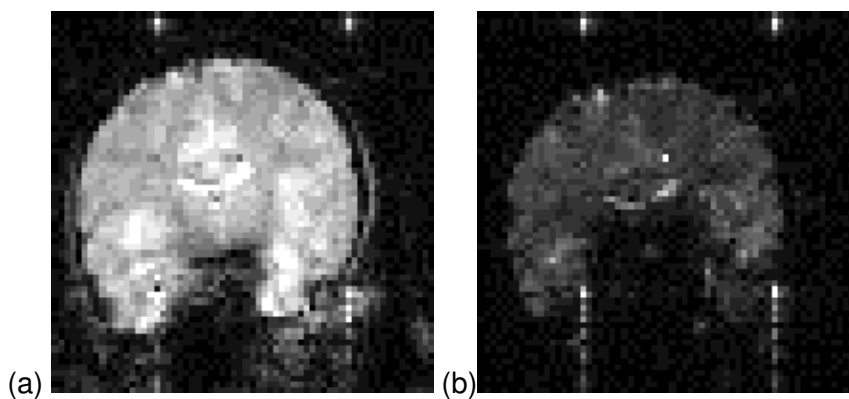


Figure 2.24 Examples of T_2^* weighted images of the brain at 3.0 T for (a) TE = 15 ms and (b) 55 ms.

2.4.3 T_2 Contrast

It is possible to obtain the real value of T_2 by refocusing the effect of field inhomogeneity on the transverse magnetisation using a spin-echo. A spin-echo is formed by applying a 180 degree pulse, a time τ after the excitation pulse. This has the effect of refocusing the signal at time 2τ (Figures 2.25, 2.26).

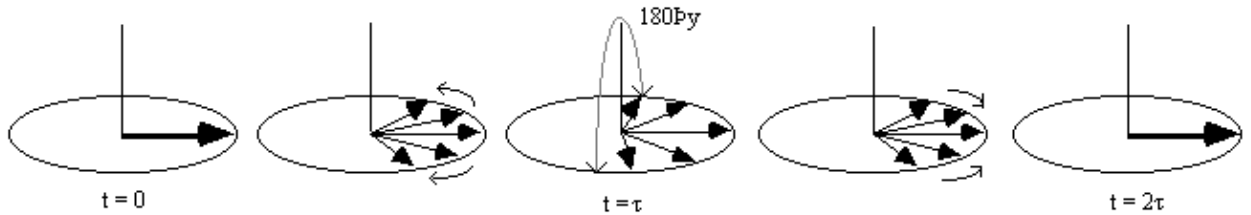


Figure 2.25. The Spin-Echo. Magnetisation evolves in the rotating frame due to field inhomogeneities (assuming no spin-spin relaxation). A 180 degree pulse along the y axis after a time τ flips the magnetisation over in the x-y plane. The magnetisation continues to evolve under the field inhomogeneities and is refocused at time 2τ .

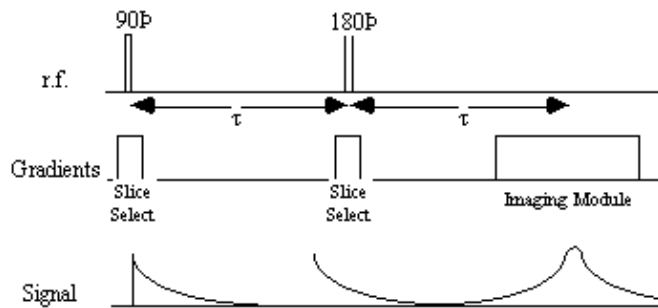


Figure 2.26 Spin echo pulse sequence to refocus signal lost due to field inhomogeneities

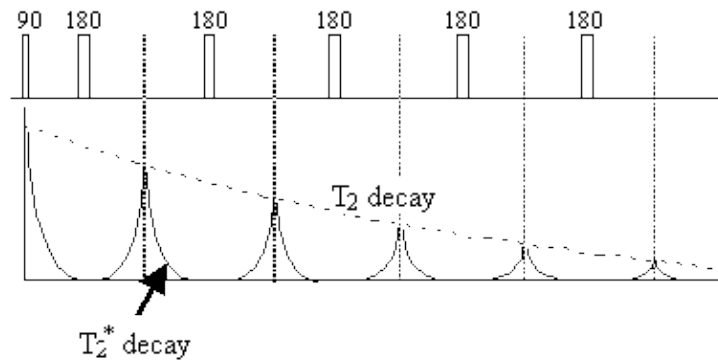


Figure 2.27 Multiple spin echo pulse sequence for measuring T_2 . The transverse magnetisation is repeatedly refocused by a series of 180 degree pulses. Each image is then only weighted by the T_2 decay curve.

Since the spin-spin relaxation is not refocused in the spin echo, the contrast in the image is dependent on T_2 and not T_2^* , with contrast being dependent on the delay between the excitation pulse and the imaging module. Again T_2 maps can be made from images with different delay times (called the echo time, TE), by fitting to the T_2 decay equation which is similar to equation 2.61. Multiple echoes can be formed by using a series of 180 degrees pulses as shown in Figure 2.27.

In order to improve the contrast of images, it is common to use some form of contrast agent. The most common of these in MRI is gadolinium, which is a paramagnetic ion, and reduces the spin-lattice relaxation time (T_1) considerably.

2.4.4 Flow and Diffusion Contrast

One of the usual assumptions about imaging using magnetic resonance is that the spins are stationary throughout the imaging process. This of course may not be true, for example if blood vessels are in the region being imaged. Take for example the situation of imaging a plane through which a number of blood vessels flow. A slice is selected and all the spins in that slice are excited, however in the time before imaging, spins in the blood have flown out of the slice and unexcited spins have flown in. This means that there may be no signal from the blood vessels.

In order to measure the rate of flow, some kind of phase encoding that is flow sensitive can be applied. This is done by applying a magnetic field gradient along the direction in which flow is to be measured. A large gradient dephases the spins depending on their position along the gradient. This gradient is then reversed, which will completely rephase any stationary spins. Spins that have moved however will not be completely rephased (Figure 2.28). If the flow is coherent within a voxel, when the spins are imaged the phase difference can be calculated, and by varying the time between the forward and reverse gradients the flow can be calculated. Diffusion is measured in a similar way, but since the motion of the spins within the voxel is not coherent, the effect of diffusion is simply to diminish the signal.

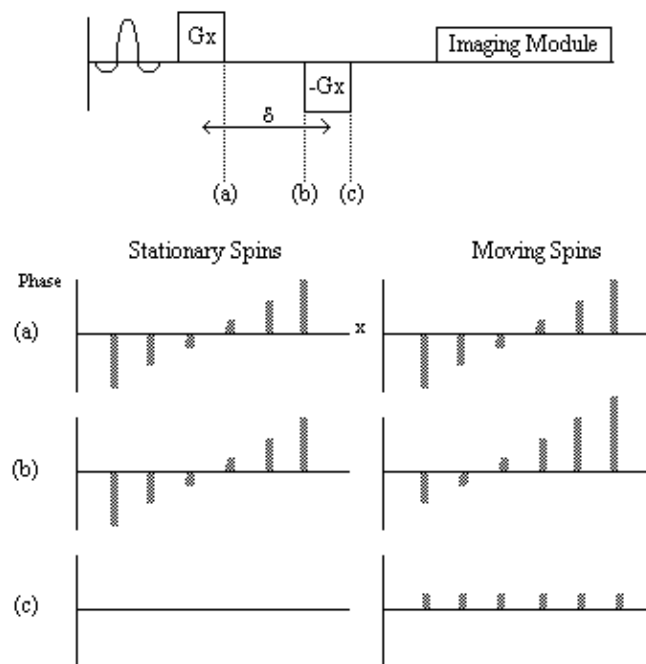


Figure 2.28 Flow encoded imaging. (a) Spins are dephased with a gradient in the x direction. (b) After a time δ the gradient is applied in the opposite direction. (c) Spins that are stationary will be completely rephased, whereas spins that have moved along x in the time δ will be left with a residual phase shift.

2.5 Image Artefacts

As with any imaging modality, magnetic resonance images suffer from a number of artefacts. In this section, a number of the common artefacts are described, together with ways by which they can be reduced.

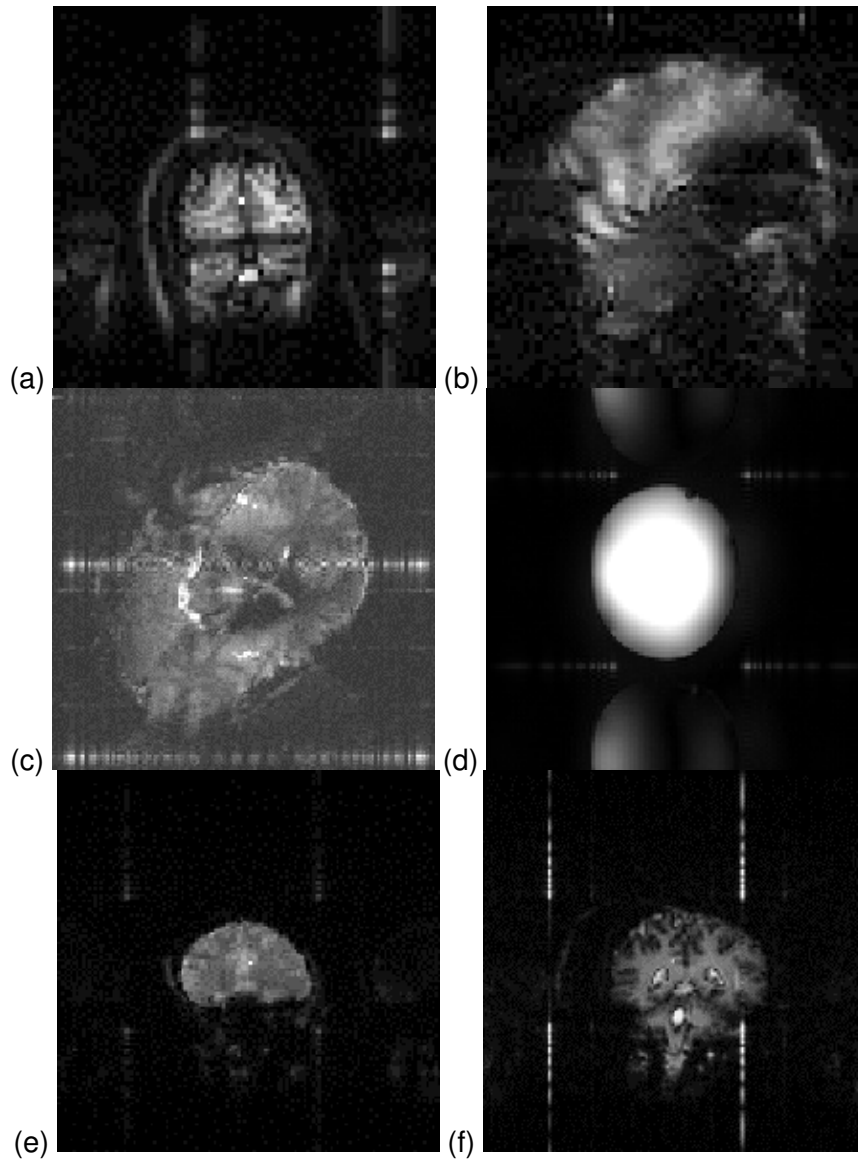


Figure 2.29 Various artefacts that affect MR images. (a) Chemical shift artefact. (b) Susceptibility artefact from a metal object. (c) Susceptibility artefact at the base of the brain. (d) Nyquist ghost. (e) Central point artefact (f) External RF interference in a non-linearly sampled EPI image.

2.5.1 Field Artefacts

The basic assumption of MRI is that the frequency of precession of a spin is only dependent on the magnitude of the applied magnetic field gradient at that point. There are two reasons why this may not be true.

Firstly, there is the chemical shift. This has the effect of shifting the apparent position in the image of one set of spins relative to another, even if they originate from the same part of the sample. The chemical shift artefact is commonly noticed where fat and other tissues border, as in the image of a brain in Figure 2.29a, where the fat around the skull forms a shifted 'halo'. The artefact can be removed by spin suppression, such that a selective pulse excites only the protons in the fat [26]. When the image excitation pulse is subsequently applied, the fat spins are already saturated, and so do not contribute to the image.

Secondly, the static magnetic field (B_0) may not be perfectly homogeneous. Even if the magnet is

very well built, the differences in magnetic susceptibility between bone, tissue and air in the body, means that the local field is unlikely to be homogeneous. If the susceptibility differences are large, such that the local magnetic field across one voxel varies by a large amount, then the value of T_2^* is short and there is little or no signal from such voxels. This effect is particularly evident if any metal object is present as shown in Figure 2.29b. If the differences are smaller, and the field is affected over a few voxels, then the effect is a smearing out of the image, as shown in Figure 2.29c as the altered field is interpreted as a difference in position. In 2DFT techniques susceptibility distortions occur in the readout direction, whereas in EPI they occur in the phase encoding, that is blipped, direction. The reason for this is because these are the directions in which the frequency separation of pixels is smallest. In EPI this separation can be very small so that even a small change in precessional frequency may be detected.

To reduce the artefact it is possible to locally correct the field using a set of shim coils. These apply shaped fields across the sample and in combination increase homogeneity. Susceptibility artefact is more apparent in the rapid imaging methods such as EPI and FLASH, and is difficult to reduce without losing the fast imaging rates. One way to reduce the distortion is to acquire two images with the phase encoding applied in opposite directions. The distortions will likewise be in opposite directions and a mathematical correction can be calculated and applied [27]. This topic is covered in more detail in Chapter 5.

2.5.2 Sampling Artefacts

When using any digital technique, the question of sampling occurs. One of the most important theories in digital sampling is the Nyquist sampling theorem, which states that the highest frequency that can be sampled accurately is given by

$$f_{\max} = \frac{1}{2T}$$

(2.62)

where T is the interval between sampling points. If the FID contains a frequency component $f_{\max} + \Delta$ then it will appear to have a frequency $f_{\max} - \Delta$. This manifests itself as 'wrap-around' of the image onto itself. It is possible to reduce this problem in the readout, or switched, direction by using a band-pass filter to cut out any frequencies that could alias. In the phase encode, or blipped direction, it is necessary to ensure that there are enough sample points for the amount of phase encoding applied. An alternative is to suppress the signal from outside the field of view, using selective r.f. excitation [28].

There are three further artefacts due to sampling, one specific to 2DFT techniques, and the other two specific to EPI. Firstly, subject motion during the scan causes localised banding. This is not a problem in EPI since the image is acquired in a fraction of a second, but is in the slower sequences such as spin-warp. Depending on the source of the movement, there are a number of solutions. Cardiac or respiratory gating, where the scanning is locked to a particular phase of the respective cycles, is often employed to image the heart. These cycles can be monitored directly, for example using the ECG, or by sampling the phase of the NMR signal just prior to gradient application, known as a navigator echo [29].

Echo planar imaging suffers from a different type of sampling artefact, known as the Nyquist, or N/2 ghost. This is because, in EPI adjacent lines in k-space are sampled under opposite read gradients. If there is any misalignment in sampling, or differences in positive and negative gradients, then there is an alternate line modulation in k-space, which leads to a 'ghosting' of the image, as shown

in Figure 2.29d. If the aliased image and the actual image overlap, then banding or fringes appear. The Nyquist ghost can be corrected to a certain extent by applying various phase corrections to the data. One such method acquires a second image with the starting direction of the switched gradient reversed to calculate the phase correction, and is described in more detail in Chapter 4.

Finally, since in EPI to switch the sign of the gradients so rapidly is difficult, the waveform of the switched gradient will not be square. In fact it is common to use a sinusoidal gradient waveform. If simple linear sampling of the signal is used with a sinusoidal gradient a complex ripple artefact in the switched direction is formed. To correct for this, the signal is usually over-sampled and then the points re-gridded to account for the sinusoidal nature of the gradients. Alternatively the sampling points can be distributed sinusoidally, sampling most densely at the peak of the gradient [30].

2.5.3 Fourier Artefacts and External R.F. Interference

There are two artefacts that result from using a Fourier transform to create the image. The first is truncation artefact, which is due to the finite number of sampling points used. It is noticeable if there is a sharp intensity change in the image. Instead of a sharp edge in the image there is 'ringing', that is light or dark lines parallel to that edge. The only way to overcome this is to use more sample points.

Another effect is the central point artefact. This is due to the constant DC offset of the FID, which upon Fourier transformation becomes a central bright dot (as shown in Figure 2.29e). This can be reduced by attempting to remove the DC component from the FID, by assuming that the extremities of k-space are unlikely to contain much signal. So the first or last few lines are averaged together and this average is subtracted from all the data. Alternatively, the point can be removed cosmetically by replacing it by the average of surrounding pixels.

One final artefact to mention is that of external r.f. interference. If there is any r.f. radiation at the frequency of the receiver then it will be picked up and appear as a bright dot in the image. The best way to remove this, is to remove all potential interference from the scanner by placing it in a screened room. Figure 2.29f shows r.f. interference from a single frequency that appears as four bars in the echo planar image. The single frequency appears in four regions due to the reversal of the echo acquisition in the alternate lines, and the fact that the quadrature detection has identified both positive and negative components of the signal. The spreading out of the points to bars, is because sinusoidal sampling was employed. A method for removing this artefact from non-linearly sampled images is described in Chapter 4.

2.6 Imaging Hardware

An MRI scanner is made up of four components: the magnet, gradient coils, r.f. transmitter and receiver, and the computer. In this section the general design and construction of these components is discussed. More specific details of the system used for the experiments in this thesis are given in the relevant chapters.

2.6.1 The Magnet

The magnet is the most expensive part of the whole scanner. The earliest systems were based around water-cooled resistive magnets, and for particular applications it is possible to use permanent magnets, but the majority of modern scanners use superconducting magnets. The reason for this is the high fields now desirable for MRI. Whole body resistive and permanent magnets are limited to around 0.3 T field strength, before their weight becomes prohibitively large. Superconducting magnets are able to generate much larger fields, and there are a number of 4.0 T

whole body scanners now available. These magnets are constructed from materials such as NbTi alloy, which below a critical temperature of about 9 K loses its resistivity. Once started the current will flow in the coils indefinitely, provided that the temperature is kept below the critical temperature by cooling with liquid helium. The fields from such magnets are very stable with time, which is essential for an MRI system.

Of course one of the most important requirements for NMR is that the field is as homogeneous as possible, with tolerances as low as 1 p.p.m. required over the volume of interest. For this purpose, upon installation, the field is evened out as much as possible using ferromagnetic blocks placed inside the bore. As well as this, a set of resistive coils known as shim coils, are placed within the bore of the magnet. These generate fields that vary with a particular function of position. Using these in combination it is possible to improve not only on the intrinsic homogeneity of the magnet, but also reduce the field effects due to susceptibility differences in the object being scanned.

2.6.2 The Gradient Coils

The requirement of the gradient coils are twofold. First they are required to produce a linear variation in field along one direction, and secondly to have high efficiency, low inductance and low resistance, in order to minimise the current requirements and heat deposition.

Linear variation in field along the direction of the field (traditionally labelled the z-axis) is usually produced by a Maxwell coil. This consists of a pair of coils separated by 1.73 times their radius as shown in Figure 2.30. Current flows in the opposite sense in the two coils, and produces a very linear gradient.

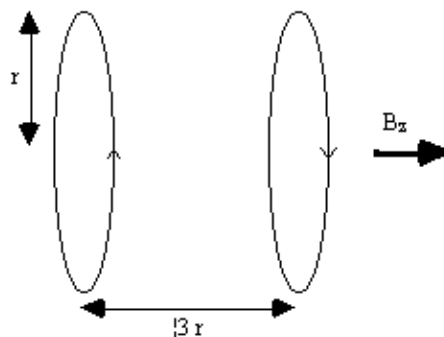


Figure 2.30 Maxwell coils used to produce a linear field gradient in B_z along the z-axis.

To produce a linear gradient in the other two axes requires wires running along the bore of the magnet. This is best done using a saddle-coil, such as the Golay coil shown in Figure 2.31. This consists of four saddles running along the bore of the magnet which produces a linear variation in B_z along the x or y axis, depending on the axial orientation. This configuration produces a very linear field at the central plane, but this linearity is lost rapidly away from this. In order to improve this, a number of pairs can be used which have different axial separations. If a gradient is required in an axis which is not along x,y or z, then this is achievable by sending currents in the appropriate proportions to G_x , G_y and G_z coils. If for example a transverse gradient G at an angle θ to the x-axis is required, then a gradient $G\cos\theta$ should be applied in the x direction, and $G\sin\theta$ in y.

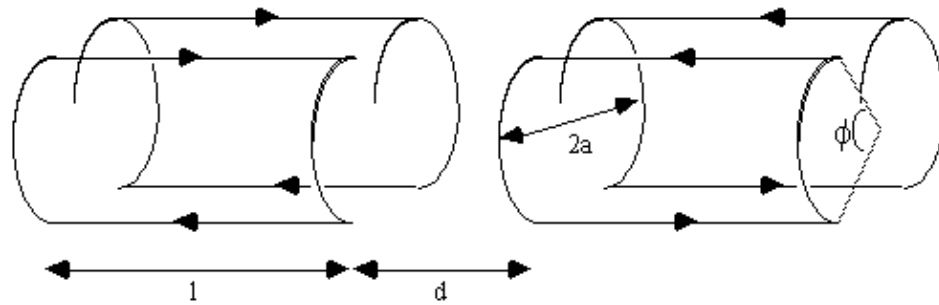


Figure 2.31. Golay coil for producing linear field gradients in B_z along the x or y axes. $l=3.5a$, $d=0.775a$ and $\phi=120$ degrees.

The magnitudes of the currents required, and the appropriate waveforms are digitally generated, and converted into analogue voltages. These are fed into power amplifiers which produce the 10's of amps required to generate the appropriate gradients. With a technique such as EPI, the readout gradient is switched from positive to negative at rates of anything up to 5kHz. This can be made easier by employing resonant driving of the gradient coils. To do this a large capacitor is placed in series with the coil, which itself is an inductor. Such a circuit has a resonance at a frequency of $1/2\pi\sqrt{LC}$, where L is the inductance of the coil and C is the capacitance of the series capacitor. When driving the coil at this frequency energy is transferred between the capacitor and the inductor, thereby reducing the load on the power amplifier.

2.6.3 R.f. Transmission and Reception

The third main component of an MRI scanner is the r.f. coil. There are many different designs of coils, but they fall into two main categories; surface coils and volume coils.

As the name suggests, a surface coil rests on the surface of the object being imaged. In its simplest form it is a coil of wire with a capacitor in parallel. The inductance of the coil, and the capacitance form a resonant circuit which is tuned to have the same resonant frequency as the spins to be imaged. In practice, since the coil is connected to a power amplifier which will have an output impedance of 50Ω , and the coil will have an input impedance of the order of kilo-ohms, then on transmission a lot of the power will be reflected back. To overcome this, a second capacitor is added in series with the coil, as shown in Figure 2.32, so as to match the coil impedance to 50Ω .

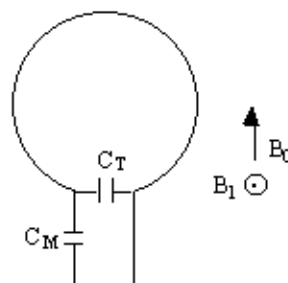


Figure 2.32. Surface r.f. coil which is tuned to resonance with the tuning capacitor C_T and matched to 50Ω with a matching capacitor C_M .

The homogeneous field produced by a simple surface coil like this is small, with the depth of penetration depending on the size of the coil. This however represents the main advantage of using a surface coil for imaging areas which lie close to the surface, as a good signal to noise ratio is achieved by inherently excluding noise signal from outside the region of interest. There are many

designs of surface coil, and other localised coils for specific purposes. If however whole body images are required, or the regions of interest are far from the surface then a volume coil must be used.

Volume coils are large enough to fit either the whole body, or one specific region, such as the head or a limb, and have a homogeneous region which extends over a large area. The most commonly used design is a birdcage coil [31], as shown in Figure 2.33. This consists of a number of wires running along the z-direction, arranged to give a cosine current variation around the circumference of the coil.

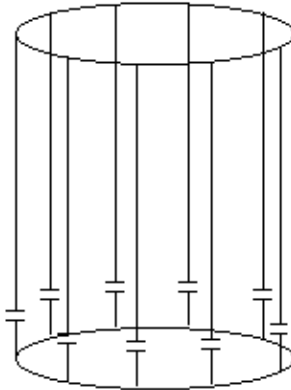


Figure 2.33. Diagram of a low-pass birdcage coil which produces a homogeneous field over a large region of interest.

The frequency supply is generated by an oscillator, which is modulated to form a shaped pulse by a double balanced mixer controlled by the waveform generator. This signal must be amplified to 1000's of watts. This can be done using either solid state electronics, valves or a combination of both.

It is possible to use the same coil to transmit and receive, or to use two separate coils. Either way it is necessary to gate the receiver side of the electronics. This is to prevent the excitation pulse, which is of the order of kilovolts, saturating or breaking the receiver electronics which are designed to detect signals of millivolts. This can again be done in a number of ways, but one such circuit for doing so is shown in Figure 2.34.

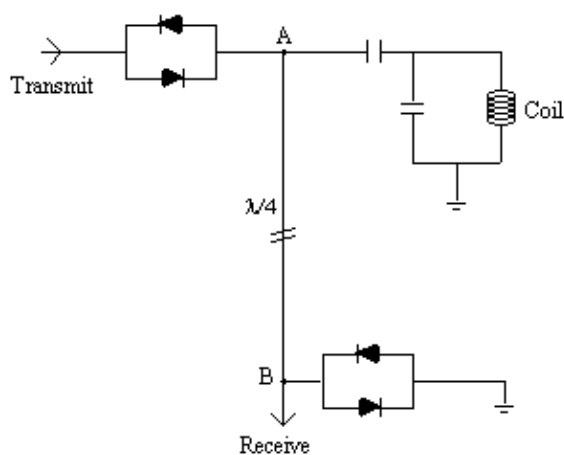


Figure 2.34. Circuit diagram for receiver isolation using a quarter wavelength cable.

During the transmission pulse both sets of diodes will conduct, and the receiver is effectively shorted out. The short circuit at point B however looks like an open circuit at point A and so all the power is transmitted to the coil. The signal induced from the sample is too small to bias the diodes, and so is detected by the receiver circuitry.

The tiny e.m.f.'s from the sample are amplified at various stages and then mixed with a reference r.f. signal in a phase sensitive detector (p.s.d). Quadrature detection requires two p.s.d.'s, with a difference in phase of the reference signal of 90 degrees between them.

2.6.4 Control and Processing

All the control of the scanner is handled by a computer. A schematic diagram of the whole system is shown in Figure 2.35.

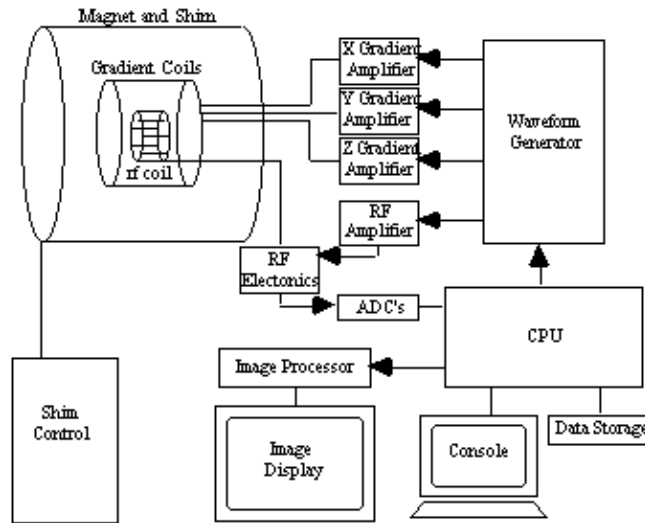


Figure 2.35 Schematic diagram of a MRI scanner.

The scanning operation is controlled from a central computer. This specifies the shape of gradient and r.f. waveforms, and timings to be used, and passes this information to the waveform generator, which outputs the signals and passes them to be amplified and sent to the coils. The NMR signal, once it has been phase sensitively detected, is turned to a digital signal by an analogue to digital converter. The digital signal is then sent to an image processor for Fourier transformation and the image is displayed on a monitor.

The raw data, that is the signal before Fourier transformation, is stored to enable the application of corrections to the data in post processing. To allow the use of fast Fourier transformation, matrix sizes of 2^n are usually used.

2.7 Safety Considerations in MRI

Since the technique of MRI is used to image humans, it is important to keep the safety of the subjects as a high priority. Since MRI does not use any form of ionising radiation, it is considerably safer than x-ray or radio-isotope techniques. However it is important, especially in a research setting, that the potential hazards of any new developments are carefully considered. In this section the major safety aspects are outlined.

2.7.1 Static Magnetic Fields

Most scanners used for MRI use magnets with field strengths of anything from 0.1 T to 4 T. There are many opinions on the effect of magnetic fields on biological tissues, and many studies carried out on the subject, ranging from epidemiological human studies, to the investigation of the development of animal embryos in high fields [32]. It is however currently concluded that there is no adverse biological effect from the static magnetic field used in MRI. Further experimentation will no doubt be carried out, and this view can be altered in the light of any new discoveries.

By far the more serious effect of the static magnetic field is the response of ferromagnetic objects to such fields. It is essential that no free ferromagnetic object is allowed near the magnet since the field will turn it into a projectile. In a laboratory setting this means that most tools, connectors, and other equipment to be used in the vicinity of the field must not be ferromagnetic. Subjects must be screened for objects like keys, pens, belts and other metal on clothing, as well as the possibility of surgical implants. Before scanning a subject it is also necessary to check that there would be no ill effects from exposure to the magnetic field. It is common to exclude people who are in the early stages of pregnancy, people who may have any kind of metal fragments in them, and those suffering from certain conditions such as epilepsy.

2.7.2 Time Varying Magnetic Fields

As well as the high static magnetic field used in MRI, it is possible that the two time varying fields, namely the gradients and the r.f. radiation, could affect the subject in the scanner.

The rapid switching of the field gradients, particularly in EPI, produce two safety concerns. Firstly there is the possibility of inducing voltages in tissue by Faraday's law. The current induced in a loop of tissue is dependent on the rate of change of the field (dB/dT), the conductivity of the tissue, and the cross section of the loop. Calculations by Mansfield and Morris [33] show that for $dB/dT = 1.0 \text{ Ts}^{-1}$, the currents induced are of the order $1 \mu\text{Acm}^{-2}$. Cohen [34] reports of subjects experiencing mild neural stimulation at gradient field variations of 61 Ts^{-1} , which is higher than the rates in normal use. It is wise however, if high switching rates are used, that subjects are warned of the possible effects, and monitored during the imaging.

A second safety concern with the gradients is that of acoustic noise levels. Since large currents are flowing through wires in a large magnetic field, a force is exerted on the wires. When the currents oscillate at audio frequencies, the resulting noise can be in excess of 100 dB. Subjects therefore must wear suitable ear protection during scanning, to reduce the noise to an acceptable level.

The heat that can be dissipated by r.f. fields is a further source of concern. The currents induced in tissues by such fields are dissipated as heat. Although most tissue has adequate blood flow to carry the heat away, some anatomical regions such as the eye do not. It is sensible to keep the heating due to r.f. radiation to a minimum, and the NRPB [35] guidelines state that the body temperature, or any mass of tissue, should not rise by more than 1 degrees centigrade. This is achieved by limiting the mean absorption rate in the whole body to 0.4 Wkg^{-1} and in any mass of tissue to 4 Wkg^{-1} .

It is also essential that there are no conductive items touching the subject's skin, since the heating of such objects by the r.f. radiation can cause serious burns.

2.7.3 Other Safety Considerations

Claustrophobia, and other psychological problems, can prevent a subject from being able to enter the scanner, and should be screened for before attempting to scan. It is necessary to check the

subject is fully informed as to the nature of the experiment and happy to proceed. Depending on the medical condition of the subject, it may be necessary to monitor them closely during the scanning, and communication is important so that the subject does not feel isolated.

2.8 References

- [1] Purcell, E. M., Torrey, H. C. and Pound, R. V. (1946) Resonance Absorption by Nuclear Magnetic Moments in a Solid. *Phys. Rev.* **69**,37-38.
- [2] Bloch, F., Hansen, W. W. and Packard, M. (1946) Nuclear Induction. *Phys. Rev.* **69**,127.
- [3] Lauterbur, P. C. (1973) Image Formation by Induced Local Interactions: Examples Employing Nuclear Magnetic Resonance. *Nature* **242**,190-191.
- [4] Mansfield, P. and Grannell, P. K. (1973) NMR 'diffraction' in solids? *J. Phys. C* **6**, L422-L426.
- [5] Abragam, A. (1961) 'Principles of Nuclear Magnetism'. Clarendon Press, Oxford.
- [6] Callaghan, P. T. (1991) 'Principles of Nuclear Magnetic Resonance Microscopy', Clarendon Press, Oxford.
- [7] Stern, O. and Gerlach, W. (1924) Uber die Richtungsquantelung im Magnetfeld. *Ann. Phys. Leipzig.* **74**,673.
- [8] Ljunggren, S. (1983) A Simple Graphical Representation of Fourier-Based Imaging Methods. *J. Magn. Reson.* **54**,338-343.
- [9] Locher, P. R. (1980) Computer Simulation of Selective Excitation in NMR Imaging. *Phil. Trans. R. Soc. Lond .B* **289**,537-542.
- [10] Morris, P. G., McIntyre, D. J. O. and Rourke, D. E. (1989) Rational Approaches to the Design of NMR Selective Pulses. *NMR in Biomed.* **2**,257-266.
- [11] Mansfield, P. (1988) Imaging by Nuclear Magnetic Resonance. *J. Phys. E: Sci. Instrum.* **21**,18-30.
- [12] Damadian, R., Goldsmith, M. and Minkoff, L. (1977) FONAR Image of the Live Human Body. *Physiol. Chem. & Phys.* **9**,97-100.
- [13] Hounsfield, G. N. (1973) Computerized Transverse Axial Scanning (Tomography). *Br. J. Radiol.* **46**,1016-1022.
- [14] Edelstein, W. A., Hutchison, J. M. S., Johnson, G. and Redpath, T. (1980) Spin warp NMR Imaging and Applications to Human Whole-Body Imaging. *Phys. Med. Biol.* **25**,751-756.
- [15] Kumar, A., Welti, D. and Ernst, R. R. (1975) NMR Fourier Zeugmatography. *J. Magn. Reson.* **18**,69-83.
- [16] Ernst, R. R. and Anderson, W. A. (1966) Application of Fourier Transform Spectroscopy to Magnetic Resonance. *Rev. Sci. Instr.* **37**,93-102.

- [17] Haase, A., Frahm, J., Matthaei, D., Hänicke, W. and Merboldt, K.-D. (1986) FLASH Imaging. Rapid NMR Imaging Using Low Flip-Angle Pulses. *J. Magn. Reson.* **67**,258-266.
- [18] Mansfield, P. (1977) Multi-Planar Image Formation using NMR Spin Echoes. *J. Phys. C* **10**,L55-L58.
- [19] Mansfield, P. and Pykett, I. L. (1978) Biological and Medical Imaging by NMR. *J. Magn. Reson.* **29**,355-373.
- [20] Johnson, G., Hutchison, J. M. S., Redpath, T. W. and Eastwood, L. M. (1983) Improvements in Performance Time for Simultaneous Three-Dimensional NMR Imaging. *J. Magn. Reson.* **54**,374-384.
- [21] Mansfield, P., Howseman, A. M., and Ordidge, R. J. (1989) Volumar Imaging using NMR Spin Echoes: Echo-Volumar Imaging (EVI) at 0.1 T. *J. Phys. E: Sci. Instrum.* **22**,324-330.
- [22] Maudsley, A. A., Hilal, S. K., Perman, W. H. and Simon, H. E. (1983) Spatially Resolved High Resolution Spectroscopy by "Four-Dimensional" NMR. *J. Magn. Reson.* **51**,147-152.
- [23] Mansfield, P. (1988) Imaging by Nuclear Magnetic Resonance. *J. Phys. E: Sci. Instrum.* **21**,18-30.
- [24] Kay, I. and Henkelman, R. M. (1991) Practical Implementation and Optimisation of One-Shot T_1 Imaging. *Magn. Reson. Med.* **22**,414-424.
- [25] Gowland, P. and Mansfield, P. (1993) Accurate Measurement of T_1 *in vivo* in Less Than 3 Seconds Using Echo-Planar Imaging. *Magn. Reson. Med.* **30**,351-354.
- [26] Haase, A., Frahm, J., Hänicke, W. and Matthaei, D. (1985) ^1H NMR Chemical Shift Selective (CHESS) Imaging. *Phys. Med. Biol.* **30**,341-344.
- [27] Sumanaweera, T. S., Glover, G. H., Binford, T. O. and Adler, J. R. (1993) MR Susceptibility Misregistration Correction. *I.E.E.E. Trans. Med. Imaging* **12**,251-259.
- [28] Mansfield, P., Ordidge, R. J. and Coxon, R. (1988) Zonally magnified EPI in real time by NMR. *J. Phys. E: Sci. Instrum.* **21**,275-280.
- [29] Ehman, R. L. and Felmlee, J. P. (1989) Adaptive Technique for High-Definition MR Imaging of Moving Structures. *Radiology* **173**,255-263.
- [30] Howseman, A. M., Stehling, M. K., Chapman, B., Coxon, R., Turner, R., Ordidge, R. J., Cawley, M. G., Glover, P., Mansfield, P. and Coupland, R. E. (1988) Improvements in Snap-Shot Nuclear Magnetic Resonance Imaging. *Br. J. Radiol.* **61**,822-828.
- [31] Hayes, C. E., Edelstein, W. A., Schenck, J. F., Mueller, O. M. and Eash M. (1985) An Efficient, Highly Homogeneous Radiofrequency Coil for Whole-Body NMR Imaging at 1.5 T. *J. Magn. Reson.* **63**,622-628.
- [32] Tenforde, T. S. (1979) 'Magnetic Field Effects on Biological Systems', Plenum Press, New York.
- [33] Mansfield, P. and Morris, P. G. (1982). 'NMR Imaging in Biomedicine', in *Advances in Magnetic*

Resonance, Academic Press, New York.

[34] Cohen, M. S., Weisskoff, R. M., Rzedzian, R. R. and Kantor, H. L. (1990) Sensory Stimulation by Time-Varying Fields. *Magn. Reson. Med.* **14**,409-414.

[35] National Radiological Protection Board (1983) Revised Guidance on Acceptable Limits of Exposure during Nuclear Magnetic Resonance Clinical Imaging. *Br. J. Radiol.* **56**, 974-977.

Chapter 3

Magnetic Resonance Imaging of Brain Function

3.1 Introduction to Neuroimaging

The idea of localisation of function within the brain has only been accepted for the last century and a half. In the early 19th century Gall and Spurzheim, were ostracised by the scientific community for their so-called science of phrenology[1]. They suggested that there were twenty-seven separate organs in the brain, governing various moral, sexual and intellectual traits. The importance of each to the individual was determined by feeling the bumps on their skull. The science behind this may have been flawed, but it first introduced the idea of functional localisation within the brain which was developed from the mid 1800's onwards by clinicians such as Jackson [2] and Broca[3]. Most of the information available on the human brain came from subjects who had sustained major head wounds, or who suffered from various mental disorders[4]. By determining the extent of brain damage, and the nature of the loss of function, it was possible to infer which regions of the brain were responsible for which function.

Patients with severe neurological disorders were sometimes treated by removing regions of their brain. For example, an effective treatment for a severe form of epilepsy involved severing the corpus callosum, the bundle of nerve fibres which connect left and right cerebral hemispheres. Following the surgery patients were tested, using stimuli presented only to the left hemisphere or to the right hemisphere[5]. If the object was in the right visual field, therefore stimulating the left hemisphere, then the subject was able to say what they saw. However if the object was in the left visual field, stimulating the right hemisphere, then the subject could not say what they saw but they could select an appropriate object to associate with that image. This suggested that only the left hemisphere was capable of speech.

With the development of the imaging techniques of computerised tomography (CT) and magnetic resonance imaging it was possible to be more specific as to the location of damage in brain injured patients. The measurement of the electrical signals on the scalp, arising from the synchronous firing of the neurons in response to a stimulus, known as electroencephalography (EEG), opened up new possibilities in studying brain function in normal subjects. However it was the advent of the functional imaging modalities of positron emission tomography (PET), single photon emission computed tomography (SPECT), functional magnetic resonance imaging (fMRI), and magnetoencephalography (MEG) that led to a new era in the study of brain function.

In this chapter the mechanisms of the techniques mentioned above are outlined, together with an assessment of their strengths and weaknesses. Then an introduction to the physical and structural anatomy of the brain is given, and some of the terminology used in neurology is introduced. This is followed by a more detailed explanation of functional MRI and how such experiments are performed.

3.1.1 SPECT and PET

The imaging modalities of single photon emission computed tomography (SPECT) and positron emission tomography (PET) both involve the use of radioactive nuclides either from natural or synthetic sources. Their strength is in the fact that, since the radioactivity is introduced, they can be used in tracer studies where a radiopharmaceutical is selectively absorbed in a region of the brain.

The main aim of SPECT as used in brain imaging, is to measure the regional cerebral blood flow (rCBF). The earliest experiments to measure cerebral blood flow were performed in 1948 by Kety and Schmidt[6]. They used nitrous oxide as an indicator in the blood, measuring the differences between the arterial input and venous outflow, from which the cellular uptake could be determined. This could only be used to measure the global cerebral blood flow, and so in 1963 Glass and Harper[7], building on the work of Ingvar and Lassen[8], used the radioisotope Xe-133, which emits gamma rays, to measure the regional cerebral blood flow. The development of computed tomography in the 1970's allowed mapping of the distribution of the radioisotopes in the brain, and led to the technique now called SPECT[9].

The radiotracer (or radiopharmaceutical) used in SPECT emits gamma rays, as opposed to the positron emitters used in PET. There are a range of radiotracers that can be used, depending on what is to be measured. For example I-123-3-quinuclidinyl 4-isodobenzilate is a neurotransmitter agonist which can be used for imaging receptors. For rCBF measurements Xe-133 can be introduced into the blood stream by inhalation. Detection is carried out using a gamma camera - a scintillation detector consisting of a collimator, a NaI crystal, and a set of photomultiplier tubes as shown in Figure 3.1.

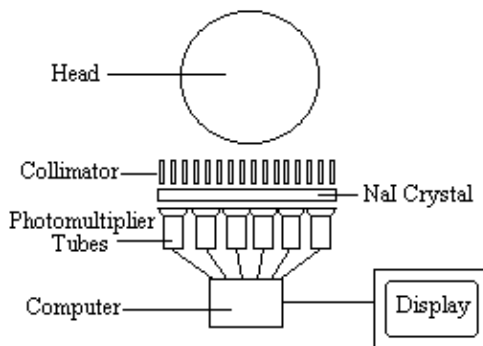


Figure 3.1 Schematic diagram of a gamma camera used in SPECT imaging

By rotating the gamma camera around the head, a three dimensional image of the distribution of the radiotracer can be obtained by employing filtered back projection (as described in section 2.3.4). The radioisotopes used in SPECT have relatively long half lives (a few hours to a few days) making them easy to produce and relatively cheap. This represents the major advantage of SPECT as a brain imaging technique, since it is significantly cheaper than either PET or fMRI. However it lacks good spatial or temporal resolution, and there are safety aspects concerning the administration of radioisotopes to the subject, especially for serial studies.

Positron emission tomography[10] has two major advantages over SPECT, namely better spatial resolution and greater sensitivity. This comes from using positron emitters such as O-15 and F-18 as the radionuclide. When such nuclei decay they emit a positron, that is a particle with the same rest mass as an electron but with charge +1. Once the positron is emitted it travels a short distance before colliding with an electron. The annihilation of the two particles creates two photons each with energy 511 keV. In order to conserve momentum, the two photons are emitted at virtually 180 degrees to each other, and it is these photons that are detected in a ring of scintillators and photomultiplier tubes surrounding the head (Figure 3.2).

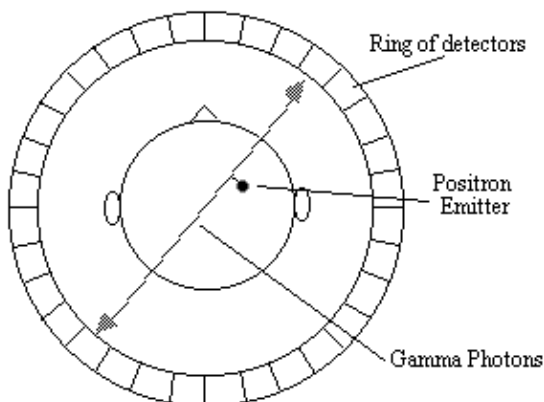


Figure 3.2 Schematic diagram of a PET scanner. A positron is emitted from a radioisotope in the brain. The positron annihilates with an electron, producing two photons emitted at 180 degrees to each other

Opposite pairs of detectors are linked so as to register only coincident photons, thus defining a set of coincidence lines. Reconstruction of these lines by filtered back projection gives an image of the source of the annihilation. Since the detectors only record the site of the annihilation, resolution in a PET scanner is limited by the distance travelled by the positron through the tissue before it meets an electron. This fundamentally restricts the resolution of the scanner to 2 - 3 mm at best.

The positron emitters used in PET have short half lives, of the order of 2 - 100 minutes. This means that the isotopes must usually be made at the site of the scanner, using an expensive cyclotron. However, this short half life means that dynamic studies of brain function can be carried out using the technique.

Functional imaging studies using PET first appeared in 1984 with a study using $C^{15}O_2$. Usually two cognitive states are imaged, one active and one resting, and by subtracting these two states a map of the regions of the brain responsible for that task made. PET is widely used as a tool for cognitive function, and much of the literature on brain function published in the last 10 years has used the technique. Positron emitting neurotransmitters such as F-18 labelled DOPA, mean that dopamine function can be followed in patients with Parkinson's disease. The main drawback of PET is its use of radioisotopes, and its very high cost, however its neurotransmitter mapping ability means that it will retain a role in the face of the less invasive, and more available fMRI.

3.1.2 EEG and MEG

Measuring the electrical signals from the brain has been carried out for several decades [11], but it is only more recently that attempts have been made to map electrical and magnetic activity. The electroencephalogram (EEG) is recorded using electrodes, usually silver coated with silver chloride, attached to the scalp and kept in good electrical contact using conductive electrode jelly. One or more active sites may be monitored relative to a reference electrode placed on an area of low response activity such as the earlobe. The signals are of the order of 50 microvolts, and so care must be taken to reduce interference from external sources, eye movement and muscle activity. Several characteristic frequencies are detected in the human EEG. For example, when the subject is relaxed the EEG consists mainly of frequencies in the range 8 to 13 Hz, called alpha waves, but when the subject is more alert the frequencies detected in the signal rise above 13Hz, called beta waves. Measurements of the EEG during sleep have revealed periods of high frequency waves, known as rapid eye movement (REM) sleep which has been associated with dreaming.

The EEG can also be measured in response to some regularly repeated stimulus such as the pattern reversal of a projected checkerboard, or more complicated task such as number memorising

and recall. The signal, from each electrode, in response to the stimulus is recorded and averaged together over a number of trials. The response is characterised by the delay, or latency, of the peak of the signal from the presentation of the stimulus. This is of the order of milliseconds for brain stem responses and 100's of milliseconds for cortical responses. For example a commonly detected response to an oddball stimulus, the P300, has a latency of 300 ms. Having found an electrical signal of interest, the magnitude of the peak can be mapped across the scalp giving an idea of the source. The major limitation of studying brain function using EEG is that the signals measured are recorded on the scalp, which may not represent the activity in the underlying cortex. However since the technique is very cheap and safe, it has many uses and can be involved in studies where the scanning techniques could not, such as continuous monitoring during sleep.

Since the magnetic signals from the firing of the neurons do not need to be conducted to the scalp, measuring them gives much greater signal localisation than measuring the currents themselves. This is the basis of the much newer technique of magnetoencephalography (MEG). The first successful measurements of these magnetic fields were made by Cohen in 1972 [12]. The magnitude of the magnetic signals, resulting from the electrical firing of the neurons is of the order of 10^{-13} Tesla, for 1 million synchronously active synapses. Such small signals are picked up using a superconducting quantum interference device (SQUID) magnetometer (Figure 3.3).

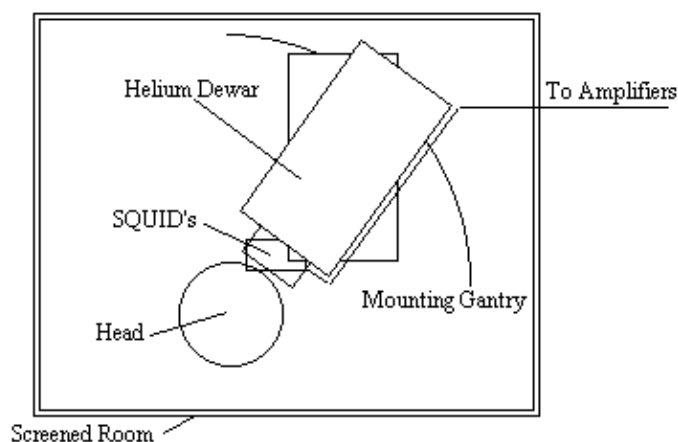


Figure 3.3 Schematic diagram of a magnetometer for measuring MEG's

Interference from external sources is a major problem with MEG, and the magnetometer must be sited in a magnetically shielded room. Current magnetometers have as many as 120 SQUIDS covering the scalp.

MEG experiments are carried out in much the same way as their EEG counterpart. Having identified the peak of interest, the signals from all the detectors are analysed to obtain a field map. From this map an attempt can be made to ascertain the source of the signal by solving the inverse problem. Since the inverse problem has no unique solution, assumptions need to be made, but providing there are only a few activated sites, close to the scalp then relatively accurate localisation is possible, giving a resolution of the order of a few millimetres.

MEG has the advantage over EEG that signal localisation is, to an extent, possible, and over PET and fMRI in that it has excellent temporal resolution of neuronal events. However MEG is costly and its ability to accurately detect events in deeper brain structures is limited.

3.1.3 Functional MRI and MRS

Since functional magnetic resonance imaging (fMRI) is the subject of this thesis, little will be said in this section as to the mechanisms and applications of the technique, as this is covered later in the chapter. The purpose of this section is to compare fMRI to the other modalities already mentioned, and also to consider the related, but distinct technique of magnetic resonance spectroscopy (MRS).

During an fMRI experiment, the brain of the subject is scanned repeatedly, usually using the fast imaging technique of echo planar imaging (EPI). The subject is required to carry out some task consisting of periods of activity and periods of rest. During the activity, the MR signal from the region of the brain involved in the task normally increases due to the flow of oxygenated blood into that region. Signal processing is then used to reveal these regions. The main advantage of MRI over its closest counterpart, PET, is that it requires no contrast agent to be administered, and so is considerably safer. In addition, high quality anatomical images can be obtained in the same session as the functional studies, giving greater confidence as to the source of the activation. However, the function that is mapped is based on blood flow, and it is not yet possible to directly map neuroreceptors as PET can. The technique is relatively expensive, although comparable with PET, however since many hospitals now have an MRI scanner the availability of the technique is more widespread.

fMRI is limited to activation studies, which it performs with good spatial resolution. If the resolution is reduced somewhat then it is also possible to carry out spectroscopy, which is chemically specific, and can follow many metabolic processes. Since fMRS can give the rate of glucose utilisation, it provides useful additional information to the blood flow and oxygenation measurements from fMRI, in the study of brain metabolism.

3.1.4 Comparison of the Functional Brain Imaging Modalities

The brain imaging techniques that have been presented in this chapter all measure slightly different properties of the brain as it carries out cognitive tasks. Because of this the techniques should be seen as complementary rather than competitive. All of them have the potential to reveal much about the function of the brain and they will no doubt develop in clinical usefulness as more about the underlying mechanisms of each are understood, and the hardware becomes more available. A summary of the strengths and weaknesses of the techniques is presented in Table 3.1.

Technique	Resolution	Advantages	Disadvantages
SPECT	10 mm	Low cost Available	Invasive Limited resolution
PET	5 mm	Sensitive Good resolution Metabolic studies Receptor mapping	Invasive Very expensive
EEG	poor	Very low cost Sleep and operation monitoring	Not an imaging technique
MEG	5 mm	High temporal resolution	Very Expensive Limited resolution for deep structures
fMRI	3 mm	Excellent resolution Non-invasive	Expensive Limited to activation studies
MRS	low	Non-invasive metabolic studies	Expensive Low resolution

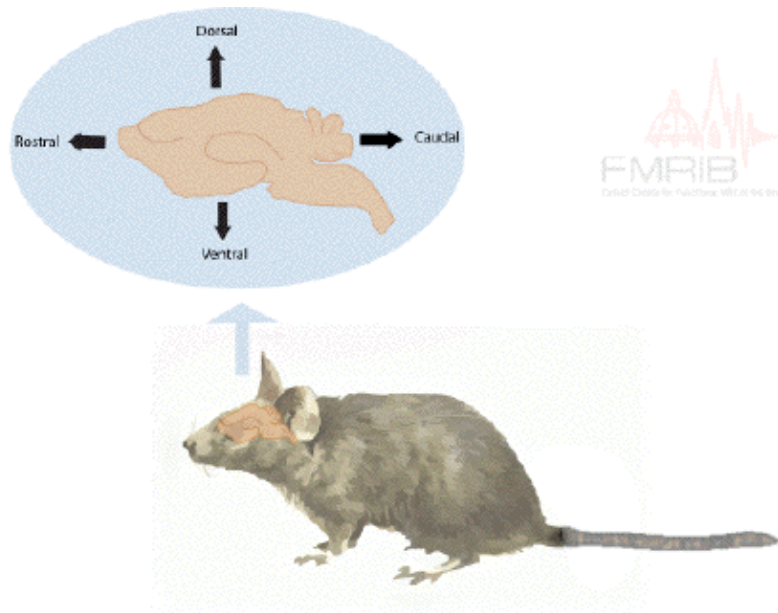
Table 3.1 Comparison of modalities for studying brain function

3.2 The Structure of the Brain

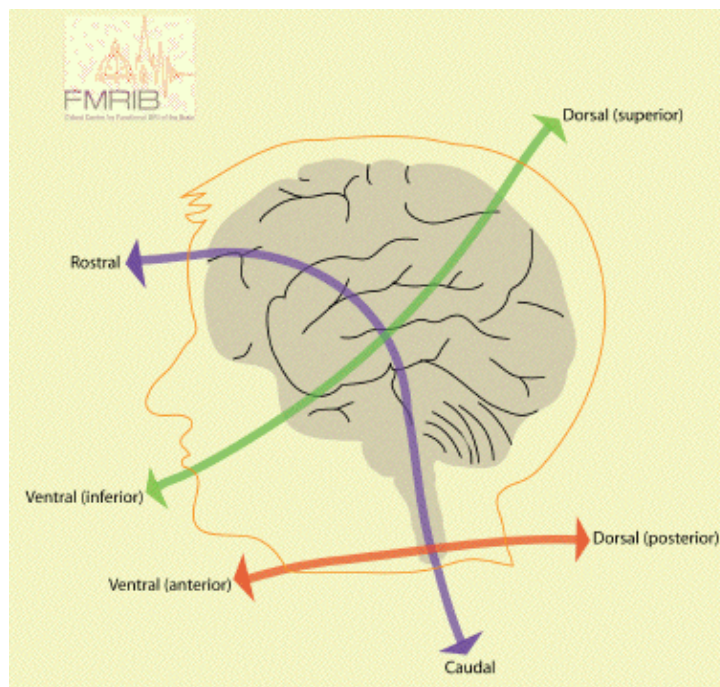
Since much of this thesis makes references to brain anatomy and function, this section deals with the terminology used in the discipline of neurology. There are four sections covering brain anatomy, brain cellular structure and brain function. Further reference can be obtained from the many good books on brain biochemistry and neuroanatomy [13,14,15].

3.2.1 Principal Axes and Planes of the Central Nervous System

In order to describe the position of structures relative to each other in the brain, neurology has a number of terms of direction, many of which are derived from the Latin or Greek. There are two axes which describe the organisation of the central nervous system (CNS). These are most easily understood in animals with the spinal cord running horizontally rather than vertically. In this case the *rostral-caudal* axis runs from nose to tail, and the *dorsal-ventral* axis runs perpendicularly to this as shown in Figure 3.4a. Now using this system in the human spinal cord, 'top to bottom' is '*caudal* to *rostral*', and 'back to front' is '*dorsal* to *ventral*' (Figure 3.4b). In the human brain however these axes turn through 90 degrees, so the front of the brain is *rostral*, top is *dorsal*, and base is *ventral*.



(a)



(b)

Figure 3.4 The axes of the central nervous system. (a) In animals, where the spinal cord runs horizontally. (b) In humans, where the spinal cord runs vertically.

In addition to these labels, there is another perpendicular set of axes which is the same for spinal cord and brain, that is *anterior*=front, *posterior*=back, *superior*=top, *inferior*=bottom.

The *midline* runs down the centre of the brain, separating left from right. If two structures are on the same side of the midline, they are said to be *ipsilateral*, whereas they are *contralateral* if they are on

opposite sides. When comparing two structures, the one closest to the midline is *medial*, as opposed to the other which is *lateral*.

When viewing sections through the brain, three mutually perpendicular planes are commonly considered, as shown in Figure 3.5. These are *axial (or transverse)*, *coronal*, and *sagittal*.

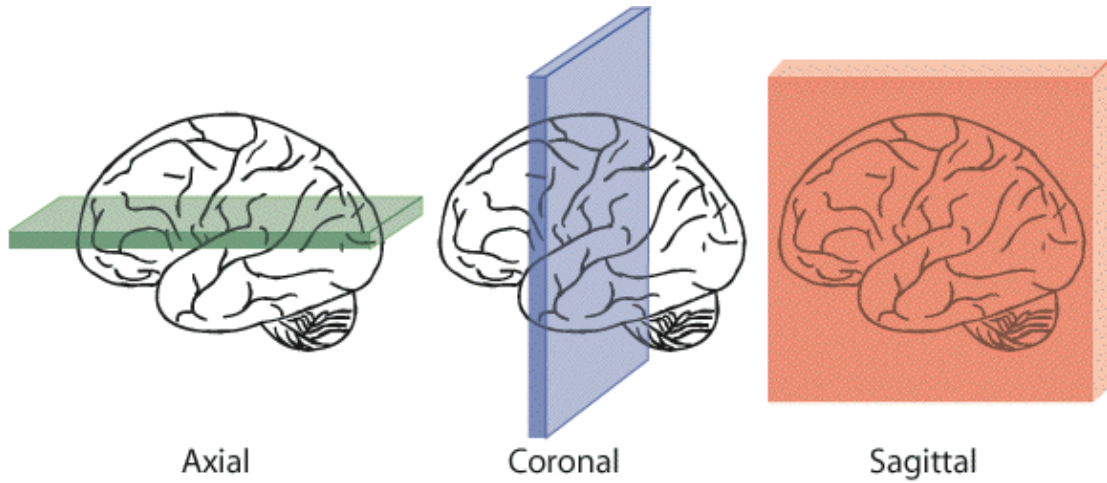


Figure 3.5 The three planes of section in the brain

3.2.2 Cellular Structure of the Brain

The neuron is the basic functional unit of the nervous system. The brain consists of several hundred billion neurons, communicating by billions of interconnections. All neurons consist of four distinct parts: *cell body*, *dendrites*, *axons* and *axon terminals* (Figure 3.6).

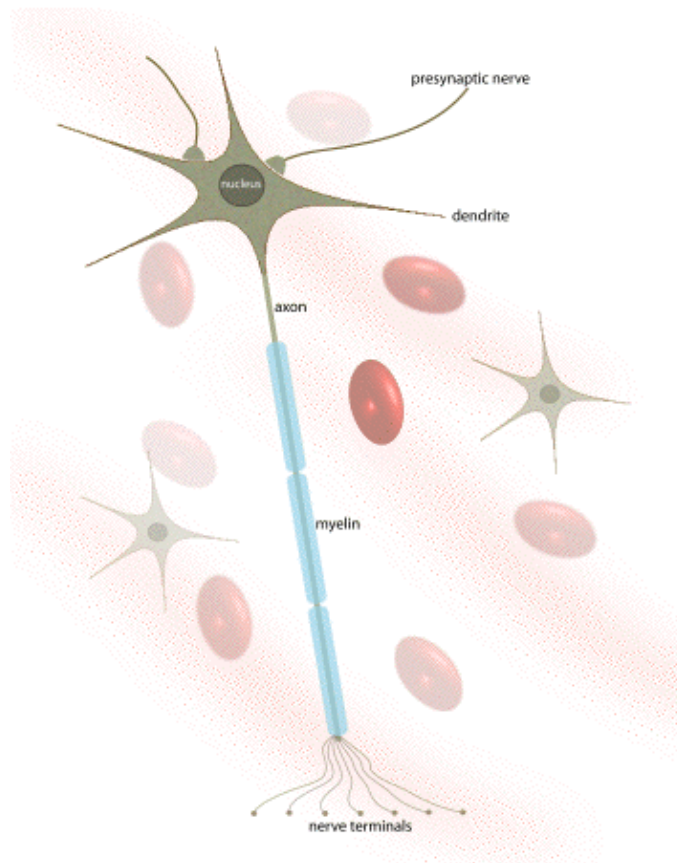


Figure 3.6 Diagram of a single motor neurone

The *cell body* (or *soma*) contains the nucleus of the cell, as well as the essential cellular organelles, such as the energy generating *mitochondria*. The cell body has many branches, called *dendrites*, which receive signals from other cells, and are often covered in *dendritic spines*. Extending from the cell body in one direction is an *axon*. The length of axons can be several centimetres or longer. Axons carry information from one neuron to another, and are terminated at the *synaptic knob*, which is attached to the dendrites or cell body of another neuron. Signals are transferred across the synapse by means of a chemical *neurotransmitter*.

Signals travel along the axon by generating and propagating an action potential. This is produced by letting the delicate balance of sodium, potassium and chloride ions across the cell membrane be altered, thus generating an electrical signal that flows along the axon. If the axon is coated in a fatty sheath, called *myelin*, the signal travels at higher speeds of anything up to 120 ms⁻¹. When the signal reaches the synapse, the synaptic knob emits a neurotransmitter which acts either to encourage the next neuron to 'fire' (*excitatory*) or discourage the neuron to fire (*inhibitory*).

The CNS contains a number of different types of neurons, which are tailored to the job they perform. Signals from sensory receptors over the body feed along the spinal cord to the brain, and signals are sent from the brain to make muscles contract. Many medical conditions are caused by the failure of the CNS to function correctly, for example in Parkinson's disease there is a deficiency of the neurotransmitter dopamine.

For every neuron in the CNS there are also ten *glial* cells. These cells provide support for neurons, for example the *microglia* which perform a scavenger role, and *oligodendrocytes* which form the myelin sheath around the axons.

3.2.3 Brain Anatomy

The central nervous system consists of the spinal cord and the brain. The brain is then further divided into the *forebrain*, *midbrain*, and *hindbrain* (Figure 3.7).

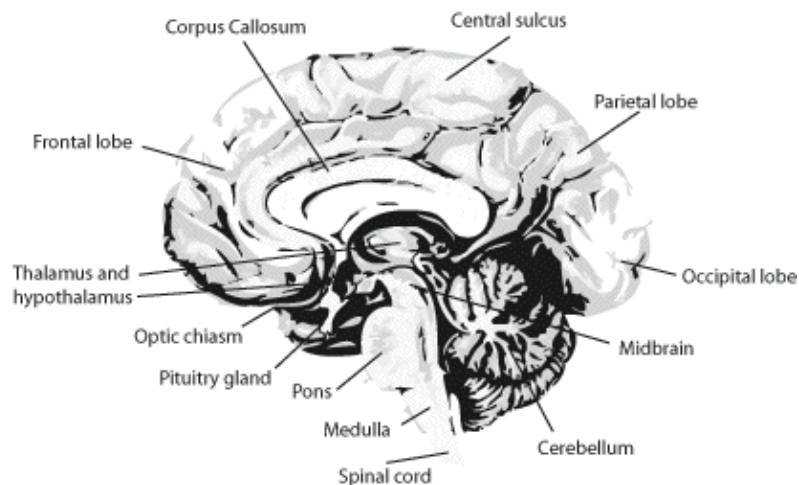


Figure 3.7 Midline section through the brain showing the cerebrum, cerebellum, midbrain and spinal cord

The largest region is the forebrain, which contains the *cerebral hemispheres*, the *corpus callosum*, *thalamus*, *hypothalamus*, and *hippocampus*. The hindbrain consists of the *cerebellum*, *pons*, and *medulla*. The structure of each of these is described below.

The cerebrum is divided into two hemispheres, the left and the right, separated by the *longitudinal fissure*. Anatomically these are identical in form, each being split into four lobes; the *frontal lobe*, the *parietal lobe* on the top, the *temporal lobe* on the side, and the *occipital lobe* at the back (Figure 3.8). The frontal and parietal lobes are separated by the *central sulcus*, and the temporal lobe separated by the *lateral fissure*. The corpus callosum joins left and right hemispheres.

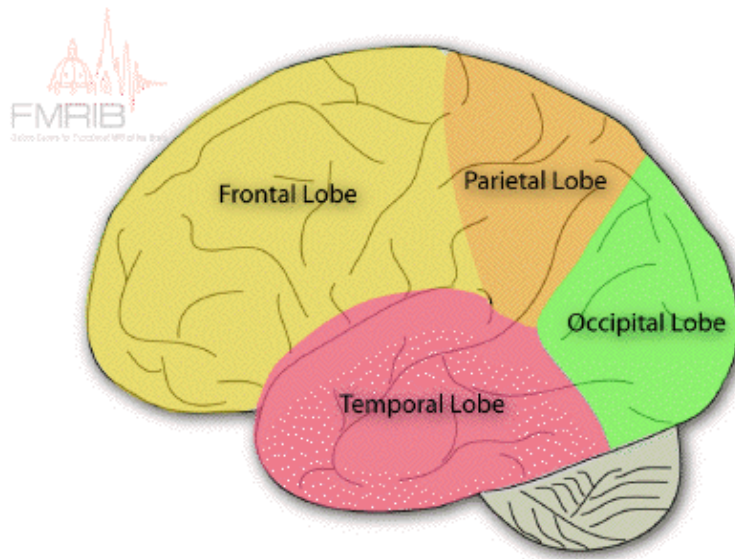


Figure 3.8 The four lobes of the cerebrum; frontal, temporal, parietal and occipital

The outer surfaces of the hemispheres contain neurons with unmyelinated axons, whereas the more central regions contain myelinated axons. The presence of the myelin sheath gives these regions of the brain a white appearance, and is termed white matter, as opposed to the grey matter of the outer surface. The grey matter is folded forming many fissures and sulci (grooves) and gyri (elevations). The whole brain is surrounded with a watery fluid that acts as a cushion from physical shocks, called *cerebrospinal fluid* (CSF). There are also four cavities within the brain which contain CSF, two *lateral ventricles*, one in each hemisphere, and two lower in the brain. The lateral ventricles show up very clearly on MR images since CSF has a long T2 (Figure 3.9).

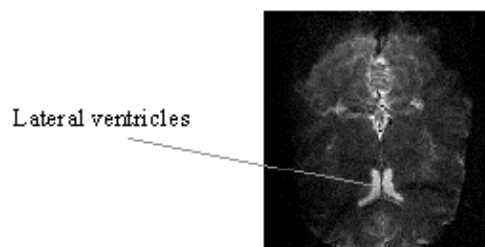


Figure 3.9 T2* Weighted image of a transaxial slice through the lateral ventricles

Under the surface of the cerebral hemispheres are bundles of fibres, the *basal ganglia*, connecting together many regions of the cerebral cortex. The thalamus, hypothalamus and hippocampus are located at the centre of the forebrain, just above the midbrain (Figure 3.10). At the rear of the brain is a more tightly folded structure called the *cerebellum*, which is connected to the *pons*, the *medulla*, and finally the spinal cord.

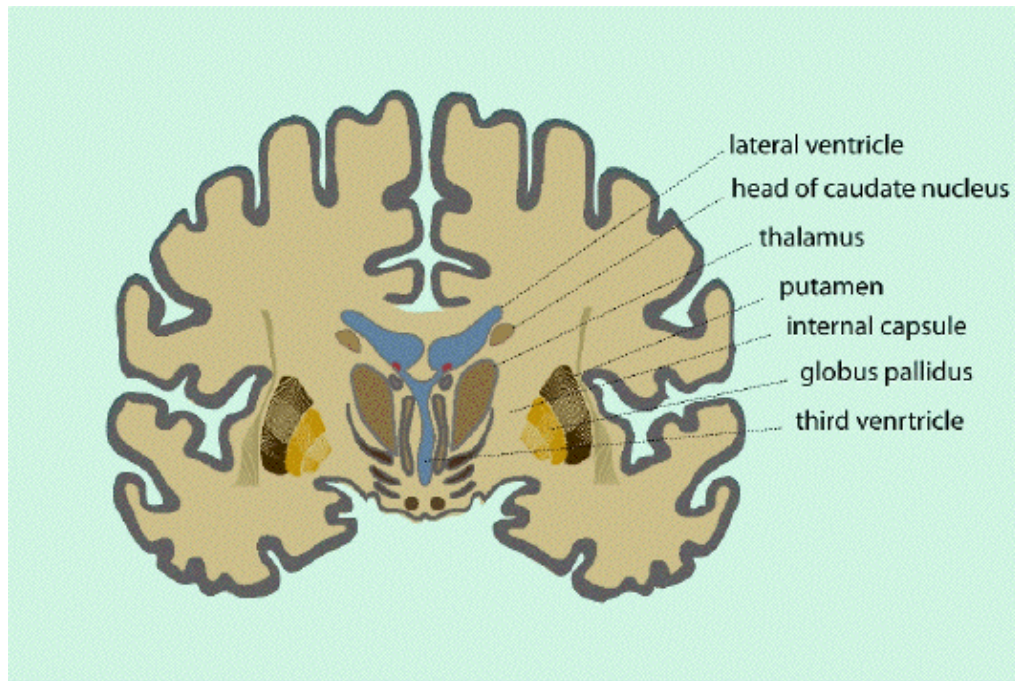


Figure 3.10 Coronal section through the brain showing the thalamus and hypothalamus

3.2.4 Functional Organisation of the Brain

The functional organisation of much of the brain is poorly understood. However many of the regions involved in sensory and motor function have been identified.

The *primary visual cortex* is located in the occipital lobe, which deals with the reception and interpretation of vision. The right visual field is mapped on to the left cerebral hemisphere, and the left visual field on to the right hemisphere (Figure 3.11). The signals from the retina travel along the *optic tracts*, which cross over at the *optic chiasm*.

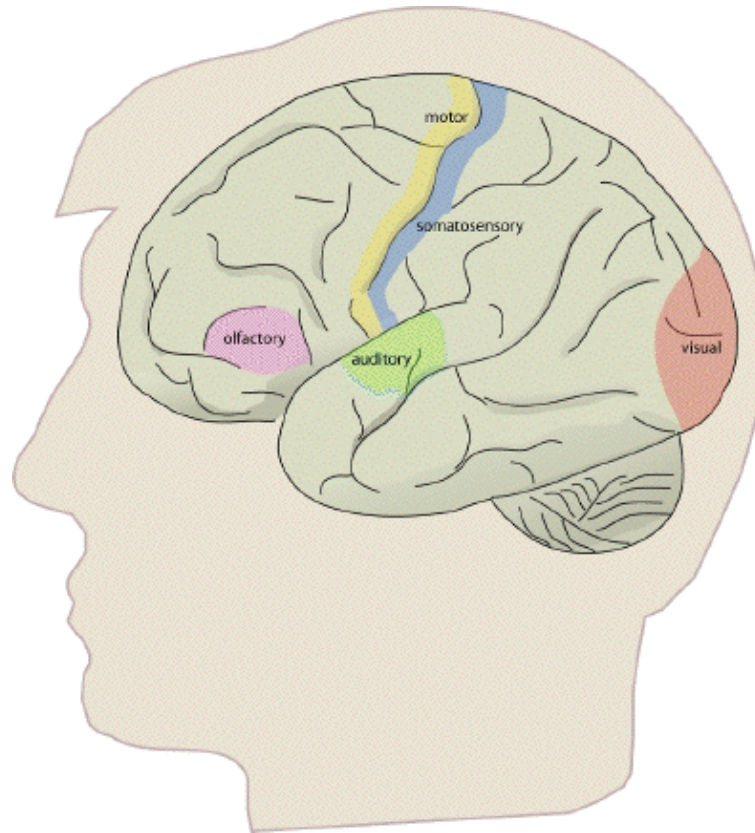


Figure 3.12 Approximate location of the five primary sensory areas and the primary motor cortex

The organisation of the somatosensory cortex shows similarity to a map of the surface of the body[16]. This is illustrated in what is known as the sensory homunculus (Figure 3.13). A much greater part of the somatosensory cortex is associated with the hand and face, compared to regions not so important in tactile tasks such as the leg. Similarly there is a motor homunculus which illustrates the layout of the motor cortex. The hand is given much more cortical surface in the motor cortex than in the somatosensory cortex, representing the highly sophisticated tasks that the hands perform.

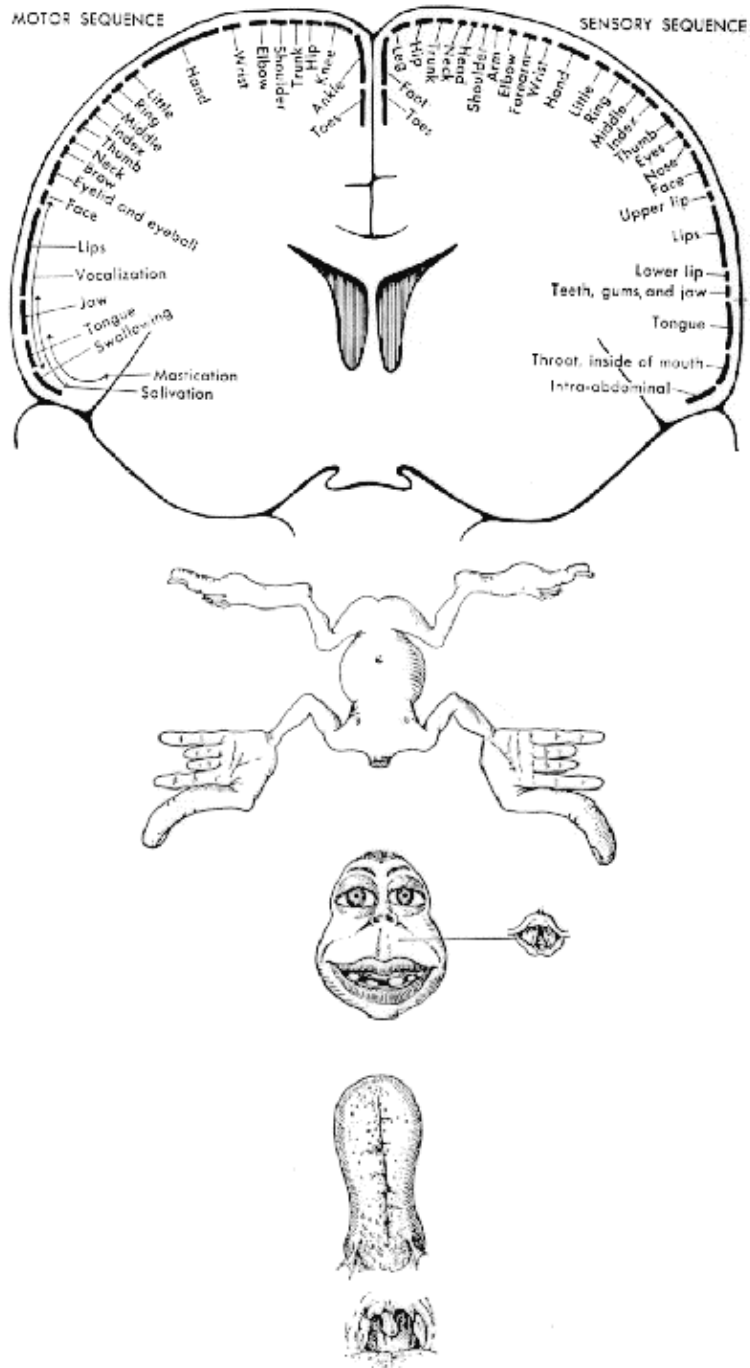


Figure 3.13 (a) A cross section through the brain, illustrating the sensory and motor sequences. (b) The motor homunculus, drawn such that the relative size of the organs represents the area of the corresponding cortex (from Penfield and Rasmussen (1952) 'The Cerebral Cortex of Man')

All the regions mentioned so far are primary cortices because they are most closely involved with the brain's input and output. Much of the rest of the brain is given over to integrating these stimuli, and interpreting how to respond. The regions responsible for these more abstract tasks are termed secondary (Figure 3.14). For example, the secondary motor regions, which are more anterior in the frontal lobes to the primary motor cortex, are responsible for planning and initiating motion, and the secondary visual area, close to the primary visual cortex is involved in interpreting colours and movement in the visual information. The tertiary areas, or association cortices, are responsible for the higher brain functions such as interpretation and memory.

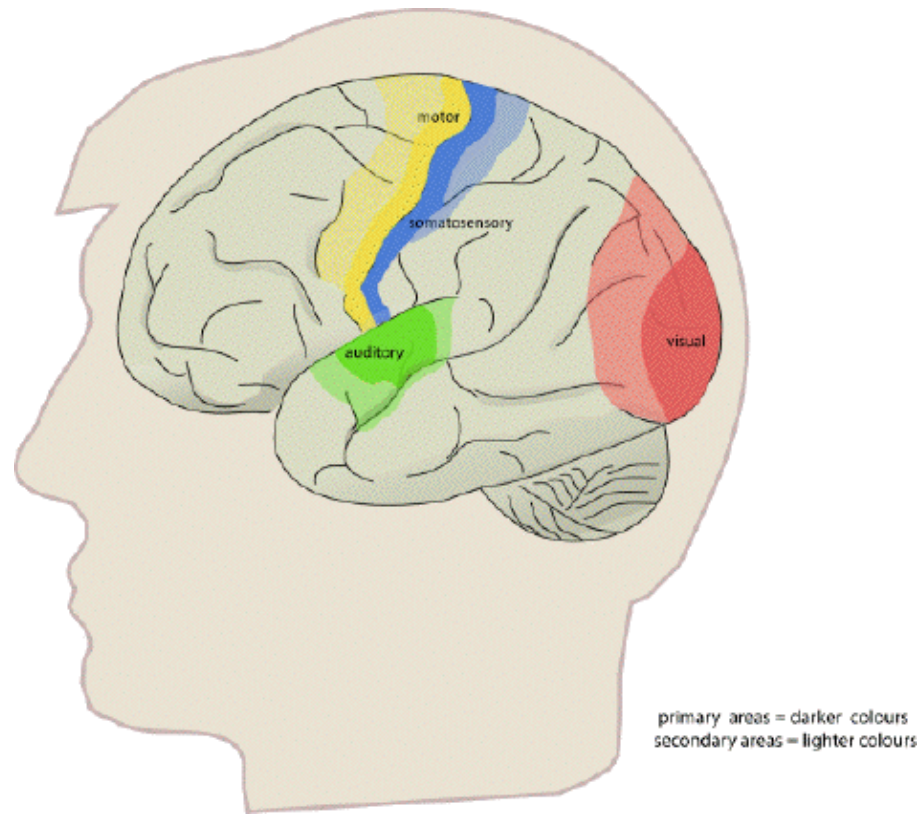


Figure 3.14 Approximate locations of the primary, secondary and tertiary sensory and motor cortices

Some specific regions of interest are those responsible for speech, which are located in the left hemisphere of most people. *Broca's area* is in the lower part of the frontal lobe (Figure 3.15), and is involved in the formation of sentences, and *Wernicke's area*, located in the temporal lobe is involved in the comprehension of speech.

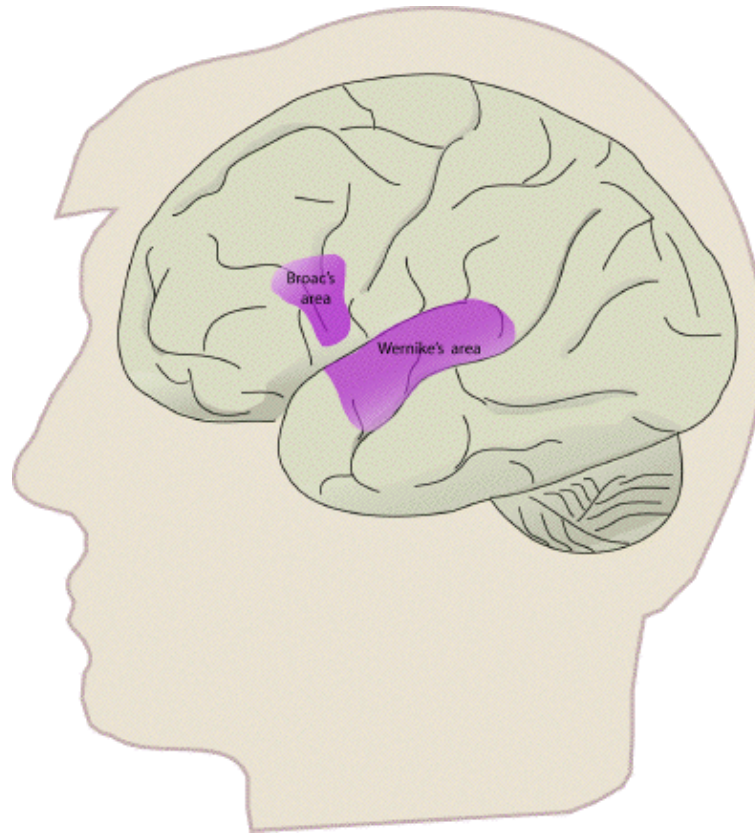


Figure 3.15 Approximate locations of Broca's area, involved in the formation of sentences and Wernicke's area, involved in the comprehension of speech

The cerebellum has a number of poorly understood functions, but is involved in the regulation of movement. Patients with damage to the cerebellum can still move, but the movements become more erratic and less controlled. The cerebellum is also involved in the 'automatic response' that is experienced when a new skill has been learnt. For example, when learning to play a piece on the piano, at first the cerebral cortex is required to control the fingers, but upon learning, the cerebellum takes over. The region at the centre of the brain, the thalamus acts as an intermediary in transferring information to the cerebral hemispheres. The hippocampus plays an important role in long term memory storage, and the hypothalamus mediates emotions, also being involved in the control of hormonal release. The lower structures in the brain, the reticular formation, medulla and pons, regulate alertness and participate in blood pressure and respiratory regulatory mechanisms.

This is just a brief sketch of brain function as it is understood at present. New literature is appearing at a rapid pace, confirming and evolving the models. The motor system is covered in more detail in Chapter 7.

3.3 Functional Magnetic Resonance Imaging

The brain, like any other organ in the body requires a steady supply of oxygen in order to metabolise glucose to provide energy. This oxygen is supplied by the component of the blood called haemoglobin. It was demonstrated as long ago as 1935 that the magnetic properties of haemoglobin depended on the amount of oxygen it carried[17]. This dependency has given rise to a method for measuring activation using MRI, commonly known as functional magnetic resonance imaging (fMRI).

3.3.1 Metabolism and Blood Flow in the Brain

The biochemical reactions that transmit neural information via action potentials and neurotransmitters, all require energy. This energy is provided in the form of ATP, which in turn is produced from glucose by oxidative phosphorylation and the Krebs cycle (Figure 3.16).

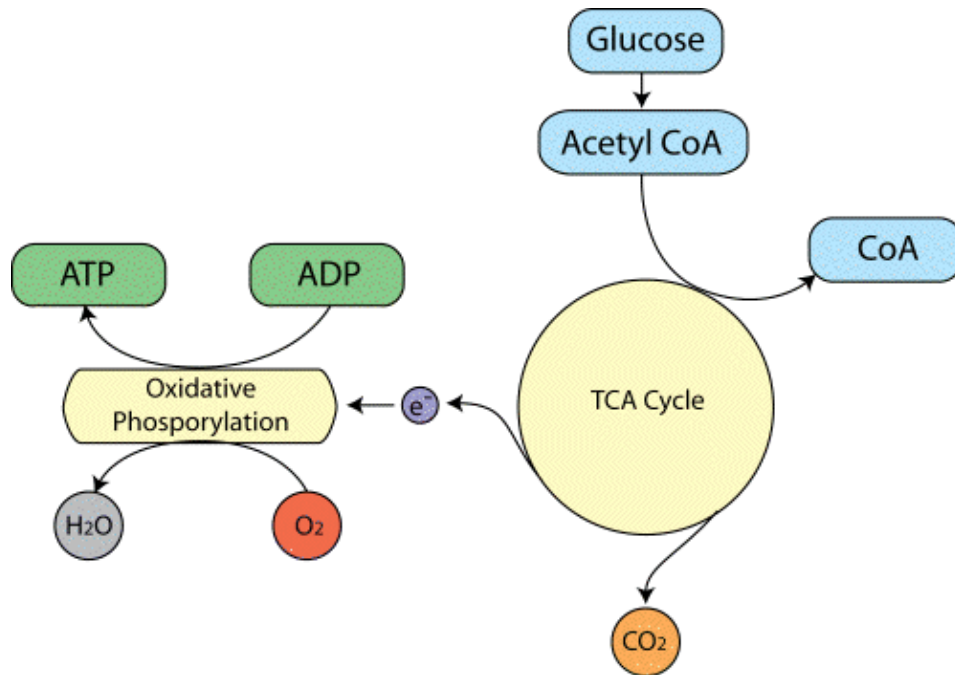


Figure 3.16 Overview of the aerobic metabolism of glucose to ATP following the Krebs cycle

As ATP is hydrolysed to ADP, energy is given up, which can be used to drive biochemical reactions that require free energy. The production of ATP from ADP by oxidative phosphorylation is governed by demand, so that the energy reserves are kept constant. That is to say, the rate of this reaction depends mainly on the level of ADP present. This means that the rate of oxygen consumption by oxidative phosphorylation is a good measure of the rate of use of energy in that area.

The oxygen required by metabolism is supplied in the blood. Since oxygen is not very soluble in water, the blood contains a protein that oxygen can bind to, called haemoglobin. The important part of the haemoglobin molecule is an iron atom, bound in an organic structure, and it is this iron atom which gives blood its colour. When an oxygen molecule binds to haemoglobin, it is said to be oxyhaemoglobin, and when no oxygen is bound it is called deoxyhaemoglobin.

To keep up with the high energy demand of the brain, oxygen delivery and blood flow to this organ is quite large. Although the brain's weight is only 2% of the body's, its oxygen consumption rate is 20% of the body's, and blood flow 15%. The blood flow to the grey matter, which is a synapse rich area, is about 10 times that to the white matter per unit volume. Regulation of the regional blood flow is poorly understood, but it is known that localised neural activity results in a rapid selective increase in blood flow to that area.

3.3.2 Blood Oxygen Level Dependent Contrast in MR images

Since regional blood flow is closely related to neural activity, measurement of the rCBF is useful in studying brain function. It is possible to measure blood perfusion with MRI, using techniques similar to those mentioned in section 2.4.4. However there is another, more sensitive, contrast mechanism which depends on the blood oxygenation level, known as blood oxygen level dependent (BOLD)

contrast. The mechanisms behind the BOLD contrast are still to be determined, however there are hypotheses to explain the observed signal changes.

Deoxyhaemoglobin is a paramagnetic molecule whereas oxyhaemoglobin is diamagnetic. The presence of deoxyhaemoglobin in a blood vessel causes a susceptibility difference between the vessel and its surrounding tissue. Such susceptibility differences cause dephasing of the MR proton signal [18], leading to a reduction in the value of $T2^*$. In a $T2^*$ weighted imaging experiment, the presence of deoxyhaemoglobin in the blood vessels causes a darkening of the image in those voxels containing vessels [19,20]. Since oxyhaemoglobin is diamagnetic and does not produce the same dephasing, changes in oxygenation of the blood can be observed as the signal changes in $T2^*$ weighted images [21,22,23].

It would be expected that upon neural activity, since oxygen consumption is increased, that the level of deoxyhaemoglobin in the blood would also increase, and the MR signal would decrease. However what is observed is an increase in signal, implying a decrease in deoxyhaemoglobin. This is because upon neural activity, as well as the slight increase in oxygen extraction from the blood, there is a much larger increase in cerebral blood flow, bringing with it more oxyhaemoglobin (Figure 3.17). Thus the bulk effect upon neural activity is a regional decrease in paramagnetic deoxyhaemoglobin, and an increase in signal.

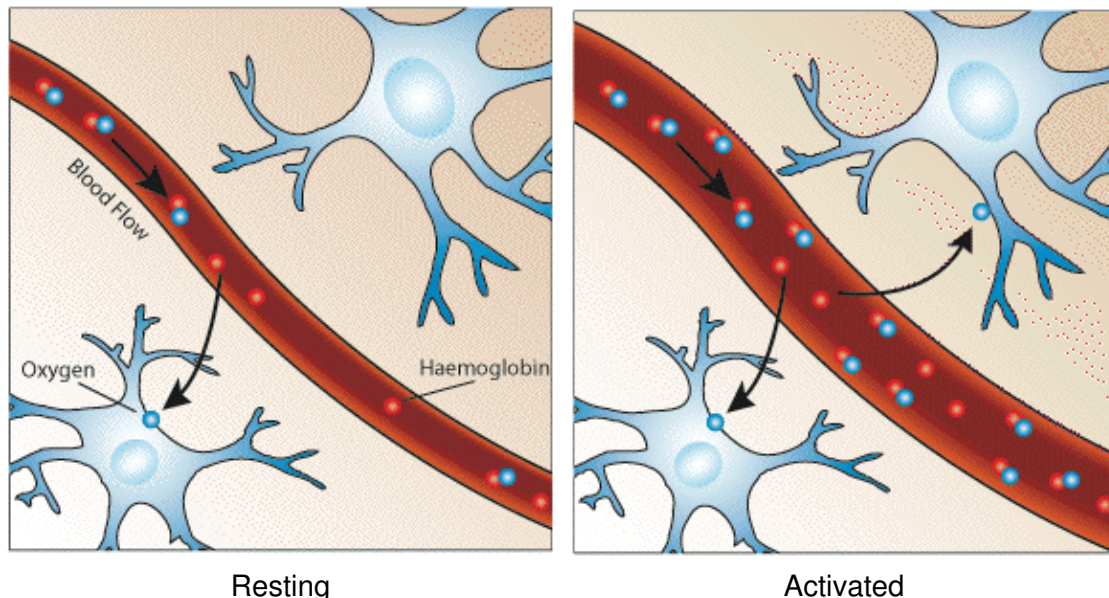


Figure 3.17 Upon activation, oxygen is extracted by the cells, thereby increasing the level of deoxyhaemoglobin in the blood. This is compensated for by an increase in blood flow in the vicinity of the active cells, leading to a net increase in oxyhaemoglobin

The study of these mechanisms are helped by results from PET and near-infrared spectroscopy (NIRS) studies. PET has shown that changes in cerebral blood flow and cerebral blood volume upon activation, are not accompanied by any significant increase in tissue oxygen consumption [24]. NIRS can measure the changes in concentrations of oxy- and deoxyhaemoglobin, by looking at the absorbency at different frequencies. Such studies have shown an increase in oxyhaemoglobin, and a decrease deoxyhaemoglobin upon activation. An increase in the total amount of haemoglobin is also observed, reflecting the increase in blood volume upon activation [25].

The time course for the BOLD signal changes is delayed from the onset of the neural activity by a few seconds, and is smooth, representing the changes in blood flow that the technique detects. This is termed the 'haemodynamic response' to the stimulus. There have also been observations of an initial small 'dip' in signal before and after the larger increase in signal [26,27], possibly reflecting a

transient imbalance between the metabolic activity and blood flow.

3.3.3 Functional Mapping using the BOLD Effect

The discovery of the BOLD effect led to many groups trying to map brain activation using the technique. The first MR human brain activation study used an introduced contrast agent to map the visual cortex[28]. Soon after that the BOLD effect was used to map visual and motor function [29,30]. References to the many early fMRI experiments can be found in the review articles on the subject [31,32].

To study brain function using fMRI it is necessary to repeatedly image the brain, whilst the subject is presented with a stimulus or required to carry out some task. The success of the experiment is dependent on three aspects; the scanning sequence used, the design of the stimulus paradigm, and the way the data is analysed.

The magnitude of the static field used is critical to the percentage signal change obtained on activation. This is because susceptibility differences have a greater signal dephasing effect at higher fields. The earliest fMRI studies were carried out at 1.5 Tesla, but now the forefront research facilities use 3 to 4 Tesla scanners. As field strength increases the magnitude of the BOLD contrast increases more rapidly than system noise, so it would appear that higher field strengths are desirable [33], however the image quality will be reduced at higher field.

The most important aspect of the imaging sequence is that it must produce T_2^* weighted images. This means that a gradient echo is most commonly used, however spin echo sequences still show BOLD contrast because of diffusion effects. Most research is carried out using EPI since its fast acquisition rate allows the activation response to short stimuli to be detected. EPI also has the benefit of reduced artefact from subject motion.

The amount of T_2^* weighting in the image is dependent on the echo time TE. If TE is too short, there will be little difference in the T_2^* curves for the activated state and the resting state, however if TE is too long then there will be no signal from either state. To obtain the maximum signal change for a region with a particular value of T_2^* , the optimal value of echo time can be shown to be equal to the T_2^* value of that tissue (Figure 3.18).

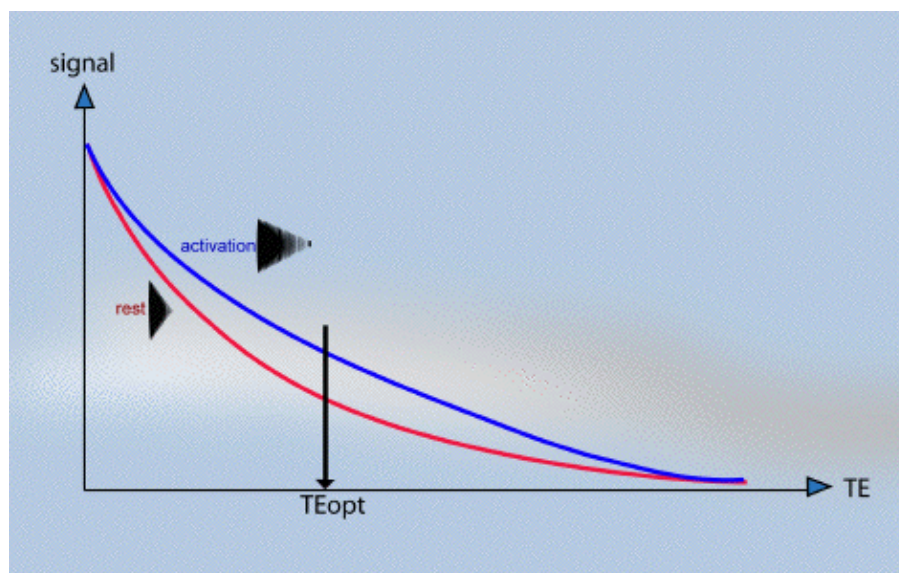


Figure 3.18 Finding the optimal value of TE for the maximum percentage signal change with the BOLD effect

The contrast to noise ratio of the BOLD signal also depends on voxel size and slice thickness. Smaller voxels have less proton signal due to the reduced number of spins, however larger voxels may reduce the contrast to noise ratio by partial volume effects. This occurs if the signal changes on activation come from only a small region within the voxel, and so makes less of an impact on the total signal change in that voxel.

During the scanning there are a number of physiological effects that can affect results. These include cardiac pulsation, respiration and general subject movement. All these problems can be dealt with in two ways, either at the time of scanning or in image post processing. Cardiac or respiratory gating, that is triggering the scanner at one part of the cardiac cycle can be used, although this introduces artefact due to changes in the spin saturation. Postprocessing strategies have been proposed and are probably the best way to deal with this problem [34]. Subject movement can also reduce contrast to noise in fMRI images, and introduce artefact in the activation maps if the movement is stimulus correlated. This problem is often solved both by restraining the head of the subject and by using a postprocessing registration algorithm.

Another source of artefact in fMRI is the signal coming from draining veins. Since gradient echo images are sensitive to vessels of diameters from micrometers to millimetres, it can be difficult to distinguish between signals from the tissue and that from the veins, which could be some distance away from the activation site [35]. There is also the problem that blood flowing into the imaging slice may be stimulus correlated. One way to reduce the signal from large vessels would be to use a spin echo sequence. This is sensitive to T2 effects only and eliminates the dephasing effects from the large vessels [36,37]. Using a spin echo sequence will result in some reduction in genuine tissue BOLD signal, so often it is better to acquire a separate set of images which are sensitive to large vessels, and use this to decide whether to reject the signal.

The choice of the optimum parameters for fMRI is always a compromise, and often depends more on what is available than what is desirable. More is said on the optimisation of MRI for brain imaging in Chapter 4.

3.3.4 Paradigm Design

As important as choosing the imaging parameters for a good experiment is designing the stimulus paradigm. A lot of experience has come from EEG and PET, but since fMRI has a temporal resolution somewhere between these two techniques new approaches can be taken. There are many issues in paradigm design, so only an overview will be given here, with more specific examples of the adaptation of paradigms given in Chapter 7.

The earliest fMRI experiments were much in the form of PET studies, that is to say a set of resting images were acquired and then a set of activation images, and one set subtracted from the other. However since the BOLD contrast is relatively rapid in its onset and decay (of the order of a few seconds) it is possible to follow time courses for much shorter events occurring more frequently.

The most common stimulus presentation pattern is that of regular epochs of stimulus and rest, usually labelled 'on' and 'off'. The duration of these epochs needs to be long enough to accommodate the haemodynamic response, and so a value of at least 8 seconds, or more commonly 16 seconds is chosen. These epochs are repeated for as long as is necessary to gain enough contrast to noise to detect the activation response. The total experimental duration however must be a balance between how long the subject can comfortably lie still without moving, and the number of data points required to obtain enough contrast to noise. There are often some technical limitations to the experimental duration, and there is the possibility of the subject habituating to the

stimulus causing the BOLD contrast to reduce with time.

Instead of epochs of stimuli, it is possible to use single events as a stimulus, much in the same way that EEG or MEG does. Again due to the haemodynamic response, these must be separated by a much longer period of time than would be required for EEG, but since this type of stimulus presentation has the major advantage of being able to separate out the relative timings of activations in different areas of the brain. One of the major disadvantages of single event paradigms is that the experiments need to be much longer than their epoch based counterparts, in order to gain the necessary contrast to noise. More is said on the design of single event paradigms in Chapter 7.

The choice of stimulus is very critical. For example, to activate the primary visual cortex is straightforward, but to determine the regions responsible for colour discrimination is more difficult. Ideally it is necessary to design the 'on' and 'off' epoch such that there is only one well defined difference between them, which will only activate those brain regions responsible for the single task. This is not always possible and so a hierarchy of experiments often need to be performed. For example to identify the regions responsible for task A, an experiment can be performed which involves task A and task B, and then one which only involves task B. The regions responsible for task A would presumably be those activated in the first experiment but not the second. This assumes that the system is a linear one, which may not be the case, or there could be some unaccounted for differences in the two paradigms, which could affect the result.

Another problem particularly when dealing with cognitive events such as memory, is that some stimulus must be presented, usually visually, and a subject response given, usually involving motor action. These must either be compensated for by being included in the 'off' period as well, or another experiment must be performed later which involves similar stimulus and response, but not the cognitive task performed in the original experiment. Alternatively the stimulus may be presented in a different way, aurally for example, and response given orally, and those regions common to both stimulus presentation types can be assumed to be responsible for the cognitive task of interest.

There are a few stimuli which are hard to present in an fMRI experiment. One obvious one is an auditory stimulus. The rapid imaging scanners are very noisy in their operation, especially if EPI is used. Although aural cues can usually be heard, they are not as easily detected as visually presented cues, and detecting activations in the primary auditory cortex is very difficult since there is always a large amount of ambient sound throughout both 'on' and 'off' periods. Requiring the subject to respond orally is also problematic since this almost always results in head movement, which would be concurrent with the stimulus. All response movements required need to be small to reduce head motion during the scanning.

The subject needs to have good instructions, and be reminded to lie still, and to concentrate. Many stimuli give better activation if a response is required to be made. There is much more that could be said on good paradigm design, and much is still being learnt, however care must always be taken and much thought be given for any new experiment.

3.3.5 Analysis of fMRI Data

The statistical analysis of fMRI data is the subject of the sixth chapter of this thesis, and covered in much more detail there. However to complete this section on functional MRI a few of the common analysis strategies are given here.

The analysis of fMRI data falls into two parts. Firstly the raw data must be analysed to produce an image showing the regions of activation and secondly, some level of significance must be calculated

so that the probability of any of producing such a result purely by chance is suitably low [38].

The most straightforward way to analyse the data is to subtract the mean 'off' image from the mean 'on' image. This has the disadvantage that any small movement of the head can drastically change the pixel intensity at the boundaries of the image. This can give rise to a ring of apparent activation near the brain boundaries. To reduce this effect, and to give a statistic of known distribution, a student's t-test can be used. This biases the result against pixels in either 'on' or 'off' set with very large variability, and so can reduce movement artefact. An image where each pixel is assigned a value based on the output of a statistical test is commonly called a statistical parametric map.

Another commonly used technique is that of correlation coefficient mapping. Here the time response of the activation to the stimulus is predicted, usually with some knowledge of the haemodynamic response, and the correlation coefficient between each pixel time course and this reference function is calculated.

Other methods that have been used include Fourier transformation, which identifies pixels with a high Fourier component at the frequency of stimulus presentation, principal component analysis, which locates regions in the brain which show synchronous activity using eigenfunctions, clustering techniques, which again look for synchrony using iterative methods, and various non-parametric tests which do not require the assumption of normality in the signal distribution. All these have their various strengths and weaknesses, and no doubt new methods or variants will be developed in due course. The main criteria for any technique however is simplicity, speed, statistical validity, and sensitivity.

Having obtained a statistical map it is necessary to display the regions of activation, together with some estimate as to the reliability of the result. If the distribution of the statistic, under the null hypothesis of no activation present, is known, then statistical tables can be used to threshold the image, showing only those pixels which show strong stimulus correlation. When displaying the results as an image usually of several thousand pixels, it is necessary to account for multiple comparisons, since the probability of any one pixel in the image being falsely labelled as active is much greater than the probability of a lone pixel being falsely labelled. There are several ways to account for this, for example the Bonferroni correction or the theory of Gaussian random fields, and this topic is explored in more detail in Chapter 6.

3.4 References

- [1] Gall, F. J. and Spurzheim, J. C. (1810) 'Anatomie und Physiologie des Nervensystems im Allgemeinen und des Gehirns insbesondere', F. Schoell, Paris.
- [2] Jackson, J. H. (1931) 'Selected Writings of John Hughlings Jackson', Hodder and Stoughton, London.
- [3] Broca, P. (1861) Sur le siège de la faculté du langage articulé. *Bull. Soc. anat. de Paris*, 2 Serie, **6**,355.
- [4] Penfield, W. and Rasmussen, T. (1952) 'The Cerebral Cortex of Man'. Macmillan, New York.
- [5] Sperry, R. W. (1968) Hemisphere Deconnection and Unity in Conscious Awareness. *American Psychologist* **23**,723-733.
- [6] Kety, S. S. and Schmidt, C. F. (1948) The Nitrous Oxide Method for the Quantitative Determination of Cerebral Blood Flow in Man: Theory, Procedure and Normal Values. *J. Clin.*

Invest. **27**,476-483.

[7] Glass, H. I. and Harper, A. M. (1963) Measurement of Regional Blood Flow in Cerebral Cortex of Man through Intact Skull. *Br. Med. J.* **1**,593.

[8] Ingvar, D. H. and Lassen, N. A. (1961) Quantitative Determination of Regional Cerebral Blood-Flow. *Lancet* **2**,806-807.

[9] Kuhl, D. E. and Edwards R. Q. (1963) Image Separation Radioisotope Scanning. *Radiology* **80**,653-661.

[10] Fox, P. T., Mintun, M. A., Raichle, M. E. and Herscovitch, P. (1984) A Noninvasive Approach to Quantitative Functional Brain Mapping with H₂¹⁵O and Positron Emission Tomography. *J. Cereb. Blood Flow Metab.* **4**,329-333.

[11] Berger, H. (1929) Über das elektrenkephalogramm des menschen. *Arch. Psychiatr Nervenkr* **87**, 527-570.

[12] Cohen, D. (1972) Magnetoencephalography: Detection of the Brain's Electrical Activity with a Superconducting Magnetometer. *Science* **175**,664-666.

[13] Bachelard, H. S. (1981) 'Brain Biochemistry'. Chapman & Hall.

[14] Kandel, E. R., Schwartz, J. H. and Jessel, T. M. (1991) 'Principles of Neural Science' Appleton & Lange.

[15] Martin, J. H. (1996) 'Neuroanatomy', Appleton & Lange.

[16] Penfield, W. G. and Rasmussen T. (1952) 'The Cerebral Cortex of Man', Macmillan, New York.

[17] Pauling, L. and Coryell, C. D. (1936) The Magnetic Properties and Structure of Hemoglobin, Oxyhemoglobin and Carbonmonoxyhemoglobin *Proc. Natl. Acad. Sci. USA* **22**,210-216.

[18] Thulborn, K. R., Waterton, J. C., Matthews, P. M. and Radda, G. K. (1982) Oxygen Dependence of the Transverse Relaxation Time of Water Protons in Whole Blood at High Field. *Biochim. Biophys. Acta.* **714**, 265-270.

[19] Ogawa, S., Lee, T. M., Nayak, A. S. and Glynn, P. (1990) Oxygenation-Sensitive Contrast in Magnetic Resonance Image of Rodent Brain at High Magnetic Fields. *Magn. Reson. Med.* **14**, 68-78.

[20] Ogawa, S. and Lee, T. M. (1990) Magnetic Resonance Imaging of Blood Vessels at High Fields: *In Vivo* and *in Vitro* Measurements and Image Simulation. *Magn. Reson. Med.* **16**, 9-18.

[21] Ogawa, S., Lee, T. M., Kay, A. R. and Tank, D. W. (1990) Brain Magnetic Resonance Imaging with Contrast dependent on Blood Oxygenation. *Proc. Natl. Acad. Sci. USA* **87**, 9868-9872.

[22] Turner, R., Le Bihan, D., Moonen, C. T. W., Despres, D. and Frank, J. (1991) Echo-Planar Time Course MRI of Cat Brain Oxygenation Changes. *Magn. Reson. Med.* **22**, 159-166.

[23] Jezzard, P., Heinemann, F., Taylor, J., DesPres, D., Wen, H., Balaban, R.S., and Turner, R. (1994) Comparison of EPI Gradient-Echo Contrast Changes in Cat Brain Caused by Respiratory

Challenges with Direct Simultaneous Evaluation of Cerebral Oxygenation via a Cranial Window. *NMR in Biomed.* **7**,35-44.

[24] Fox, P. T., Raichle, M. E., Mintun, M. A. and Dence, C. (1988) Nonoxidative Glucose Consumption During Physiologic Neural Activity. *Science* **241**, 462-464.

[25] Villringer, A., Planck, J., Hock, C., Schleinkofer, L. and Dirnagl, U. (1993) Near Infrared Spectroscopy (NIRS): A New Tool to Study Hemodynamic Changes During Activation of Brain Function in Human Adults. *Neurosci. Lett.* **154**, 101-104.

[26] Ogawa, S., Tank, D. W., Menon, R., Ellermann, J. M., Kim S. G., Merkle, H. and Ugurbil, K. (1992) Intrinsic Signal Changes Accompanying Sensory Stimulation: Functional Brain Mapping with Magnetic Resonance Imaging. *Proc. Natl. Acad. Sci. USA* **89**, 5951-5955.

[27] Ernst, T. and Hennig, J. (1994) Observation of a Fast Response in Functional MR. *Magn. Reson. Med.* **32**,146-149.

[28] Belliveau, J. W., Kennedy, D. N., McKinstry, R. C., Buchbinder, B. R., Weisskoff, R. M., Cohen, M. S., Vevea, J. M., Brady, T. J. and Rosen, B. R. (1991) Functional Mapping of the Human Visual Cortex by Magnetic Resonance Imaging. *Science* **254**, 716-719.

[29] Kwong, K. K., Belliveau, J. W., Chesler, D. A., Goldberg, I. E., Weisskoff, R. M., Poncelet, B. P., Kennedy, D. N., Hoppel, B. E., Cohen, M. S., Turner, R., Cheng, H. M., Brady, T. J. and Rosen, B. R. (1992) Dynamic Magnetic Resonance Imaging of Human Brain Activity During Primary Sensory Stimulation. *Proc. Natl. Acad. Sci. USA* **89**, 5675-5679.

[30] Bandettini, P. A., Wong, E. C., Hinks, R. S., Tikofsky, R. S. and Hyde, J. S. (1992) Time Course EPI of Human Brain Function During Task Activation. *Magn. Reson. Med.* **25**,390-397.

[31] Kwong, K.K. (1995) Functional Magnetic Resonance Imaging with Echo Planar Imaging. *Magnetic Resonance Quarterly* **11**,1-20.

[32] Cohen, M.S. and Bookheimer, S. Y. (1994) Localization of Brain Function using Magnetic Resonance Imaging. *Trends in Neuroscience* **17**,268-277.

[33] Turner, R., Jezzard, P., Wen, H., Kwong, K. K., Le Bihan, D., Zeffiro, T. and Balaban, R. S. (1993) Functional Mapping of the Human Visual Cortex at 4 and 1.5 Tesla Using Deoxygenation Contrast EPI. *Magn. Reson. Med.* **29**,277-279.

[34] Le, T. H and Hu, X. (1996) Retrospective Estimation and Correction of Physiological Artifacts in fMRI by Direct Extraction of Physiological Activity from MR Data. *Magn. Reson. Med.* **35**,290-298.

[35] Gao, J. H., Miller, I., Lai, S., Xiong, J. and Fox, P. T. (1996) Quantitative Assessment of Blood Inflow Effects in Functional MRI Signals. *Magn. Reson. Med.* **36**,314-319.

[36] Fisel, C. R., Ackerman, J. L., Buxton, R. B., Garrido, L., Belliveau, J. W., Rosen, B. R. and Brady, T. J. (1991) MR Contrast Due to Microscopically Heterogeneous Magnetic Susceptibility: Numerical Simulations and Applications to Cerebral Physiology. *Magn. Reson. Med.* **17**,366-347.

[37] Hykin, J., Bowtell, R., Mansfield, P., Glover, P., Coxon, R., Worthington, B. and Blumhardt, L. (1994) Functional Brain Imaging using EPI at 3T. *Magma* **2**,347-349.

[38] Bandettini, P. A., Jesmanowicz, A., Wong, E. C. and Hyde, J. S. (1993) Processing Strategies for Time-Course Data Sets in Functional MRI of the Human Brain. *Magn. Reson. Med.* **30**,161-173.

Chapter 4

Optimisation of MRI for Functional Imaging

4.1 Introduction

For each region of the brain, or cognitive paradigm that is to be studied with MRI there are specific issues regarding the optimisation of the fMRI experiment. These are covered in the chapter on functional MRI applications. There are however issues that relate more generally to fMRI experiments, such as dealing with artefacts and the optimisation of echo time. These subjects are covered here.

The first section deals with the effect of echo time on the magnitude of the signal detected as a result of the BOLD effect. A single shot technique for obtaining images with different echo times is described, and this is also used to produce T_2^* maps during brain activation. Next, two artefact reducing methods are discussed. The first to reduce the N/2 ghost, and the other to remove artefact from external r.f. interference. A pulse sequence which reduces the time taken to acquire inversion recovery anatomical reference scans is presented, and in the final section the rationale behind a standard experimental protocol for fMRI experiments is explained.

4.2 The Effect of Echo Time on fMRI Signal

4.2.1 Introduction

As was described in Chapter 3, task performance causes a local increase in the value of T_2^* in the region of the brain that is involved in the task, which can be detected in T_2^* weighted images. The amount of T_2^* weighting that is seen in an image depends on the echo time, TE (see section 2.4.2). For a given value of T_2^* , images obtained with a value of TE equal to T_2^* will be optimal at detecting any change in T_2^* (see section 3.3.3). The magnitude of T_2^* depends on a number of factors that are scanner dependent, such as field strength and quality of shimming, and others that are object dependent, such as the orientation of the boundaries between regions with differing magnetic susceptibility.

Given this, it becomes important to find the value of TE which will give the best detection of even the smallest changes in T_2^* in the region of brain that is being studied. This has been done previously by carrying out several experiments, each using different echo times [1]. Changes in the value of T_2^* upon visual activation have also been measured using spectroscopy [2], and multi echo FLASH [3]. More recently, a double echo time approach to T_2^* mapping has been demonstrated [4]. Here, a technique is presented which obtains a set of low resolution images with six different echo times from a single FID. This enables activation images from each different echo time to be obtained for precisely the same task. By fitting T_2^* curves to the data, it has also been possible to obtain maps of T_2^* during activation. This sequence has been used in activation experiments involving visual and auditory stimulation, and motor tasks on five normal volunteers.

4.2.2 Methods

In EPI, a gradient echo is formed in the broadening direction by applying an initial dephasing gradient, and then a series of 'blips' of the opposite polarity which form the echo. The time from the

r.f. excitation pulse to the centre of the echo is defined as the echo time in EPI (see Figure 4.1). This is distinct from the repeated set of echoes formed by the switching of the read gradient.

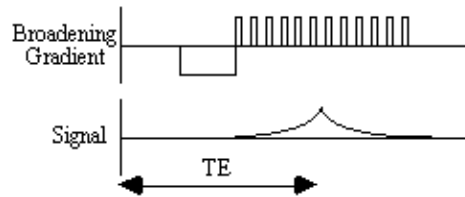


Figure 4.1. Formation of a Gradient Echo in EPI using the Broadening Gradient.

Having formed one gradient echo, it is possible to form other echoes simply by reversing the polarity of the blipped gradient. These echoes all form under the T_2^* decay envelope, and have different echo times (Figure 4.2). This is distinct from the multiple spin echo experiment described in section 2.4.3, in which the echoes form under the T_2 decay envelope.

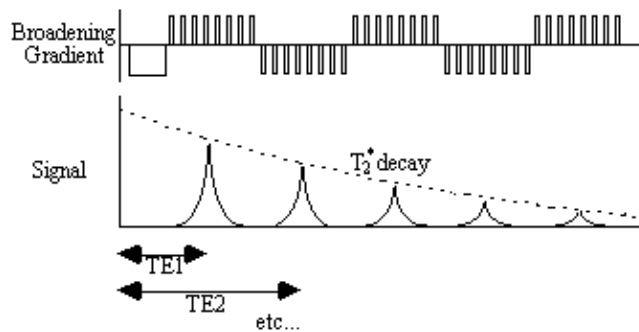


Figure 4.2. Multiple Gradient Echo Sequence for Sampling the FID at a series of different echo times.

The signal can continually be recalled in this way, provided that T_2^* has not already reduced the signal to zero.

The above sequence was implemented on a dedicated EPI 3.0 Tesla scanner, with purpose built head gradient coils, birdcage r.f. coil, and control. In order to sample at 6 echo times between 10 and 55 ms, a matrix size of 32×32 and a switching rate of 1.9 kHz was chosen. This gave echo times of approximately 12, 20, 28, 36, 44 and 52 ms, and a voxel resolution of $5 \times 5 \times 10$ mm³. The ordering of the rows in the 2nd, 4th and 6th echo time image was reversed prior to Fourier transformation to maintain the equivalent orientation of the images.

A T_2^* map was calculated for every FID by fitting the data from each echo time, on a pixel by pixel basis, to an exponential decay curve of the form

$$S(TE) = S_0 \exp(-TE/T_2^*) \tag{4.1}$$

This was done by taking the logarithm of the pixel intensity and calculating the linear regression, intercept and correlation coefficients between these and the echo time. These values were used to form images of T_2^* , S_0 and correlation.

The activation experiments were designed to produce a response in the visual, motor and auditory cortices. For the visual and motor experiment, the subject observed an LED display. During the task

condition, an outer ring of LED's lit, and a central bar flashed at a rate of 2 Hz. The subject was required to respond to the stimulus by pressing a hand held button at the same rate as the flashing LED. The whole brain was imaged, in 16 slices, every 4 seconds. The experiment consisted of 16 seconds of rest followed by 16 seconds of activity, repeated 32 times, and was carried out on 5 normal volunteers.

The auditory experiment consisted of imaging 6 slices through the temporal lobes in 600 ms, each set of slices being acquired every 14 seconds. In alternate gaps, a 14 second recording of speech was played to the subject. Thus for each cycle one volume set of images was obtained directly after a 14 second period of auditory stimulation, and one set was acquired after a 14 second period of silence. The advantage of carrying out the experiment in this way is that the auditory stimulation from the scanner does not interfere with the auditory stimulation of the speech. Each experiment consisted of 20 cycles of speech and silence, and was carried out on 5 normal volunteers.

The analysis of the data was carried out using the techniques and software described in Chapter 6. Following image formation, the echo time data was normalised, spatially filtered with a 3D Gaussian kernel with FWHM of 6 mm, and temporally filtered with a Gaussian kernel of FWHM 3 s. For the visual and motor experiment the time course was correlated to a delayed and smoothed reference waveform (square wave convolved with a Poisson function with $\lambda = 6$ s), on a pixel by pixel basis to produce one statistical parametric map (SPM) for each echo time.

The auditory activation data was analysed using a t-test comparison between the mean of the speech and silence images, again forming one SPM for each echo time. The correlation coefficients and t-scores were transformed to z-scores and thresholded to the same p-value using both peak height and spatial extent of the SPM.

For each echo time, the mean percentage change between activation and rest was calculated, for all the pixels in the active regions. In order to ascertain which echo time yields the optimum results, the product of the mean percentage change and the number of pixels in the activated region was calculated.

Similar statistical analysis was performed on the T_2^* maps.

4.2.3 Results

Examples of the activation images produced, for each echo time and for the T_2^* maps, are shown in Figure 4.3. The colours in the active regions refer to the level of percentage change in each region, and these are overlaid on the mean of the images acquired at that echo time. The levels of significance of the activation (p value) were less for the T_2^* maps than for the T_2^* weighted images, however discrete regions of activation in the same regions can be seen. The general trend is for the percentage change to increase with echo time, however the extent of the activation detected reduces with the longer echo times. This is illustrated in the graphs of the product of percentage change and number of active pixels, shown in Figure 4.4 for each of the subjects. The dotted line on these plots represents the activation from the T_2^* maps. The level of percentage change observed in the T_2^* maps upon activation was usually greater than that observed in the T_2^* weighted images, but the regions were generally smaller. No significant change was detected in the maps of S_0 during the tasks.

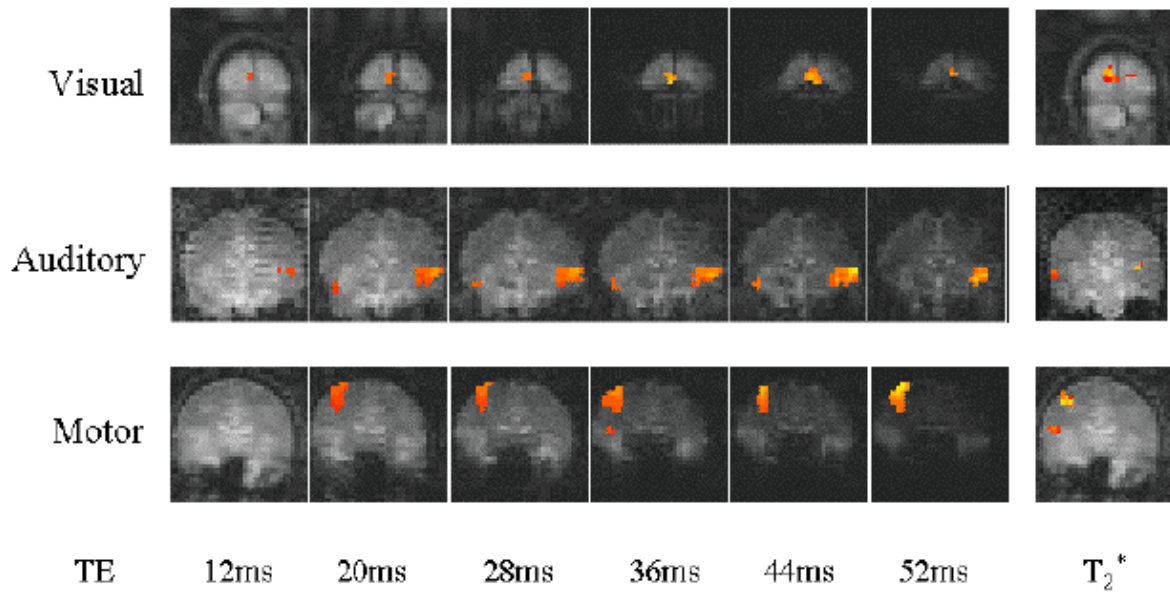
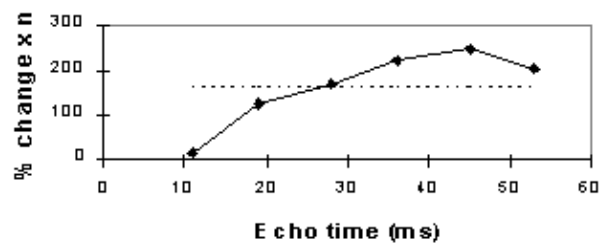
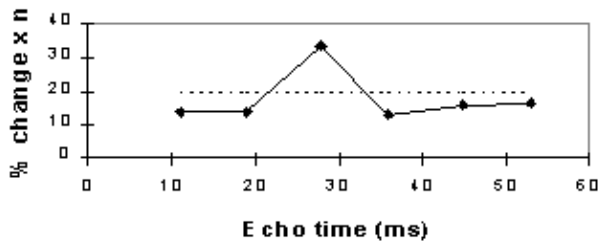
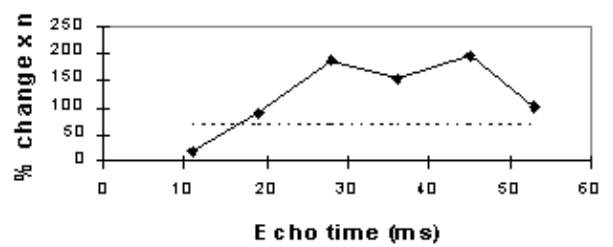
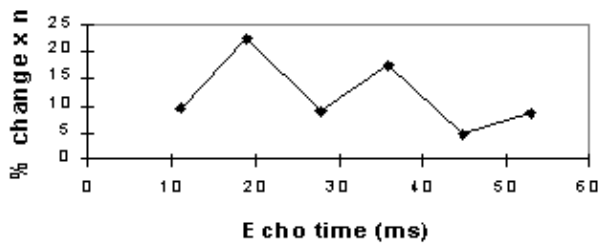
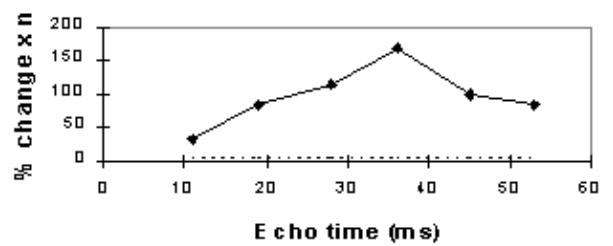
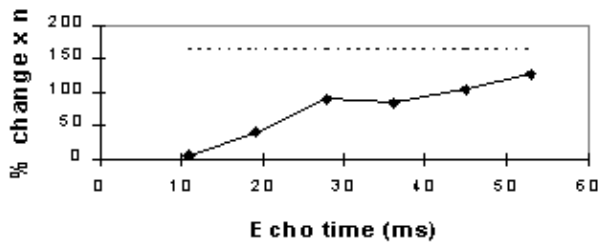
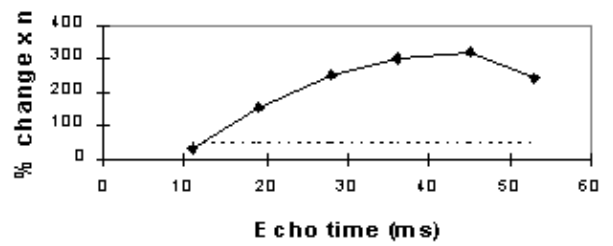
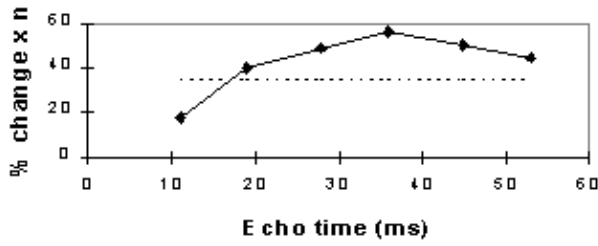
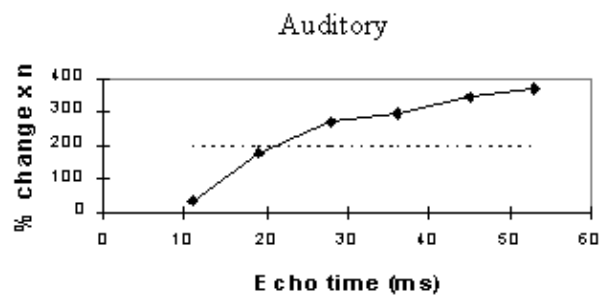
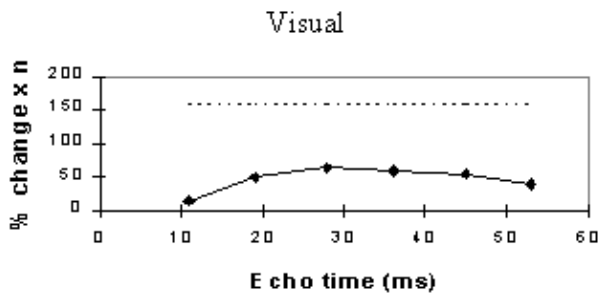


Figure 4.3. Examples of the activation maps for each echo time and the T_2^* images. The colour scale (from red to yellow) represents the percentage signal change observed in that region. The echo time activation maps are overlaid on the actual images acquired at each echo time, and the T_2^* activation maps overlaid on T_2^* weighted images.



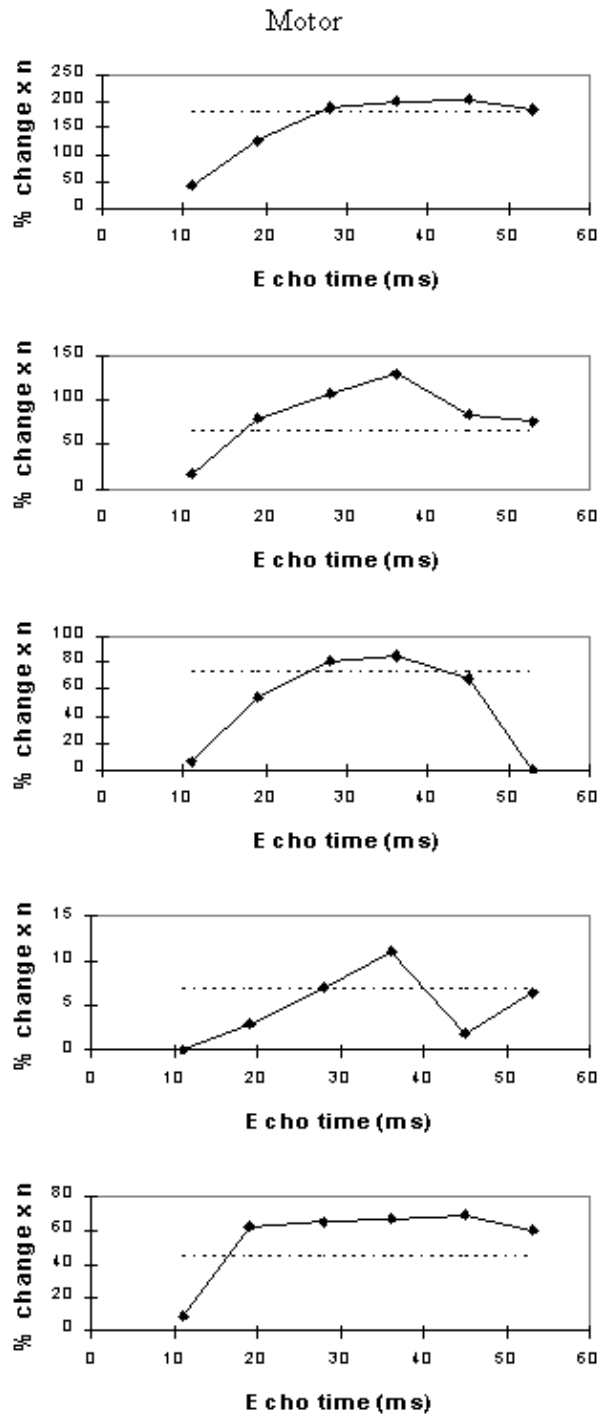


Figure 4.4a. Plots of mean percentage change multiplied by number of active pixels against echo time for five subjects in the visual, auditory and motor cortices. The dashed line represents the activation obtained from the T2* images.

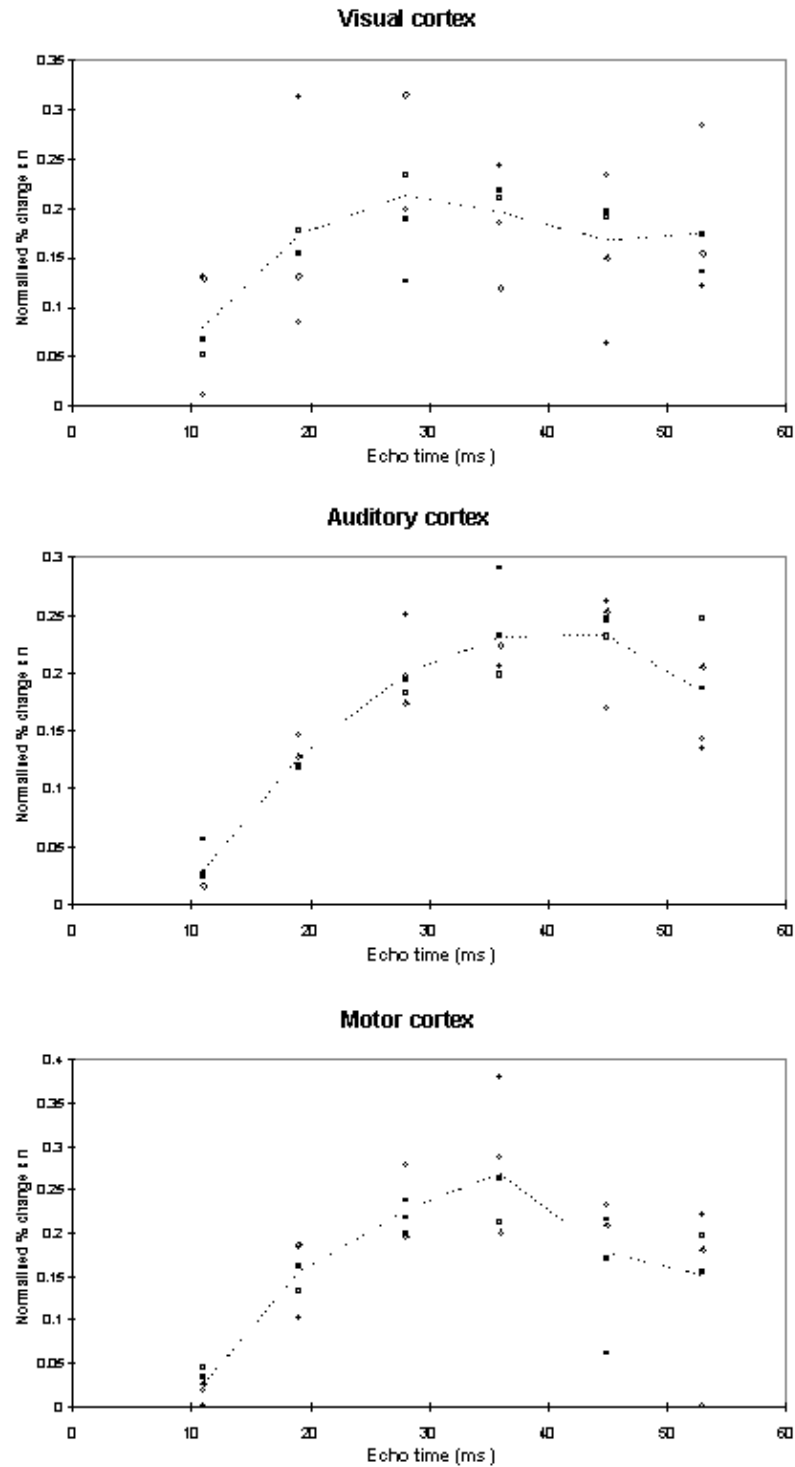


Figure 4.4b. Plots of percentage change multiplied by number of active pixels (normalised to have the same area under the curve for each subject) against echo time.

An appropriate choice of echo time for the motor and auditory cortices, would appear to be between 30 and 40 ms, and between 25 and 35 for the visual cortex. If the echo time is too short, the percentage change is so small that the activation response is lost in the contrast to noise of the time series. However if the echo time is too long, the signal from the cortex has fallen to zero due to T_2^* decay and no change is seen on activation.

4.2.4 Discussion

The multiple gradient echo technique produces, from a single FID, a set of images with different values of echo time. Measuring several echo times in one experiment has the advantage of reducing the total experimental duration, and eliminating the effects that habituation, subject restlessness, or repositioning could have on the results if separate experiments were carried out at each echo time. The results suggest that an echo time of between 25 and 40 ms would be optimum for experiments in the visual, motor and auditory cortices at 3 T. More results would be required in order to be confident of using a similar echo time for studies in other regions of the brain, but this technique offers a quick and simple way to carry out such an experiment.

The relatively thick slices used, will mean that through slice dephasing will reduce the values of T_2^* . The slice thickness of 10 mm used in this experiment is comparable to that used in many whole brain studies, however the choice of optimum echo time may be different for the thinner slices used in some experiments.

The use of T_2^* maps, instead of T_2^* weighted images for fMRI has the additional benefit that the results will not be so affected by in-flow effects, or through slice movement artefact. If higher resolution images were required, the number of echo times recorded could be reduced, so that the number of lines in the image could be increased. For example four 64×64 images could be acquired with echo times of 16, 32, 48 and 64 ms, and T_2^* curves fitted to this data, allowing an in plane resolution of up to 3 mm.

4.3 Artefact Reduction in fMRI Data

4.3.1 Reduction of Ghost Artefact

One type of artefact which is specific to EPI is the Nyquist, or N/2 ghost. This arises because odd and even echoes are acquired under opposite read gradients, and the data requires reversal prior to image reconstruction. Inaccurate timing of the sampling relative to the switched gradient, temporal asymmetries in the analogue filter or inhomogeneities in the static field cause a modulation of alternate lines in k-space. This leads to a ghost image shifted by N/2 pixels in the phase encode direction. An example of this effect is shown in Figure 4.5a, where the phase of alternate lines in k-space has been altered by a small amount. If the image and ghost overlap, interference occurs leading to fringes in the image as shown in Figure 4.5b.

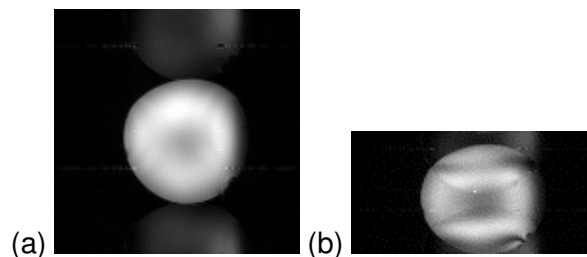


Figure 4.5. Examples of the effect of the N/2 ghost on phantom images, (a) where ghost and image do not overlap and (b) where ghost and image overlap.

In fMRI, ghosting artefact can cause a number of problems. In the first place, the ghosting can spoil the look of the image, and ghosting of activated regions could lead to apparent 'activation' appearing outside the head. More serious effects occur if the artefact changes with time. Movement of the subjects head causes the interference fringes, of overlapping ghost and image, to change dramatically, with even small displacements having a large effect. Since subject motion is often

stimulus correlated, particularly if the experimental paradigm involves movement, the changes of the interference pattern can show up in the statistical analysis as 'activation', as shown in Figure 4.6. It has also been observed on our scanner that the ghosting can change with time as shown in Figure 4.7, from an experiment lasting eight minutes. This probably results from changes in the switched gradient waveform as the coil heats up and its resistance increases.

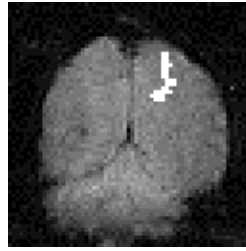


Figure 4.6. If the interference fringes, caused by the ghost and image overlapping, change with the same period as the stimulus, they appear on the activation images as artefact.

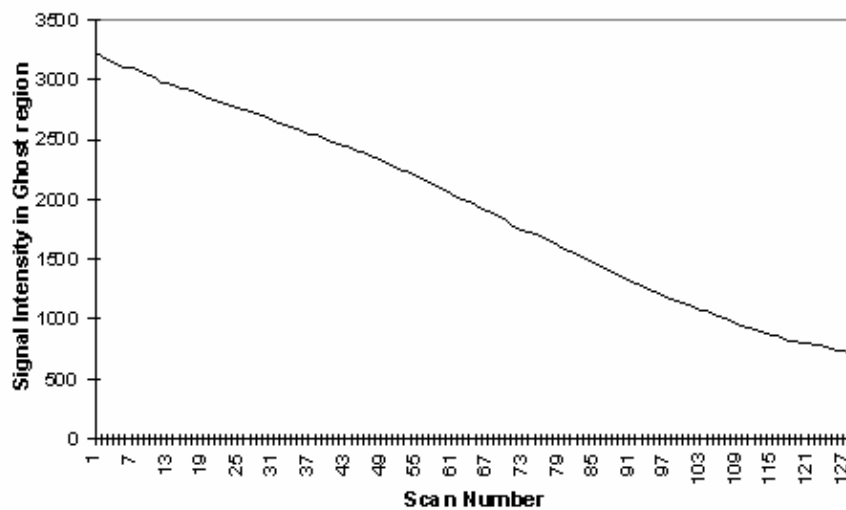


Figure 4.7. Plot of the signal intensity in a region of the ghost against scan number. Taken from images of a phantom scanned continuously for eight minute.

The N/2 ghost can be reduced by making hardware improvements in filter performance and reducing eddy currents. There is however a limit to the technical improvements that can be made, so a number of techniques for correcting such artefact in post-processing have been proposed. These techniques are described in this section and are tested on phantom and head fMRI data sets to compare their usefulness in this application.

The simplest form of ghost reduction is to apply a phase angle correction to each point in alternate lines of the k-space data. The required phase correction can be determined by eye, and applied to every image in the fMRI data set. The effect of eddy currents can be modelled by an alternate echo phase variation in the read (x-) direction

$$d(x) = d_0 + x d_1 \tag{4.2}$$

so by applying a first order correction, ghosting from such effects can be reduced. A mismatch in the sampling can be corrected by a linear shift of the real and imaginary time data.

All these methods go some way towards removing the N/2 ghost, but will not remove ghosts caused by more complicated phase errors. The subject of N/2 ghosting is extensively covered in a paper by Bruder *et. al.* [5] in which a method based on a calibration scan is proposed. Such a scan is acquired with no broadening gradient so, in an ideal case, equivalent points in all the echoes would have the same phase. Bruder's method applies a phase correction to force each echo in the calibration scan to have the same phase, and then applies this same phase correction to the (broadened) image. So if the i th line of the calibration scan has phase $\theta_i(x)$ then the corresponding line in the image is phase corrected by an angle $-\theta_i(x)$. This can be carried out practically on a time-point by time-point basis, without directly calculating the phase angles, using the formula

$$r' = \frac{r \cdot r_c + i \cdot i_c}{\sqrt{r_c^2 + i_c^2}} \quad i' = \frac{i \cdot r_c - r \cdot i_c}{\sqrt{r_c^2 + i_c^2}} \quad (4.3)$$

where r and i represent the real and imaginary components of the data point and the subscript c represents the calibration scan data.

An alternative form of calibration scan has been proposed by Hu [6]. In this case the reference scan consists of an image acquired under reversed switching gradients. That is to say, if the first line of the normal image is acquired under a positive read gradient, then the first line of the reference image is acquired under a negative read gradient. These two images could be spliced together, so that the final image is made up from only lines that were acquired under a positive read gradient, much in the way that EPI was first proposed [7]. However Hu proposed that the even lines of the reference scan be used to correct the odd lines of the actual image, so that a single reference scan can be used to phase correct a whole set of images. Initially all the lines of the normal images and the reference scan are Fourier transformed in the read direction. Next the even lines of the reference image are reversed. The phase correction θ that must be applied to these lines in the corresponding normal image in order for them to have the same phase as the reference image is given by

$$\cos \theta = \frac{r_1 \cdot r_2 + i_1 \cdot i_2}{\sqrt{r_1^2 + i_1^2} \cdot \sqrt{r_2^2 + i_2^2}}$$

$$\sin \theta = \frac{i_1 \cdot r_2 + r_1 \cdot i_2}{\sqrt{r_1^2 + i_1^2} \cdot \sqrt{r_2^2 + i_2^2}} \quad (4.4)$$

where the subscript 1 refers to the normal image and the subscript 2 refers to the reference image. This correction can then be applied to all the images using

$$r' = r \cos \theta + i \sin \theta$$

$$i' = i \cos \theta - r \sin \theta \quad (4.5)$$

again where r is the real component and i is the imaginary component of the complex data point. Finally the images are Fourier transformed along the phase encode direction to form the corrected image.

This technique can be further extended by collecting two reference scans, without the broadening gradient applied, one with a positive read gradient for the first echo and the other with a negative gradient. This has the advantage that there is more signal present in the earlier and later lines of

k-space to enable a better calculation of the phase correction required in these lines.

An alternative method that requires no reference scans has been proposed by Buonocore [8]. If two images are constructed, one from only the odd echoes, with the even echoes zero filled prior to Fourier transformation, and one from only the even echoes, with the odd echoes zero filled, then both images will display ghosting, one with a positive ghost, and one with a negative ghost (see Figure 4.8). If there were no phase errors in the odd and even echoes then the phase difference in the object only region (that is where there is no ghost) between these two images would be zero. However if there are phase errors, then a phase difference between equivalent points in the odd and even image of $2\theta(x,y)$ can be detected. If the ghost and image do not overlap, it is possible to add the two images together, having applied an appropriate phase correction to one, to form a ghost free image. However if they do overlap then the phase differences are calculated as a function of x only (that is along the read direction) and averaged through all the lines in the object only region as defined by the user. Having determined the phase difference, the original time data can be corrected by Fourier transformation in the read direction, multiplying the odd lines by $\exp(i\theta(x))$ and the even lines by $\exp(-i\theta(x))$.

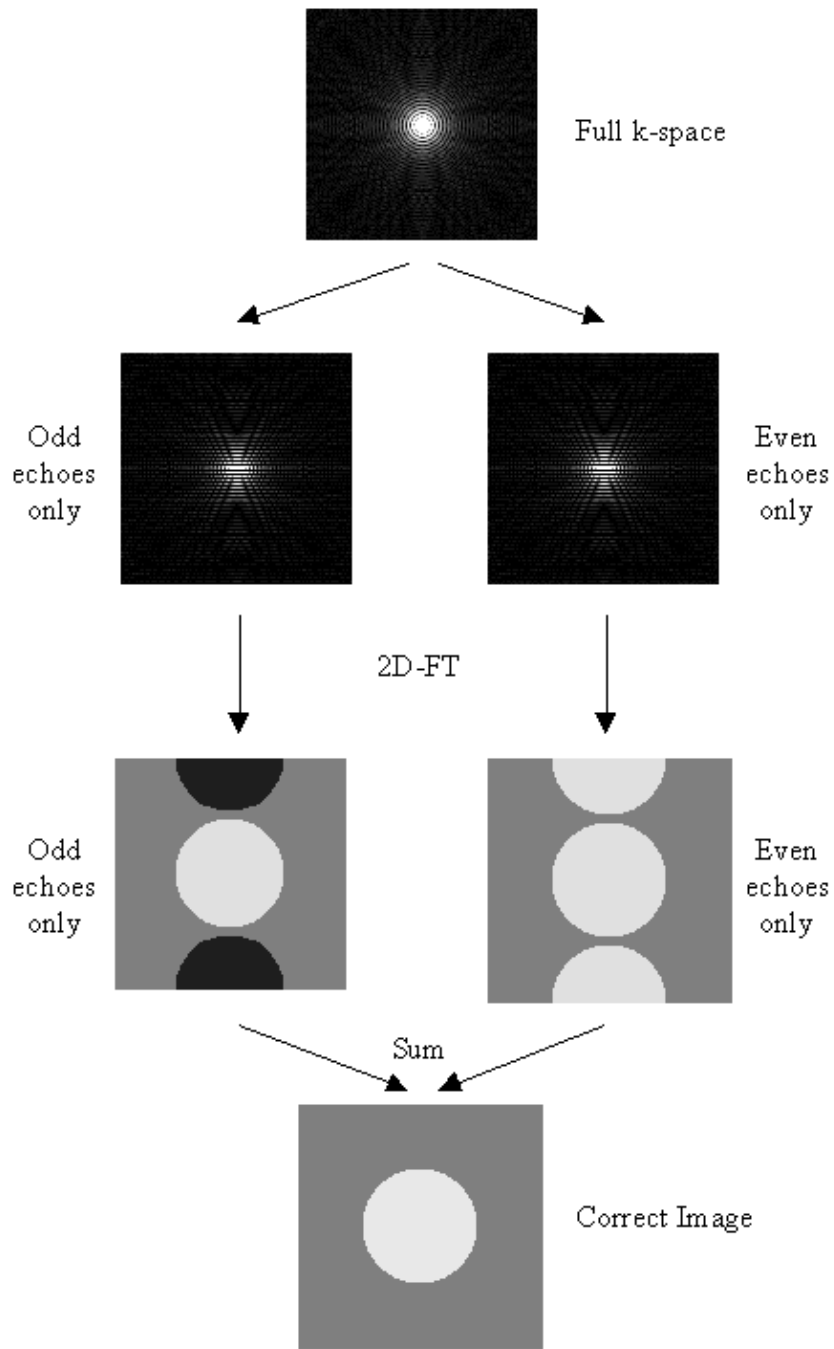


Figure 4.8. For an image with no ghosting, splitting k-space into even echoes only, or odd echoes only, causes ghosting to appear upon Fourier transformation. The image resulting from the even lines has a positive ghost, whilst the image resulting from the odd lines has a negative ghost. Summing these two image together forms a correct image.

The above five methods were tested on both phantom and head data, with objects that fill and half-fill the field of view. Examples of their ability to correct the ghosting are shown in Figure 4.9a-b. Most of the corrections reduce the ghosting partially in the phantom images. Where the ghost and object overlap, the Hu correction with broadening is slightly better at reducing the ring the edge of the ghost.

To quantify the level of ghosting, regions of interest (ROI) were drawn around the object and the ghost region of the images in which the object half-filled the field of view. Six images of the same

phantom, each with different levels of ghosting, were corrected using all five techniques. The mean intensity of the ghost as a percentage of the mean intensity of the object for each technique is shown in Figure 4.9c. The Hu correction without broadening, does not perform as well as might be expected. This is because of the complete failure of the technique in correcting the column in which the external r.f. interference appears, thus producing bright streaks in the ghost region. The Buonocore method appears in both cases to be the best method.

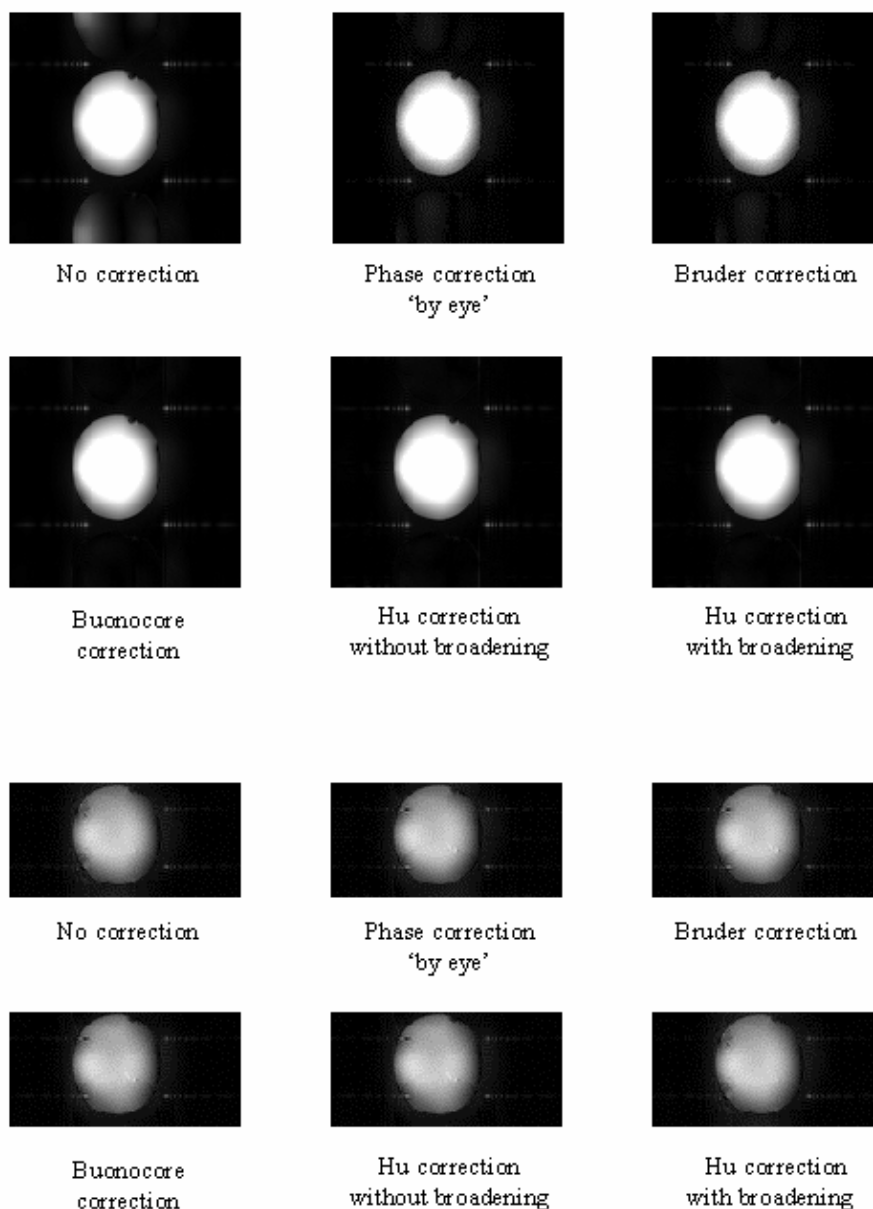


Figure 4.9a. Examples of the five ghost correction techniques described in the text, applied to 128 x 128 and 128 x 64 matrix size phantom images.

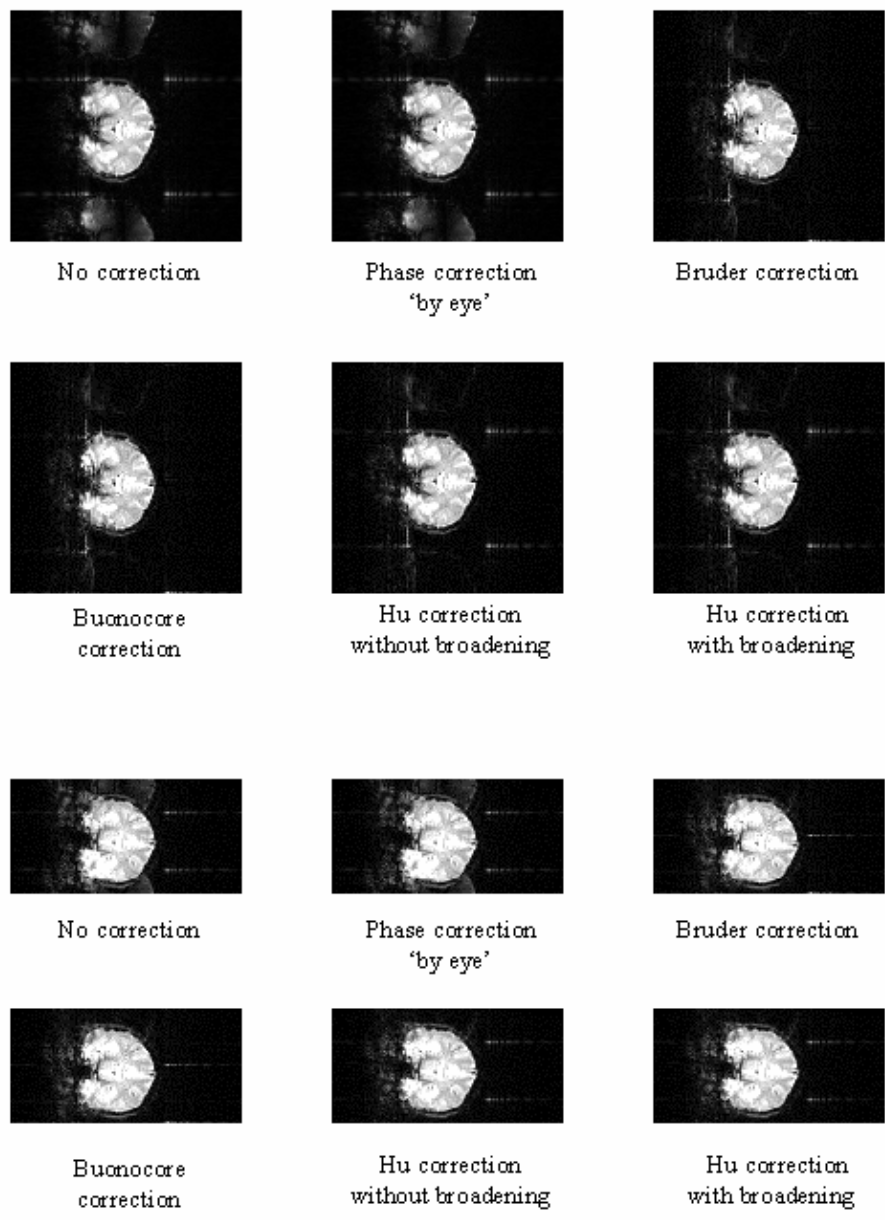


Figure 4.9b. Examples of the five ghost correction techniques described in the text, applied to 128 x 128 and 128 x 64 matrix size coronal head images.

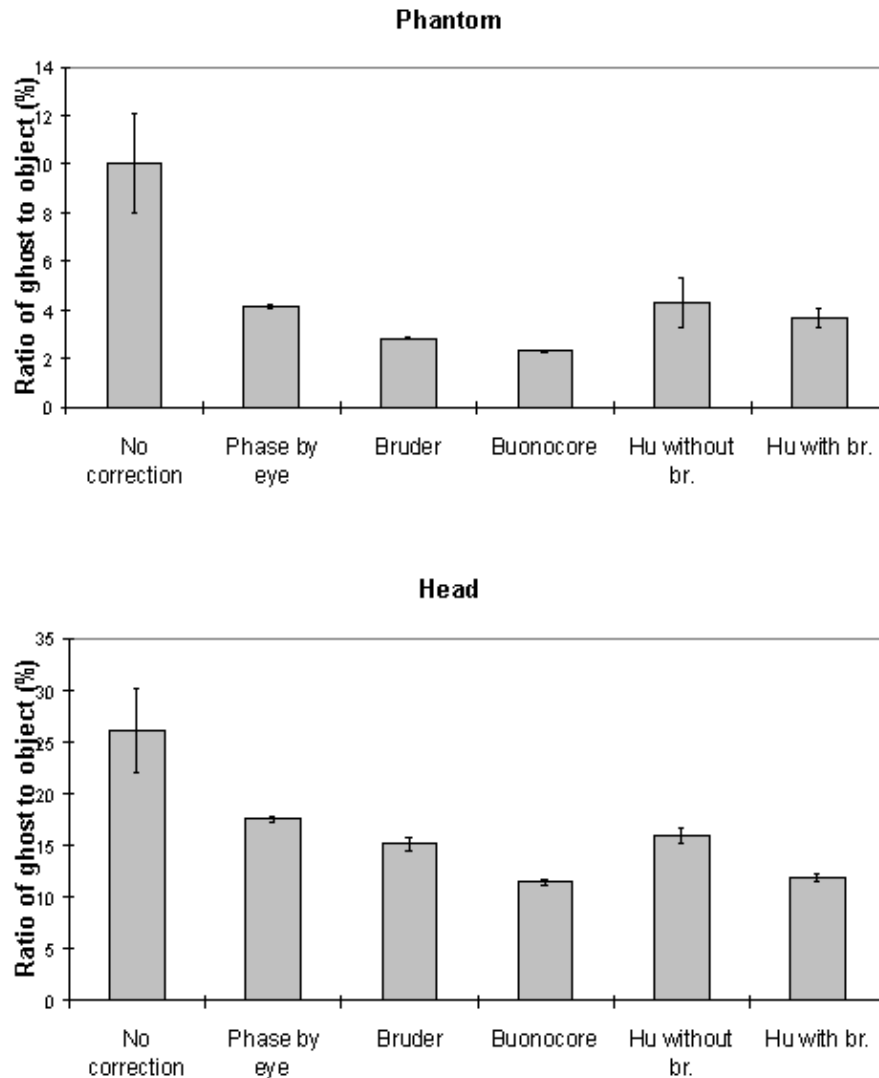


Figure 4.9c. Ratio of image intensity within the ghost to within the object for the five correction methods explained in the text, based on six images (128 x 128 matrix size) each with slightly different ghosting.

All the above techniques, apart from the Buonocore method, will not correct phase errors that change with time. Since changes in the ghost do occur with time, adaptations of the above techniques are needed if they are to deal with such situations. If ghost only and object only regions can be defined, as is the case if the object does not fill the field of view, then a zeroth or first order alternate line phase correction can be applied which minimises the signal in the ghost region relative to the object region. This technique can work very well in some cases, however if there is any overlap of image and ghost, then the minimisation can occasionally produce obviously incorrect results. Alternatively, the ghost can be minimised by eye on the first image in the set, and then the zeroth and first order phase corrections used to minimise the sum of the square difference between subsequent images and the first. This technique again can generate ridiculous solutions, particularly since this correction has to be carried out before motion correction has been applied. If the assumption is made that the phase errors change linearly with time then a calibration scan can be obtained before and after the fMRI experiment, phase correction calculated, and a linear interpolation of the two angles used to correct intermediate images.

These methods were applied to a test fMRI data set of 64 volume images of a phantom and of a head, acquired over a time of 8 minutes. The first order phase correction method used was one

where the signal intensity in the ghost region was minimised by applying the correction shown in equation 4.2. The Bruder correction and the two forms of the Hu correction were applied, such that one correction map was calculated, based on the first image in the set, and the same map applied to all images. Reference scans were also acquired at the end of the experiment in order to produce a correction map for every image, that was a linear interpolation between that for the first and that for the last. The graphs shown in Figure 4.10 show how well each technique corrected the ghost. The striking feature of these plots is that many of the methods, in particular the Hu correction without broadening, made the ghosting worse. This occurs in the columns in the image where the external r.f. interference is at its worse. The effect that this has on the image is shown in Figure 4.11a. Again the Buonocore method works the best in this situation for both head and ghost data. However, this technique does not always work, as is shown in Figure 4.11b. Since this correction is only based on those lines in which the ghost and image do not overlap, the method has failed where the signal intensity in the central rows is low. An appropriate choice of threshold can prevent low signal intensity having an adverse affect on image quality, but this highlights the care that must be used in applying any technique.

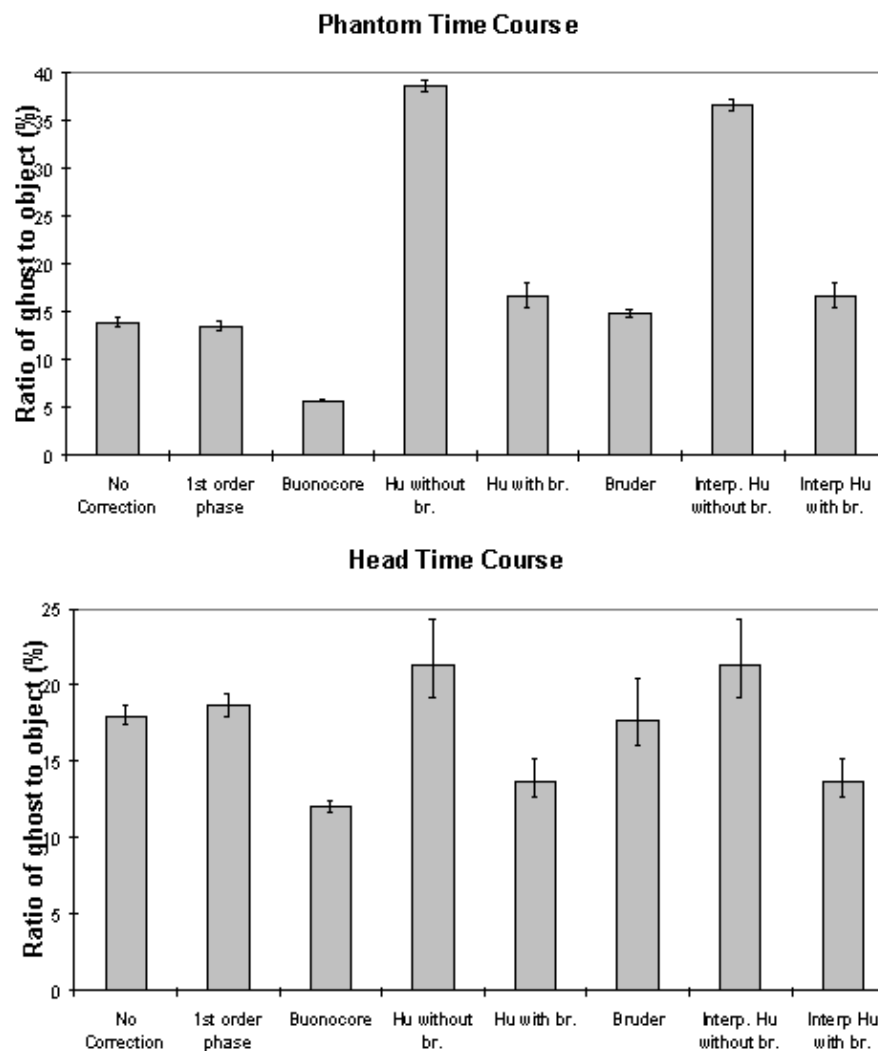


Figure 4.10. Ratio of image intensity within the ghost to within the object for the five correction methods explained in the text, based on six images (128 x 128 matrix size) each with slightly different ghosting.

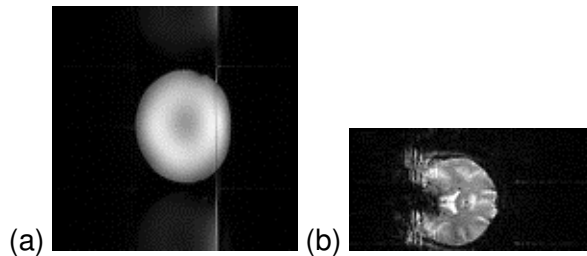


Figure 4.11. Examples of the failure of two correction methods to remove the $N/2$ ghosting. (a) Hu correction without broadening, (b) Buonocore correction.

Reducing the ghost artefact is not always easy. A technique that works well on one set of data fails completely on another, and because of this it is useful to be aware of all the possible corrections that could be applied. Since it does not require a reference scan, the Buonocore method would appear to be the most appropriate first choice, however more results obtained from using the method in practice will be necessary to confirm this.

4.3.2 Removal of External RF Interference

As described in section 2.5.3, external r.f. radiation can cause bright dots of artefact to appear in the image. Provided that this interference is at a single discrete frequency, and the sampling is linear, only one or two pixels in the image will be affected and the image can be cleaned up by replacing these pixels by the average of their neighbours. Non-linear sampling however means that the single frequency interference is spread over a wide range of frequencies after Fourier transformation, and consequently appears as a line in the image. Not only does such interference spoil the appearance of the images, fluctuations in its intensity can cause problems with the analysis of the data. In order to cosmetically remove the interference in such a case, it is easier to re-grid the data, such that it appears that it was linearly sampled, and then to remove the few pixels which now contain the interference. The process is illustrated in Figure 4.12.

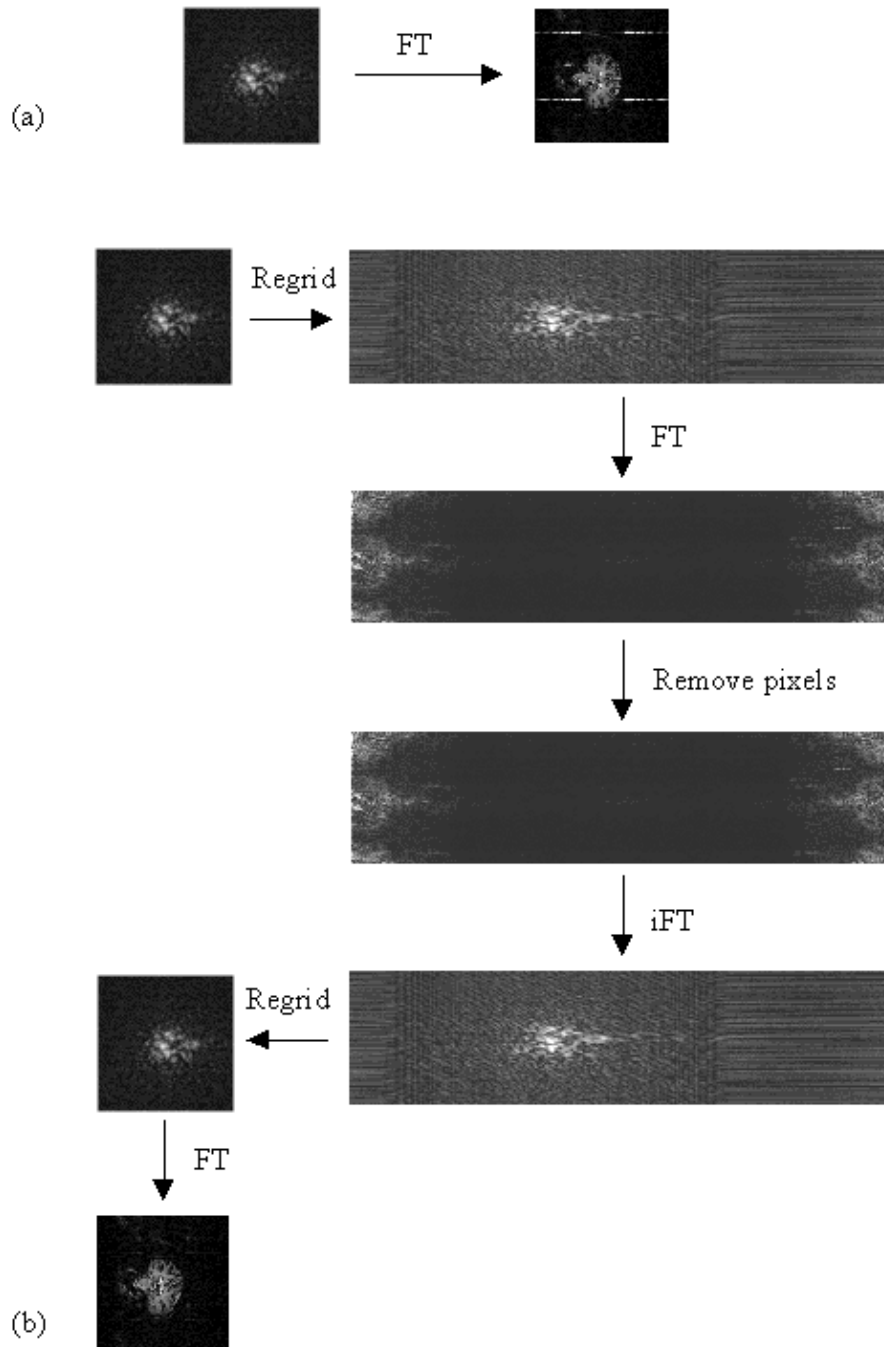


Figure 4.12. Schematic diagram of process for the removal of r.f. interference bands. (a) Normal image reconstruction using a 2D Fourier transform. (b) The time data is re-gridded to a larger matrix size and Fourier transformed. The interference now appears as a few discrete points on the image and can be removed.

The most effective re-gridding of the time data occurs if each line in the image is expanded to fill a much larger grid, and then the gaps filled in by linear interpolation. The positions in the new grid of length n , of the existing N data points are found by summing under the sinusoidal gradient waveform, and finding the set of points $X_1 \dots X_k \dots X_N$, such that

$$\int_{X_i \pi/n}^{X_{i+1} \pi/n} \sin(x) dx = \frac{1}{N} \int_0^\pi \sin(x) dx$$

(4.6)

The values of the intermediate points are obtained by linear interpolation, so that the intensity at the location X in the new grid is given by

$$T(X) = T(X_k) + (T(X_{k+1}) - T(X_k)) \left(\frac{X - X_k}{X_{k+1} - X_k} \right) \quad (4.7)$$

Re-gridding back from the linear to the sinusoidal grid simply involves extracting the values at the points $X_1 \dots X_k \dots X_N$.

The exact pixels to remove are not easy to determine blindly. It is often the case that they are the brightest pixels, but not always, and because of this software was written so that the user could easily select the pixels that should be removed by looking at the re-gridded image. The application was written in the *perl* scripting language [9], with all the data manipulations and calculations carried out in C programs. The user selects the pixels to remove from the expanded image using the mouse.

Examples of data sets before and after cleaning up are shown in Figure 4.13.

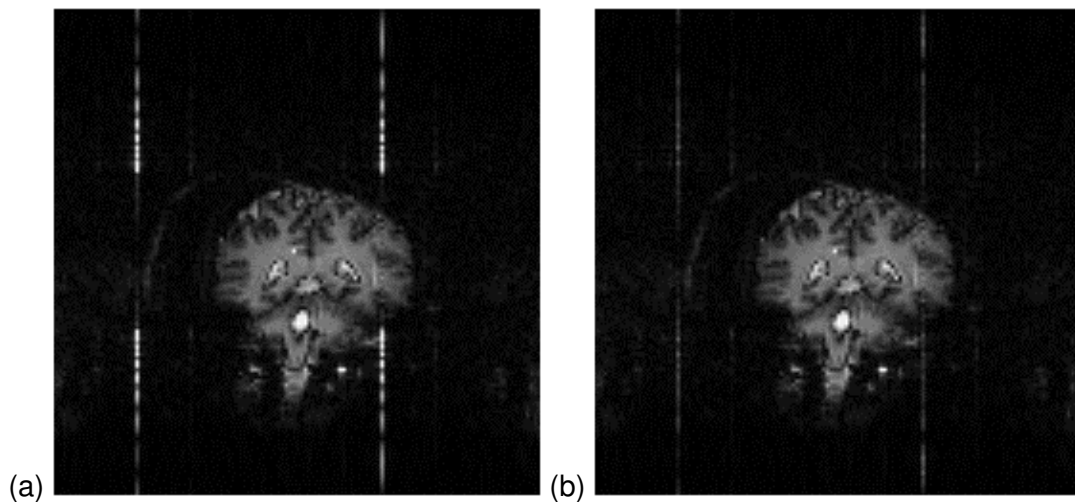


Figure 4.13. Example of the removal of external r.f. interference using the regridding method. (a) Before removal. (b) After removal.

4.4 Fast IR Sequence for Anatomical Reference Scans

The localisation of the activation response from an fMRI experiment depends on obtaining reference scans which highlight the anatomy of the subjects brain. For this purpose an inversion recovery image can be particularly beneficial, since the contrast in the grey and white matter regions of the brain can be altered by the use of a magnetisation inversion r.f. pulse and an appropriate delay before imaging (see section 2.4.1).

The pulse sequence diagram for a standard inversion recovery experiment is shown in Figure 4.14. At 3.0 Tesla the values of the inversion time, TI, required are 400 ms and 1200 ms for white matter null, and grey matter null respectively.

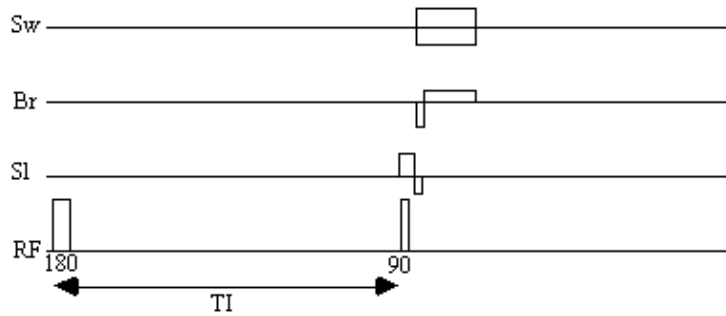


Figure 4.14. Inversion recovery pulse sequence diagram.

Acquiring the reference set, with a suitable number of repeats to gain sufficient signal to noise, can take several minutes. Much of this time is taken up by the inversion time delay. The fast inversion recovery sequence uses this time to invert other slices, before going back to image them, as shown in Figure 4.15.

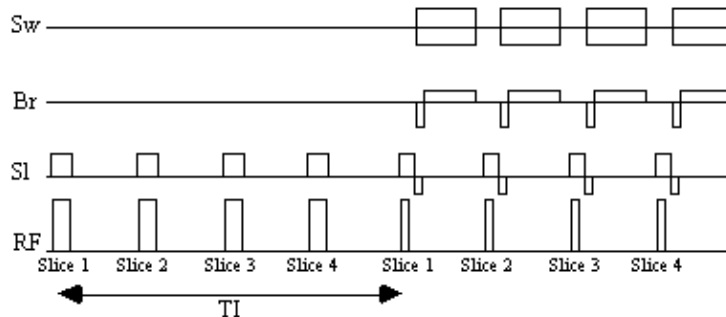


Figure 4.15. Fast inversion recovery pulse sequence diagram.

A constant repetition rate is chosen which is an integer multiple of the required inversion time. For example, to obtain grey matter null images with an inversion time of 1200 ms, four slices are inverted at a repetition rate of 300 ms. A comparison of images obtained using the conventional IR sequence with those obtained using the fast IR sequence shows no difference between the two, however for a typical set of white and grey matter images the fast sequence takes just over 5 minutes compared to 12 minutes for the standard IR method. The main limit to the speed of the fast IR acquisition is the rate of inversion pulses that it is safe to use, because of SAR considerations.

This reduction in time that the subject stays in the scanner helps to keep the subject motivated, and minimises discomfort, which in turn will reduce motion artefact.

4.5 Standard fMRI Protocol

If the results from fMRI experiments are to be reliable, comparable and efficiently obtained, it is necessary to standardise the way that such experiments are carried out. To this end, a standard fMRI protocol was written. The aim of this was to provide an experimental outline that contained the basic procedures that should be carried out, but could be adapted to fit the study in question. The standard fMRI protocol is given in Appendix A.

Correct configuration of the scanner is given purely as a reference, as it is assumed that the operator will be familiar with the operation of the 3.0 Tesla scanner [10]. The standard cylindrical phantom used on the 3.0 T scanner contains structure that can enable its orientation to be

determined from the images. A standard orientation of the phantom is given to avoid confusion when looking at the images at a later date, and for this reason a phantom reference set of images is always stored with the data from that particular experiment. The stability of the scanner is tested each day that fMRI is carried out, by imaging a single slice of a phantom for about 5 minutes. A repetition rate of 10 seconds ensures that the effect of stimulated echoes does not interfere with the result. The stability can be calculated on a pixel by pixel basis by dividing the standard deviation of the pixel time course by its mean. The stability is regarded as satisfactory if this ratio is less than 0.5% throughout the phantom.

Anatomical reference scans are acquired with each data set, so that the precise location of the activation can be determined. If thick slices (> 1 cm) of the brain are to be imaged in the fMRI experiment, then it is better to acquire thinner slices for the reference scans, since the reduction in through slice susceptibility dephasing that this brings will improve the image quality considerably. A method for acquiring these thin slices such that they directly correspond to the thick slices is described in the protocol.

No details of how the stimulus paradigm should be designed are included in the standard protocol. This is because each paradigm may need to be developed depending on many factors such as the size of signal change observed on activation, how the stimulus is presented, how the subject is to respond, and the length of time a subject is able to stay in the scanner. For an initial experiment, a 16 cycle paradigm, with each cycle consisting of 16 seconds of rest and 16 seconds of activity has been shown to be reliable in a number of situations. The results presented later in this thesis, however, show that functional imaging of a single cognitive event is possible, and paradigms that exploit this may yield extra results over those obtained in an epoch based paradigm.

4.6 References

- [1] Van Gelderen, P., Duyn, J. H., Liu, G. and Moonen, C. T. W. (1994) Optimal T_2^* weighting for BOLD-type Functional MRI of the Human Brain. *Proc. Indian Acad. Sci. (Chem. Sci.)* **106**,1617-1624.
- [2] Singh, M., Patel, P. and Khosla, D. (1996) Estimation of T_2^* in Functional Spectroscopy during Visual Stimulation. *IEEE Trans. Nucl. Sci.* **43**,2037-2043.
- [3] Menon, R. S., Ogawa, S., Tank, D. W. and Ugurbil, K. (1993) 4 Tesla Gradient Recalled Echo Characteristics of Photic Stimulation-Induced Signal Changes in the Human Primary Visual Cortex. *Magn. Reson. Med.* **30**,380-386.
- [4] Born, P., Rostrup, E. and Larsson, H. B. W. (1997) Dynamic R_2^* Mapping in Functional MRI. *in* Book of Abstracts, 5th Annual Meeting, *International Society of Magnetic Resonance in Medicine* p.1633.
- [5] Bruder H., Fischer, H., Reinfelder, H.-E. and Schmitt, F. (1992) Image Reconstruction for Echo Planar Imaging with Nonequidistant k-Space Sampling. *Magn. Reson. Med.* **23**,311-323.
- [6] Hu, X., and Le, T. H. (1996) Artefact Reduction in EPI with Phase-encoded Reference Scan *Magn. Reson. Med.* **36**,166-171.
- [7] Mansfield, P. (1977) Multi-Planar Image Formation Using NMR Spin Echoes. *J. Phys. C.* **10**,L55-L58.

[8] Buonocore, M. H. and Gao, L. (1997) Ghost Artefact Reduction for Echo Planar Imaging Using Image Phase Correction. *Magn. Reson. Med.* **38**,89-100.

[9] See Wall, L. and Schwartz, R. Programming Perl, O Reilly & Associates.

[10] Mansfield, P., Coxon, R. and Glover, P. (1994) Echo-Planar Imaging of the Brain at 3.0 T: First Normal Volunteer Results. *J. Comput. Assist. Tomogr.* **18**,339-343.

Chapter 5

Functional MRI using Interleaved EPI

5.1 Introduction

One of the largest problems in using echo planar imaging is the level of image distortion due to susceptibility, that is observed. This can make some structures in the brain, such as the basal ganglia, hard to detect using EPI especially at 3 Tesla. As was mentioned in Chapter 2, the Fourier imaging techniques (2DFT) suffer much less from susceptibility distortion than EPI does, and this is one reason why these techniques are used in routine clinical scans. It is not impossible to carry out fMRI using 2DFT methods, particularly the fast techniques such as FLASH [1], but EPI will always have the speed advantage over such techniques. This is because the entire image is acquired from a single free induction decay (FID), whereas FLASH only acquires one line from each FID.

In order to improve the quality images in fMRI experiments, an approach that can be taken is to use a technique which is a hybrid of EPI and 2DFT, called interleaved EPI. This technique acquires the image in two or more FIDs, thereby trading some of the speed of EPI to gain some of the image quality of 2DFT.

Interleaved EPI was first proposed by McKinnon [2], as a way of implementing EPI on a standard clinical scanner, which did not have the necessary fast ramping gradients. Later it was also demonstrated that the technique could be used for fMRI [3]. Interleaved EPI also has benefits however for scanners which can carry out conventional EPI, ranging from reducing distortion, improving linewidth, to increasing signal to noise.

This chapter describes the theory and implementation of interleaved EPI at 3 Tesla, for use in fMRI experiments. It outlines some of the benefits of using interleaved EPI, and the problems that occur in its use for fMRI.

5.2 The Theory of Interleaved EPI

5.2.1 K-Space Coverage and Gradient Waveforms

Interleaved EPI acquires all the data points required to make up the image in several FIDs. The easiest way to picture how this is done is to look at the k-space coverage diagram (Figure 5.1) for a two shot interleaved EPI sequence. The first interleave covers the whole of k-space in alternate lines, and then the second pass fills in the lines between. The same principle holds for any number of interleaves, up until the technique essentially becomes a 2DFT experiment.

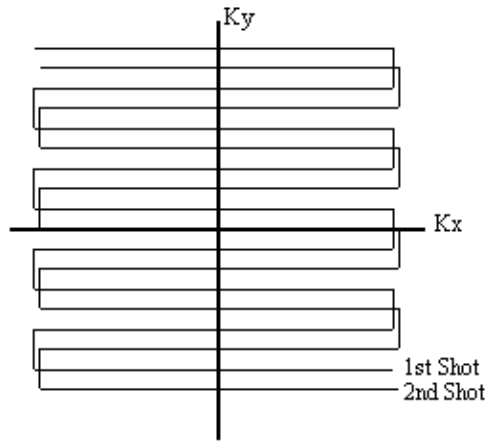


Figure 5.1. K-space coverage diagram for a two shot interleaved EPI sequence.

The technique is sometimes referred to as segmented EPI, since k-space is covered in two or more segments. There are other ways that k-space can be segmented, for example, acquiring the positive k_y values in the first shot, and negative values in the second. It seems appropriate to refer to the kind of technique shown in Figure 5.1 as interleaved EPI, since the two shots are indeed interleaved on reconstruction, and to refer to other multi-shot techniques as segmented EPI.

The pulse sequence diagram required for two shot interleaved EPI is shown in Figure 5.2. Both shots are essentially MBEST modules, but with three differences between the first and second shot. Firstly there is a difference in the length of the pre excursion of the blipped gradient. This ensures that the phase encoding is slightly different for each shot, so that every line of k-space is acquired. Assuming that the magnitude of the blipped pre-excursion gradient is the same as the blipped gradient itself, then the excursion must increase in length by half of the duration of one blip, for each interleave. Since increasing the length of the pre-excursion delays, albeit slightly, the time of the echo, an appropriate delay must be added in the earlier interleave to compensate.

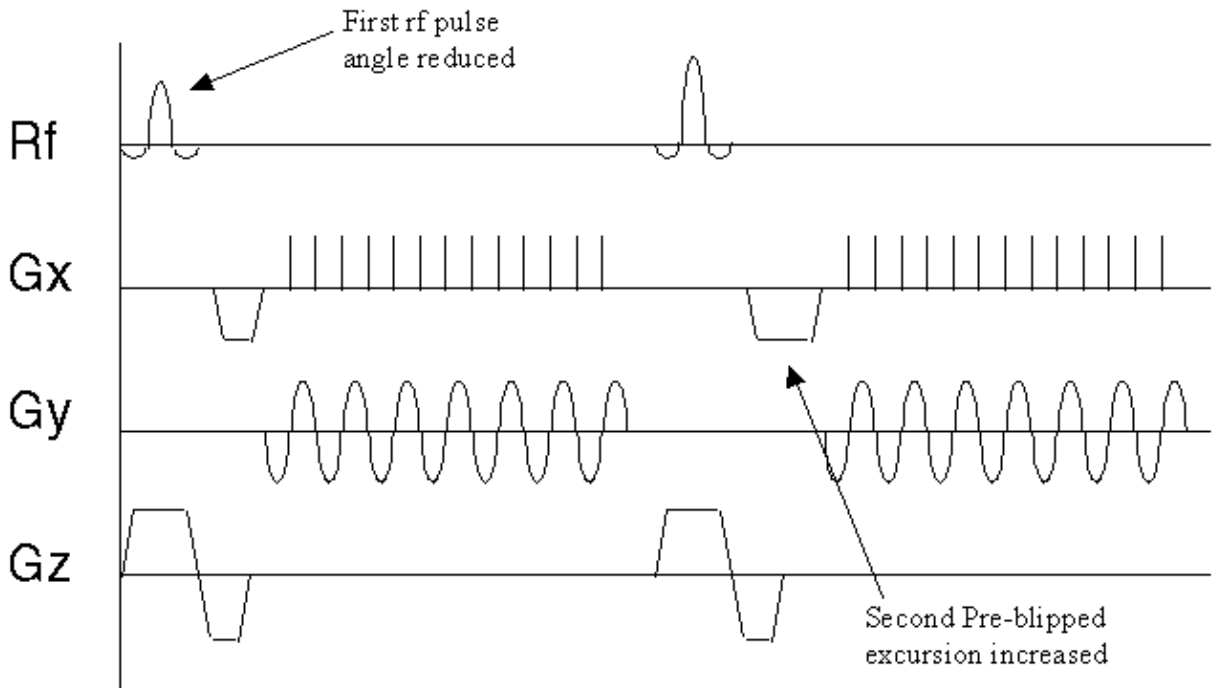


Figure 5.2. Pulse sequence diagram for a two shot interleaved EPI experiment.

The other two differences relate to discontinuities in the phase and magnitude of the signal along the k_y direction in the final image.

5.2.2 Correcting for Discontinuities in K-Space

The second difference between shots in the pulse sequence diagram relates to the magnitude of the transverse magnetisation vector after the r.f. pulse. If the magnitude of the longitudinal magnetisation prior to the experiment is M_0 , then following a 90 degree pulse the transverse magnetisation will be M_0 , and the longitudinal magnetisation will be zero. In the duration, TR , between the first and second r.f. pulses the longitudinal magnetisation will recover through T_1 relaxation, and following a second 90 degree pulse the transverse magnetisation will be

$$M = M_0 [1 - \exp(-TR/T_1)] \quad (5.1)$$

Unless $TR \gg T_1$, the signal intensity of the two interleaves will therefore be significantly different. This leads to discontinuities in k-space and causes ghosting artefact, as demonstrated in Figure 5.3. The effect can be compensated for by reducing the flip angle of the first pulse.

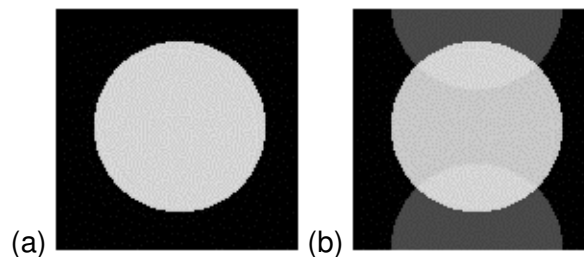


Figure 5.3. Differences in the amplitude or phase between the two interleaves that make up the image, causes ghosting.

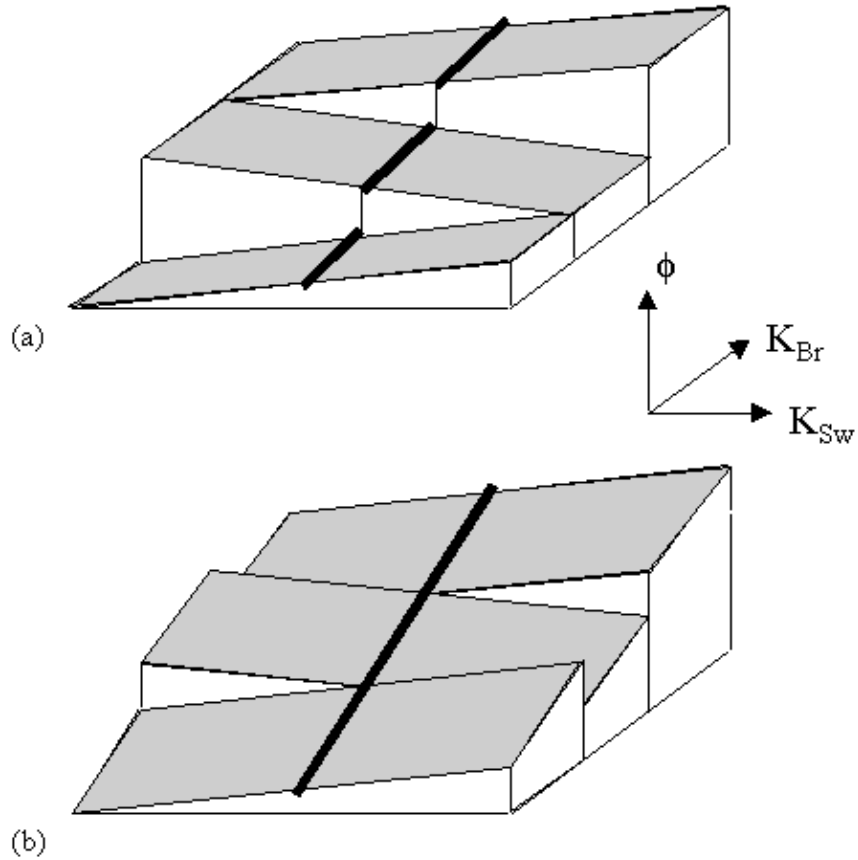
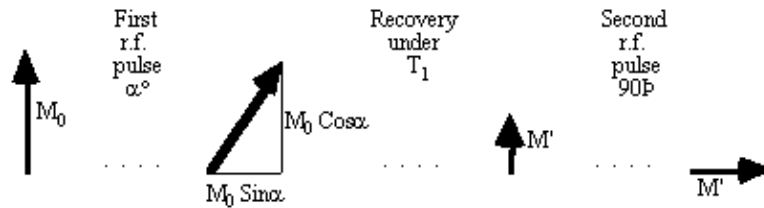


Figure 5.4. (a) Discontinuities along the central line of k-space lead to ghosting artefact. (b) By shifting the echo time of successive interleaves, these discontinuities are smoothed out.



The z-magnetisation prior to the n th interleave is given by

$$M_n = M_0 - (M_0 - M_{n-1} \cos(\alpha_{n-1})) \exp(-TR/T_1) \quad (5.2)$$

and for constant signal following each excitation

$$M_n \sin(\alpha_n) = M_{n-1} \sin(\alpha_{n-1}) \quad (5.3)$$

These equations can be solved iteratively, with the last flip angle being 90 degree, to find the flip angles for each of the interleaves. These equations only hold for one value of T_1 , and so discontinuities between interleaves in the signal from tissue with a different value of T_1 will still

occur. To reduce this problem McKinnon suggests calculating a slightly longer series than necessary, and only using the first part of the series [4].

In using interleaved EPI for fMRI, many images are obtained with a constant repetition rate. This means that a constant flip angle can be used, and after the first few images have been acquired the magnitude of the longitudinal magnetisation reaches a steady state.

The third difference in the pulse sequences between interleaves, acts to reduce phase discontinuities in the time data. Off-resonance phase errors, due to field inhomogeneity, susceptibility and chemical shift, evolve constantly with time. Since in each interleave alternate lines are acquired under opposite read gradients, these lines must be reversed in the time data matrix prior to Fourier transformation. This leads to steps in the phase, which may cause ghosting artefact. This can be a problem in conventional EPI, but the problem is compounded in N shot interleaved EPI, since the first N lines are all acquired at the same time in the echo train, and thus the steps are N times longer (see Figure 5.4a).

To compensate for this, at least along the central line of k -space, a slight time delay of magnitude

$$\Delta t = n \cdot \frac{T_x}{N} \tag{5.4}$$

is added to the n th interleave (T_x is the time needed to acquire one line in k -space). This has the effect of smoothing out the discontinuities (see Figure 5.4b) [5,6].

5.2.3 Multi-Slice Interleaved EPI

Since it is commonly required to image several slices when carrying out an fMRI experiment, the signal to noise ratio can be improved by employing a multi-slice technique. The k -space diagram for multi-slice interleaved EPI is shown in Figure 5.5.

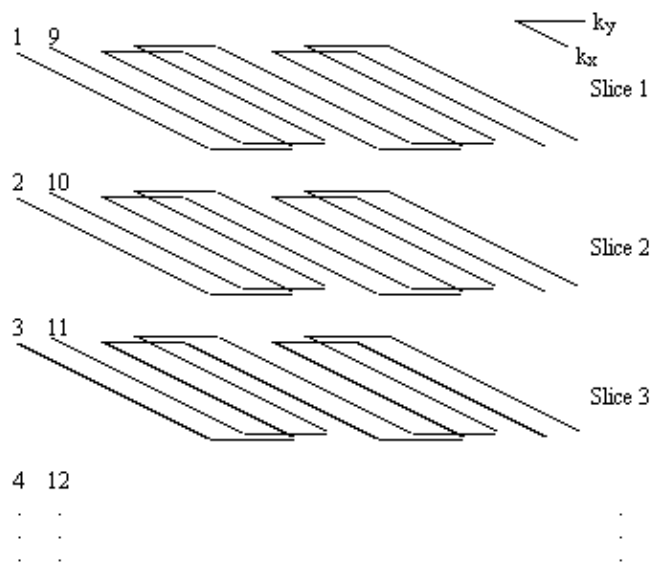


Figure 5.5. K-Space diagram for multi-slice interleaved EPI.

The first shot of every slice is acquired before returning to acquire the second interleave. This increases the steady state transverse magnetisation available after each pulse, and therefore increases the signal to noise ratio.

The benefits are slightly offset by the risk of subject movement during the acquisition. If the movement occurs between the first and second shot of one slice, that image will show artefact as a result. The chances of this occurring is much greater if there is a long delay between shots, as is the case in the multi-slice experiment.

5.3 The Benefits and Problems of Using Interleaved EPI

5.3.1 Reduction in Distortion

As was mentioned in Chapter 2, since MRI uses a knowledge of the precise magnetic field at any position, at any time, to create a map of proton density, any irregularities in the field are manifested in the image as distortion. Even if the B_0 field produced by the magnet is very homogeneous, the presence of a sample containing regions with different magnetic susceptibilities, causes local inhomogeneities in the field. This effect is particularly bad at high field, in the temporal lobes and basal ganglia. Although shimming the sample can reduce the effect, there is always some inhomogeneity in the sample.

The amount by which the inhomogeneities affect the image depends on the frequency per point of the image. Take for example the signal shown in Figure 5.6.

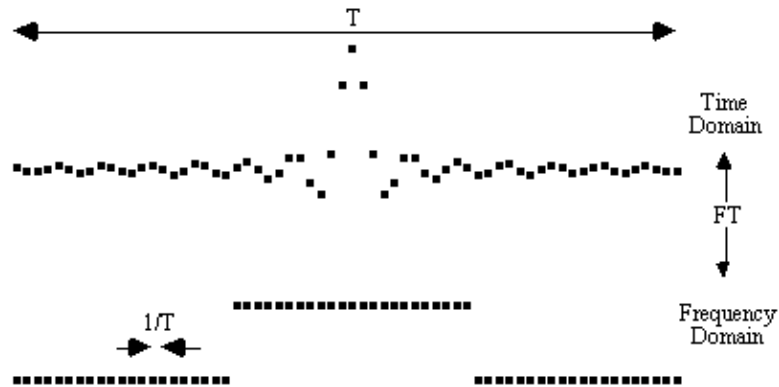


Figure 5.6. The frequency per point in the frequency domain is the inverse of the length of time sampled.

Upon Fourier transformation, the separation in Hertz of adjacent points in the frequency domain is the inverse of the length of time sampled. So that, for example, if the signal is sampled for 100 ms the frequency per point is equal to 10 Hz. Now consider the effect of a local field inhomogeneity of 0.5 parts per million. The proton resonance frequency at 3.0 Tesla is 128 MHz, and so the 0.5 ppm inhomogeneity represents a 64 Hz frequency offset from the expected value. If the difference between adjacent pixels in an image is 10 Hz, then the 64 Hz offset causes a distortion of just over 6 pixels.

In EPI, the broadening direction has a longer sampling time than the switched direction, so distortion occurs mainly in the broadening direction. This is in contrast to 2DFT where distortion only occurs in the read direction. However, the sampling length in 2DFT is usually much shorter than the broadening direction sample time in EPI (see Figure 5.7), making EPI more sensitive to susceptibility induced distortion than 2DFT. With a field inhomogeneity of fixed magnitude, the effect

on the image can be reduced by increasing the frequency per point. This can be done by using multi-shot EPI instead of the single shot technique.

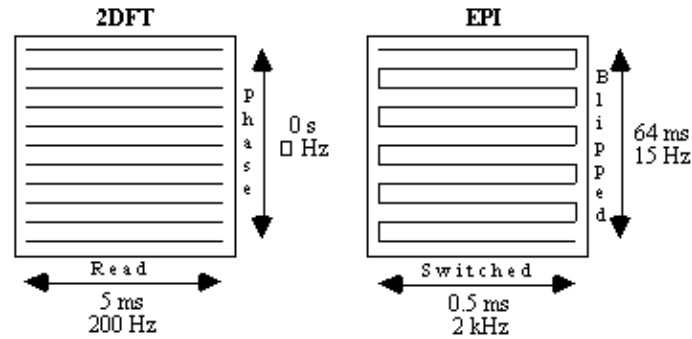


Figure 5.7. Comparison of the typical sampling times and frequency per point, between read and phase encode directions in 2DFT, and between switched and blipped directions in EPI.

If a two shot technique is used, for example, the time spent sampling each FID is reduced by half, thereby increasing the frequency per point by a factor of two. So for an n shot acquisition the distortion is reduced by a factor of n .

An example of the reduction in image distortion is shown in Figure 5.8. These three transaxial slices through the brain have matrix size 128×128 , and were acquired using single shot (conventional) EPI, two shot and four shot interleaved EPI. They were acquired with a read gradient switching rate of 615 Hz, meaning that the sampling times for the single, two and four shot images were 104 ms, 52 ms and 26 ms respectively. The reduction in distortion in going from single shot to four shot is very apparent, however it can be noted that there is a greater level of ghosting artefact on the four shot image than on the single shot one.

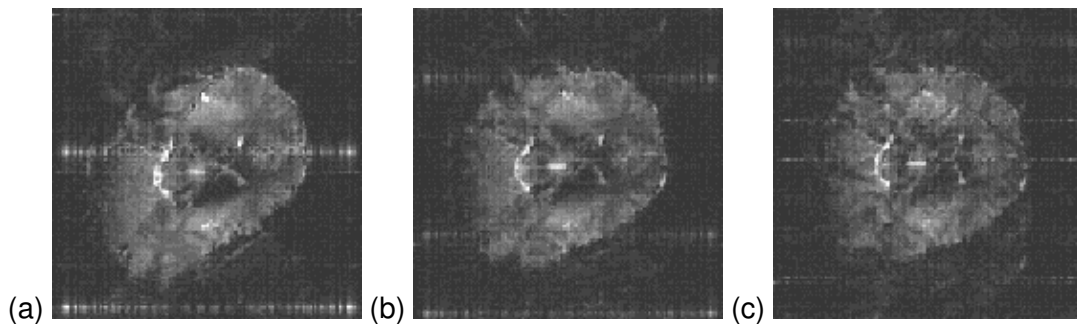


Figure 5.8 A transaxial slice through the brain acquired using (a) single shot, (b) two shot and (c) four shot interleaved EPI. The level of distortion is greatly reduced in the four shot case, compared to the single shot.

This is the most significant benefit of using interleaved EPI, that by increasing the number of interleaves, the level of the distortion in the image due to field inhomogeneity reduces.

5.3.2 Improvement in Linewidth

A second benefit of interleaved EPI is in the reduction in linewidth, which results again from the increase in frequency per point in the image.

As was described in Chapter 2, spin-spin relaxation and the effect of field inhomogeneity causes the transverse magnetisation to decay, with a time constant T_2^* . This has the effect of convolving the image with a point spread function, as shown in Figure 5.9.

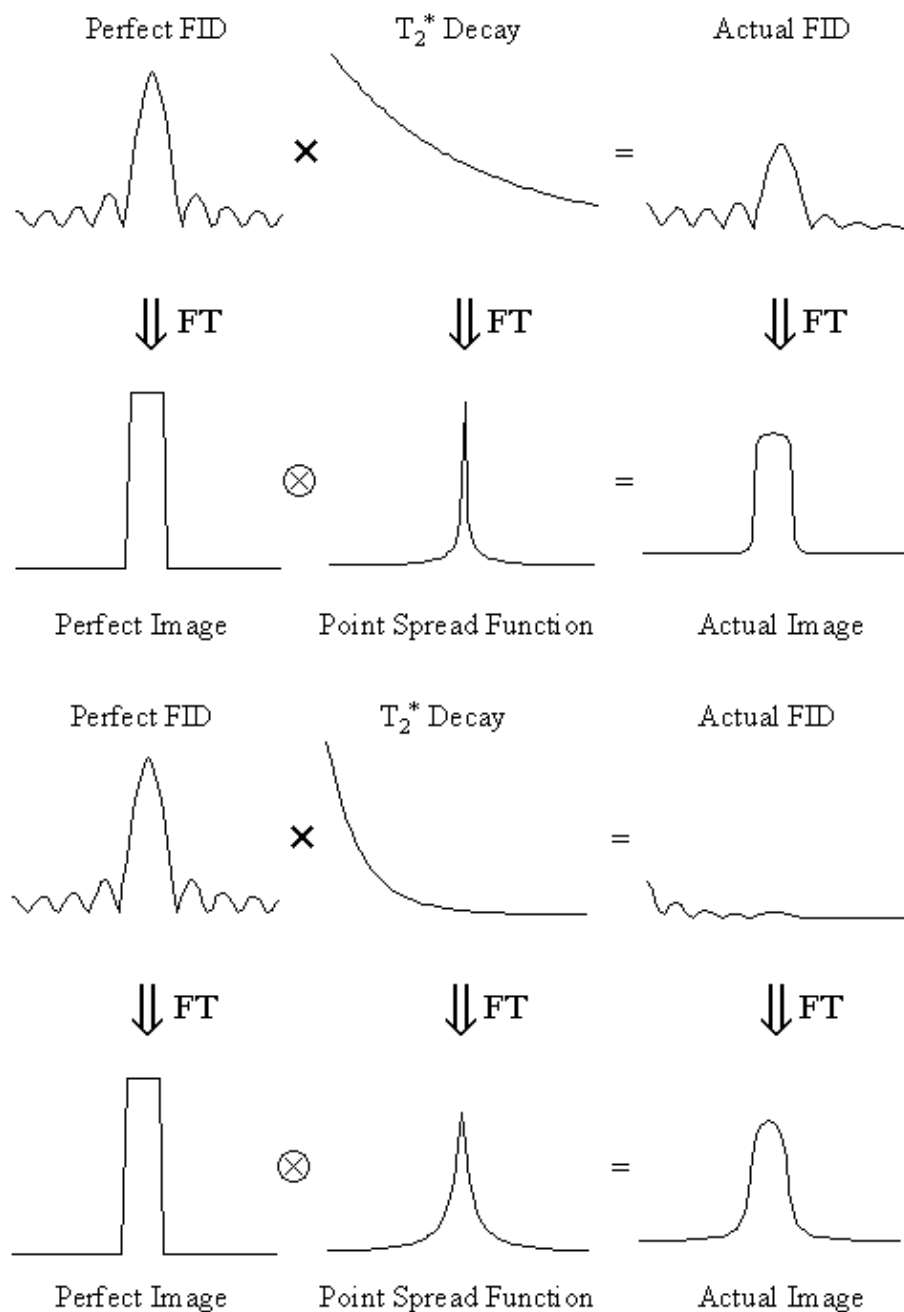


Figure 5.9 The effect of T_2^* decay on the sharpness of a line through an image. The smaller the value of T_2^* , the wider the point spread function, and the more smoothed the profile becomes.

The point spread function is the Fourier Transform of the T_2^* decay

$$f(t) = \exp(-t/T_2^*), \tag{5.5}$$

and has the form

$$F(\omega) = \frac{T_2^*}{1 - i\omega T_2^*}.$$

If two points of equal magnitude in the image are separated by $\Delta\omega$, then the total signal as a function of ω is of the form

$$F'(\omega) = \frac{T_2^*}{1 - i\omega T_2^*} + \frac{T_2^*}{1 - i(\omega - \Delta\omega)T_2^*}$$

The Rayleigh criterion [7] states that two pixels are resolved when two pixels of intensity S_0 , are separated by one of intensity less than $0.81 S_0$, as shown in Figure 5.10.

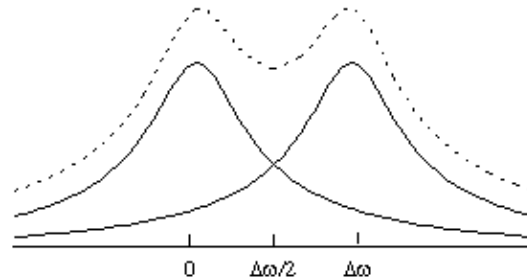


Figure 5.10. The Rayleigh criterion applied to the resolution of two pixels subject to T_2^* line broadening. The intensity of the central pixel must be less than 0.81 that of the intensity of the two pixels it separates.

So using the condition

$$|F'(\Delta\omega/2)| = 0.81|F'(0)|$$

the minimum frequency per point separation required to obtain true pixel resolution is given by

$$\Delta\omega/2 = \frac{0.96}{T_2^*}$$

Thus for a typical value of T_2^* at 3 T of 60 ms, the required frequency per point is 16 Hz. If high resolution imaging is being carried out then it is quite possible that the pixel resolution is not the true resolution. For example, acquiring a 256^2 matrix with a switched gradient frequency of 500 Hz using conventional EPI will give a frequency per point of just under 4 Hz. This is below the 16 Hz frequency per point required for true pixel resolution. However by using a two shot interleaved EPI technique the frequency per point will increase to 8 Hz, and a four shot technique will double this value again to about 16 Hz.

Figure 5.11 shows three images of a cylindrical phantom containing a 3 mm diameter glass rod, surrounded by water doped to have a T_2^* similar to the brain. The phantom is imaged to a pixel resolution of 1 mm, with single shot, two shot and four shot EPI, and line profiles through the rod, as indicated by the black line on the images, are shown. The line profile shows a clear increase in definition of the glass rod in the four shot case, compared to the single shot case, indicating the

improvement in real resolution obtained in this case by using interleaved EPI.

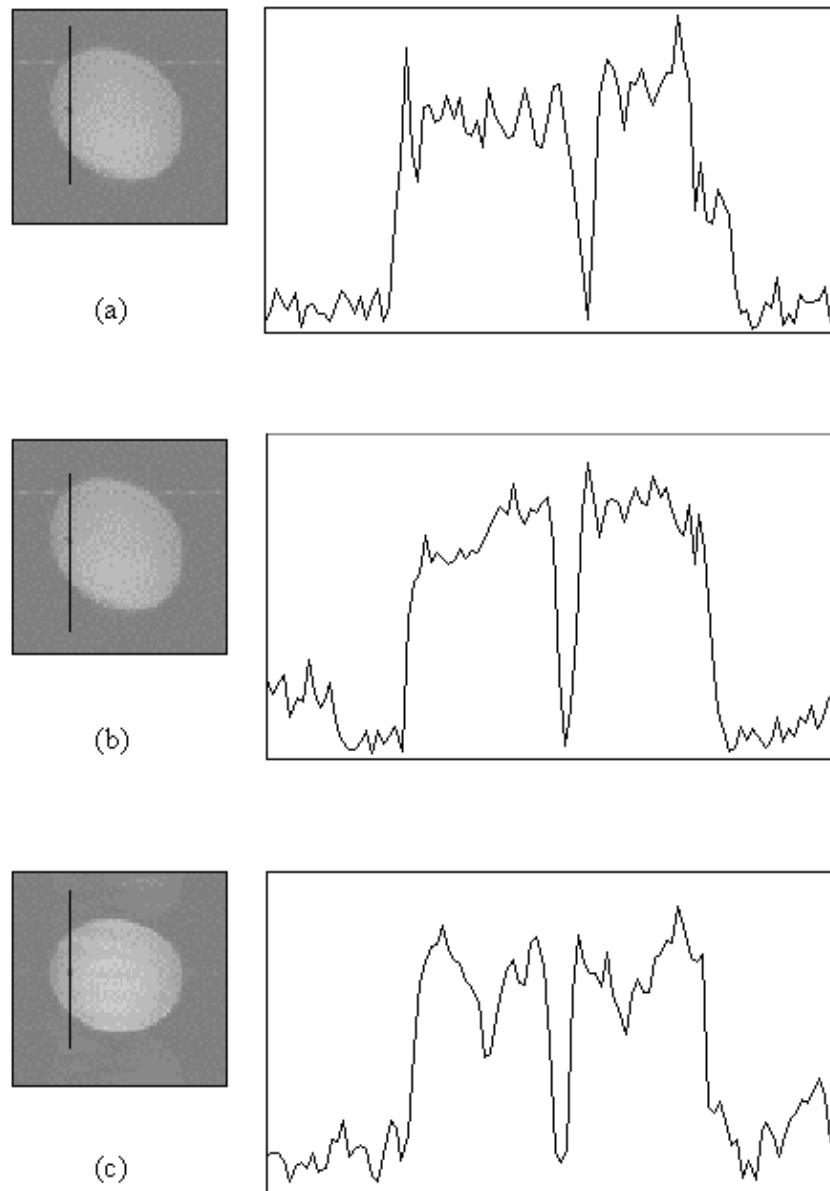


Figure 5.11 Line profile through a phantom imaged using (a) single shot, (b) two shot and (c) four shot interleaved EPI. The pixel resolution is $1 \times 1 \text{ mm}^2$ and the glass rod in the phantom has diameter 3 mm. The narrower point spread function, in the broadening direction, of the four shot image means that the rod is better defined than in the single shot case.

5.3.3 The Benefits of using Interleaved EPI for fMRI

There are several approaches that can be taken in using interleaved EPI to improve the results of an fMRI experiment.

If for example the fMRI image is of poor quality, due to susceptibility distortions, the distortion can be reduced by using interleaved EPI whilst maintaining the same resolution. The distortion in this case will be reduced by the number of interleaves used.

Alternatively, if the level of distortion is acceptable, the resolution can be increased by reducing the switched gradient frequency by half and doubling the number of interleaves. The frequency per

point in this case will stay the same, and so therefore will the distortion. Interleaved EPI offers real benefits in carrying out high resolution fMRI at high field.

Without increasing the resolution or the distortion, the benefits of interleaved EPI can be seen in an increased signal to noise ratio, and reduced gradient current requirements. This can be achieved by lowering the switched gradient frequency, thereby increasing the time taken to sample one line in k-space. This reduces the sampling bandwidth required and increases the signal to noise ratio by the square root of the number of interleaves used. By reducing the current requirement, the level of gradient heating is also reduced.

For larger matrix sizes and lower gradient switching rates, the linewidth broadening may become a limitation. In this situation, interleaved EPI can be used to regain true resolution.

The combination of gradient switching rate, and matrix size, with the number of interleaves, can bring benefits in resolution, distortion, gradient heating, and signal to noise, although the increased number of acquisitions means that the experimental duration may be longer.

Recently a number of groups have demonstrated the use of interleaved EPI for high resolution fMRI of the visual cortex at high field [8],9] and also the development of the technique to carry out interleaved echo volumar imaging (EVI) [10].

5.3.4 Ghosting Artefact in Interleaved EPI

As already mentioned above, any differences in phase or intensity between interleaves will show up in the images as ghosting artefact. These differences can be due to subject movement or instability in the scanner hardware. In addition, the ghosting caused by the reversal of lines acquired under the negative read gradient (Nyquist or N/2 ghost) is made worse since the positive and negative gradient pulses are grouped in blocks by the interleaving. Such artefacts, which change with time make fMRI difficult to perform, particularly at high resolution where signal to noise is low and small movements mean a large pixel displacement. The magnitude of the changes in the image due to artefact are often greater than the contrast changes due to the BOLD effect.

The first line of attack on such problems is to attempt to remove them at source. Motion can be reduced by restraining the subject's head, and by careful planning of the stimulus paradigm. Unfortunately high resolution fMRI using interleaved EPI requires long experiments, due to its low signal to noise. This makes the subject more uncomfortable and prone to move. To reduce the N/2 ghosting problem an asymmetric EPI experiment could be used [11]. This only acquires the data under one polarity of read gradient and so is not quite as efficient as conventional interleaved EPI.

Instability from shot to shot in the hardware can be measured using a navigator echo [12,13]. In its simplest form, a navigator echo is a sample of the FID, prior to the application of the imaging gradients. The phase of this sample can be calculated for each of the interleaves in the image, and then a bulk phase correction applied to normalise the data. This technique was included in the interleaved EPI pulse sequence, acquiring a number of sample points prior to the imaging gradients. The mean phase of these data points was calculated and a phase correction determined to normalise these values for each interleave. These factors were applied to the actual image data prior to Fourier transformation.

Other forms of navigator echoes have been proposed for the correction of interleaved EPI data [14]. In particular, the obvious extension of applying a gradient in one direction during the navigator echo acquisition, so as to make the echo sensitive to uni-directional movement, has been suggested.

Even after applying the navigator correction there is still a significant amount of ghost present, most probably due to subject movement. To reduce this, it is necessary to apply some form of correction to the data in post-processing. The most straightforward correction is a zeroth order phase shift, where the same phase change is applied to every point in the interleave. In order to successfully use such a correction as a post-processing technique on fMRI data, it is necessary to decide upon some measure of the amount of ghosting.

The Fourier transform (FT) of the central column of k-space, represents the D.C. component of each line in the image. The amount of ghost can be determined by selecting this column, applying the phase correction and FT, and measuring the ratio of the central points to the edge points, as shown in Figure 5.12. This method works well for a two shot technique, where the ghost appears at the edges, but is less successful if more interleaves are used and the ghost appears throughout the image.

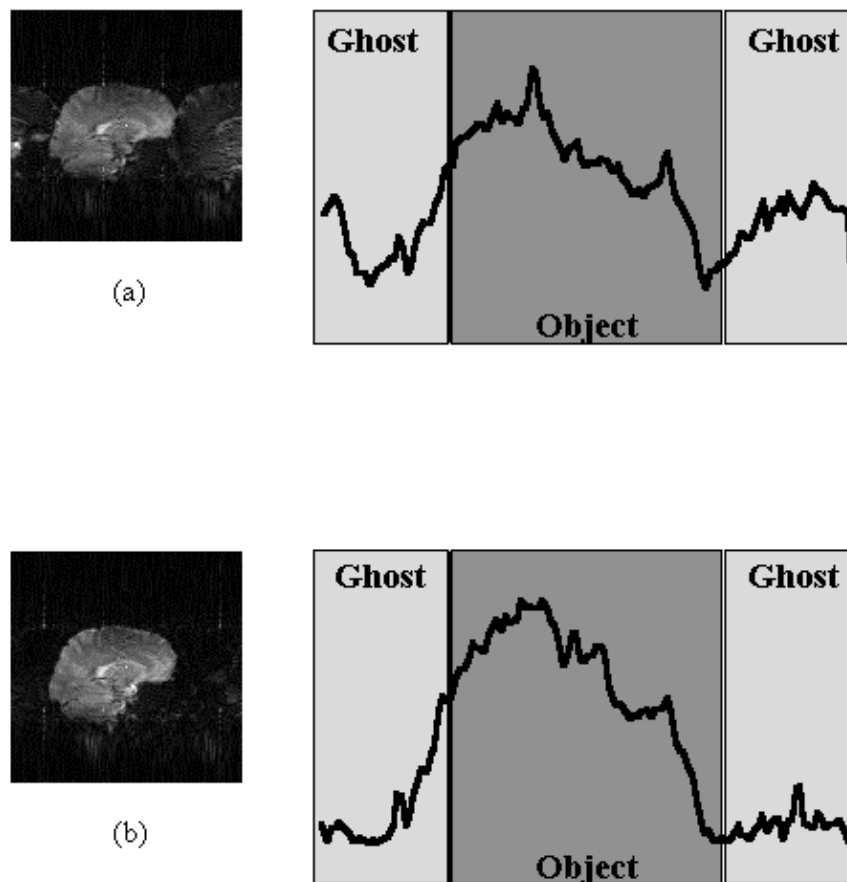


Figure 5.12 Profile of Fourier Transform of the central line of k-space for two shot interleaved EPI images, (a) with severe ghosting and (b) with little ghosting. The ratio of the central lines of this profile to the outside lines is a maximum for a ghost free image.

Since the origin of the artefact is motion, it seems appropriate to apply some form of motion correction. To do this it is necessary to have some measure of how well any processing corrects the data. One possibility is to define the regions where any ghosting would be expected to be manifested and try to reduce the signal intensity in this area [15]. If this is not possible then some other measure of the level of ghosting is required. Atkinson and Hill [16] have suggested that an entropy term of the form

$$\sum s_i \ln(s_i)$$

where S_i is the intensity of the i th pixel in the image, would be one such measure. They propose motion correcting the interleaves until the term in equation 5.10 is a minimum.

Until a suitable solution for the problem of the ghosting is found, high resolution interleaved EPI will be difficult to use in practice.

5.4 Implementation at 3.0 Tesla

To demonstrate the viability of using interleaved EPI to carry out fMRI at 3.0 Tesla, three experiments were performed.

5.4.1 High Resolution fMRI

A two shot multislice interleaved EPI technique was used to acquire a 256×256 matrix size image, using a switching rate of 1.04 kHz. Eight slices of thickness 4.5 mm, covering the visual cortex were acquired in eight seconds, during periods of visual stimulation from the pattern reversal (4 Hz) of a checkerboard pattern. There were 32 seconds of stimulation followed by 32 seconds of rest, repeated 16 times. The in-plane resolution was $0.75 \times 0.91 \text{ mm}^2$. A zeroth order phase correction was applied to one interleave, until the Fourier transform of the central line of k-space had the maximum ratio of signal in the inner points to signal in the outer points. The images were re-registered, but no spatial or temporal smoothing applied. The fMRI data was correlated to a square wave of the same period and phase as the stimulus and p-values calculated on the basis on peak height and spatial extent of the correlation maps using the theory of Gaussian random fields (see Chapter 6).

The resulting activation map is shown in Figure 5.13. The coloured regions represent the regions that correlate well to the stimulus ($p > 0.05$). The background images are the average of the actual fMRI data set, so that the resolution seen in these images is the same as that of the activation maps. Regions of activation can be seen in the primary visual cortex and visual association areas. The change in the primary visual cortex upon activation was approximately 20%.

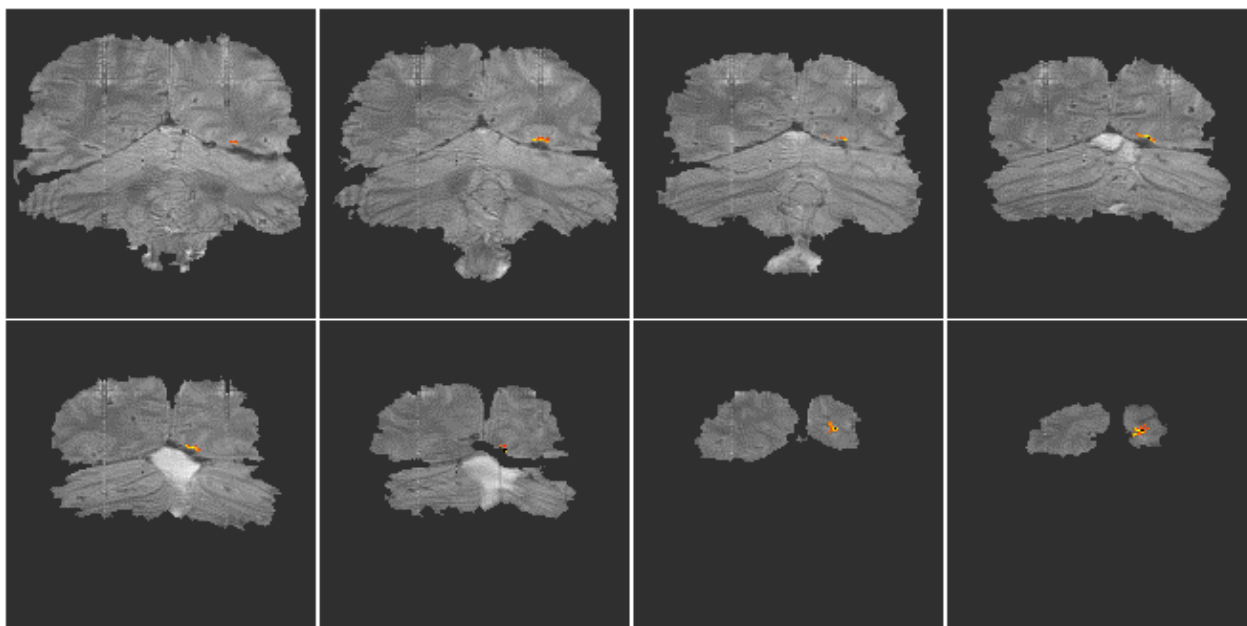


Figure 5.13 High resolution two shot interleaved EPI functional images for a visual stimulus in the right visual field. Activation ($p > 0.005$) is overlaid on the average of the images used for the fMRI analysis.

5.4.2 Low distortion fMRI

Low distortion EPI images were acquired using a two shot multislice interleaved EPI technique with a matrix size of 128×128 and a switching rate of 1.9 kHz. These were compared with images from a single shot experiment with the same matrix size. The activation paradigm consisted of 32 seconds of the subject observing the pattern reversal (4 Hz) of a checkerboard display whilst finger tapping, followed by 32 seconds of rest, repeated eight times. The whole brain, in each experiment, was scanned in 16 slices, in a period of 8 seconds. The images were registered and spatially smoothed (FWHM 4 mm), and correlated to a square wave of the same period and phase as the stimulus. Activation maps were thresholded, using the theory of Gaussian random fields, based on peak height and spatial extent. The activation maps were overlaid on white matter inversion recovery images (TI 1200 ms) acquired using either the single shot or two shot technique.

The resulting images are shown in Figure 5.14. Both methods produced very similar activation maps, with slightly more activation detected in the single shot technique. This is because the shot-to-shot signal to noise was not quite as good in the two shot experiment, presumably due to slight subject movement between interleaves. The level of distortion is slightly less in the two shot case and these results demonstrate the viability of carrying out low distortion interleaved EPI at 3.0 T.

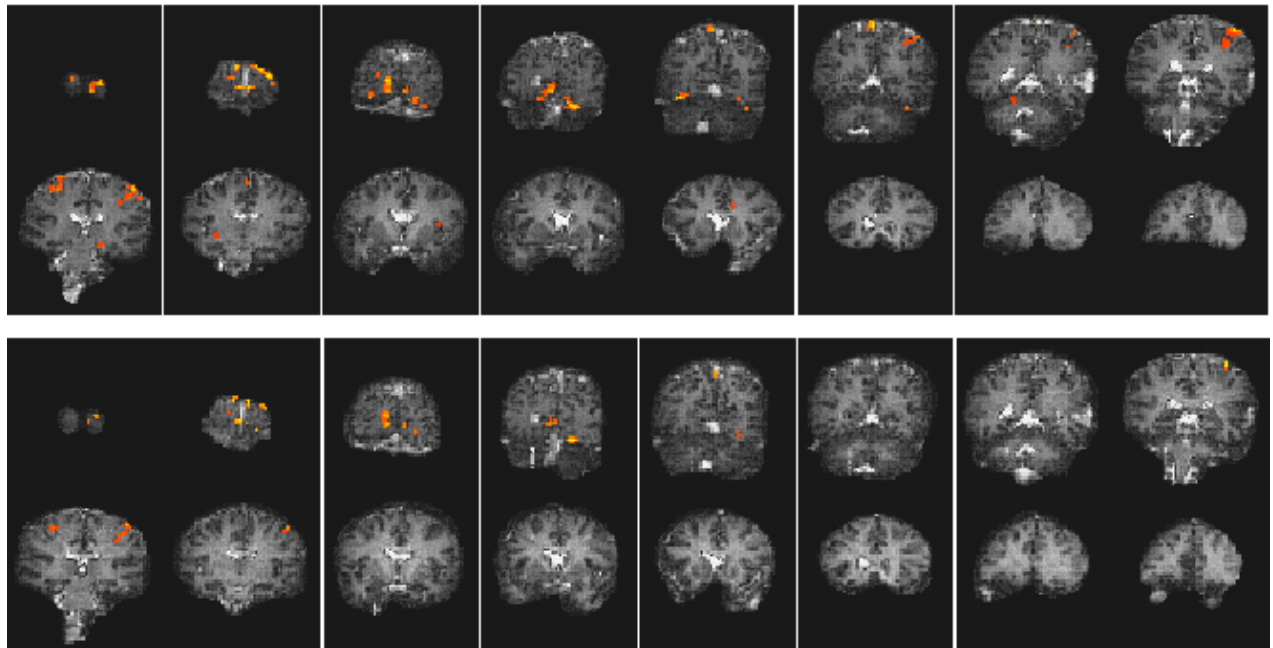


Figure 5.14 Activation images from two experiments both involving a the same visually cues motor task. The top set of images were acquired using single shot EPI, and the bottom set acquired using two shot interleaved EPI.

5.4.3 High Resolution Anatomical References Images for fMRI.

One final application of interleaved EPI is to produce high resolution anatomical images to overlay the activation data on, with the level of distortion being the same in each case, allowing direct superposition.

A single shot EPI, functional imaging experiment was performed using a matrix size of 128×64 , and a switching rate of 1.04 kHz. The activation paradigm consisted of 16 seconds of viewing a

flashing LED display, and pressing a hand held button at the same rate, followed by 16 seconds of rest, repeated 16 times. The visual cortex was scanned in eight slices, every 2 seconds (resolution $3 \times 3 \times 9 \text{ mm}^3$). Following the activation experiment, the switched and broadening gradient strengths were doubled and four volume images of the same slices were obtained using a two shot interleaved EPI sequence, having twice the in-plane resolution ($1.5 \times 1.5 \text{ mm}^2$). These were used as background images for the activation maps to be overlaid upon. The activation maps were interpolated up to twice their size, and registered to the high resolution images. The activation images are shown in Figure 5.15.

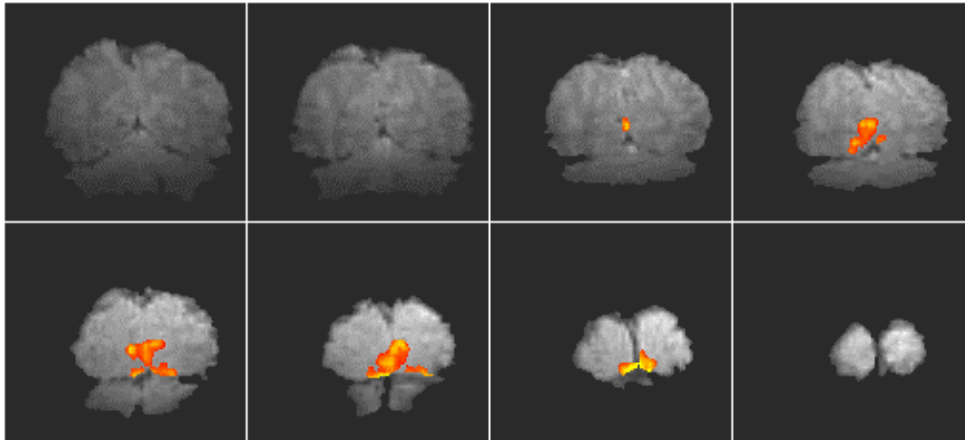


Figure 5.15 Low resolution activation images ($3 \times 3 \text{ mm}^2$ in-plane) for a visual stimuli, overlaid on high resolution ($1.5 \times 1.5 \text{ mm}^2$ in-plane) background T_2^* weighted images.

5.5 Summary

The results show that high resolution fMRI has the potential to detect small regions of functional activity. If such high resolution images are to be obtained then a multi shot EPI sequence is most probably required so that the images do not suffer too greatly from distortion. The main problem with high resolution interleaved EPI is the artefact caused by subject movement, and until a robust post-processing correction technique has been demonstrated, it is going to be difficult to gain useful results.

The interleaved EPI sequence however still has other applications on a high gradient performance 3.0 Tesla scanner. The reduction in distortion that the multi shot techniques brings, will benefit studies of the basal structures of the brain in particular. The ability to obtain high resolution anatomical images, with the same distortion as the original activation images, allows confident anatomical localisation of the activation, since the resolution is higher than the single shot images, but there will be less risk of mis-registration of structures in the functional images to the anatomical images that might be the case if 2DFT images were used.

5.6 References

- [1] Frahm, J., Merboldt, K.-D. and Hänicke, W. (1993) Functional MRI of Human Brain Activation at High Spatial Resolution. *Magn. Reson. Med.* 29,139-144.
- [2] McKinnon, G. C., Eichenberger, A. C., von Weyarn, C. A. and von Schulthess, G. K. (1992) Ultra-Fast Imaging Using an Interleaved Gradient Echo Planar Sequence *in* Book of Abstracts, 11th Annual Meeting, *Society of Magnetic Resonance in Medicine* p.106.

- [3] Butts, K., Riederer, S. J., Ehman, R. L., Thompson, R. M. and Jack, C. R. (1994) Interleaved Echo Planar Imaging on a Standard MRI System. *Magn. Reson. Med.* 31,67-72.
- [4] McKinnon, G. C. (1993) Ultrafast Interleaved Gradient-Echo-Planar Imaging on a Standard Scanner. *Magn. Reson. Med.* 30,609-616.
- [5] Feinberg, D. A. and Oshio, K. (1994) Phase Errors in Multi-Shot Echo Planar Imaging. *Magn. Reson. Med.* 32,535-539.
- [6] Mugler III, J. P. and Brookeman, J. R. (1996) Off-Resonance Image Artefacts in Interleaved-EPI and GRASE Pulse Sequences. *Magn. Reson. Med.* 36,306-313.
- [7] Lord Rayleigh (1879) Investigations in Optics with special reference to the Spectroscope. *Phil. Mag.* 8,261-274.
- [8] Kim, S.-G., Hu, X., Adriany, G. and Ugurbil., K. (1996) Fast Interleaved Echo-Planar Imaging with Navigator: High Resolution Anatomic and Functional Images at 4 Tesla. *Magn. Reson. Med.* 35,895-902.
- [9] Thulborn, K. R., Voyvodic, J., Chang, S. Y., Song, D., Blankenberg, F., Davis, D. and Zeki, S. (1997) High Spatial Resolution, Echo-Planar fMRI at 3.0 Tesla Resolves Specialized Functions of the Human Visual Cortex *in Book of Abstracts, 5th Annual Meeting, International Society of Magnetic Resonance in Medicine* p.7.
- [11] Tan, S. G., Wong, E. C., Li, S.-J., Song, A. W. and Hyde, J. S. (1995) Interleaved Echo Volumar Imaging *in Book of Abstracts, 3rd Annual Meeting, Society of Magnetic Resonance* p.620.
- [12] Hennel, F. and Nédélec, J.-F. (1995) Interleaved Asymmetric Echo-Planar Imaging. *Magn. Reson. Med.* 34,520-524.
- [13] Ehman, R. L. and Felmlee, J. P. (1989) Adaptive Technique for High-Definition MR Imaging of Moving Structures. *Radiology* 173,255-263.
- [14] Hu, X. and Kim, S.-G. (1994) Reduction of Signal Fluctuation in Functional MRI Using Navigator Echoes. *Magn. Reson. Med.* 31,495-503.
- [15] Kim, S.-G., Hu, X., Adriany, G. and Ugurbil., K. (1996) Fast Interleaved Echo-Planar Imaging with Navigator: High Resolution Anatomic and Functional Images at 4 Tesla. *Magn. Reson. Med.* 35,895-902.
- [16] Robson, M. D., Anderson, A. W. and Gore, J. C. (1997) Diffusion-Weighted Multiple Shot Echo Planar Imaging of Humans without Navigation. *Magn. Reson. Med.* 38,82-88.
- [17] Atkinson, D. and Hill, D. *Private communication.*

Chapter 6

The Analysis of fMRI Data

6.1 Introduction

This chapter deals with the way in which the raw data from an fMRI experiment is analysed. The aim of such analysis is to determine those regions in the image in which the signal changes upon stimulus presentation. Although it is possible to devise many different techniques for detecting activation, if these techniques are to be used in practice it is necessary to know how much confidence can be placed in the results. That is to say, what is the probability that a purely random response could be falsely labeled as activation. This requires an understanding of the statistics behind the technique used.

Many of the statistically robust techniques used to analyse fMRI data have been developed from PET. These try to model the time course that is expected, and determine how well each pixel's temporal response fits this model. However, since fMRI experiments allow a much greater time resolution than PET, it is possible to carry out experiments which determine the order in which different cognitive events occur. Analysis of the data from such an experiment requires a 'non-directed' technique which makes few assumptions about the timings of the activation responses expected.

There are three stages to the analysis of the data from any fMRI experiment (Figure 6.1). Firstly there are the pre-processing steps, which can be applied to the data to improve the detection of activation events. These include registering the images, to correct for subject movement during the experiment, and smoothing the data to improve the signal to noise ratio. Next, the statistical analysis, which detects the pixels in the image which show a response to the stimulus, is carried out. Finally the activation images must be displayed, and probability values, which give the statistical confidence that can be placed in the result, quoted.



Figure 6.1 Steps involved in the processing of fMRI data

In order to analyse the data from the experiments explained in Chapter 7, a suite of programs were written, which implement existing and novel analysis techniques for carrying out the steps outlined above. These techniques are described in detail in the following sections.

6.2 Preparing MR Images for Statistical Analysis

There are a number of steps that can be carried out prior to the statistical analysis of the data. Each of these steps is independent and offers different benefits. There is an analysis time penalty to be paid for each of the steps, some of which can take times of the order of hours. The theory and implementation of each step is described below, with an integrated package explained in the final section.

6.2.1 Image Formation, Data Reduction and Global Normalisation

The raw time data from the scanner requires Fourier transformation to form the image. The raw data is stored as complex numbers, one for each pixel in the image. Correction for N/2 ghost artefact (see Section 4.3.1) can be carried out at this stage by changing the phase angle between real and imaginary data points of alternate lines. The extent of correction required can be determined by eye, adjusting the phase angle until the N/2 ghost in the first image in the set is minimised. The same correction can then be applied to every image in the fMRI data set. Alternatively one of the methods suggested in Chapter 4 can be utilised. Failure to eliminate any ghost artefact can cause activations from within the head to be aliased in the ghost.

Two dimensional fast Fourier transformation (FFT) is carried out using a standard routine[1], with the images being stored as 4 byte signed integers (shorts). The data is also scaled to utilise the whole range of the short data type (+/- 32767).

Two data reducing steps are performed, which cut down on the number of calculations that need to be carried out. Experimental pre-scans (saturation scans), which ensure that the effects of T₁ recovery have reached a steady state, can be removed from the beginning of the data set. Also the matrix size can be reduced so that it covers only the brain.

Changes in the global blood flow to the brain (gCBF), as well as instability in the scanner hardware, can cause the mean intensity of the images to vary with time, regardless of functional activity. A plot of the mean intensity of an image of a single slice, acquired every 2 seconds is shown in Figure 6.2.

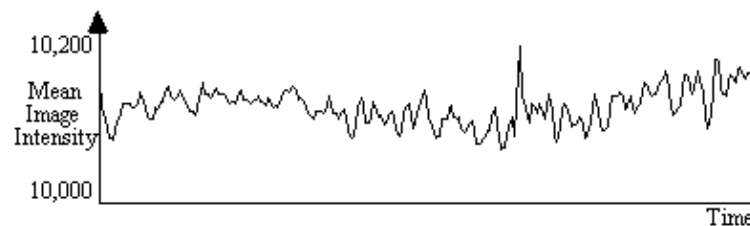


Figure 6.2 Plot of the fluctuations in global intensity of a single slice throughout an fMRI experiment lasting 15 minutes.

Such fluctuations mean that the response to each stimulus is not identical, and reduces the power of any statistical test performed. In order to remove this effect, each image can be scaled so that it has a mean equal to some pre-determined value, or to the global mean of the whole data set. Since there are fluctuations in the intensity of the artefact caused by external r.f. interference, which are independent of the variation in the true image intensity, it is necessary to exclude these regions from the calculation of the image mean. Regions to exclude are chosen by the user, prior to the normalisation.

6.2.2 Motion Correction

Subject head movement, during the experiment is a major source of artefact in fMRI data. Changes in pixel intensity at the edges of the brain, upon even slight movement, can be far greater than the BOLD activation response. It is common therefore in fMRI data analysis to perform some correction which reduces this effect[2].

The approach taken here is to correct only for in-plane translations and rotations of the head within the image. Working on a slice-by-slice basis, the first image is taken to be the reference image, to which all other images of that slice are to be aligned. Two dimensional rotations and translations are applied to the second image, and the sum of the squares of the difference (ssd) between pixels in the first and second image are calculated. Further translations and rotations are applied to the image until the ssd is minimised, using a standard routine. All subsequent images are realigned in the same way.

This technique is quite robust, and does not have difficulty in converging. One obvious extension of this would be to go to a three dimensional technique. This would have the advantage of more fully correcting the head motion, and would also be a faster technique, but introduces the problem of interpolating the data to give isometric voxels. Additional corrections that could be applied include those which remove cardiac and respiratory effects[3], and those which correct for the history of the spins[4].

6.2.3 Spatial Smoothing

Any reduction in the random noise in the image will improve the ability of a statistical technique to detect true activations[5]. Spatially smoothing each of the images improves the signal-to-noise ratio (SNR), but will reduce the resolution in each image, and so a balance must be found between improving the SNR and maintaining the resolution of the functional image.

The simplest form of smoothing to apply is a 9 point filter, such as the one shown below.

1	2	1
2	4	2
1	2	1

If $S(x,y)$ is the image intensity of a pixel at position (x,y) in the image, then upon applying the above filter this pixel will have value

$$S'(x,y) = \frac{S(x,y)}{4} + \frac{S(x-1,y) + S(x+1,y) + S(x,y-1) + S(x,y+1)}{8} + \frac{S(x-1,y-1) + S(x+1,y-1) + S(x-1,y+1) + S(x+1,y+1)}{16} \quad (6.1)$$

Such a filtering technique is simple and quick, but lacks control of the width of the filter. An alternative is to convolve the image with a three dimensional Gaussian function, of the form

$$f(x,y,z) = \exp \left\{ - \left(\frac{x^2}{2s_x^2} + \frac{y^2}{2s_y^2} + \frac{z^2}{2s_z^2} \right) \right\} \quad (6.2)$$

where s_x , s_y and s_z are the standard deviations of the Gaussian in each direction. A good estimate

of the extent of such a smoothing is given by the full width at half maximum (FWHM) of the Gaussian kernel. The relationship between standard deviation and FWHM is

$$\text{FWHM} = 2.35s. \quad (6.3)$$

So to smooth an image of resolution $3 \times 3 \times 5 \text{ mm}^3$ with a Gaussian kernel of FWHM 4 mm, the required parameters are

$$s_x = \frac{4}{2.35 \times 3} = 0.57$$

$$s_y = \frac{4}{2.35 \times 3} = 0.57$$

$$s_z = \frac{4}{2.35 \times 5} = 0.34$$

To carry out the filtering, a smoothing matrix is constructed which is the same size as the image. This image matrix is convolved with the smoothing matrix by Fourier transforming both the image and the filter, with a three dimensional FT. Since fast Fourier transformation (FFT) is considerably faster than a discrete Fourier transform, the image and smoothing matrix are zero filled to the nearest 2^n points in each direction. The smoothing matrix is scaled so that its maximum point is equal to one, ensuring that the image is not scaled out of the range of the short data type used to store the smoothed image. The two transformed matrices are multiplied together and then inverse Fourier transformed back to give the smoothed image. Such a method of convolution would attempt to smooth the opposite edges of the image with each other, and so zero filling is carried out to the next largest 2^n points to prevent this.

There is no straightforward answer to the question of which is the best smoothing width to use in the analysis of the data set. Standard filter theory shows that the best kernel is one which matches the size of the activation region sought. Thus a filter of FWHM of 4 mm would be optimum for regions of this sort of extent, but may reduce the signal from smaller regions (Figure 6.3). A wider filter will reduce the noise to a greater extent, and so a compromise must be reached.

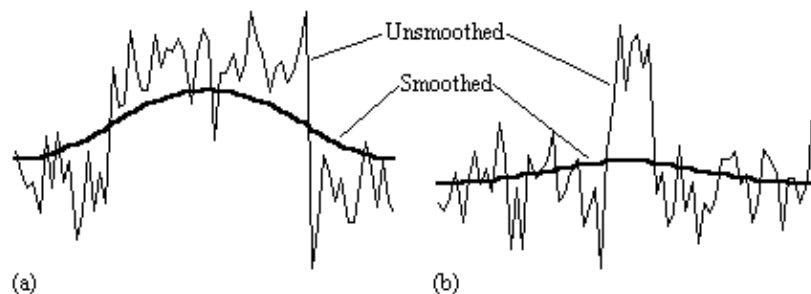


Figure 6.3. The choice of filter width greatly affects the detection of activation. Here two signals are filtered with the same Gaussian kernel. In (a) the width of the activated region is the same as the size of the filter, and smoothing optimises the signal to noise. However in (b) the filter width is greater than the width of the activated region, which barely remains detectable after the smoothing.

In practice, for most purposes a FWHM of 4 mm is suitable, but larger filters may be useful if the signal to noise ratio is particularly bad, and the activation expected to cover a large area, whilst a narrower filter can be used if the SNR is good enough. An example of the use of three different filters in the analysis of the same data set is shown in Figure 6.4.

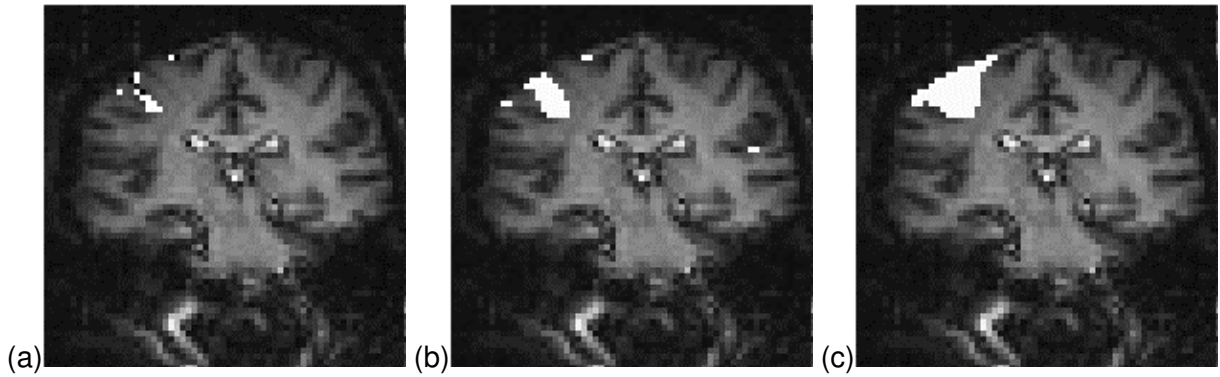


Figure 6.4. The use of three different smoothing filters on the same fMRI data set of a hand clenching experiment, of 3 x 3 mm² in-plane resolution. Areas that correlate well to the task are shaded in white, with the same p-value used for all three activation maps. (a) No filtering applied. (b) 7 mm FWHM filter applied. (c) 15 mm FWHM filter applied.

6.2.4 Temporal Smoothing

As well as smoothing in the spatial domain, improvements in the signal-to-noise ratio can be made by smoothing in the temporal domain. Since the BOLD contrast effect is moderated by blood flow, the rate at which the signal changes, in a genuinely activated region, is limited. Therefore smoothing each pixel's time series with a filter of similar shape will improve the SNR. From our observations, and figures quoted in the literature[6], a Gaussian of width 2.8 seconds, is a good approximation to the haemodynamic response function, and so this is used to smooth the pixel time courses.

As well as removing the high frequency fluctuations from the time series, it can be beneficial to remove any long term drift that may appear in the data. Such drifts can arise from instability in the scanner hardware, and will reduce the power of the statistical technique in detecting activations.

Both types of temporal filtering are carried out in the Fourier domain. First, an appropriate Gaussian vector, with the same length as the time course, is constructed using the function

$$f(t) = \exp\left(\frac{-t^2}{2w^2}\right), \quad (6.4)$$

where w is the width of the Gaussian. This function is Fourier transformed, scaled so that it has a maximum value of one, and the Fourier components from 1 to $n-1$ are set to zero, where n is the number of cycles in the fMRI experiment. This high-pass filtering will remove low frequency variations in the data, without significantly altering signals correlated to the stimulus. For each pixel in the image, the time course is extracted, Fourier transformed, multiplied by the filter, and inverse Fourier transformed. To use the fast Fourier transform technique it is necessary to have a vector of length $2n$. Zero filling can therefore be employed, but it is necessary to subtract the mean from the time course prior to this, to avoid undesirable steps in the data. This mean is added back on to the data after filtering. The effects at the ends of time course must be taken into account, particularly if there is a lot of drift in the data. Figure 6.5 shows an example of a time course taken from a 8 cycle experiment, prior to filtering. Upon filtering, the effects at the edge of the data can be seen. This can reduce the power of the statistical test used, and it might be necessary to exclude the first and last cycles from the statistical analysis.

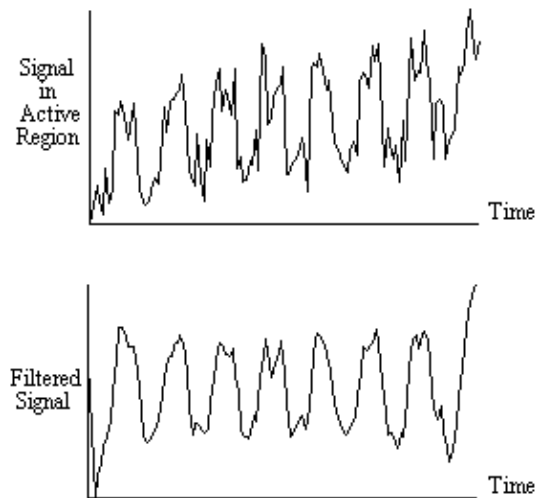


Figure 6.5. If there is a large drift in the time course of the data, then upon filtering, the points at the beginning and the end of the series can be skewed.

Experience has shown that care must be taken in using the temporal filtering, particularly in the way that it affects the independence of the data points, a subject covered later in this chapter. However, the improvement in the detection of activation that results, justifies its use.

6.2.5 Software Implementation

Each of the above pre-processing steps was coded as a separate 'C' program[7], reading in the data from one file, and outputting it to a new file. Each step takes a reasonable amount of time; a few hours for the registration and tens of minutes for the two filtering steps with data sets of a few thousand images. The programs were therefore joined to form a single pre-processing software suite. The programs were rewritten as functions, with the parameters such as file names and matrix sizes being passed from a main routine. Each step still saves its output in a file, but the software automatically deletes the files once they are no longer required, meaning that less disk space is taken up during the processing. The input parameters for the program are read from an initialisation file. This initialisation file is produced by a separate graphical user interface, allowing the main processing to be run in the background on a UNIX workstation, with no terminal input required once the program is started.

The graphical user interface (GUI) is shown in Figure 6.6. It allows the selection of some or all of the steps to be carried out on the data. Upon completion of each step, the file name is appended with a letter, so that the pre-processing that has been carried out on that file can easily be seen. If all the processing steps are carried out the files will be named

- input file <file>.tim
- after image processing <file>.img
- after extracting images <file>.e.img
- after segmenting images <file>.es.img
- after scaling images <file>.esn.img
- after registering images <file>.esnr.img
- after spatial smoothing <file>.esnrf.img
- after temporal filtering <file>.esnrft.img.

For any image files that are created, a header file compatible with the Analyze display software[8], is also created. Other features of the GUI include the ability to start the processing at a later time

specified by the user, and the option to print out the settings used, which can be kept as a record. The GUI was written in 'C', using the *xview*, library routines. The time taken to pre-process fMRI data is significantly reduced using the new software, largely because all the steps can be set off to run in a few minutes, and allowed to run without the need for user interaction, overnight if necessary.

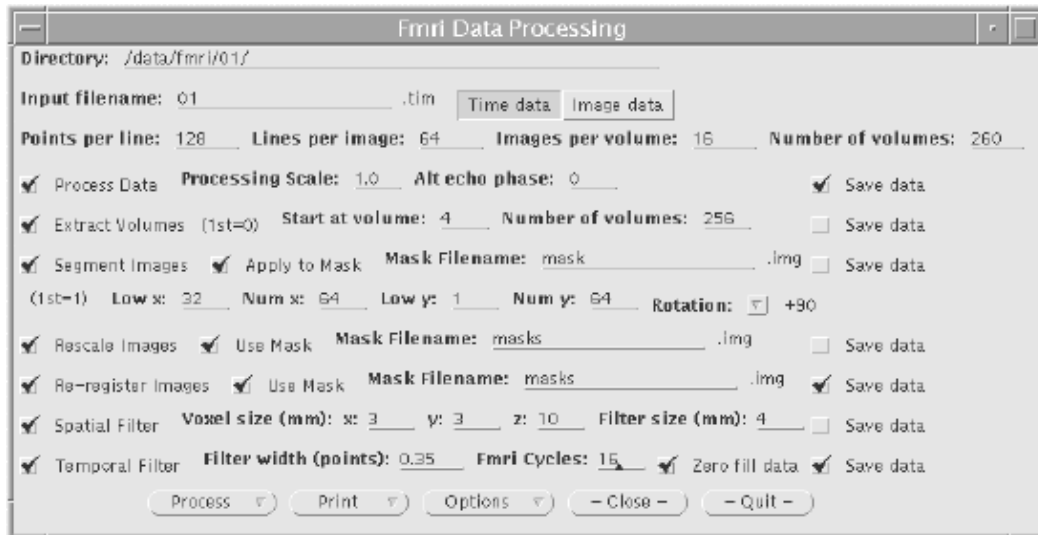


Figure 6.6 The front panel of the graphical user interface for the fMRI data pre-processing package.

The user instructions for the fMRI pre-processing package is included as Appendix B.

6.3 Statistical Analysis of the Data

Many techniques have been proposed for statistically analysing fMRI data, and a variety of these are in general use. The aim of such analysis is to produce an image identifying the regions which show significant signal change in response to the task. Each pixel is assigned a value dependent on the likelihood of the null hypothesis, that the observed signal changes can be explained purely by random variation in the data consistent with its variance, being false. Such an image is called a statistical parametric map. The aim of this section is to show how such maps can be produced.

All the methods described below have been used, at one time or another, in the analysis of the data presented in this thesis. The majority have been implemented as 'C' programs, with the notable exception of using the *SPM*[10] implementation of the general linear model.

Throughout this section, the analysis techniques described are demonstrated on an example data set. The experiment performed was intended to detect activations resulting from a visually cued motor task. The whole brain of the subject was imaged, in 16 coronal slices of resolution 3 x 3 x 10 mm³, every four seconds. As cued by an LED display, they were required to squeeze a ball at the rate of 2 Hz. The experiment involved 16 s of rest, followed by 16 s of task performance, repeated 32 times.

Further detail of the statistics mentioned in this chapter can be found in many statistics text books, for example those by Zar[11], and Miller and Freund[12].

6.3.1 Subtraction Techniques

One of the simplest methods for obtaining results from a two state fMRI experiment is to perform a simple subtraction. This is carried out by averaging together all the images acquired during the 'on' phase of the task, and subtracting the average of all the 'off' images. The disadvantage of such a technique is that it is extremely sensitive to head motion, leading to large amounts of artefact in the image. Figure 6.7a shows a single slice through the motor cortex from the example data set, and Figure 6.7b shows the result of subtracting the 'off' images from the 'on' images. Although signal increase can be seen in the primary motor cortex, there is also a large amount of artefact, particularly at the boundaries in the image.

Such a method does not yield a statistic that can be tested against the null hypothesis, so instead of straight subtraction it is more common to use a Student's t-test. This weights the difference in means, by the standard deviation in 'off' or 'on' values, giving high t-scores to large differences with small standard deviations, and low t-scores to small differences with large standard deviations. The t-score is calculated on a pixel by pixel basis, for a time series X, using the formula

$$t = \frac{\bar{X}_1 - \bar{X}_2}{s_{\bar{x}_1 - \bar{x}_2}} \quad (6.5)$$

where

$$s_{\bar{x}_1 - \bar{x}_2} = \sqrt{\frac{s_p^2}{n_1} + \frac{s_p^2}{n_2}} \quad (6.6)$$

and s_p^2 is the pooled variance

$$s_p^2 = \frac{\sum (X_1 - \bar{X}_1)^2 + \sum (X_2 - \bar{X}_2)^2}{n_1 + n_2 - 2} \quad (6.7)$$

The suffix '1' refers to the n_1 images acquired during the 'on' period of the task, and '2' refers to the n_2 images acquired during the rest period. Figure 6.7c shows the statistical parametric map of t-scores for the sample data set. Again motor cortex activation is clearly seen, but the movement artefact is reduced compared to the subtraction technique.

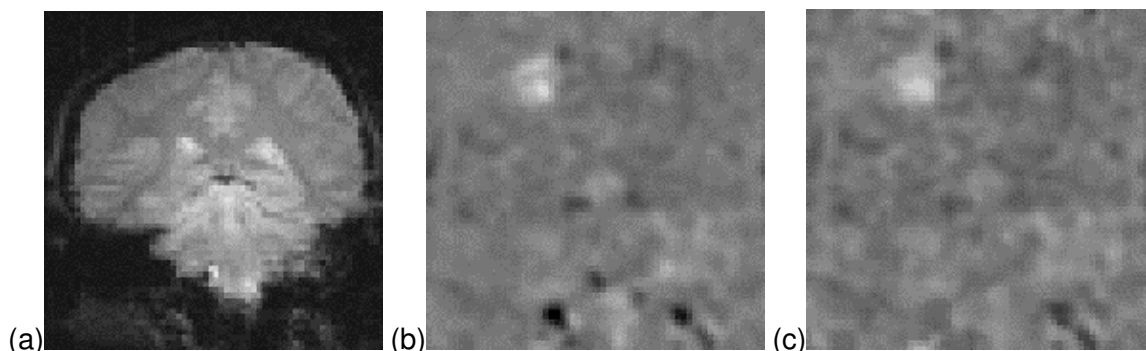


Figure 6.7 Use of subtraction techniques to analyse fMRI data. (a) A single slice coronal EPI image through the primary motor cortex. (b) The mean of the images acquired during the 'off' period of the fMRI experiment subtracted from the mean of the images acquired during the 'on' period. (c) The t-statistical parametric map corresponding to image (b).

6.3.2 Correlation techniques

Since we know that the BOLD response is mediated by blood flow, it is possible to improve the detection of activations by predicting the shape of the response to the stimulus, and calculating correlation coefficients between each pixel time course and this reference waveform. This is less sensitive to other physiological changes during the experiment, and to movement. For a time course X , and a reference waveform Y , the correlation coefficient is calculated as

$$r = \frac{\sum(X - \bar{X})(Y - \bar{Y})}{\sqrt{\sum(X - \bar{X})^2 \sum(Y - \bar{Y})^2}}, \quad (6.8)$$

and has a value of 1 for perfect correlation, a value of zero for no correlation, and a value of -1 for perfect anti-correlation.

The choice of an appropriate reference waveform is vital for the success of this technique in finding activations. The first approximation might be a square wave, which is high for scans acquired during the task, and low for scans acquired during rest (Figure 6.8a). Such a waveform however takes no account of the delay and smoothness of the haemodynamic response which regulates the BOLD contrast. An improvement to this would be to change the phase of the square wave (Figure 6.8b), with the delay being between 3 and 6 seconds.

To improve the reference waveform further, it is necessary to look more closely at the actual haemodynamic response. In an experiment such as the one used for the example data set, where there is both visual and motor activation, it is possible to use the response to one type of stimulus to form the reference waveform for finding the other. In this case the time series for one or more pixels in, say the visual cortex is extracted (Figure 6.8c), and correlation coefficients are calculated between this waveform and that of every other pixel in the image. Such an analysis detects only those regions in the brain which respond to the stimulus in the same way as the visual cortex. The major disadvantage of this technique is that it is particularly sensitive to motion artefact, since if such artefact is present in the reference waveform then the movement of other regions will be highly correlated. To attempt to reduce this, the response in the visual cortex to each stimulus can be averaged together, producing a mean response to the single cycle. The reference waveform is then made up of a repetition of these single cycle average responses (Figure 6.8d).

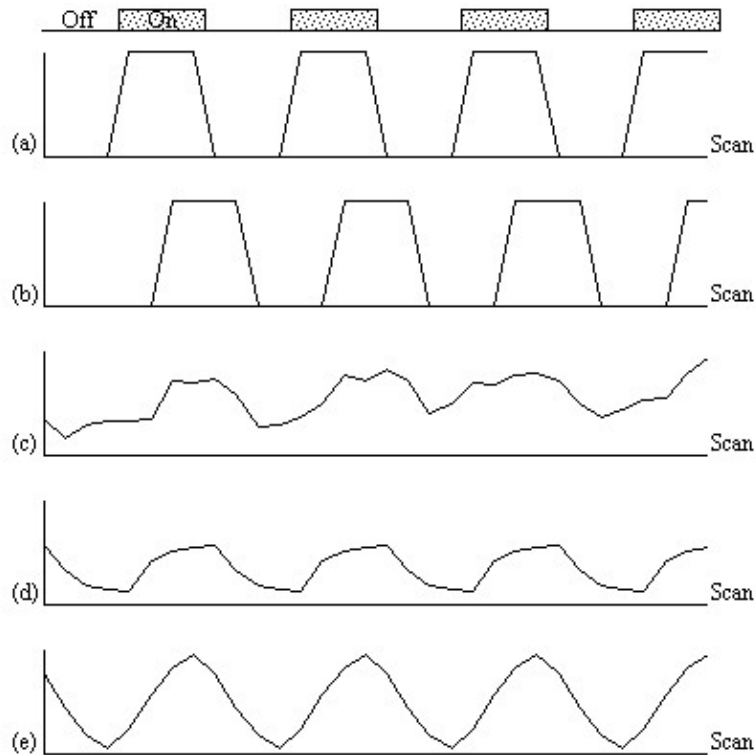


Figure 6.8. Various reference functions that can be used to correlate with a pixel time course to detect activations (see text for descriptions)

To be more general in predicting the haemodynamic response, so that a reference waveform can be constructed for any length of stimulus, it is necessary to know the response to a single stimulus. Friston[13] suggested that a haemodynamic response function could be considered as a point spread function, which smoothes and shifts the input function. By deconvolving the response from a known area of activation with the stimulus function, the haemodynamic response function can be obtained. The haemodynamic response function is not completely uniform across the entire brain however, and the shape obtained from one region may not be optimum for another. As an alternative, the response can be modelled by a mathematical function, such as a Poisson or beta function. The Poisson function

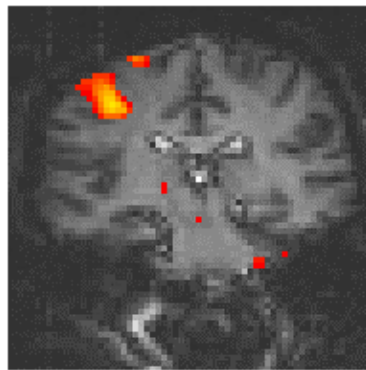
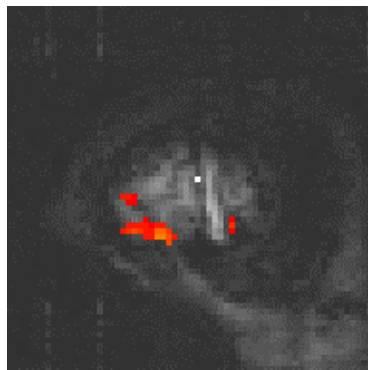
$$f(x) = \frac{\lambda^x e^{-\lambda}}{x!} \quad (6.9)$$

with width $\lambda = 6$ seconds, seems to fit well to observed haemodynamic responses (Figure 6.8e).

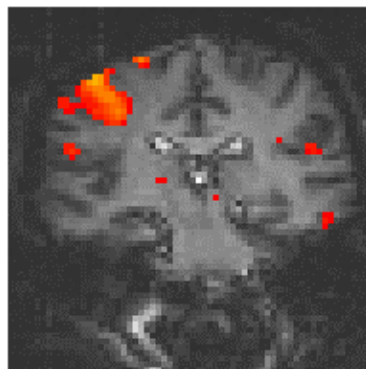
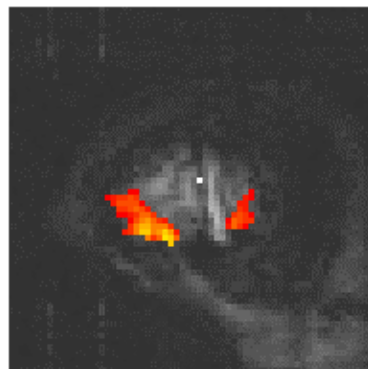
Since in general each slice of the volume imaged is not acquired at the same instant, it is necessary to accommodate timing differences in the correlation with the reference waveform. In order to do this, the relative magnitude of the activation at the time each slice was acquired is predicted, by convolving the input stimulus with a Poisson function. Then from this series, the correlation coefficients can be calculated on a slice by slice basis, constructing the reference waveform from the appropriate points in the predicted time series.

Examples of the effect of the reference waveform on the result is shown in Figure 6.9. Here, pixels in the head which correlate to the reference waveforms (shown in Figure 6.8), with $r > 0.20$ are shown in red, on top of the base image. The square wave correlation is the least effective in detecting activations (a), however a considerable improvement is obtained by delaying the waveform by 4 seconds (b). The correlation of the visual cortex with itself (c) is, not surprisingly,

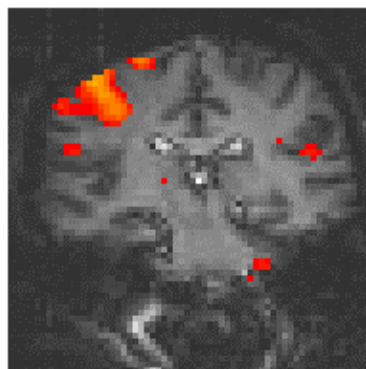
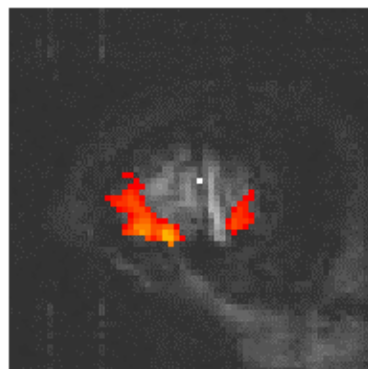
high, but using the average visual cortex response (d) improves the correlation in the motor cortex. The Poisson function model of the haemodynamic response (e) improves slightly on the delayed square wave, and is a good model.



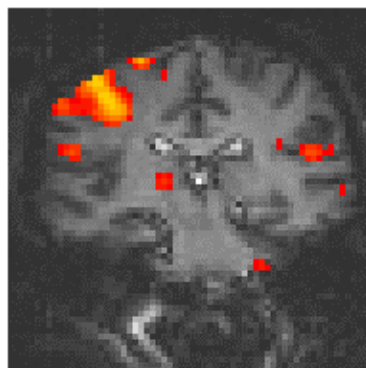
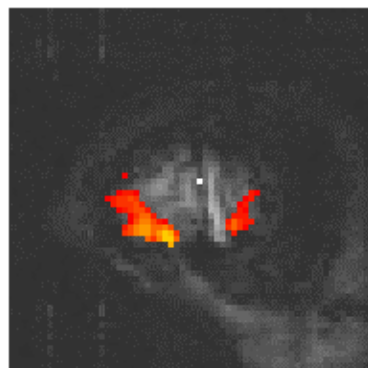
(a) Square wave



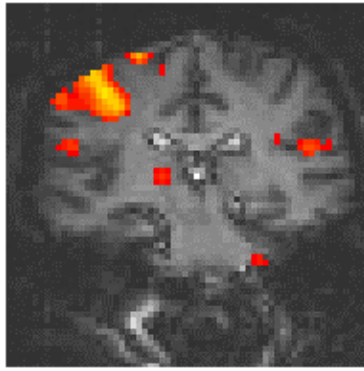
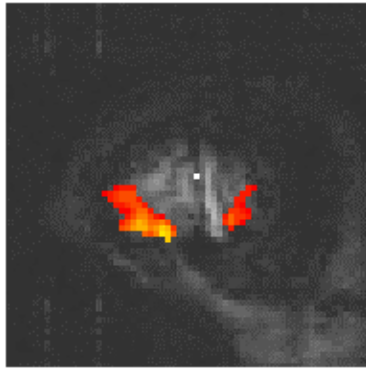
(b) Delayed Square Wave



(c) Visual Cortex Response



(d) Average Visual Cortex Response



(e) Poisson Distribution Model

Figure 6.9 Activation images obtained by correlating the test data sets with the reference waveforms shown in Figure 6.8.

6.3.3 The General Linear Model

The statistical techniques described above are both parametric tests. That is to say, they assume that the observations are taken from normal populations. Most parametric modelling techniques are special cases of the general linear model. This framework for analysing functional imaging data, first developed for PET and then extended for fMRI, is implemented in the software package *SPM*[14]. The general linear model is only outlined here, since the theory is extensively covered in the literature[15].

The aim of the general linear model is to explain the variation of the time course $y_1 \dots y_i \dots y_n$, in terms of a linear combination of explanatory variables and an error term. For a simple model with only one explanatory variable $x_1 \dots x_i \dots x_n$, the general linear model can be written

$$y_i = x_i \beta + \varepsilon_i \quad (6.10)$$

where b is the scaling, or slope parameter, and e_i is the error term. If the model includes more variables it is convenient to write the general linear model in matrix form

$$\mathbf{Y} = \mathbf{X}\boldsymbol{\beta} + \boldsymbol{\varepsilon}, \quad (6.11)$$

where now \mathbf{Y} is the vector of observed pixel values, \mathbf{b} is the vector of parameters and \mathbf{e} is the vector of error terms. The matrix \mathbf{X} is known as the design matrix. It has one row for every time point in the original data, and one column for every explanatory variable in the model. In analysing an fMRI experiment, the columns of \mathbf{X} contain vectors corresponding to the 'on' and 'off' elements of the stimulus presented. By finding the magnitude of the parameter in \mathbf{b} corresponding to these vectors, the presence or absence of activation can be detected.

\mathbf{b} can be determined by solving the 'normal equations'

$$\mathbf{X}^T \mathbf{Y} = (\mathbf{X}^T \mathbf{X}) \hat{\boldsymbol{\beta}} \quad (6.12)$$

where $\hat{\boldsymbol{\beta}}$ is the best linear estimate of \mathbf{b} . Provided that $(\mathbf{X}^T \mathbf{X})$ is invertible then $\hat{\boldsymbol{\beta}}$ is given by

$$\hat{\boldsymbol{\beta}} = (\mathbf{X}^T \mathbf{X})^{-1} \mathbf{X}^T \mathbf{Y}. \quad (6.13)$$

Such parameter estimates are normally distributed, and since the error term can be determined, statistical inference can be made as to whether the \mathbf{b} parameter corresponding to the model of an activation response is significantly different from the null hypothesis.

The general linear model provides a framework for most kinds of modelling of the data, and can eliminate effects that may confound the analysis, such as drift or respiration, provided that they can be modelled.

6.3.4 The Serial T-Test

All the techniques described above require the prediction of the time course that active regions will follow. For many experiments, the use of rapid imaging, and carefully designed paradigms, makes the separation of the order of cognitive events possible. One such example, which is part of our study of Parkinson's disease and described in more detail in Chapter 7, is a paradigm involving the initiation of movement. In this experiment, the subject was required to respond, by pressing a hand held button, to the visual presentation of the number '5', and to make no response to the presentation of a '2'. This paradigm presented two differences to conventional, epoch based experiments. Firstly, the activations of interest, which are those responsible for the button pressing, occurred at an irregular rate. Secondly, all the cognitive processes involved in the task, including both the planning and execution of the movement, occurred in a time period of a few hundred milliseconds, as opposed to the sustained activation used in epoch based paradigms. Such an experiment requires a new form of analysis. Two techniques have been evaluated, both of which make no assumptions about the time course of activations during the task: the serial t-test, described here, and an analysis of variance technique, explained in the next section.

The basis of the serial t-test is to define a resting state baseline, and compare the images acquired at each time point before, during and after the task with this baseline. Figure 6.10 illustrates the technique. For each time point following the stimulus, a mean and standard deviation image is constructed, as is a baseline mean and standard deviation image. Then a set of t-statistical parametric maps are formed by calculating, on a pixel by pixel basis, the t-score (using equations 6.5 - 6.7) for the difference between mean image one and the mean baseline image, mean image two and baseline, and so on.

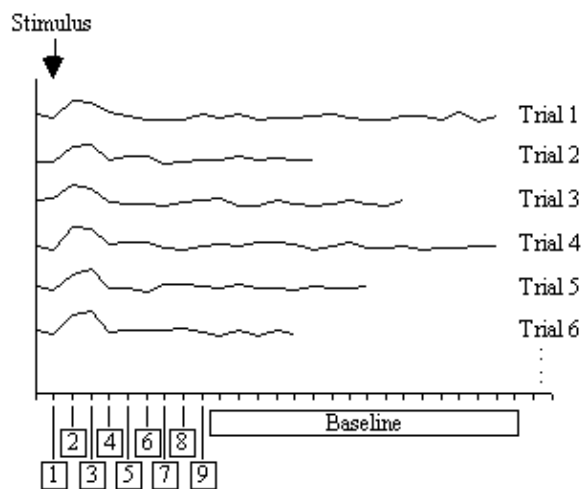


Figure 6.10. fMRI analysis using the serial t-test

Figure 6.11 shows the result of analysing the example data set using this technique. Such a data set does not really show the benefit of the serial t-test analysis. Results shown in Chapter 7 better illustrate its use in looking at event timings, and unpredictable waveforms.

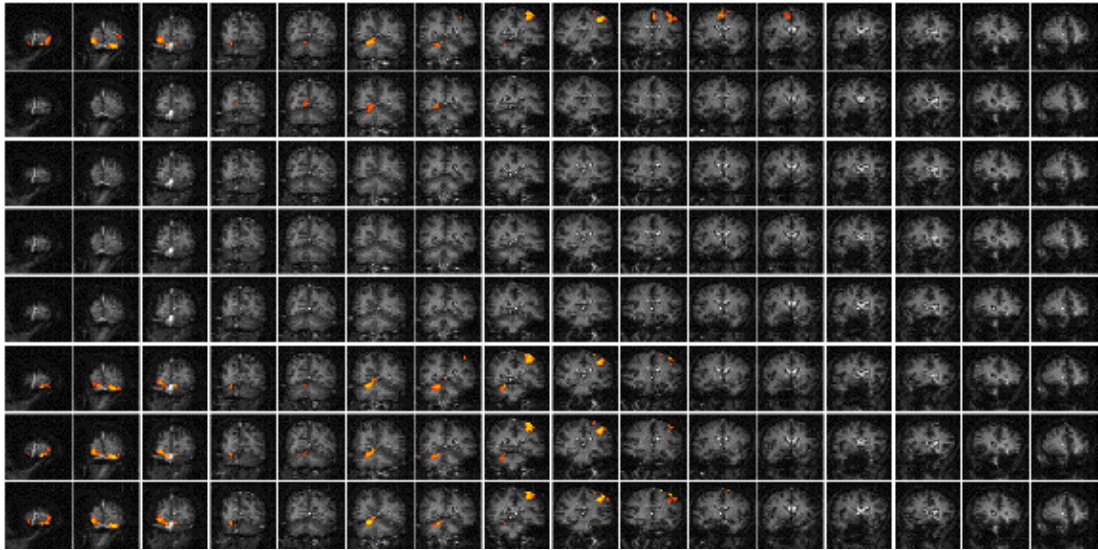


Figure 6.11 Results of processing the test data set using the serial t-test. Eight volume image sets are shown as rows, the top four corresponding to the 'rest' periods of the experiment, and the next four corresponding to the 'task' periods. Activation can be seen in both the primary motor and visual cortices.

The technique has two major disadvantages. The first is that, in order to achieve a sufficient signal to noise ratio, it is necessary to have many more cycles than in an epoch based paradigm, thus leading to longer experiments. This can be uncomfortable for the subject, and puts additional demands on the scanner hardware. There is some scope for bringing the single event tasks closer together, but there must be a sufficient interval to allow the BOLD signal to return to baseline. This delay is at least ten seconds in length. The second disadvantage is that the analysis results in many statistical parametric maps, which have to be interpreted as a whole. However the fact that the technique makes few assumptions about the data time course makes it a strong technique, and opens up the possibility of more diverse experimental design, and a move away from the epoch based paradigms.

6.3.5 Analysis of Variance

A second technique which does not require any assumptions about the shape of the activation time course, looks at the changes in variance upon averaging. The technique is based on simple signal averaging theory[16]. Take, for example, the response measured to a repeated signal as shown in Figure 6.12. The time series contains two components, one is a genuine response to the signal, and the other is the random fluctuations due to uncorrelated physiological events and noise in the image. Upon averaging 32 cycles together, the magnitude of the noisy component is reduced but that of the repeated signal is not. The reduction of the noisy component can be measured by calculating the variance of both the unaveraged and averaged data set.

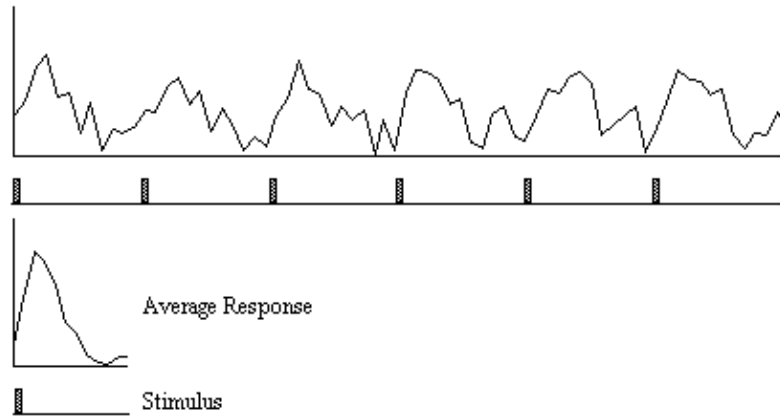


Figure 6.12. Signal Averaging. The variance of the noise in the average signal is N times less than it is in the original signal, where N is the number of cycles.

To detect regions of activation, the ratio of the variance of the averaged data set to the variance of the unaveraged data set is calculated for each pixel in the image. For pixels in regions of purely random intensity variations, this ratio will be around $1/n$, where n is the number of cycles averaged together. Pixels in regions of activation, however, will have a significantly higher ratio than this, since the variance of both unaveraged and averaged data sets is dominated by the stimulus locked intensity variations of the BOLD effect, which does not reduce upon averaging.

The technique is more formally explained as an analysis of variance (ANOVA)[17]. If X_{ij} refers to the i th time point after the stimulus, of the j th cycle of an experiment

time t	$X_{11}, X_{12}, \dots, X_{1j}, \dots, X_{1n}$	\mathbf{X}_1
time $2t$	$X_{21}, X_{22}, \dots, X_{2j}, \dots, X_{2n}$	\mathbf{X}_2
.....
time it	$X_{i1}, X_{i2}, \dots, X_{ij}, \dots, X_{in}$	\mathbf{X}_i
.....
time kt	$X_{k1}, X_{k2}, \dots, X_{kj}, \dots, X_{kn}$	\mathbf{X}_k
		\mathbf{X}

with n cycles and k points per cycle. The null hypothesis is that there is no significant difference in the means, \bar{X}_i . This can be tested by comparing two estimates of the population variance, s^2 , one based on variations in measurements of the same time point, and one based on the variance between time points.

The variance within measurement of any time point can be calculated by

$$s_i^2 = \sum_{j=1}^n \frac{(X_{ij} - \bar{X}_i)^2}{n-1}, \quad (6.14)$$

and so the mean variance within time points is given by

$$\hat{\sigma}_W^2 = \sum_{i=1}^k \frac{s_i^2}{k} = \sum_{i=1}^k \sum_{j=1}^n \frac{(X_{ij} - \bar{X}_i)^2}{k(n-1)}, \quad (6.15)$$

and is based on $k(n-1)$ degrees of freedom. The variance of the time point means is given by

$$s_{\bar{x}}^2 = \sum_{i=1}^k \frac{(\bar{X}_i - \bar{X})^2}{k-1}, \quad (6.16)$$

and since

$$\sigma_{\bar{x}}^2 = \frac{\sigma^2}{n} \quad (6.17)$$

then s_2 can be estimated by

$$\hat{\sigma}_B^2 = n \cdot s_{\bar{x}}^2 = n \cdot \sum_{i=1}^k \frac{(\bar{X}_i - \bar{X})^2}{k-1} \quad (6.18)$$

which is based on $k-1$ degrees of freedom. Under the null hypothesis, both $\hat{\sigma}_W^2$ and $\hat{\sigma}_B^2$ independently estimate the population variance s_2 . This means that the ratio

$$F = \frac{\hat{\sigma}_B^2}{\hat{\sigma}_W^2} \quad (6.19)$$

will have an F distribution with $k-1$ and $k(n-1)$ degrees of freedom. If there is any signal change that is time locked to the stimulus, the value of $\hat{\sigma}_B^2$ will be larger than expected under the null hypothesis.

In the analysis of fMRI data, equations 6.15 - 6.19 are used to form an F-statistical parametric map. These equations are implemented using the following short-cut formulas

$$\begin{aligned} F &= \frac{SS_B/(k-1)}{SSE/k(n-1)} \\ SSE &= SST - SS_B \\ SST &= \sum_{i=1}^k \sum_{j=1}^n X_{ij}^2 - \frac{T^2}{kn} \\ SS_B &= \frac{\sum_{i=1}^k T_i^2}{n} - \frac{T^2}{kn} \\ T_i &= \sum_{j=1}^n X_{ij} \quad T = \sum_{i=1}^k T_i \end{aligned} \quad (6.20)$$

To assess the validity of this approach on real data, phantom and head images were analysed. The phantom data set consisted of 256 volume images, each of 128 x 128 x 16 matrix size, obtained at a repetition rate of 4 seconds. The head data set consisted of 256 head images, of the same matrix size, with the subject performing no specified task. Both data sets were pre-processed in the same way that a functional imaging data set would be, and the analysis of variance was then carried out assuming 16 points per cycle and 16 cycles. Histograms of F for each data set are shown in Figure 6.13, with the appropriate F distribution, shown as a dotted line, given by

$$h(F) = \frac{\Gamma((s_1 + s_2)/2)}{\Gamma(s_1/2)\Gamma(s_2/2)} \left(\frac{s_1}{s_2}\right)^{\frac{s_1}{2}} \frac{F^{\frac{s_1-2}{2}}}{\left(1 + \frac{s_1 F}{s_2}\right)^{\frac{s_1+s_2}{2}}} \quad F > 0 \quad (6.21)$$

where m_1 is the number of points per cycle minus one, and m_2 is the total number of data points minus the number of points per cycle[18]. All three histograms show a good fit to the F distribution, confirming the validity of applying this technique to fMRI data.

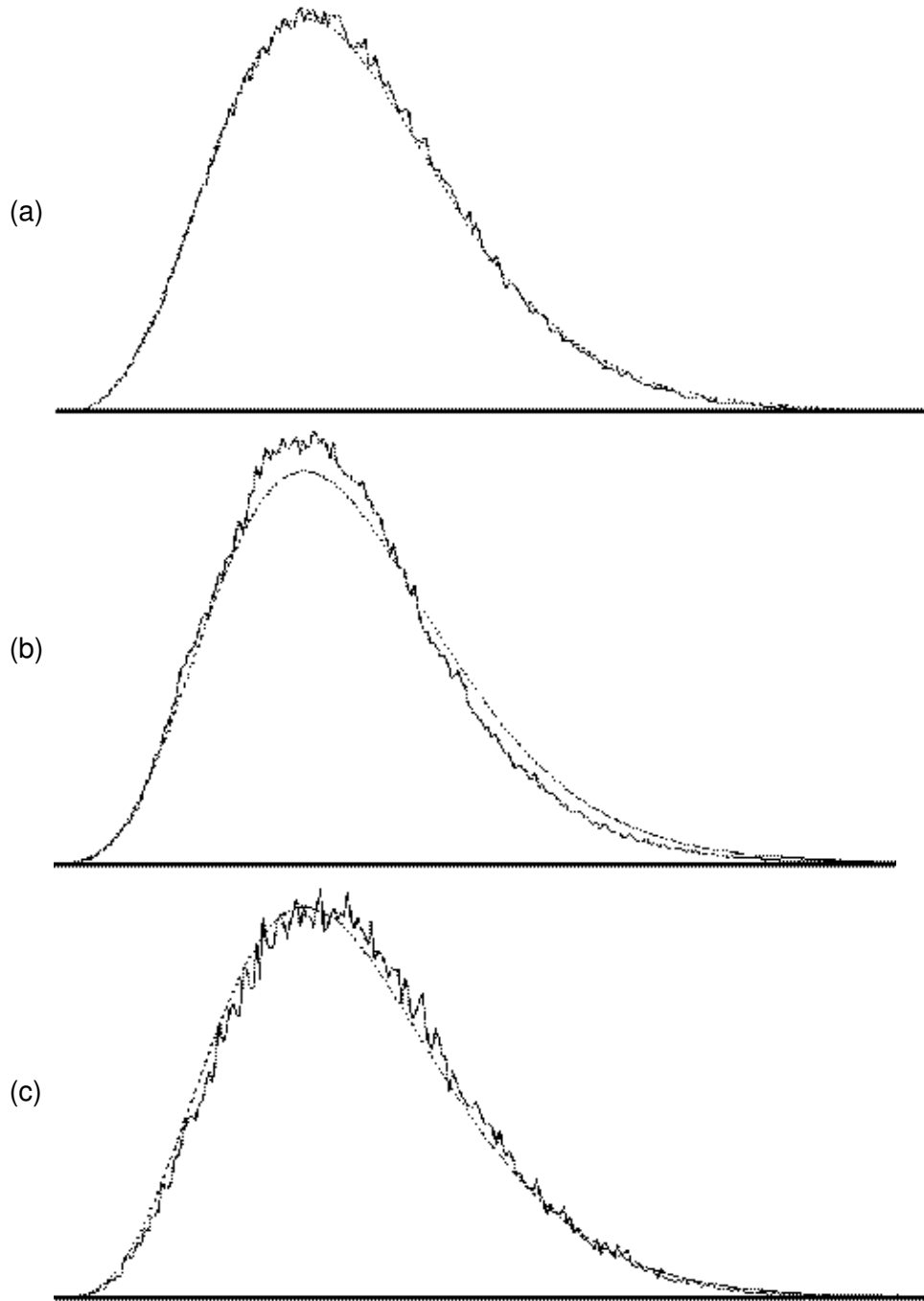


Figure 6.13 Plots of calculated F-scores (solid line) and the appropriate F-distribution (dotted line) for (a) simulated data, (b) phantom data, and (c) head data.

The results of analysing the example activation data set using the ANOVA technique are shown in Figure 6.14. As with the serial t-test, such a data set does not best show the potential of this technique. A better example comes from the analysis of a study to investigate short term memory.

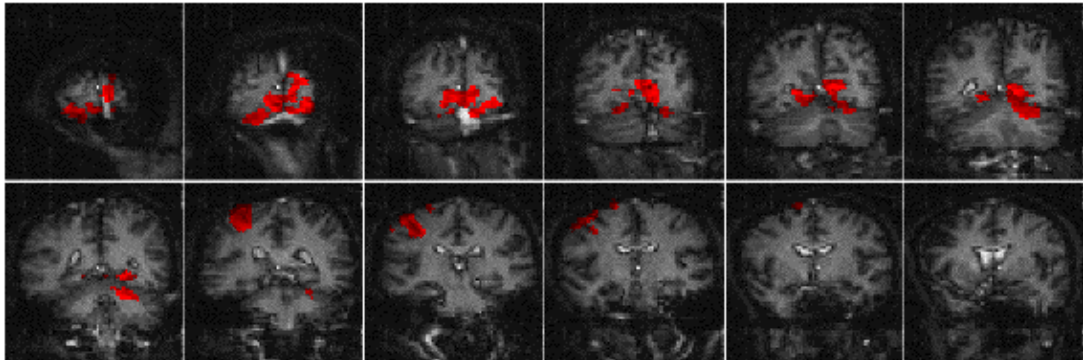
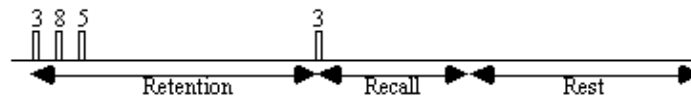


Figure 6.14 Results of processing the test data set using the analysis of variance technique. Those pixels shaded in red correspond to regions which vary in some way that is time locked to the stimulus.

The stimulus paradigm for this experiment had three stages. First three digits in succession were presented to the subject. Eight seconds later a fourth digit was presented, and the subject was required to respond by pressing a button in their right hand if this final digit was the same as any of the three previously presented, or by pressing the button in their left hand if not[19]. The final stage was a period of rest, to provide a baseline. The whole test was repeated 32 times.



It would be expected that some regions of the brain would only be active during the presentation of the digits, some during the retention period, some only in the recall stage and others throughout the whole memory task. To analyse such data using a correlation technique would mean predicting a whole set of reference waveforms. The ANOVA technique, however, detected the responses of different shapes in one test. Figure 6.15 shows the activation maps obtained from the ANOVA analysis of the short term memory experiment, together with time course plots from several of the areas.

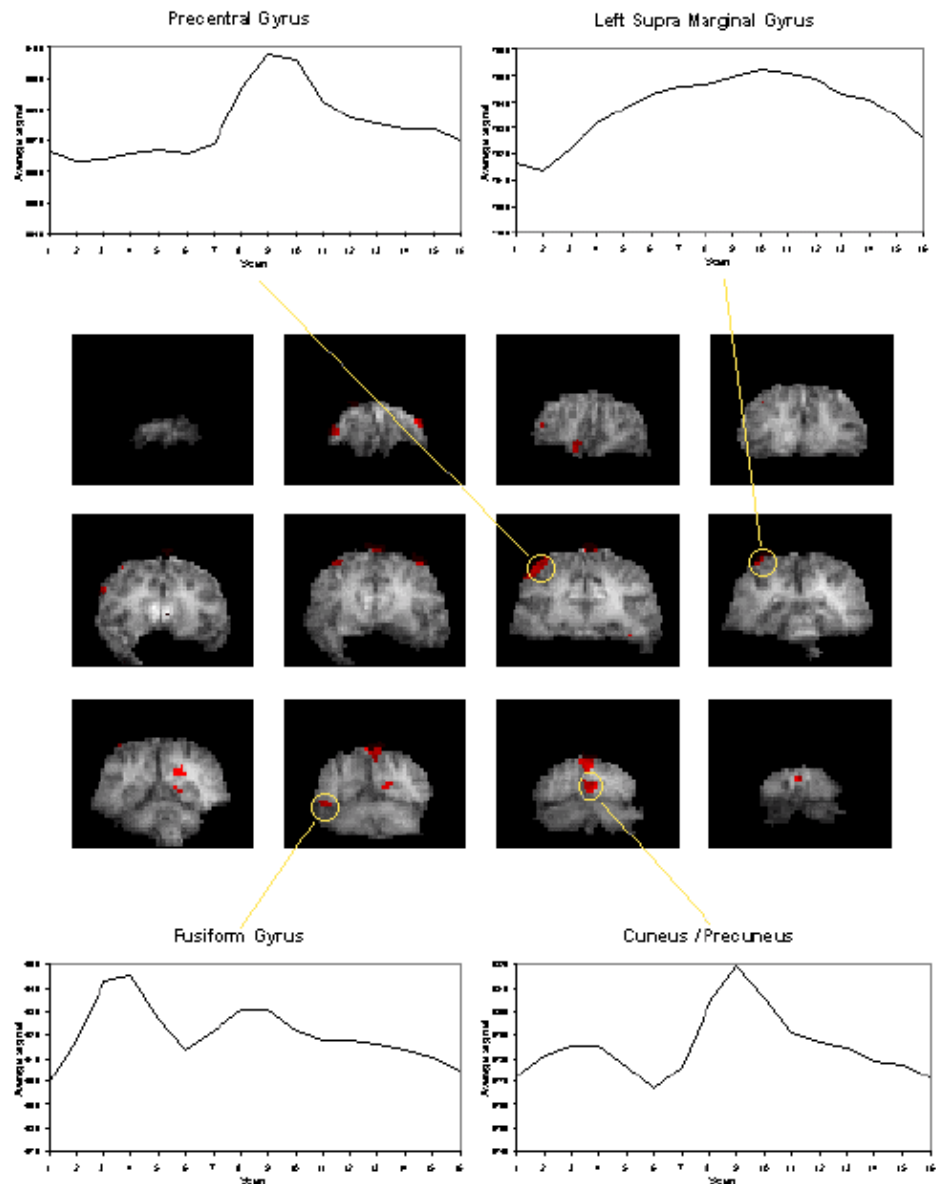


Figure 6.15 Analysis of Variance technique applied to data from the short term memory experiment described in the text, together with average cycle plots for several regions of interest. Areas of the brain which act in different ways to the stimulus can be seen in a single activation image.

The final image of an ANOVA analysis, essentially shows all the regions which vary in some way that is synchronous to the presentation of the stimulus. It is equally good at picking up deactivations as activations. This makes these images a good starting point for other forms of analysis, such as principal component analysis or cluster analysis, so as to glean all the information that is available.

6.3.6 Software Implementation

Due to the diversity of tests that can be carried out on one data set, software for implementing the tests described above was written as a set of separate programs.

The program *correlate* constructs a reference waveform, from user specified values, and optionally convolves this with a Poisson function of user specified width. Correlation coefficients are calculated using equation 6.8. If the reference waveform is made to vary between 0 and 1 then a measure of the percentage change upon activation can be obtained by calculating a linear regression of the

form

$$X = a + bY$$

where

$$b = \frac{\sum(X - \bar{X})(Y - \bar{Y})}{\sum(Y - \bar{Y})^2} \quad (6.22)$$

and

$$a = \bar{X} - b\bar{Y}.$$

The percentage change can be calculated as $(b/a) \times 100\%$.

The software also calculates the appropriate image of z-scores using Fishers Z transform and the reduced degrees of freedom as explained in the following sections. The file names for each of these outputs is

cc_<file>.img correlation coefficients saved as 'shorts' x 10,000

pc_<file>.img percentage change saved as 'shorts' x 1,000 (such that 1% signal change x 1,000)

cz_<file>.img z-scores saved as 'floats' (not scaled)

The serial t-tests are performed by *tmap* and *tmapnc*, the first appropriate for cyclic experiments and the second for non-cyclic experiments. For the non-cyclic version the stimulus times are obtained from a text file, and both output t-score maps saved as 'shorts', scaled by 1000, in a file named tt_<file>.img.

ANOVA tests are carried out by the programs *anova*, and *anovanc*, which both output f-scores scaled by 1000, in a file named va_<file>.img.

6.4 Statistical Inference

The statistical analysis techniques discussed in the last section all result in a statistical parametric map (SPM), where each pixel in the image is assigned a value based on the likelihood that the null hypothesis is false. However for the localisation and comparison of brain function, what is required is an image which only highlights those pixels which can confidently be labelled as active. This is done by thresholding the statistical parametric map.

6.4.1 Confidence levels for T-scores, Correlation Coefficients and F-scores

Before approaching the problem of the significance of whole images, it is necessary to consider the question of the confidence that can be placed in the result of a single t-test, correlation or ANOVA. Such levels come from an understanding of the distribution, under the null hypothesis, of the statistic being considered. If for example a statistic had a normal distribution, as shown in Figure 6.16, a critical value Z_α can be defined such that

$$\int_{Z_\alpha}^{\infty} F(Z) dZ = \alpha \int_{-\infty}^{\infty} F(Z) dZ \quad (6.23)$$

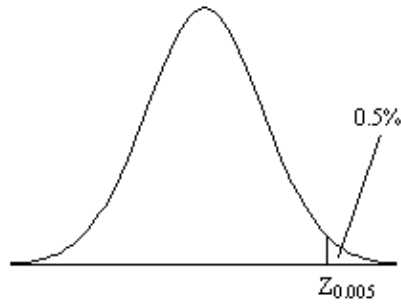


Figure 6.16. The area under a normal distribution between $Z_{0.005}$ and Z_{inf} is 0.5% that of the total area under the curve.

This means that if the value of Z obtained in the statistical calculation is greater than $Z_{0.005}$, we can be 99.5% confident the null hypothesis is false. The number 0.005 in such a case is said to be the p-value for that particular test. Such values are tabulated in standard statistical texts, or can be obtained directly from expressions for the distributions themselves.

The distribution for a correlation coefficient is dependent on the number of degrees of freedom in the time course being analysed. For a time course of n independent time points, there are $n-2$ degrees of freedom. The question of whether time points from an fMRI experiment are independent is addressed later in this section. The correlation coefficient, r , can be transformed so that it has a Z distribution (that is a Gaussian distribution with zero mean and unit variance), by applying the Fisher Z transform

$$z = \frac{\sqrt{n-3}}{2} \cdot \ln \frac{1+r}{1-r} \quad (6.24)$$

This transform may therefore be applied to the SPM of correlation coefficients, yielding an SPM of z scores.

The theory of Gaussian random fields (as described later, in section 6.4.3), applies to images of z scores. Therefore it is necessary to transform the t and f scores to z scores as well. This is done by calculating the area under the distribution (p value) between t and infinity (or f and infinity), and choosing an appropriate value of z such that the area under the Z distribution between z and infinity is the same.

P-values for the t -statistic are related to the incomplete beta function

$$I_x(\alpha, \beta) = \frac{\Gamma(\alpha + \beta)}{\Gamma(\alpha) \Gamma(\beta)} \int_0^x t^{\alpha-1} (1-t)^{\beta-1} dt \quad (6.25)$$

such that

$$p(t > T) = 1 - I_{\frac{v}{v+T^2}} \left(\frac{v}{2}, \frac{1}{2} \right) \quad (6.26)$$

where n is the number of degrees of freedom, which is equal to the number of data points that were used to construct the statistic minus one.

Similarly p-values for the f -statistic can be derived from

$$p(f > F) = I_{\frac{v_1}{v_1 + v_2 F}} \left(\frac{v_1}{2}, \frac{v_2}{2} \right) \quad (6.27)$$

where n_1 is the number of points per cycles minus one and n_2 is the total number of points minus the number of points per cycle ($n_1=k-1$, $n_2=k(n-1)$).

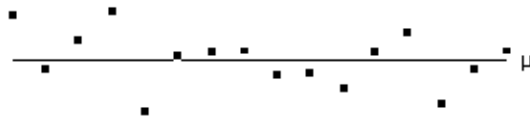
The transforms are carried out using pre defined functions in the package MATLAB[20], to calculate the incomplete beta function and the inverse error function.

6.4.2 The Effect of Temporal Smoothing on Degrees of Freedom

All the statistical tests assume that the data points are independent samples of the underlying population. This however may not be the case, since the effect of the haemodynamic response function, and any temporal smoothing that is applied to the data, means that adjacent time points are no longer independent. This has an effect on the effective number of degrees of freedom in the sample.

A detailed analysis of this problem is given in by Friston *et. al.*[21-23], but a more intuitive explanation of his result is given here.

Consider a series of n independent observations of a population of mean m .



The variance of the population is given by

$$\sigma^2 = \frac{\sum (X_i - \mu)^2}{N} \quad (6.28)$$

which is best estimated by the sample variance

$$s^2 = \frac{\sum (X_i - \bar{X})^2}{n - 1} \quad (6.29)$$

The denominator in this expression is the number of degrees of freedom of the sample, and is one less than the number of observations, since only $n-1$ points are needed to describe the sample, the 'last' point being determined by the mean.

Now if the above data set is smoothed with a three point running filter such that

$$X_n = (X_{n-1} + X_n + X_{n+1})/3$$

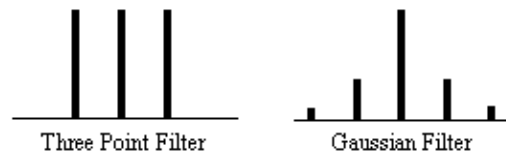


The sum of the square deviations from the mean of the data is now (on average) three times less than that of the unsmoothed data. This means that the population variance is now best

approximated by

$$s^2 = \frac{\sum (X_i - \bar{X})^2}{(n-1)/3} \quad (6.30)$$

and implying that the smoothed data set has $(n-1)/3$ degrees of freedom. In the case of the pre-processing described above, the smoothing filter is a Gaussian kernel, as opposed to the three point running average.



In this case it is necessary to evaluate the effect of neighbouring data points on any one point, and so the reduction in the number of degrees of freedom is given by the area under the Gaussian kernel. The number of degrees of freedom in the sample variance for a data set of n sample points, smoothed with a Gaussian of standard deviation s is therefore

$$s = \frac{(n-1)}{\sqrt{2} \pi s^2} \quad (6.31)$$

Simulations of the effect of smoothing data before carrying out an analysis of variance calculation show that such a degrees of freedom reduction does not hold in this case. Temporal smoothing of the data is unlikely to improve the ability of the ANOVA test to detect activations, and is therefore best not applied, however high pass filtering is likely to improve the test and should still be used.

A summary of the number of degrees of freedom for the tests described earlier is given below.

6.4.3 The Multiple Comparisons Problem and the Theory of Gaussian Random Fields

All the reasoning so far in this section is to do with the p values concerned with one statistical test. That is to say, for one individual pixel, we can be confident to a certain value of p, that its time course is correlated to the stimulus. When we form an image from the results of such statistical tests, it is necessary to consider how confident we are that none of the pixel labelled as 'active', are in fact due to random fluctuations. Take for example the SPM shown in Figure 6.17.

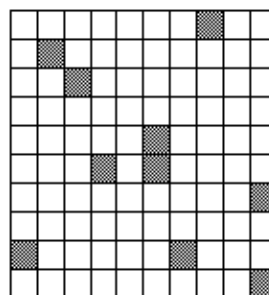


Figure 6.17 A 10 x 10 pixel matrix, with pixels shaded if they are shown to be 'active' by some statistical test with $p > 0.1$

Here a pixel is shaded if a statistical test shows that the pixel is active, with a p value greater than 0.1. Since there are 100 pixels in the image, it is probable that 10 pixels will, by chance, be falsely labelled as active. The p value for such an image would therefore be 1.0, that is to say that we are certain that at least one of the pixels is falsely labelled. This situation is called the multiple comparisons problem, and is well studied in statistics[24].

If all the pixels can be considered to be independent, then a Bonferroni correction can be applied. This states that for an image of N pixels, the overall probability of any false positive result is P , if the individual pixel false positive probability is P/N . However with thousands of pixels in an image, such a technique is very stringent, and the risk of falsely rejecting true activations is very high. There is also the question of whether each pixel in the image can truly be regarded as independent. The point spread function of the imaging process means that adjacent pixels cannot vary independently, and this situation is worse if additional smoothing is applied.

Such problems were first addressed in PET data analysis, and the results carried over to fMRI. The theory of Gaussian random fields[25], was developed for the analysis of functional imaging data by Friston *et. al.*[26] and an overview of their important results is presented here.

For a completely random, D -dimensional, z-statistical parametric map consisting of S pixels, the expected number of pixels that are greater than a particular z score threshold, u , is given by

$$E\{N\} = S \int_u^{\infty} (2/\pi)^{-1/2} \exp(-x^2/2) dx \quad . \quad (6.32)$$

This is the area under the Gaussian distribution as shown in Figure 6.16. The theory attempts to estimate the number of discrete regions there will be above this threshold. Take for example the SPM shown in Figure 6.18a. This is formed from a simulated data set with completely independent pixels. Those pixels with z-scores above a certain threshold are shown in white with those lower in black. The same data set, spatially smoothed before analysis is shown in Figure 6.18b. The number of white pixels in each SPM is about the same, but the number of discrete regions of white pixels is much less in the smooth case.

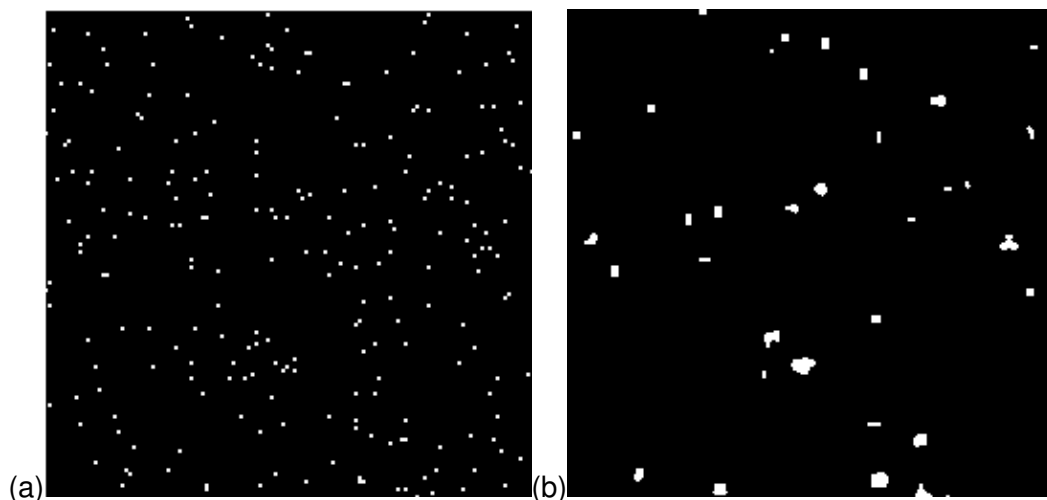


Figure 6.18. Two SPM's thresholded at the same Z-score. (a) Values obtained from unsmoothed data. (b) Values obtained from smoothed data

The expected number of regions appearing above u is estimated by

$$E\{m\} \approx S \cdot 2^{-(D+1)/2} W^{-D} u^{D-1} \exp(-u^2/2) \quad (6.33)$$

where W is a measure of the 'smoothness', or resolution of the map. This is obtained by measuring the variance of the first derivative of the SPM along each of the dimensions

$$W = \prod_{i=1}^D \text{Var}(\text{SPM}_i)^{-1/2D} \quad (6.34)$$

The average size of a region is thus given by

$$E\{n\} = \frac{E\{N\}}{E\{m\}} \quad (6.35)$$

Once these quantities have been estimated, the question is, what is the probability that a region (of activation) above a certain threshold u of size k pixels, could occur purely by chance. If k is of the order of $E\{n\}$ then this probability is quite high, but if $k \gg E\{n\}$ then the probability reduces. The form of this probability distribution is taken as

$$P(n_{\max} \geq k) = 1 - \exp[-E\{m\} \cdot \exp(-k^{2D})] \quad (6.36)$$

where n_{\max} is the size of the maximum region above u , in a random SPM, and

$$\mathcal{F} = \left(\frac{\Gamma(D/2 + 1)}{E\{n\}} \right)^{2D} \quad (6.37)$$

Thus for a given SPM the smoothness parameter W can be calculated, and only those regions above a chosen value of u that are of size greater than a chosen k are shown, the p value for the activation image can be calculated using equations 6.32 - 6.37.

6.4.4 Image Presentation and Inter Subject Comparisons

Having thresholded the SPM to display only those 'active' regions, these regions must be superimposed on background images to enable anatomical localisation. If the EPI images that the fMRI data comes from are of suitable quality, then these can be used as the base images. Better contrast may come from some inversion recovery images (see Section 2.4.1) showing only white matter, or grey matter. This is the practice used for the images shown in Chapter 7, and has the advantage that any distortions in the images will be the same for both activation and background, and no image realignment is needed. Higher resolution EPI images with equal distortion can be obtained using interleaved EPI as discussed in Chapter 5. To obtain really high quality base images it is necessary to use a 2DFT technique, however the distortions in such an image will be much less than the EPI functional images, and some form of alignment and 'warping' is required in this case.

The subject of comparing results from a number of different experiments, either on the same person at different times, or between different people, raises many issues, only a few of which are covered here.

Qualitative comparisons between subjects can be made by a good radiologist, familiar with EPI images, however in order to quantify differences it is necessary to try and 'normalise' the differences between the brains of the subjects. This has traditionally been done in functional imaging by using the atlas of Talairach and Tournoux[27], based on slices from the brain of a single person. It uses a proportional grid system based on the location of two anatomical landmarks, the Anterior Commissure (AC) and the Posterior Commissure (PC). Having identified the locations of the AC, PC, and the superior, inferior, left, right, anterior and posterior edges of the brain, these co-ordinates are rotated until the line joining the AC and PC is along the x axis, and the line joining the left and right markers is parallel to the z axis (Figure 6.19).

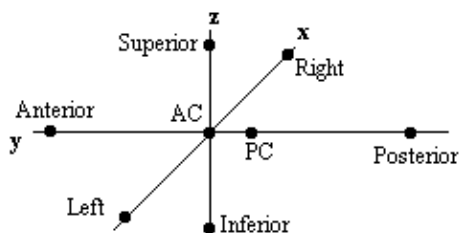


Figure 6.19 Co-ordinate system in the transformation to Talairach space

The same rotations are performed on any 'activation' region, and the co-ordinates are then scaled to give a distance in millimetres from the AC in each dimension, such that

- AC - PC = 23 mm
- AC - Anterior = 70 mm
- AC - Posterior = 102 mm
- AC - Superior = 74.5 mm
- AC - Inferior = 43 mm
- AC - Left = 68.5 mm
- AC - Right = 68.5 mm

These readings can then be looked up in the atlas to determine the location of the activation. Alternatively the whole image set can be similarly transformed to give a Talairach normalised set of images.

The main drawback of this technique is that it is based only on the brain of one person, and since gyri and sulci vary significantly between people, the reliability of using such an atlas is questionable. It is also questionable as to whether the proportional grid system is reliable enough to transform the images. As an alternative it is possible to warp the image until it fits the Talairach atlas brain[28]. If warping is used, then there are more appropriate templates available, which are based on MRI scans of a number of subjects. These templates attach probabilities to the spatial distribution of the anatomy[29], and are more reliable than a single subject template.

Even if the brains of several subjects are in some way normalised, there are questions as to how significant are differences in the magnitude of the signal change from one subject to another. A large amount of subject movement during the scanning will reduce the statistical likelihood of detecting activations. This could mean that activation which is present, but not detectable due to poor signal to noise, could be interpreted as no activation at all. Such problems have no easy solution, and more work is required in this area.

Consideration of these problems for a specific experiment is given in Chapter 7.

6.4.5 Software Implementation

Software was written which allowed the user to interactively change the values of u and k , and to look at the effect that this has on the activation image and its p-value. The graphical user interface (shown in Figure 6.20) is written in the scripting language 'perl'[30], which calls other 'C' programs to carry out most of the calculations and data manipulation.

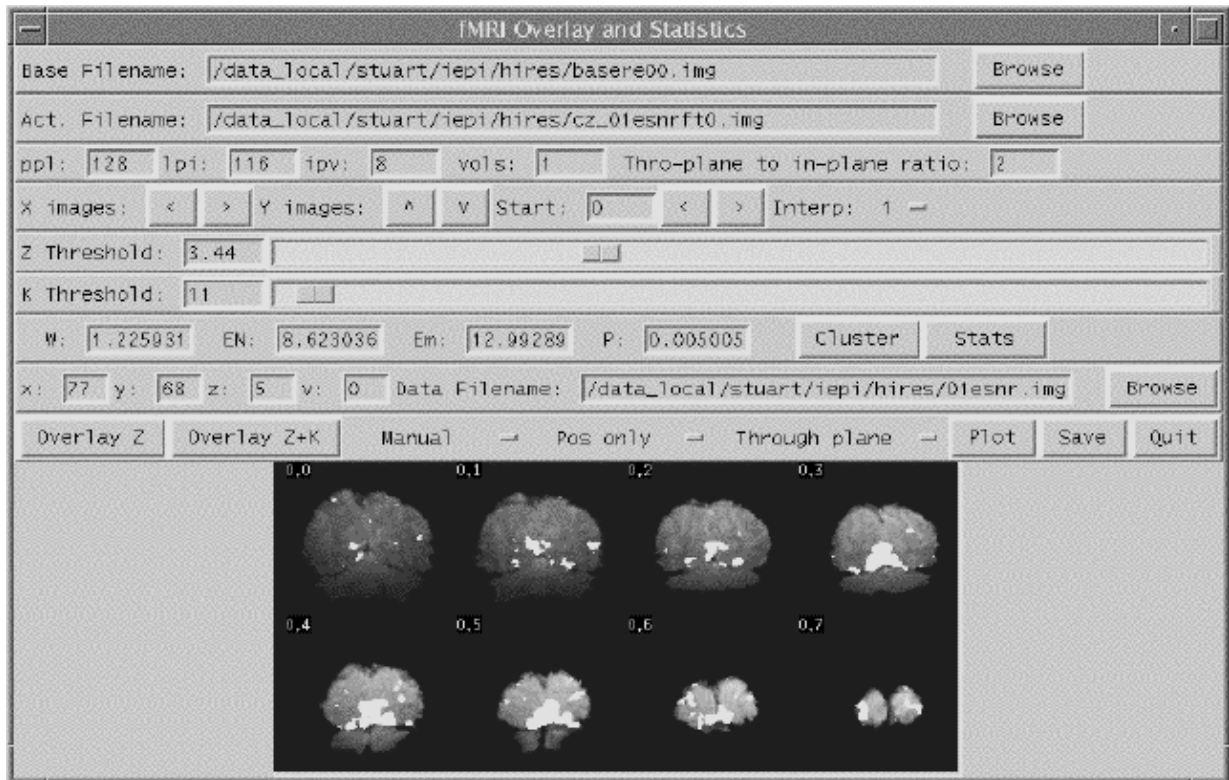


Figure 6.20 The front panel of the graphical user interface for the fMRI overlay and statistics software.y

SPMs of z-scores, stored as floats, are read in and thresholded at a z-score specified by a slider. These are displayed as white pixels, above a greyscale base image. The user can choose an appropriate cluster size threshold by either changing the slider or clicking on one of the regions with the mouse, and asking for the calculation of the size of that cluster. The activation image, with both thresholds applied can be displayed, and the p-value for such a combination calculated. It is necessary to change both thresholds interactively to find the optimum activation image for a given p-value, however results from Friston[31] suggest that wide signals are best detected using low z-thresholds and sharp signals with high z-thresholds.

The time course plots for any selected region can be displayed, with the 'plot' option. Any file can be chosen to take the plot intensities from, allowing the whole experiment time course, the average for one cycle, or Fourier components for the region to be displayed, provided that an image file containing such data exists.

Having chosen an appropriate set of thresholds, the images can be saved for display. The 'save' option allows any image file to be overlaid upon the base file, masked by the thresholded SPM. The base images are scaled between 0 and 20,000, and the 'active' regions scaled between 20,000 and 32,000, which allows an appropriate image viewing package to display the base images in greyscale and the activation in colour-scale. If the statistic used is also a good indicator of the magnitude of activation signal change, for example the t-statistic for the difference between 'rest'

and activity, then it is appropriate to display in colour-scale the pixel values from the SPM. However for statistics such as the correlation coefficient, the values do not represent the amount of signal change. In these cases it is more appropriate to display values from a percentage change image in colour, masked by the thresholded SPM. In order to appropriately identify the anatomical location of the activation, it is sometimes desirable to see the brain structure that underlies the activation. In this case it is appropriate to use the base images as the source of the values for the activation regions. This means that the effect can be created where the background image is in greyscale, and the active regions are 'shaded' in red-scale. Examples of overlaying SPMs, regressions and base sets are shown in Figure 6.21.

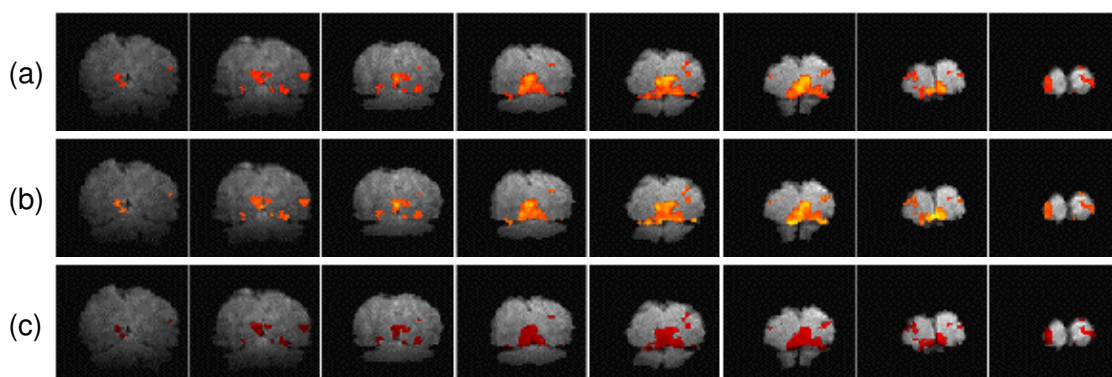


Figure 6.21 Three ways of presenting the final results of an fMRI experiment. (a) Active regions are shown in colour scale, with the colour (red to yellow) being determined by the magnitude of values from the statistical parametric map. (b) The colour scale represents the percentage signal change in that voxel upon activation. (c) The active regions are displayed as the red shaded regions of the base image set.

The software can also calculate the Talairach co-ordinates of any region, provided that the appropriate landmarks can be identified (or deduced) from the images. Having entered the co-ordinates of the landmarks, and chosen a region of interest, the co-ordinate system is rotated and proportionated, to give the distances in millimetres from the Anterior Commissure, of the centre of mass of that region in Talairach space.

The user instructions for the software is included as Appendix C.

6.5 Summary

The most important aspects of fMRI data analysis, as used on the data in this thesis have been presented above. The pre-processing steps improve the ability of the statistical analysis to detect activations. The choice of an appropriate statistical test depends on the assumptions that can be reasonably made, and the questions that need to be addressed. Decisions about the statistical significance of the results must take into account the multiple comparisons problem, and the reduction in degrees of freedom resulting from smoothing. Finally the results must be presented in an appropriate form, to enable the comparison of results between subjects.

In the whole process, many informed decisions need to be made, and it is difficult to propose a single 'black box' approach to the analysis, where data is fed in and an activation image is automatically fed out. However in order to formalise the analysis procedure to some degree, a standard analysis protocol was written. This is included as Appendix D.

There are many more issues in the analysis that have not been mentioned here, and much work that can be done. For example the Fourier Analysis methods for detecting periodic activations[32], principal component analysis[33], clustering techniques which detect clump together pixels having time courses which vary in the same way, and nonparametric tests[34]. There are other methods for

solving the multiple comparison problem [35] and for carrying out inter subject comparisons. It is this last area which requires the most attention, since, as fMRI becomes more and more a tool for neurologists to detect abnormality in brain function, the reliability of inter subject comparisons will become more important. It has been well shown that fMRI can give colourful pictures of the brain working, and it is necessary to take the techniques for data analysis onward if fMRI is to fulfil its clinical and neurological research potential.

6.6 References

- [1] *four1()* from Press, W. H., Teukolsky, S. A., Vetterling, W. T. and Flannery B. P. (1992) 'Numerical Recipes in C', Cambridge University Press.
- [2] The motion correction software described was written by Dr. A. Martel, Department of Medical Physics, University of Nottingham.
- [3] Hu, X., Le, T. H., Parrish, T. and Erhard, P. (1995) Retrospective Estimation and Correction of Physiological Fluctuation in Functional MRI. *Magn. Reson. Med.* **34**,201-212.
- [4] Friston, K. J., Williams, S., Howard, R., Frackowiak, R. S. J and Turner, R. (1996) Movement-Related Effects in fMRI Time-Series. *Magn. Reson. Med.* **35**,346-355.
- [5] Oppenheim, A. V. (1978) 'Applications of Digital Signal Processing', Prentice Hall.
- [6] Friston, K. J., Holmes, A. P., Poline, J.-B., Grasby, P. J., Williams, S. C. R., Frackowiak, R. S. J. and Turner, R. (1995) Analysis of fMRI Time-Series Revisited. *Neuroimage* **2**,45-53.
- [7] See Kernighan, B. W. and Ritchie, D. M. (1978) 'The C Programming Language', Prentice-Hall.
- [8] Analyze. Biomedical Imaging Resource, Mayo Foundation.
- [9] Bandettini, P. A, Jesmanowicz, A., Wong, E. C. and Hyde, J. S. (1993) Processing Strategies for Time-Course Data Sets in Functional MRI of the Human Brain. *Magn. Reson. Med.* **30**,161-173.
- [10] SPM from the Wellcome Department of Cognitive Neurology <http://www.fil.ion.ucl.ac.uk/SPM>.
- [11] Zar, J. H. (1996) 'Biostatistical Analysis', Prentice-Hall.
- [12] Miller, I. and Freund, J. E. (1977) 'Probability and Statistics for Engineers', Prentice-Hall.
- [13] Friston, K. J., Jezzard, P. and Turner, R. (1994) Analysis of Functional MRI Time-Series. *Human Brain Mapping* **1**,153-171.
- [14] SPM from the Wellcome Department of Cognitive Neurology <http://www.fil.ion.ucl.ac.uk/SPM>.
- [15] Friston, K. J., Holmes, A. P., Worsley, K. J., Poline, J.-B., Frith, C. D. and Frackowiak, R. S. J. (1995) Statistical Parametric Maps in Functional Imaging - A General Linear Approach. *Human Brain Mapping* **2**,189-210.
- [16] Lynn, P. A. (1989) 'An Introduction to the Analysis and Processing of Signals'. Macmillan.
- [17] Guenther, W. C. (1964) 'Analysis of Variance'. Prentice-Hall.

- [18] Mood, A. M. and Graybill, F. A. (1963) 'Introduction to the Theory of Statistics'. McGraw-Hill, Second Edition p232.
- [19] Hykin, J., Clare, S., Bowtell, R. Humberstone, M., Coxon, R., Worthington, B., Blumhardt, L. D. and Morris, P. A Non-directed Method in the Analysis of Functional Magnetic Resonance Imaging (fMRI) and it's Application to Studies of Short Term Memory *in Book of Abstracts, 13th Annual Meeting, European Society of Magnetic Resonance in Medicine and Biology* 366.
- [20] MATLAB. The Math Works, Inc.
- [21] Friston, K. J., Jezzard, P. and Turner, R. (1994) Analysis of Functional MRI Time-Series *Human Brain Mapping* **1**,153-171.
- [22] Friston, K. J., Holmes, A. P., Poline, J.-B., Grasby, P. J., Williams, S. C. R., Frackowiak, R. S. J. and Turner, R. (1995) Analysis of fMRI Time-Series Revisited *Neuroimage* **2**,45-53.
- [23] Worsley, K. J. and Friston, K. J. (1995) Analysis of fMRI Time-Series Revisited - Again *Neuroimage* **2**,173-181.
- [24] Zar, J. H. (1996) 'Biostatistical Analysis', Prentice-Hall. p.211.
- [25] Cox, D. R. and Miller, H. D. (1990) 'The Theory of Stochastic Processes', Chapman and Hall.
- [26] Friston, K. J., Frith, C. D., Liddle, P. F. and Frackowiak, R. S. J. (1991) Comparing functional (PET) images: The assessment of significant change. *J. Cereb. Blood Flow Metab.* **11**,690-699.
- [27] Talairach, J. and Tournoux, P. (1988) 'Co-planar Stereotaxic Atlas of the Human Brain', Thieme.
- [28] Collins, D. L., Neelin, P., Peters, T. M. and Evans, A. C. (1994) Automatic 3D Intersubject Registration of MR Volumetric Data in Standardized Talairach Space. *J. Comput. Assist. Tomogr.* **18**,192-205.
- [29] Mazziotta, J. C., Toga, A. W., Evans, A., Fox, P. and Lancaster, J. (1995) A Probabilistic Atlas of the Human Brain: Theory and Rationale for its Development. *Neuroimage* **2**,89-101.
- [30] See Wall, L. and Schwartz, R. L. 'Programming Perl', O'Reilly & Associates.
- [31] Friston, K. J., Worsley, K. J., Frackowiak, R. S. J., Mazziotta, J. C. and Evans, A. C. (1994) Assessing the Significance of Focal Activations Using their Spatial Extent *Human Brain Mapping* **1**,214-220.
- [32] Lange, N. and Zeger, S. L. (1997) Non-linear Fourier Time Series Analysis for Human Brain Mapping by Functional Magnetic Resonance Imaging. *Applied Statist.* **46**,1-29.
- [33] Backfrieder, W., Baumgartner, R., Sámal, M., Moser, E. and Bergmann, H. (1996) Quantification of Intensity Variations in Functional MR Images Using Rotated Principal Components. *Phys. Med. Biol.* **41**,1425-1438.
- [34] Holmes, A. P., Blair, R. C., Watson, J. D. G. and Ford, I. (1996) Nonparametric Analysis of Statistic Images from Functional Mapping Experiments. *J. Cereb. Blood Flow Metab.* **16**,7-22.

[35] Forman, S. D, Cohen, J. D., Fitzgerald, M., Eddy, W. F., Mintun, M. A. and Noll, D. C. (1995) Improved Assessment of Significant Activation in Functional Magnetic Resonance Imaging (fMRI): Use of a Cluster-Size Threshold. *Magn. Reson. Med.* **33**,636-647.

Chapter 7

Functional MRI of Motor Function

7.1 Introduction

The ability to control our movement is something that most of us take for granted. From the swift responses required to hit a cricket ball, to the delicate and steady action of surgeon, the brain is able to control the muscles in the body in a precise and efficient way. Motor function is controlled by four major regions in the frontal lobes; the primary motor cortex, supplementary motor area (SMA), lateral premotor cortex and the cingulate motor area (shown in Figure 7.1). The primary motor cortex is responsible for the direct production of movements via its outputs to the pyramidal tract, and damage to these areas resulting from stroke produces a weakness in the corresponding part of the body. The other three areas are responsible for higher order control of motor function.

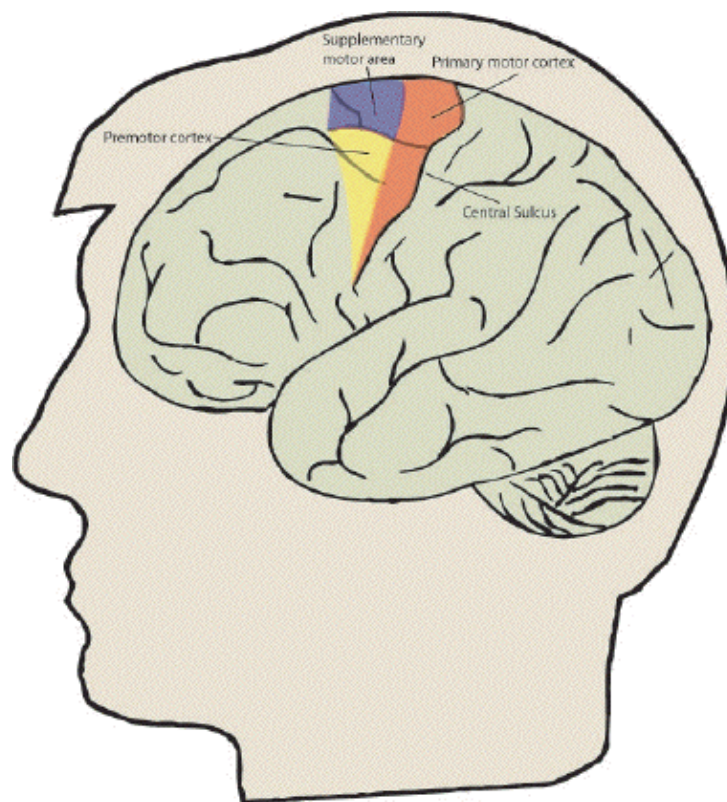


Figure 7.1 Locations of the primary motor cortex, premotor cortex and supplementary motor area.

Studies of the SMA using PET have shown that it is involved in motor task sequencing and movement initiation [1], however it has more recently been suggested on the basis of animal studies that the SMA could be divided into two discrete areas; the preSMA and the SMA proper [2]. The SMA proper, projecting to and receiving inputs from the primary motor cortex, it is suggested is more directly responsible for movement execution, whereas the pre-SMA, receiving inputs from the prefrontal cortex and the cingulate motor areas, might be responsible for movement decision making.

In order to test this hypothesis on humans, using fMRI, it was necessary to use an experiment that allows the elements of decision making and movement to be separated. Such an experiment would

be difficult to carry out in a standard epoch based paradigm with activation lasting for a number of seconds. This would require a number of movement decision making tasks to be carried out in each epoch, and separation of the areas responsible for the execution of the movement from those responsible for the decision making would be impossible. Instead of this, single event paradigms were developed, where one movement decision task was performed every 20 seconds or so, allowing discrimination between areas activated when the decision to move was made and those activated when the decision not to move was made.

In this study the paradigm design, subject handling and data analysis and inference was carried out by Dr. Miles Humberstone [3].

7.2 Methods

7.2.1 Stimulus Presentation

For most paradigms involving the motor cortex, it is necessary to provide some form of cue to the subject to move and, in most cases, a measurement of the movement made.

All our studies involve hand movements since these are the simplest to measure. The cue to move was given from a 6 cm single digit LED display, as sketched in Figure 7.2.

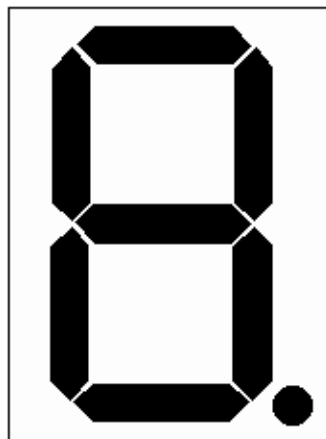


Figure 7.2 Sketch of the single digit display used to present visual cues to the subject.

This allowed the presentation of symbols, individual bars or the dot as well as numbers. To measure response times the subject was given two hand held buttons, one for the left hand and one for the right hand, operated by a thumb press. A schematic diagram of the stimulus rig is shown in Figure 7.3.

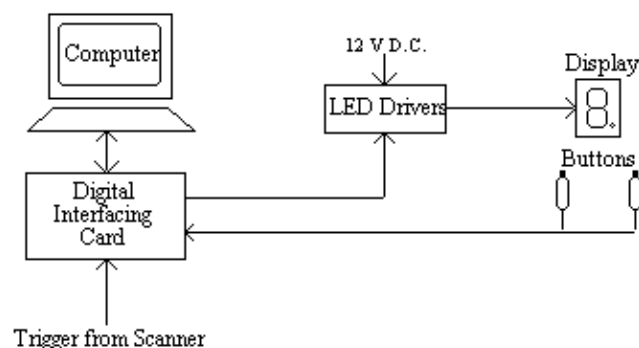


Figure 7.3 Schematic diagram of stimulus presentation equipment.

The experiment was controlled by a PC fitted with an interfacing card [4]. This card had a number of analogue input and output ports, 18 digital lines that could be configured in ports of eight to be either input or output, and three counter-timers. The card produced a 5 V D.C. power supply, which was not enough to drive the LED's, so a Darlington driver IC was used as a buffer to provide the 12 V required. The hand held buttons consisted of a 10 cm tube with a micro-switch mounted on the top. The switch required little force to depress and travelled a couple of millimetres. It had a clear action however, so that the subject would know they had pressed it. The switch formed part of a circuit that held the digital input line to the interfacing card at ground normally, and to 5 V when depressed. A 5 ms TTL trigger from the scanner was obtained for every scan, and this fed to one of the digital input lines on interfacing card.

The counters on the card were arranged in a cascade. Counter 1 received triggers from the PC's internal clock at the rate of 2 MHz, and was set to output one pulse every 2000 triggers, that is every millisecond.

This millisecond trigger was sent to the second counter, which was set to count to 1000, thereby producing a trigger every second.

Counter 3 received this signal and counted to its limit (60,000). Thus any length of time could be measured to a accuracy of milliseconds by reading counters 2 and 3 (see Figure 7.4).

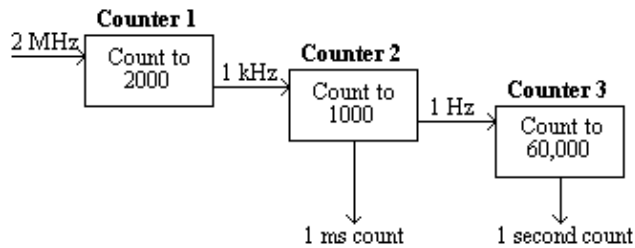


Figure 7.4. Cascading three counters to count in milliseconds and seconds.

The software to control the stimulus was written in 'C' [5]. The general flow of programs consisted of a loop to count over the cycles, loops to count over the number of stimuli presented per cycle and a loop to repeatedly monitor the scanner triggers, counters and subject buttons. Figure 7.5 shows an example flow diagram for an experiment that presented a 200 ms visual cue every 10 scans and measured the time it took the subject to respond by pressing the button. In this example there are 50 scans of activity and 50 scans of rest, repeated 10 times. Other experiments were programmed in a similar way. Triggering the experiment from the scanner ensured that there were no timing errors. The response times were stored in a data file on the computer for later analysis if required.

The display and buttons could be connected locally to the computer, for testing and subject practice, and connected remotely during the scanning itself. The single digit display was mounted on a plastic support inside the scanner, about 50 cm away from the subjects face.

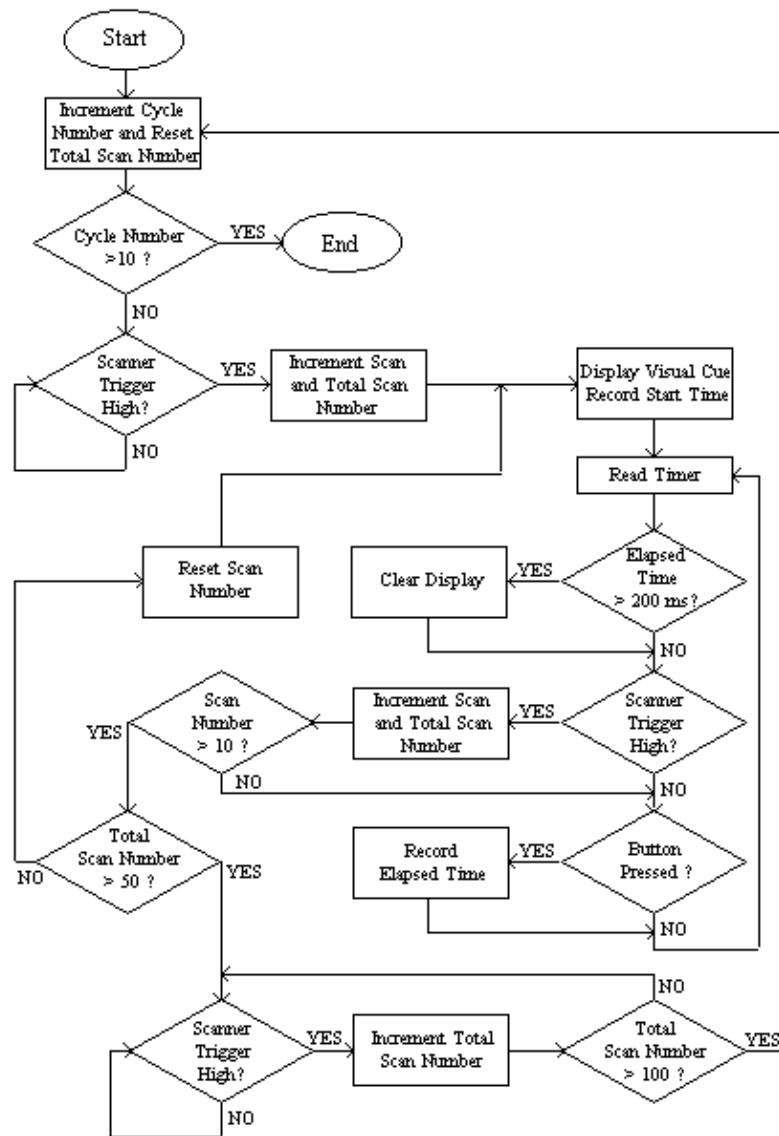


Figure 7.5. Example flow diagram of software to control stimulus presentation and measure reaction times, kept in pace by triggers from the scanner.

7.2.2 Paradigm Development

The initial basis of the paradigm used came from electrophysiological experiments. The oddball paradigm consists of the regular presentation of a stimulus, for example the visual presentation of the digit '2', and infrequently presenting an 'oddball' stimulus such as a '5'. On the presentation of the '5' the subject is required to respond by pressing a button. Regardless of the form the cue stimulus takes, EEG signals from a subject carrying out such a task reveal a peak with a latency of 300 ms, labelled the P300, in response to every oddball stimulus [6].

The implementation of this paradigm for fMRI involved presenting the digits using the LED display described above, at a rate of 2 Hz, with the oddball stimulus occurring at a pseudo-random interval of average 12 s. Analysis of the brain activation of the oddball responses, compared to the interval in between, should reveal those areas involved directly in the movement, including the SMA.

A slight change to the paradigm enabled discrimination between areas involved in the movement decision making and those involved more directly in the movement itself. If the stimuli are presented

at a less frequent rate (one every 18 seconds) and the '2' or '5' presented with equal probability, the paradigm is of the form of a 'go, no-go' experiment [7]. The subject again responds only to the '5', but the brain response to the '2' will reveal areas responsible for the movement decision making process. The use of the digits '2' and '5' on the LED display make the stimuli symmetrical and of equal luminance. In total 50 stimuli were presented, with equal numbers of go and no-go stimuli presented in pseudo-random order. Six normal volunteers were studied using the 'go, no-go' paradigm.

7.2.3 Imaging

The imaging for this experiment was carried out on a dedicated EPI scanner [8]. The static 3.0 Tesla field was produced by a superconducting magnet (Oxford Magnet Technology).

The gradient coils were designed for high uniformity, low heating and high efficiency, especially in the z-axis [9]. The efficiencies of the three axis are: $G_x = 0.087 \text{ mTm}^{-1}\text{A}^{-1}$; $G_y = 0.087 \text{ mTm}^{-1}\text{A}^{-1}$; $G_z = 0.35 \text{ mTm}^{-1}\text{A}^{-1}$. Due to its high efficiency, the z-axis gradient coil was used as the switched axis. This coil was driven as part of a tuned resonant circuit at a frequency of 1.9 kHz, by a bank of 8 power amplifiers (Techron) connected in parallel. The blipped and slice select gradients were driven by 2 and 6 power amplifiers respectively.

A birdcage radiofrequency coil was used, to give the most uniform r.f. field over the whole volume of the brain. R.f. power amplification came from a 10 kW amplifier. Gradient and RF control is carried out by a set of in-house built waveform synthesis modules. These are controlled by a UNIX workstation (Sun Microsystems) via a VME bus [10].

For the motor function experiments there were two requirements of the scanning; whole brain imaging and fast repetition rate. The rate of scanning is largely limited by the heating of the gradient coils and the rate that data can be processed and stored. Using a matrix size of 128×128 , with an in-plane resolution of $3 \times 3 \text{ mm}^2$, had the advantage that the brain filled only half of the field of view, meaning that the N/2 ghost did not overlap and interfere with the image (see section 4.3.1). The gradient heating and rate of saving data limited the acquisition of images of this matrix size to four a second ($TR = 250 \text{ ms}$).

To improve the repetition rate, a matrix size with half as many lines (128×64) was used, allowing a TR of 150 ms if scanning continuously for less than 5 minutes and a TR of 187 ms for less than 30 minutes continuous scanning. The other advantage of using the smaller matrix size is that the total sampling time is reduced by half (from 33 to 16.5 ms), thereby doubling the frequency per point in the broadening direction and halving the distortion (see section 5.3.1).

To cover the whole brain in 9 mm contiguous slices would take 2.4 seconds at the fastest repetition rate (150 ms). To reduce the time taken to acquire each volume required a reduction in the number of slices acquired, either by increasing the slice thickness or reducing the area of brain that is covered. Earlier experiments were carried out using thicker slices, or with volume repetition rates of greater than 2 seconds. When the regions of the brain that were of interest had been ascertained, the slice thickness was kept at 9 mm and 10 slices chosen that covered this region, reducing the volume repetition rate to 1.5 seconds.

Anatomical reference images were obtained for each subject using the fast inversion recovery sequence described in section 4.4. Grey matter null images were obtained using an inversion time of 1200 ms and white matter null images with an inversion time of 400 ms. The slice thickness was reduced to 3 mm for these images and the slices acquired such that three of these images corresponded exactly to one of the functional images.

Various methods were used to restrain the subjects head during scanning. Polystyrene foam, wedged between the perspex former of the r.f. coil and either side of the subjects head was effective but became uncomfortable after 10 minutes or so. In addition the subject could still move their head forward and backward. A more rigid restraint was also tried, with foam ended rods that went into either ear, and a bridge that went across the nose. This was hard to adjust, and extremely uncomfortable for the subject after only a few minutes. The head was well restrained with this method, but the subjects often made deliberate movements during scanning to reduce discomfort.

A third and more successful method was to use inflatable sphygmomanometer cuffs either side of the head. These could be inflated until the subject was comfortable but well restrained. An open-cell polyurathane foam was used underneath the head which was softer and therefore more comfortable than the polystyrene foam. Although the subject was free to move the head forward and backward, the increased comfort attained made them less likely to move in this way. Representations of the three types of restraint are shown in Figure 7.6.

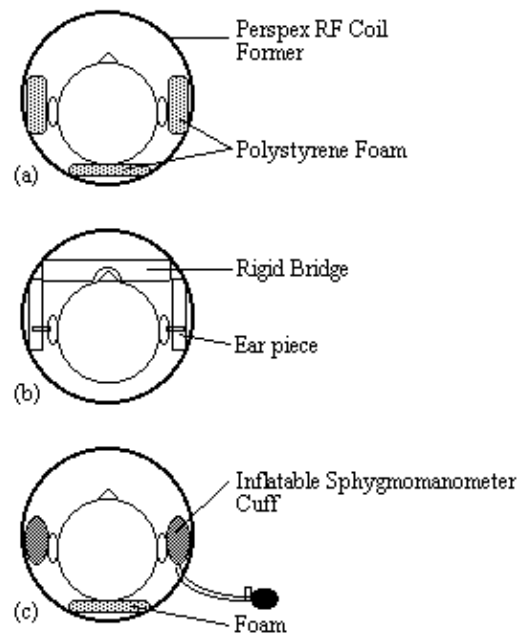


Figure 7.6 Three methods of subject restraint. (a) Polystyrene foam padding, (b) rigid head restraint and (c) inflatable cuff.

7.2.4 Analysis

The data from this experiment were analysed using the methods described in Chapter 6. Registration, normalisation, spatial and temporal filtering were carried out using the pre-processing package described in section 6.2.

The statistical analysis used was a serial t-test (section 6.3.4), with a baseline period defined at 3 to 6 seconds prior to the stimulus presentation. The responses to the 'go' stimulus were processed separately to the responses to the 'no-go' stimuli, with any errors in the response excluded from the analysis. This produced two sets of t-statistical parametric maps, which could be analysed using the theory of Gaussian random fields (section 6.4.3).

The activation maps were interpolated up to 60 slices and superimposed directly on the inversion recovery images, displayed as 3-D volumes to help anatomical localisation of the activated regions. Talairach co-ordinates were obtained for each active region.

For each subject the point in the time course of maximal activation in the rostral and caudal medial premotor cortex was identified, and the percentage changes in response to the 'go' and 'no-go' tasks from the rest state measured. Similarly the points of maximal activity during the 'go' and the 'no-go' task were identified in the primary motor cortex. Paired t-test comparisons between the 'go' and 'no-go' percentage changes were performed across subjects for these regions of maximum activity.

7.3 Results

Figure 7.7 shows the activation at 0 s, 3 s, 6 s and 9 s following the stimulus, for one subject in the 'go, no-go' experiment. Maximum activation occurs at 3-6 seconds from the delivery of the stimulus. During the 'no-go' task, activation was seen in the medial premotor cortex for all the subjects. This region was rostral to the anterior commissural (AC) line. Activity was observed in these regions during the 'go' task as well (see Figure 7.8). During the 'go' task activation was also seen in a region of the premotor cortex caudal to the AC line.

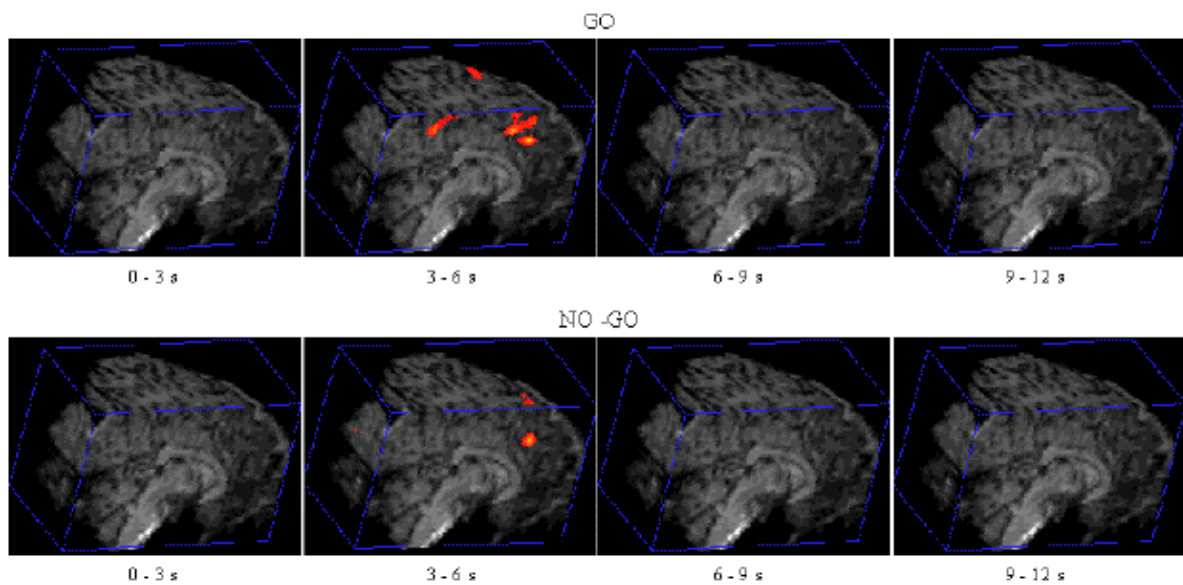
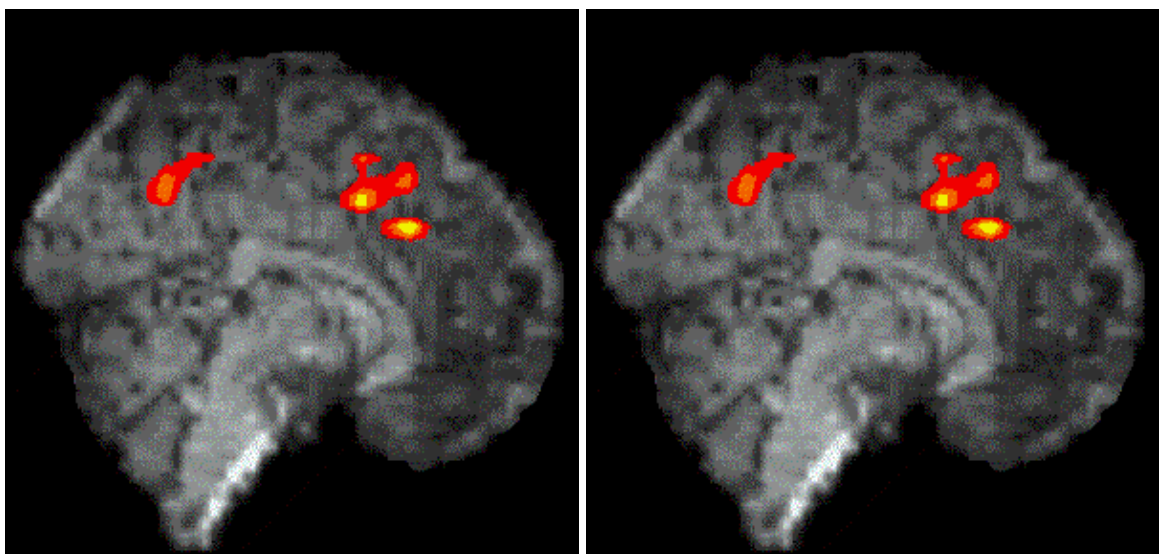


Figure 7.7 Volume images acquires between 0 and 12 seconds after the presentation of either a 'go' or 'no-go' stimulus



Go

No-Go

Figure 7.8 View of the medial surface of the left hemisphere, three seconds after the stimulus in a go, no-go paradigm.

The mean value of the percentage change upon activation of the areas involved in the motor task are shown in Figure 7.9. This shows the rostral part of the premotor cortex (labelled pre-SMA) to be active in both 'go' and 'no-go' tasks, with the caudal part (labelled SMA) being only active in the 'go' task. This suggests that the pre-SMA is involved in the movement decision making aspect of the task, whereas the SMA proper is more intimately involved in the movement itself.

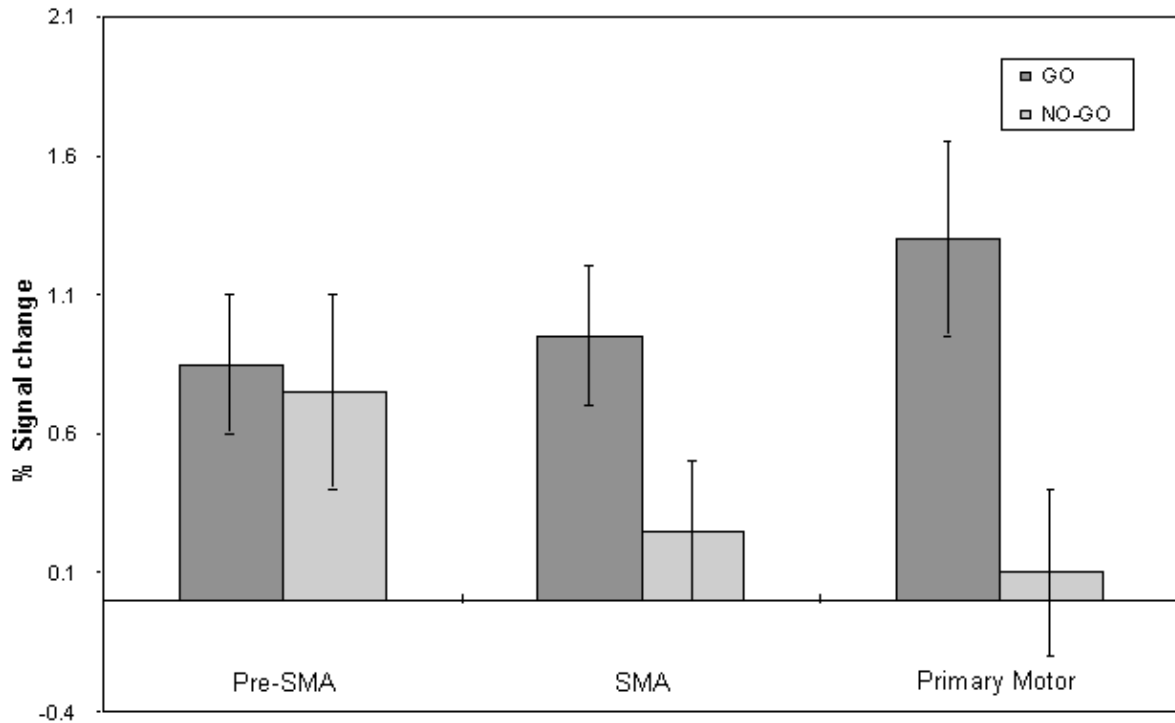


Figure 7.9 Plots of the percentage signal change in the Pre-SMA, SMA and primary motor cortex, for the 'go' and the 'no-go' task.

7.4 Discussion

The results presented illustrate that the imaging of single events is possible. As was mentioned earlier, such a study of movement decision making would be difficult to carry out using a traditional epoch based paradigm. From the electrophysiological measurements of such tasks, it is clear that the neural activity only lasts a few hundred milliseconds, however such short neural events can be detected using fMRI. This is important since many other interesting cognitive paradigms do not adapt easily to providing periods of sustained activity. Since similar techniques of stimulus presentation are used in brain studies using evoked potentials, the same experiments can be used with both modalities.

Single event paradigms require longer experiments than their epoch based counterparts, in order that the required signal to noise ratio is achieved. A delay of at least 10 seconds is required between each stimulus to enable the blood flow changes to return to the baseline.

7.5 References

- [1] Passingham, R. (1993) 'The Frontal Lobes and Voluntary Action'. Oxford University Press.
- [2] Matsuzaka, Y., Aizawa, H. and Tanji, J. (1992) A Motor Area Rostral to the Supplementary Motor Area (Presupplementary Motor Area) in the Monkey: Neuronal Activity During a Learned Motor Task. *J. Neurophysiol.* **68**,653-662.
- [3] Humberstone, M., Sawle, G. V., Clare, S., Hykin, J., Coxon, R., Bowtell, R., Macdonald, I. A. and Morris, P. (1997) Functional MRI of Single Motor Events *Annals of Neurology* In Press.
- [4] Lab PC+, National Instruments Corporation.
- [5] Turbo C++, Borland.
- [6] Rohrbaugh, J. W., Parasuraman, R. and Johnson, R. (1990) 'Event-Related Brain Potentials', Oxford University Press.
- [7] Leimkuhler, M. E. and Mesulam, M. M. (1985) Reversible Go-No go Deficits in a Case of Frontal Lobe Tumour. *Ann. Neurol.* **18**,617-619.
- [8] Mansfield, P., Coxon, R. and Glover, P. (1994) Echo-Planar Imaging of the Brain at 3.0 T: First Normal Volunteer Results. *J. Comput. Assist. Tomogr.* **18**,339-343.
- [9] Peters, A. M., Mansfield, P. and Bowtell, R. (1996) A short head gradient set for EPI at high magnetic field. *in* Book of Abstracts, 13th Annual Meeting *European Society of Magnetic Resonance in Medicine and Biology*. Abstract 138.
- [10] Glover, P. (1993) High Field Magnetic Resonance Imaging. PhD Thesis, University of Nottingham.

Chapter 8

Discussion

As was said at the start of this thesis, the field of fMRI is rapidly finding clinical application and is exciting scientists from a range of disciplines including neurologists, psychiatrists and psychologists. However, there is still much research and development that needs to be done on the technique itself.

The effect of echo time (TE) on the ability to detect signal change due to the BOLD effect is striking, in particular the lack of detectable BOLD contrast at low echo times (< 15 ms). The results from the echo time measurement experiment described in Chapter 4, that the most suitable echo time to use for fMRI of the auditory, visual or motor cortices 3.0 T being between 30 and 40 ms, takes some of the guess work out of the choice of imaging parameters to use when engaging in a new fMRI study. There are other parameters that may also have a significant effect on the level of BOLD contrast, such as slice thickness, voxel size and repetition rate (TR), and these will need to be investigated. The single shot T_2^* measurement technique not only provides a quick and reliable way to find the optimum echo time, but also provides a way to map the actual changes in T_2^* upon functional stimulation. This will give a more direct handle on one of the effects of changes in blood oxygenation, and may prove useful in determining the underlying mechanisms of the BOLD effect.

Image quality is always important in MRI, since artefact can be misleading to a clinician trying to interpret results. The N/2 ghost is one of the most obvious artefacts in echo planar images, and its presence not only spoils the appearance of the images, but can also prevent the detection of signal changes due to the BOLD effect. The assessment of various methods for correcting this particular artefact in Chapter 4 suggested that the method by Buonocore, which does not require a reference scan, is the most appropriate to use on fMRI data. However this result will have to be verified by its routine use on 'real' fMRI data sets. The second artefact correction technique described in Chapter 4, the removal of the effect of external r.f. interference, is purely cosmetic, however its use again means that the final activation images are clearer for clinical assessment.

The fast inversion recovery pulse sequence presented has enabled the reduction in the time a subject spends in the scanner. Any such methods for reducing the experimental duration are desirable, not only since they make precious scanner time more efficient, but also because subject discomfort is reduced. The standard experimental protocol, as given in Appendix A, and explained in Chapter 4, gives a framework to enable the consistent acquisition of fMRI data. The activation maps show a great deal of variability between subjects, and some variability within subjects scanned at different times, due to physiological effects, and so any standardising procedure that reduces variability in the way that the scanning is carried out is helpful. The protocol will need to be developed with time, as changes in scanner hardware and software are made, and as new information on optimum imaging parameters becomes available.

The main conclusion from the experience of using interleaved EPI for high resolution fMRI, is that methods for correcting the effect of subject movement need to be developed if the technique is to provide useful results. However the results that are shown in Chapter 5 indicate that effort in this area is worthwhile, since greater detail can be obtained from sub-millimetre resolution fMRI. In the meantime, the technique will be useful in reducing the distortion in activation images or for providing high resolution anatomical images with identical distortion to the overlaid activation maps.

The statistical analysis of fMRI data is being actively researched in many functional imaging centres and much effort is needed in this area. The new methods for the non-directed analysis of data

explained in Chapter 6 offer the possibility of detecting regions of activation exhibiting many different time courses and allow the analysis of single event cognitive paradigms. More techniques of this kind are needed, all of which must be put on a firm statistical footing, and methods that are powerful in detecting activations and statistically robust will find great application amongst clinicians not familiar with the fMRI analysis. In the suite of programs that have been developed, and that are documented in Chapter 6, a straightforward and minimal input way of analysing fMRI data has been offered.

The results presented in Chapter 7 show that single event functional imaging, where the subject undertakes a single task, relatively infrequently, can yield important neurological results. The separation of motor planning events from execution has confirmed the sub-division of supplementary motor area, and its role in motor function.

It has now been firmly established that magnetic resonance imaging can be used to map brain function. The main impetus of research and development of the technique, needs to be directed in several areas if fMRI is to become more than 'colour phrenology', intriguing in its results yet having little clinical value. The mechanisms behind the BOLD effect need to be better understood, as does the physiological basis of the observed blood flow and oxygenation changes. The combination of the functional imaging modalities needs attention, since it is unlikely that any one method will provide the full picture. Finally, robust and simple techniques for data analysis need to be developed, allowing those who do not specialise in fMRI, to carry out experiments and interpret results. All that said, functional MRI offers possibilities for basic neurological research and clinical application that could not have been imagined ten years ago, and I am sure that the next ten years will be just as exciting.